Simulation of superparamagnetic particle trajectories in a microfluidic device for magnetic separation purposes



Tim David Grob
St. Catherine's College

Department of Engineering Science
University of Oxford

A thesis submitted for the degree of *Doctor of Philosophy*
Trinity Term 2018

Abstract

Magnetic particle separation in microfluidic systems is a method for enriching or isolating biological entities such as cells or biomarkers of diseases using magnetic beads that covalently bind to a target; it is compatible with lab-on-a-chip technology and has potential to be integrated with other functional blocks. This thesis describes the operation of a magnetic particle separator using a novel configuration of permanent magnets to provide higher separation efficiency with minimum trapping of particles. The novel magnet configurations consisted of two (Double Magnet) or four (Quadrupole) rectangular permanent magnets arranged around a microfluidic channel. The magnet configurations guide magnetic particles along adjustable trajectories by simply varying the separation distance between the magnets or their aspect ratio. Influence of the salient geometrical parameters on the behaviour of the trajectory was studied and experimental verifications are presented using particle suspensions of 1 μm and 2.8 μm sized magnetic beads. In addition, it was discovered that the magnetic beads gather along a line that can be uniquely positioned within the fluidic cell leading to improved performance.

The performance of the magnetic separator was studied for five magnetic particle types by simulating 400 individual particle trajectories following an Eulerian-Lagrangian model. The model incorporated experimentally found particle properties such as size and susceptibility. Magnetic separation was performed in continuous flow and pulse mode operation. In continuous separation a maximum separation

efficiency of 35% and 55% was found experimentally for the Double Magnet and Quadrupole configuration, respectively, and in pulse mode operation a separation efficiency of more than 80% could be achieved in experiments and simulations. Further, in order to improve the accuracy of the magnetophoretic force calculations, the magnetic responsiveness of the particle types across a magnetic field range of $38 - 70$ mT was studied using a particle tracking system and SQUID relaxometry. The susceptibility of all particle types showed a magnetic field dependence and a promising correlation between the two measurement techniques could be found.

Acknowledgements

I would like to bestow significant credit for this work to Prof. Steve Sheard, who has accepted me as a research student. I could not have imagined having a better advisor and mentor for my doctoral work with such patience, motivation, enthusiasm, and immense knowledge. Without his guidance, insights, and creativity, many of the advances reported here would not have been realized. Over the course of my PhD I have learned so much and grown in a number of ways both professionally and personally thanks to a considerable part of Steve.

Very special thanks goes to Naomi Wise, who has supported me over endless hours in the laboratory and who made these sometimes frustrating and seemingly hopeless moments a lot more bearable.

I also want to thank Olayinka Oduwole and Duo Zhang for their inspiring and stimulating discussions.

I am also grateful for the financial support I got from the Janggen-Poehn Stiftung from the city of St. Gallen in Switzerland, which supported me financially for my time at Oxford University.

Last but not least, I wish to express sincerely gratitude to my beloved family for their understanding and endless love and to my dear friends for their help and warm encouragement.

Contents

Abstract **i**

List of Figures **xi**

List of Tables **xix**

Nomenclature **xxi**

Publications **xxix**

1 Introduction **1**

1.1 Microfluidics and micro total analysis systems 1

1.1.1 Microfluidics bio-sensors for point-of-care diagnostics 4

1.2 Magnetic micro- and nanoparticles 7

1.3 Cell separation in microfluidic systems for biomedical applications . . 9

1.3.1 Passive particle separation 13

1.3.2 Active particle separation 18

1.4 Magnetophoresis 24

1.4.1 Batch mode magnetophoresis 26

1.4.2 Continuous magnetophoresis 30

1.5 Numerical particle trajectory simulation 44

1.6 Motivation 48

1.7 Aims and objectives 50
1.8 Outline 51
1.9 Contribution 52

2 Fundamentals of magnetophoresis and its simulation 53

2.1 Introduction 53
2.2 Fluid motion in microfluidic systems 53
2.2.1 Steady unidirectional flow in a rectangular duct 55
2.2.2 Particle laden flow in microfluidic systems 58
2.2.3 Hydrodynamic focusing 60
2.3 Magnetism 62
2.3.1 Magnetic field 63
2.3.2 Magnetic hysteresis and saturation 65
2.3.3 Magnetic materials and properties 66
2.4 Theory of magnetophoresis 69
2.4.1 Lagrangian particle tracking 72
2.5 Mathematical formulation of finite element equations for magnetostatic problems 73
2.5.1 Error estimation of the finite element method 76
2.6 Statistical data analysis 80
2.6.1 Significance testing 81

3 Experiments and simulations 84

3.1 Introduction 84
3.2 Particle suspension 84
3.2.1 SEM imaging of magnetic beads 86
3.3 Microfluidic devices and chambers 86
3.3.1 Microfluidic hydrodynamic focusing device 87

3.3.2 Microfluidic separation device 88
3.3.3 Microfluidic counting slide 88
3.3.4 Hydrostatic fluid chamber 89
3.4 Magnetic field measurement 90
3.5 Magnetophoretic mobility experiment 92
3.6 SQUID measurement 93
3.7 Hydrodynamic focusing 94
3.7.1 Hydrodynamic focusing simulation 95
3.7.2 Hydrodynamic focusing experiment 96
3.8 Magnet configurations 98
3.8.1 Double Magnetic configuration 98
3.8.2 Quadrupole configuration 99
3.9 Static gathering points experiments 100
3.9.1 Magnet height variation 102
3.9.2 Magnet vertical separation variation 103
3.9.3 Magnet geometry 103
3.10 Magnetic particle trajectory simulation 104
3.10.1 Magnetic field simulation 104
3.10.2 Discrete particle trajectory simulation 105
3.11 Magnetic separation efficiency 108
3.11.1 Separation efficiency simulation 108
3.11.2 Separation efficiency experiment 110

4 Magnetophoretic mobility **112**

4.1 Introduction 112
4.2 Magnetophoretic mobility of superparamagnetic beads 114
4.2.1 Properties of the static magnetic field 116
4.2.2 Size characterization of superparamagnetic beads 118

4.2.3 Magnetically induced velocity on superparamagnetic beads . . 120
4.3 Magnetophoretic mobility of superparamagnetic bead agglomerates . 123
4.4 Magnetization of superparamagnetic beads 130
4.5 Comparison of the susceptibility based on the mobility and magnetization study 135
4.5.1 Analysis of variance 137
4.5.2 Regression analysis 138
4.5.3 Numerical scaling analysis 139
4.6 Discussion 140
4.7 Conclusion 143

5 Hydrodynamic flow in a microfluidic device 150
5.1 Introduction 150
5.2 Hydrodynamic flow in a microfluidic separation device 150
5.3 Hydrodynamic focusing in a microfluidic separation device 152
5.3.1 Entrance length 153
5.4 Conclusion 155

6 Magnetic separation configuration 159
6.1 Introduction 159
6.2 Magnet configurations 159
6.2.1 Double Magnet configuration 160
6.2.2 Quadrupole configuration 168
6.3 Gathering line formation 172
6.3.1 Gathering of particle agglomerates 178
6.4 Discussion 180
6.5 Conclusion 184

7 Magnetic particle separation simulation **186**

7.1 Introduction 186

7.2 Continuous separation of the two novel magnet configurations 187

7.2.1 Magnetic separation using the Double Magnet configuration . 188

7.2.2 Magnetic separation using the Quadrupole configuration . . . 198

7.3 Wall effects on the motion of a single particle 202

7.4 Magnetic separation in pulse mode 205

7.4.1 Magnetic separation efficiency experiment in pulse mode . . . 207

7.5 Discussion and Conclusion 209

8 Summary and Outlook **214**

8.1 Summary of achievement 214

8.2 Future Work 219

8.2.1 Simulation of suspension with higher order agglomerates . . . 219

8.2.2 Magnetic microparticle synthesis 220

8.2.3 Optimisation of magnet geometry and configuration 220

8.2.4 Localised particle injection 221

Bibliography **223**

A Magnetic bead imaging **273**

A.1 SEM images of magnetic beads 273

B Magnetic bead separation **276**

B.1 Magnetic bead separation in continuous flow 276

C Superparamagnetic microspheres in an external magnetic field **277**

C.1 Interaction between single superparamagnetic microspheres 277

C.2 Interaction between superparamagnetic agglomerations 277

List of Figures

1.1 Example of a microfluidic device 2

1.2 Concept of a lab-on-a-chip 3

1.3 Two composition structure of superparamagnetic beads 8

1.4 Magnetic bead labelling via antibodies 9

1.5 Particle manipulation methods and manipulation range 19

1.6 Schematic of magnetic particle separation principle using free-flow magnetophoresis 25

1.7 Batch mode magnetic particle separation 26

1.8 Magnetic activated cell sorting principle 27

1.9 Micro-machined bio-separator with an integrated electromagnet . . . 28

1.10 Examples of μ-MACS integrated on a LOC or μTAS 29

1.11 Integrated magnetophoretic particle diverter in microfluidic systems . 32

1.12 Lateral magnetophoresis microseparators 34

1.13 HGMS microseparator for separating red and white blood cells 35

1.14 Micro-fabricated comb shaped HGMS microfluidic device 36

1.15 Microfluidic HGMS devices using an electromagnet 37

1.16 Circular quadrupole magnetic flow sorter 39

1.17 Free-flow magnetophoresis in a microfluidic separation chamber to sort different sized magnetic particles 40

1.18 Diamagnetic plug trapping technique 42

2.1 Schematic of a 3D velocity profile of a unidirectional flow in a rectangular duct of a viscous fluid 57
2.2 Hydrodynamic focusing schematic in a three inlet fluidic device . . . 61
2.3 Magnetic domains in magnetic materials 63
2.4 Magnetic hysteresis cycle 65
2.5 Overview and comparison of the different types of magnetism 66
2.6 Hysteresis loops for soft and hard magnetic materials 67
2.7 Typical finite elements: triangular element and tetrahedral element . 75
2.8 Interpolation points on a single element in FEM 75
2.9 Illustration how large angles in element negatively effect FEM results 77
2.10 Box flow diagram of an adaptive mesh refinement algorithm 78

3.1 Microfluidic hydrodynamic focusing device 87
3.2 Schematic of the customized iBidi μ-slide 88
3.3 FastRead 102 Slide schematic 89
3.4 Hydrostatic fluid chamber fabrication procedure 90
3.5 Magnetic flux density measurement setup 91
3.6 Magnetophoretic velocity measurement experiment setup 93
3.7 SQUID experiment sample holder preparation 94
3.8 3D model of entrance of the microfluidic iBidi channel 95
3.9 Tubing connections to iBidi μ-Slides III 3in3 interface for the hydrodynamic focusing experiment 97
3.10 Experimental setup of the Double Magnet configuration 99
3.11 Experimental setup of the Quadrupole configuration 100
3.12 Experimental setup to verify static gathering points 101
3.13 Tapered magnet attached to holding block 104
3.14 Box flow diagram for particle separation simulation 105
3.15 Noisy numerical magnetophoretic driving force 107

3.16 Schematic of the bead trajectory starting points for the magnetic particle separation simulation 109

4.1 Schematic of experimentally used particle velocity tracking setup . . . 115
4.2 Magnetic flux density map of a N42 Neodymium bar magnet 116
4.3 Magnetic flux density of a N42 Neodymium bar magnet along its centre line 117
4.4 Magnetic flux density of a N42 Neodymium bar magnet around the region of interest 118
4.5 SEM images of different superparamagnetic particles 119
4.6 Magnetically induced velocities of Chemicell's ScreenMAG beads at different magnetophoretic driving forces 121
4.7 Magnetically induced velocities of Chemicell's SiMAG beads at different magnetophoretic driving forces 122
4.8 Magnetically induced velocities of Dynabeads' MyOne beads at different magnetophoretic driving forces 123
4.9 Magnetically induced velocities of Dynabeads' M280 beads at different magnetophoretic driving forces 124
4.10 Magnetically induced velocities of Dynabeads' M270 beads at different magnetophoretic driving forces 125
4.11 Magnetically induced velocities of different particle types 126
4.12 Magnetophoretic mobility of different particle types 127
4.13 Histogram of magnetophoretic mobility of various superparamagnetic particles 128
4.14 Schematic of magnetic bead agglomerates travelling towards a permanent magnet 129
4.15 Normalized magnetophoretically induced velocity of different particle chain lengths 130

4.16 Magnetization curves of Chemicell and Dynabeads particles in the range of ±1 T 132
4.17 Magnetization curves of Chemicell and Dynabeads particles in the range of ±75 mT 133
4.18 Magnetization curves of an air filled sample in the range of ±75 mT . 134
4.19 Box plot of particle susceptibility 146
4.20 Regression of susceptibility for two different models 147
4.21 Residual plot of regression analysis 148
4.22 Dimensionless normalized magnetically induced particle travelling distance for a given time interval 149

5.1 Velocity profile across half the cross-section of the microfluidic separation device 151
5.2 Hydrodynamic focusing comparison between simulations and experiments 157
5.3 Hydrodynamic focusing in iBidi μ-slide: normalized width ratio for different inlet flow rate ratios at various centre inlet flow rates 158

6.1 3D Schematic of the magnet configurations 160
6.2 2D diagram of the Double Magnet configuration 161
6.3 Simulated vector field and flux density of the Double Magnet configuration 162
6.4 Magnetic flux density and flux density gradient of the Double Magnet configuration 163
6.5 Magnetic driving force of the Double Magnet configuration on a superparamagnetic bead 164
6.6 Magnetophoretic driving force of the Double Magnet configuration for different magnet aspect ratio 165

6.7 Observed behaviour of position of the static gathering point as a function of the magnet aspect ratio 166
6.8 Magnetophoretic driving force of the Double Magnet configuration for different separation ratio 167
6.9 Observed gathering position as a function of the magnet separation ratio for different particle types 168
6.10 Gathering positions as a function of the magnet separation ratio for different particle suspension concentration 169
6.11 Diagrams of the tapered magnet configurations 170
6.12 Simulation of the magnetophoretic driving force for different magnet tapers 171
6.13 Static particle gathering band for tapered Double Magnet configuration 172
6.14 2D diagram of the Quadrupole configuration 173
6.15 Simulated vector field and flux density of the Quadrupole configuration 174
6.16 Magnetic driving force simulation of the Quadrupole configuration for different aspect and relative gap ratios 175
6.17 Vector field of the magnetic driving force of the Quadrupole configuration across the iBidi μ-slide 176
6.18 Elliptical band of beads after various time intervals 177
6.19 Experimental visualisation of the elliptical particle band and gathering positions for different vertical separations 178
6.20 Elliptical equilibrium band width of different particle types 179
6.21 Elliptical equilibrium band width for different particle suspension concentrations 180
6.22 Close up view of elliptical particle band 181
6.23 Particle band formation of magnetic bead aggregates 182

7.1 Particle inlet and outlet schematic 188

7.2 Scatter plot of starting and end position of magnetic particles for different flow rates using the Double Magnet configuration 190

7.3 Relative magnetic separation efficiency and throughput of the analysed magnetic bead types for different flow rates using the Double Magnet configuration 191

7.4 Magnetic separation experiment of the Double Magnet configuration in continuous flow 192

7.5 Experimental magnetic bead separation efficiency of the Double Magnet configuration in continuous flow 193

7.6 Relative magnetic separation efficiency and throughput of magnetic bead agglomerates for different flow rates using the Double Magnet configuration 195

7.7 Schematic of vertical misalignment of the microfluidic separation device 196

7.8 Relative magnetic bead separation efficiency and throughput when the microfluidic channel has a displacement compared to the two magnets of the Double Magnet configuration 196

7.9 Relative magnetic separation efficiency and throughput when a viable or non-viable cell cargo is attached to a magnetic bead for different flow rates using the Double Magnet configuration 198

7.10 Relative magnetic separation efficiency and throughput for different flow rates using different magnet geometries for the Quadrupole configuration 200

7.11 Magnetic separation experiment of the Quadrupole configuration in continuous flow 201

7.12 Schematic of spherical beads moving in proximity to a planar wall . . 202

7.13 Wall correction factor for rigid sphere in proximity to a planar wall . 204

7.14 Schematic of spherical particle in a flow field in proximity to a planar wall . . . 205
7.15 Pulse mode separation efficiency of the Double Magnet and Quadrupole configuration . . . 207
7.16 Particle separation efficiency of the Quadrupole configuration in pulse mode . . . 208

8.1 Bead injection through a nozzle . . . 222

A.1 SEM images of magnetic Chemicell beads . . . 274
A.2 SEM images of magnetic Dynabead microspheres . . . 275

B.1 Comparison of the magnetic bead separation efficiency in continuous flow with and without the Double Magnet configuration . . . 276

C.1 Repellent force between individual dipoles . . . 278
C.2 Interaction between magnetic particle and particle agglomerates . . . 279

List of Tables

1.1 Separation method summary 13

1.2 Summary of continuous magnetophoretic separation techniques 43

3.1 Bead types used in the experiments 85

3.2 Chemicals used in the experiments 86

4.1 Physical characteristics of the five tested bead types 114

4.2 Experimentally found averaged magnetophoretic mobility and susceptibility of superparamagnetic particles using magnetophoresis . . . 126

4.3 Number of observed bead agglomerates 130

4.4 Experimentally found magnetophoretic mobility and susceptibility of superparamagnetic beads using SQUID 134

4.5 Measured particle susceptibility at different magnet positions from the magnetophoretic mobility study 136

4.6 Measured particle susceptibility at different magnet positions from the magnetization study 136

5.1 Sample stream width and flow conditions used in the hydrodynamic focusing experiment 154

Nomenclature

Symbols

A	Cross sectional area	[m^2]
$\mathbf{B}$	Magnetic flux density	[T]
C	Constant	[−]
D_H	Hydraulic diameter of channel	[m]
D_p	Hydraulic diameter of particle	[m]
E	Energy functional	[−]
$\mathbf{F}$	Force	[N]
$\mathbf{H}$	Magnetic field intensity	[A/m]
H_0	Null hypothesis	[−]
H_a	Alternative hypothesis	[−]
H_C	Coercivity	[A/m]
J	Current density	[A/m^2]
L_H	Hydrodynamic entrance length	[m]
$\mathbf{M}$	Magnetization	[A/m]
M_S	Saturation magnetization	[A/m]
M_R	Remanence	[A/m]
N	Number of particles	[−]

P	Wetted perimeter	[m]
$\dot{Q}$	Volume flow	[m^3/s]
R_H	Hydraulic resistance	[kg· s/m^2]
Re	Reynolds number	[−]
S	Magnetophoretic driving force	[T·A/m^2]
Stk	Stokes number	[−]
T	Temperature	[K]
V	Volume	[m^3]
X_i	Independent variable	[−]
$\hat{X}_p$	Normalized particle travelling distance	[−]
a	Vertical magnet separation	[m]
b	Horizontal magnet separation	[m]
c	Particle release distance in z	[m]
d	Diameter	[m]
d_m	Distance to magnet	[m]
e	Element	[−]
g_w	Gap between particle and wall	[m]
h	Height	[m]
k_B	Boltzmann constant	[m^2·kg/s^2·K]
l	Length	[m]
l_w	Distance between particle midpoint and wall	[m]
m	Magnetic moment	[A·m^2]
n	Number of particles in particle chain	[−]
p	Pressure	[N/m^2]

r_p	Particle radius	[m]
s	Sample standard deviation	[$*$]
t	Time	[s]
δt	Time step	[s]
Δt	Time interval	[s]
$\mathbf{u}$	Velocity vector	[m/s]
$\bar{u}$	Mean velocity	[m/s]
w	Width	[m]
x	Sample point	[$*$]
α	Significance acceptance level	[$-$]
β	Particle velocity wall correction factor	[$-$]
δ	Fluid channel displacement	[m]
γ	Velocity ratio	[$-$]
η	Dynamic viscosity	[kg/m·s]
ϵ	Discretization error	[V·s/m]
ε	Residual	[A/m^2]
θ	Finite element aspect ratio	[$-$]
$\bar{\theta}$	Average finite element aspect ratio	[$-$]
ϑ	Finite element aspect ratio benchmark	[$-$]
κ	Dimensionless scaling factor	[$-$]
μ	Mean of population	[$*$]
μ_0	Magnetic permeability of free space	[N/A^2]
μ_r	Relative permeability	[$-$]
ν	Magnetophoretic mobility	[m^3/T·A·s]

π	Constant $\pi = 3.14159\cdots$	[−]
ρ	Density	[kg/m^3]
ϱ_{in}	Inner diameter of finite element	[m]
ϱ_{out}	Outer diameter of finite element	[m]
σ	Standard deviation	[−]
τ	Relaxation time	[s]
τ_0	Characteristic time scale	[s]
υ	Volume ratio	[−]
φ	Wall distance to particle radius ratio	[−]
χ	Magnetic susceptibility	[−]
ω	Grid element size	[m]
ξ	Percentage energy error in FEM system	[−]
ζ	Separation efficiency	[−]
Δ	Difference operator, Laplace operator	[−]
∇	Nabla operator	[−]
Λ	Magnetic anisotropy energy density	[J/m^3]
Θ	Dimensionless magnetophoretic velocity	[−]
Φ	Magnetic vector potential	[V·s/m]
$\tilde{\Phi}$	Magnetic vector potential approximation	[V·s/m]
Ω	Simulation domain	[−]
$\partial\Omega$	Simulation domain boundary	[−]
Γ	Domain boundary	[−]
Π	Plane where beads are released from	[−]

Indices

a	Absolute
b	Elliptical particle band
c	Centre
d	Drag
e	Element
ext	External
f	Fluid
i, j	Iteration parameter
k	Exit channel
m	Magnet
M	Manufacturer
p	Particle
r	Relative
R	Remanence
s	Sheath
S	Saturation
w	Wall
x	x direction
y	y direction
z	z direction
in	Incoming
out	Outgoing
min	Minimum

$\parallel$	Parallel
$\perp$	Perpendicular
0	Fluidic channel

Acronyms and Abbreviations

2D	Two dimensional
3D	Three dimensional
AC	Alternating current
ANOVA	Analysis of variance
CCD	Charge-coupled device
CD	Compact disk
CFC	Circulating fetal cells
CFD	Computational fluid dynamics
CFL	Courant-Friedrichs-Lewy
CTC	Circulating tumour cells
CTV	Cell tracking velocimetry
DEP	Dielectrophoresis
pDEP	Positive dielectrophoresis
nDEP	Negative dielectrophoresis
DC	Direct current
DI	Deionised water
DLS	Dynamic light scattering
DLD	Deterministic lateral displacement
DNA	Deoxyribonucleic acid

E. coli	Escherichia coli
ELISA	Enzyme linked immunosorbent assays
FFF	Field-flow fractionation
FEM	Finite element method
Fe_3O_4	Magnetite
$\gamma-Fe_3O_4$	Maghemite
HGMS	High gradient magnetic separation
LFT	Lateral flow test
LOC	Lab-on-a-chip
LOD	Lab-on-a-disk
MACS	Magnetic activated cell sorting
MEMS	Micro-electro-mechanical systems
MRI	Magnetic resonance imaging
NdFeB	Neodymium Iron Boron
PBS	Phosphate buffered saline
PDE	Partial differential equation
PDMS	Polydimethylsiloxane
PCR	Polymerase chain reaction
qPCR	Quantitative polymerase chain reaction
POC	Point-of-care
PNU	Pusan National University
SEM	Scanning electron microscope
SQUID	Superconducting quantum interference device
μ-TAS	Micro Total Analysis Systems

Publications

Grob, D. T., Wise, N., Oduwole, O., & Sheard, S. (2017). Magnetic susceptibility characterisation of superparamagnetic microspheres. *Journal of Magnetism and Magnetic Materials*, 452: 134-140.

Oduwole, O., Grob, D. T., & Sheard, S. (2016). Comparison between simulation and experimentally observed interactions between two magnetic beads in a fluidic system. *Journal of Magnetism and Magnetic Materials*, 407: 8-12.

Wise, N., Grob, D. T., Morten, K., Thompson, I., & Sheard, S. (2015). Magnetophoretic velocities of superparamagnetic particles, agglomerates and complexes. *Journal of Magnetism and Magnetic Materials*, 384:328-334.

Chapter 1

Introduction

1.1 Microfluidics and micro total analysis systems

This work was aimed to develop a 3D model to predict the trajectories of individual magnetic beads in a magnetic field. The model was used to understand the transport of the beads in a microchannel during magnetic separation. Simulations and experiments are combined to perform a comprehensive study of the effects of multiple parameters on the efficiency of magnetic particle separation.

The separation and sorting of biological material from complex mixtures represents a critical task in a variety of biomedical applications including diagnostics, therapeutics, and fundamental cell biology. As biological samples are often heterogeneous, containing different populations of cells, vesicles, proteins, etc., techniques are required to isolate specific components.

One possible approach to sort heterogeneous mixtures is with the help of microfluidics. Microfluidics involves the techniques to actuate, control and manipulate small volumes of fluids (10^{-9} to 10^{-18} litres) in channels, where the channel dimensions are of microscopic scale (typically in the order of tens to a couple of hundred of micrometres) [1]. Figure 1.1 shows a schematic and a photograph of a microfluidic

device example from the literature [2].

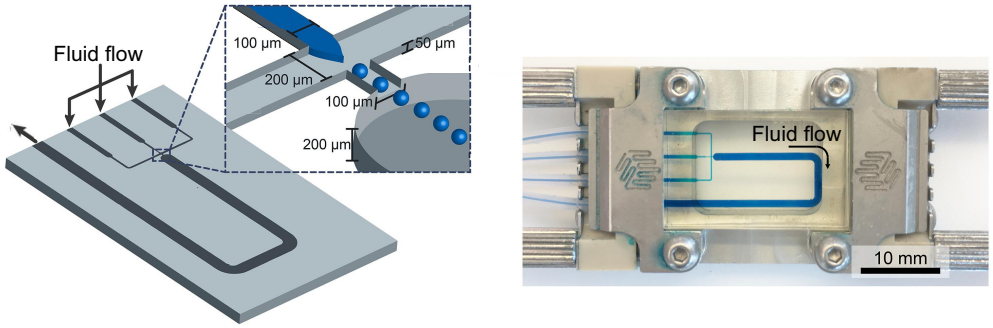
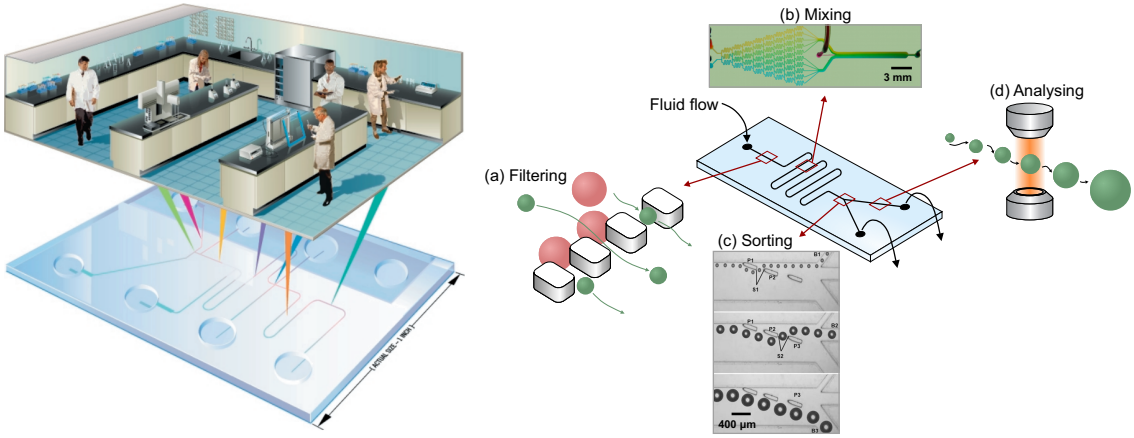


Figure 1.1: Schematic and photograph of an example for a microfluidic device. The device features channels with a width of 100 μm and a height of 50 μm. Figure has been adapted from [2].

The science of miniaturization was initially fuelled by the microelectronics industry during the development of miniature silicon-based electronic devices. Techniques for silicon microfabrication and miniaturization were then extended to the fabrication of mechanical devices that became known as microelectromechanical systems (MEMS) [3]. A later trend in MEMS technology was the development of devices for applications in the medical and life science areas. The term biological microelectromechanical systems (BioMEMS) was coined to describe devices and systems with a biolocial application, although subsequently they did not all necessarily have the components normally found in traditional MEMS devices. Hence, a broad definition of BioMEMS would include some devices and applications made using the modern implementation of microfluidics, which was developed by Manz *et al.* in 1990 [4]. With the reduced size came the concept of a micro total analysis system (μTAS) or lab-on-a-chip (LOC). The two terms essentially mean the same and thus, are used interchangeably in this work. Both can be regarded conceptually as a fluidic equivalent of conventional silicon integrated circuits, which involve miniaturization and integration of electronics. Instead of an electronic circuit, LOC and μTAS have microchannels for guidance and manipulation of fluids. As the name suggests, an ideal LOC or μTAS integrates multiple laboratory functions on a single microflu-

idic device. This includes sample preparation, incubation, detection and analysis procedures on a single device, no bigger than the size of a microscope slide [5, 6]. Consequently, labour intensive and expensive benchtop processes can be replaced and eliminated. LOC can be thought of as the shrinking of an entire laboratory into a miniature device. The LOC concept is schematically illustrated in Figure 1.2.



(a) (b)

Figure 1.2: (a) Schematic illustration of a lab-on-a-chip, where laboratory processes are integrated onto a microfluidic device. Figure has been reproduced from [7]. (b) Conceptual example of a lab-on-a-chip device where various processes, e.g. filtering, mixing, sorting and the analysis, are all integrated on a single device. Photographs adapted from [8] and [9].

With the development of LOC and their integrated micro-scale fluidic systems, it is now possible to manufacture inexpensive, fast and high-throughput biomedical devices which need little sample volume and reagents. These benefits, however, are not yet readily available at low-cost for many benchtop techniques [10, 11]. Therefore, LOC has shown considerable potential for a wide variety of bioanalysis applications including: organic synthesis [12, 13], forensic analysis [14, 15], DNA extraction [16, 17] and analysis [18], polymerase chain reaction (PCR) amplification [18], chemical and biological assays [19], environmental monitoring [20, 21] and various separation and detection techniques in analytical chemistry [22, 23].

1.1.1 Microfluidics bio-sensors for point-of-care diagnostics

A biomarker is a measurable characteristic that reflects the severity or presence of a disease state. In this thesis, the term *biomarkers* refers to molecules in body fluids, typically proteins in blood [24].

Biomarkers are conventionally detected using immunoassays. Clinical immunoassays are traditionally based on 96-well microtiter plates and are widely used for the quantification of target molecules in many applications such as clinical diagnostics, pharmaceutical research, and basic biological investigations [25–27]. Immunoassays, such as enzyme linked immunosorbent assays (ELISA) for the detection of proteins [28] or quantitative polymerase chain reaction (qPCR) for the detection of nucleid acids [29], have been established as *gold standard* detection technologies for specific biomarkers. However, most conventional immunoassays involve time consuming and labour intensive protocols, because they include a series of washing, mixing and incubation steps [30]. It often takes several hours, and in some cases days, for a single assay to be processed [31]. Much of the time taken in immunoassays is due to the long incubation time, because analyte molecules must rely on diffusion to encounter antibodies on the surface where the conjugation occurs [32]. Moreover, these protocols require highly trained personnel, bulky and expensive instruments, and expensive reagents [33]. This ultimately makes this approach costly and due to its size not well suited for point-of-care (POC) analysis.

However, there are POC diagnostic tests commercially available and to provide context relevant to the thesis a few breakthrough examples will be discussed. A current major class of such tests is the Lateral Flow Immunoassay test (LFT), which uses a membrane or paper strip to indicate the presence of biomarkers such as pathogen antigens or antibodies [34]. On a membrane, addition of a sample induces capillary action which lets the sample migrate along the membrane. As the sample flows across the membrane, it gathers detection reagents embedded in the membrane, and

then flows over a band that contains capture molecules (antibodies). The captured antibodies and detection reagent labelled analytes form a visible band which can be interpreted by eye. This diagnosis is most notably used to test for pregnancy, infections with streptococcus, the flu or HIV [34]. LFTs are simple to perform and are extremely versatile, consequently, they have found clinical, veterinary, agricultural, food industry and environmental applications. The single-flow action, however, does not mimic the multi-step procedures of laboratory-based assays that are crucial for highly reproducible, quantitative, and sensitive results [35].

The other major class of successful POC tests is the blood glucose test, which almost serves as a textbook example for a high-impact POC product that has improved diabetic patients' lives, and now acts as a pillar of the entire diagnostics industry. The glucose test is also performed on membranes, but is typically classified differently compared to lateral flow immunoassays as the analytical method is altogether different. It uses signal amplification by a redox enzyme and is typically analysed via an electrochemical readout [35, 36]. However, testing for glucose is somewhat unique in a sense that the analyte concentration is in the range of millimole per litre, which is well above the concentration of most biomarkers. Additionally, the test typically needs to be taken multiple times a day, which outnumbers that of most other biological tests.

With the advance in microfluidics technology, the miniaturized fluidic systems (LOC or μTAS) became an attractive alternative for running multiplexed on-chip immunoassays due to the integration of various compatible components on a single device, such as pumps, mixers or valves. Researchers have successfully developed micropumps [37–40], microvalves [41], micromixers [42, 43] and other active as well as passive microfluidic liquid handling components [44, 45]. With the integration of these components on a single microfluidic bio-sensor, it is possible to perform full sample analysis including continuous sampling [46], sample separation and mix-

ing [4], and sample pre-treatment and pre-concentration [47]. Integrating and combining multiple microfluidic components offers enhanced analytical performance, high throughput, real-time detection, fast reaction rates and portability [48, 49]; making detection adaptable to POC applications.

For instance, Lee *et al.* [50] successfully developed an automated microfluidic biosensor for the detection of breast cancer. The device uses multiple channels to detect the interaction between anti-rabbit immunoglobulin G and rabbit immunoglobulin G using a micro-arrayed immunoassay. The experimentally achieved sensitivity was found to be 10^{-4} mg/mL (0.67 nM). The total time needed for the on-chip analysis was approximately 8 hours.

Kong *et al.* [51] demonstrated a LOC design for the rapid detection of clenbuterol which has been used to treat chronic breathing disorders but also for performance-enhancing in bodybuilding. They performed an ELISA in the interrogation section of the microchannel network. Pneumatic valves were utilized to control the introductions of different reagents. Under optimal conditions, 5 ng/mL could be detected in less than 30 minutes.

Another example for the integration of a microfluidic device and biosensor is demonstrated by Yao *et al.* [52]. They reported a fully automated microfluidic-based detection system for the rapid determination of insulin concentration based on a chemiluminescence immunoassay. The system is a double-layered PDMS device embedded with interconnecting micropumps, microvalves, and a micromixer. The chemiluminescence assay can detect insulin in the range of 1.5 pM to 391 pM in less than 10 minutes. These results were achieved with the help of magnetic microparticles, which will be explained in the next section.

1.2 Magnetic micro- and nanoparticles

Micron-sized magnetic beads are intensely investigated due to their physiological properties and diagnostic potential, since they are very promising carriers for biomarkers in biomedicine or bioanalysis, e.g. for drugs [53, 54], DNA [55, 56], antibodies [57] or cells [58, 59], and due to their size can be seamlessly integrated in microfluidic devices.

Magnetic beads usually consist of an ensemble of nano-sized ferromagnetic grains in the order of $5 - 15$ nm, embedded in a nonmagnetic host matrix. The nonmagnetic matrix seals the magnetic grains and prevents them from further chemical reactions and degradation. The inner morphology of the particles, which is determined by the size and the number of enclosed magnetic grains, influences the overall magnetic behaviour [60, 61].

The ferromagnetic grains are generally an iron oxide, such as magnetite (Fe_3O_4) or maghemite ($\gamma - Fe_2O_3$), because of a high saturation magnetization and non-toxicity [62, 63]. Other magnetic materials such as cobalt, nickel and neodymium-iron-boron may offer improved magnetic properties, however, these materials may be toxic and/or susceptible to oxidation [64].

The nonmagnetic host matrix is often a polymer or silica. These materials allow the production of a wide range of different particle sizes, ranging from as small as 6 nm to more than 20 μm and a uniform size distribution can be achieved [65–67]. These polymer and silica hosts also permit a wide choice of possible surface coatings, which ensure that the magnetic particles are compatible with biological materials [56, 68, 69].

The loading of iron oxide within the beads occurs either as fixed dispersion of single domain nano-sized grains within the host matrix or concentrated in the core of the bead, as shown in Figure 1.3. If the magnetic grains are small enough and spaced sufficiently far apart inside the host matrix, then the bead will behave superparamag-

netically and will have a large induced dipole moment due to the collective response of the magnetic grains. Due to their superparamagnetic behaviour the beads are attracted to magnetic fields but do not retain any magnetism after removal of the magnetic field, which will be explained in more detail in Section 2.3. This property has revolutionized particle based separation because they can be easily manipulated through the control of an external magnetic field [70].



(a) (b)

Figure 1.3: Two types of superparamagnetic beads. The iron oxide can either be found as (a) nano-sized magnetic grains dispersed in a core with a surrounding shell containing no magnetic material, or (b) a fixed dispersion of single domain nano-sized magnetic grains within the nonmagnetic host matrix.

Further, magnetic beads have become popular mobile carriers due to their large specific surface area (total surface area per unit of mass). Beads can be coated with antibodies to bind to biomolecules and thereby providing a controllable means of identifying a specific target species [71]. These antibodies are shown as surface extensions in the schematic of Figure 1.4. Hence, the beads act as mobile reaction substrates, able to directly interact with biological entities over a wide size range, e.g. cells ($1 - 100$ μm), viruses ($20 - 450$ nm), proteins ($5 - 50$ nm) or genes (2 nm wide and $10 - 100$ nm long) [72–74]. Several excellent reviews on the synthesis and the use of magnetic particles in medical and biological applications exist in the literature [75, 76].

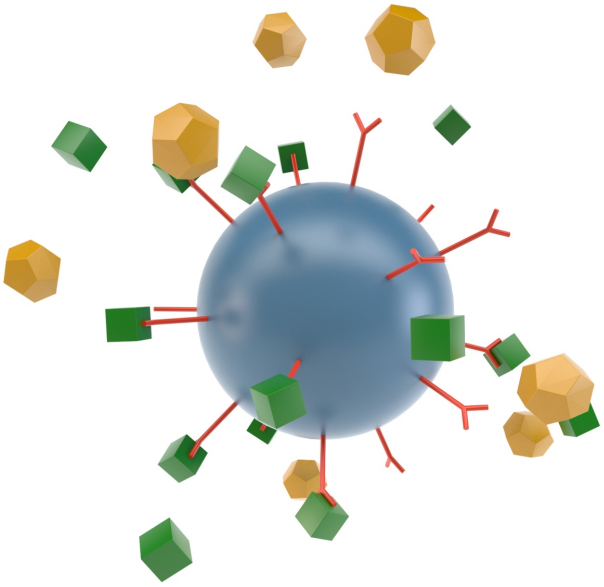


Figure 1.4: Schematic of an immunomagnetically labelled magnetic beads. Antibodies (red Y-shapes) are used to target specific biological cells or material (green cubes) and bind them to the surface of the bead (blue sphere). Non-targeted molecules (yellow dodecahedrons) do not interact with the antibodies and thus are not bound to the magnetic beads.

1.3 Cell separation in microfluidic systems for biomedical applications

Cell separation underpins many discoveries in biology and is further enabling research in areas as diverse as regenerative medicine [77, 78], cancer therapy [79] and HIV pathogenesis [80]. Thus the ability to isolate and enrich a population of cells extracted from their complex native environment is often the first processing step in the analysis [78].

Numerous cell isolation and sorting techniques have been developed for clinical settings that are based on the differences in cell size, shape, density or the cells' dielectric and magnetic properties [33, 81, 82].

Density-based separation techniques such as differential centrifugation techniques are commonly used in laboratories and are also routinely used clinically [83]. Dif-

ferential centrifugal separation relies upon sedimentation that is accelerated by centrifugal force and requires a difference in density between the constituent phases. Cells of different densities and volume in a suspension will settle at different rates, with the larger and denser cells pelleting more rapidly [84]. Cell separation based on differential centrifugation allows for the isolation of cells from a large initial cell sample, which makes this technique particularly applicable for separations involving the use of blood. Indeed, the most commonly used clinical cell separation method is apheresis of whole blood to isolate mononuclear cells for treatment of a variety of conditions, including leukaemia [85]. Furthermore, centrifugation is also widely employed for the isolation and purification of viruses, subcellular organelles, proteins, and nucleic acids that are dissolved or dispersed in biologically relevant solvents [86]. In situations where cell size or density differences are not significant, however, effective cell separation of individual cell types is not straight forward using centrifugation. Problems can be overcome, however, by performing repeated centrifugations using differing concentrations of centrifugation medium and differing angular velocities. By using this more elaborate approach, it is possible to isolate different cell types from a complex mixture, such as disrupted solid tissues as demonstrated for mouse liver [87]. However, although technically feasible, this is still challenging to perform with high specificity. As such, centrifugation methods are generally used if specificity is not absolutely necessary, as in apheresis, or as a pre-enrichment stage to remove cells like red blood cells and platelets.

Advances in bioanalysis, along with the promise of POC and personalized medicine, have increased the need to separate specific biological entities from their native environment in order to prepare concentrated samples for subsequent analysis and testing in both basic research and clinical applications. Thus, the need to separate cells and other biological material is rapidly expanding toward the isolation of rare target populations (cell abundance is less than 10^3 in 1 mL [88]), examples include

the enrichment of circulating tumour cells (CTC), hematopoietic stem cells, and circulating fetal cells (CFC) from blood [89, 90].

The low abundance of rare cell populations preclude the use of conventional benchtop separation techniques, such as centrifugation, because of their low selectivity and the impact of sample loss. In order to improve selectivity, cells can be labelled with tags using antibody binding and isolated by other means.

The fluorescent-activated cell sorting (FACS) technique harnesses the ability to label specific cells with fluorescent dye tags, which allows for cell sorting based on the individual labelling profile of a particular cell population [91]. The cell suspension is entrained in the centre of a narrow, rapidly flowing stream of liquid. The flow is arranged so that all the cells are in a line with a large separation (relative to their diameter) between each cell. A vibrating mechanism causes the stream of cells to break into individual aerosol droplets. Just before the stream breaks into droplets, the cells in the flow encounter a focused laser beam that scatters light into a detector where the fluorescent signal of each cell of interest is measured. Depending on the scattering and fluorescent profile, each cell encapsulated in an aerosol droplet is then given an electric charge and then physically sorted using electrostatic deflection plates [91]. Current state-of-the-art FACS devices typically use up to seven lasers which enables them to sort six different types of cell based on morphological and fluorescent cell signatures (e.g., cell surface labels, cell size, or granularity) [33, 92].

Although still one of the most highly-used cell isolation platforms, a serious limitation to FACS systems remains their price and complexity. The complexity of operation also requires dedicated highly-trained personnel to ensure reliable cell sorting efficiency and purities. It is reported in the literature that FACS systems are susceptible to cross-contamination, clogging in the nozzle, require high reagent consumption and have safety concerns due to the sorting of aerosol samples [93]. Ad-

ditionally, even if modern flow cytometers offer sample rates of upwards of $50,000$ cells/s and multichannel detector analysis, it is not a feasible technique for processing clinical samples ($>$ 500 million cells). These limitations must be overcome to enable more efficient clinical application and further commercialization.

Consequently, the next generation of cell sorting devices should ideally meet higher standards of performance, versatility and convenience. They should include: faster sorting rates, improved sorting accuracies, improved sorting purity, high cell recovery, ability to process native biological fluids, ability to process diverse cell types, enhanced capabilities for multiplexed sorting, simpler operating procedures enabling fully automated systems, reduced hazardous risk by eliminating aerosols, reduced cost and reduced size for operational convenience and portability.

With the rapid development in lab-on-a-chip technology, recent advances in microfluidics have been providing robust solutions for rare cell analysis. Microfluidic devices capable of cell separation and sorting are emerging at an increased pace [94]. The ability to design advanced microfluidic networks in combination with both actuation and sensing/monitoring is driving novel concepts for advanced on-chip cell studies, as well as new means to capture/retain, separate and/or concentrate cell species from complex biological fluids. The advance in microfabrication technology has made it possible to design microfluidic devices with design features that are commensurate with single cells [95].

Current developments in cell separation and cell enrichment in microfluidic devices encompass the employment of active separation methods, where cells are manipulated by an external field, and passive separation methods which induce a force onto the cells by controlled hydrodynamics. Most cell separation methods rely on the use of active manipulation techniques, such as optical [96, 97], electrical [98], acoustical [99], or magnetic fields [100–102]. There is also research in passive separation methods, where cells are separated solely based on hydrodynamics effects [103].

This enables the sample preparation step to be avoided because no specific labelling is needed (*label-free separation*). The various methods are summarised in Table 1.1 and each method with its advantages and disadvantages is briefly reviewed and discussed below.

Table 1.1: Summary of the different separation methods.

	Separation method	Advantages	Disadvantages
Passive	Filtration	- Label-free - No need for external forces	- Risk of blockages - Complex fabrication
	Hydrodynamic	- Label-free - No need for external forces	- Complex chip design - Flow needs to be carefully controlled
	Centrifugation	- Label-free - Large sample volumes	- Lacking specificity
Active	Optical	- Label-free - Contactless - Precise control over individual particles	- External power supply and laser needed
	Electrical	- Label-free - Electric force can be adjusted	- Buffer solution needed - External power supply needed - Joule heating
	Acoustic	- Label-free - Contactless	- External power supply needed
	Magnetic	- Contactless - Inexpensive magnetic setup	- Requires magnetic labelling

1.3.1 Passive particle separation

Passive separation systems consist of a variety of methods, such as inertial forces, mechanical filtration, and immobilization, that do not solely rely on labels, particles or biochemical markers [81]. Instead, these methods rely on the inherent physical differences between particle groups (e.g., size, shape, compressibility, and density). Since these techniques often do not require the addition of an attached particle or

ligand (such as a fluorescent or magnetic particle tag), they are attractive methods when affinity ligands are not available [104].

In the following, some of the most important passive particle separation techniques for microfluidic devices are described.

1.3.1.1 Filtration separation

Filtration is based on particle size differences and selective segregation by dimensioned pores. This method makes it easy to extract the liquid phase of a suspension and is commonly used for blood applications with varying degrees of success [105–107].

A major limitation of filters is that they often clog when trapping larger cells or debris. This means that filter systems are only efficient for a certain time defined by saturation (until clogging occurs). They are best suited for highly diluted samples and for a given volume at low flow rates. For this reason, several designs of size-based microfilters exist including membrane filters, pillar filters, weir filters and crossflow filters [106]. The separation performance of different filter types have been experimentally validated and reviewed by Ji *et al.* [106].

One of the most typical separation strategies in microfluidic filters uses micro-fabricated pillars which are equally spaced, or a membrane containing an array of micro-pores on the floor or the ceiling of the channel, which acts as a sieve, to remove or enrich cells from a blood sample [108–111].

The simplest filter exploiting microchannels are weir filters that contain a dam or barrier to retain particles. Sato *et al.* fabricated such a microfluidic weir filter which halts the movement of particles through the chip without stopping the fluid flow, after which assays or reactions can be performed on the particle surfaces [112]. Particles can also be trapped between two weirs, whereupon solutions can be drawn over them, allowing solid phase extraction and chromatography techniques to be

employed [113].

Crossflow filters, also known as tangential-flow filters, are derived from the concept of pillar filters except that the pillars are placed tangential to the main flow direction. This method of filtration has a major advancement over early types of filters such as weir, pillar, and membrane because they are less prone to clogging because they behave more like a sieve than a conventional filter, where the fluid is directly propelled into the filter [114]. Several cross-flow filter designs have been developed for size-based sorting applications such as the separation of white blood cells from whole blood, plasma from whole blood, and myocytes from non-myocytes [115, 116]. More recently, sophisticated grids with tiered (i.e., decreasing) spacing as a function of distance or oscillating flow patterns have been used for sorting cells in a non-binary fashion and to reduce the risk of clogging. Mohamed *et al.* developed a size exclusion filter to isolate circulating fetal cells from maternal blood by arranging multiple pillar filters in series with different spacings [117]. Later, McFaul *et al.* as well as Preira *et al.* showed how structural ratchets can be used to sort cells based on their size in combination with oscillatory applied pressures [118, 119]. Lately, Yoon *et al.* demonstrated a μ-sieve which has a low oscillating frequency added to the fluid flow. This made it possible to release unwanted polystyrene particles trapped between the larger target polystyrene particles. With this structure, a high separation efficiency as well as a high recovery rate could be achieved [120].

1.3.1.2 Hydrodynamic separation

Hydrodynamic cell separation techniques make use of the fluid flow and the laminar flow profile alone to separate particles based on their size. Therefore, parameters such as flow rate control through one or more inlets, the channel geometry, and the configuration of outlets, dictates the flow character and ultimately the cell isolation performance.

Blom *et al.* developed an on-chip hydrodynamic chromatography device in which particles were introduced into a channel and separated according to size [121, 122]. The separation principle is based on the parabolic profile caused by pressure-driven flow, which allows smaller particles to migrate closer to the walls of the channel such that they have a slower average velocity than larger particles that are farther from the wall, thus achieving separation.

Yamada *et al.* used pinched-flow fractionation to sort different particle sizes [123]. Pinched flow fractionation occurs when a flow stream of cells is *pinched* by a narrow channel cross-section such that cells are constrained and aligned against a side wall. Smaller particles migrate closer to the side wall compared to larger particles and are subsequently separated by size once the channel broadens since they follow different stream lines. The technique was refined by asymmetric amplification of the flow in the system [124], the incorporation of PDMS valves [125], and by replacing pressure-driven flow with electroosmotic flow [126].

Separation methods, where hydrodynamic properties are combined with physical obstacles, as used in filter separation techniques, are known as *deterministic lateral displacement* (DLD). In DLD, cells navigate through an array of posts for sorting by size. In these systems, control over sorting is given by the design of the array features such that cells smaller than a critical radius move with the convective flow and cells larger than a critical radius move in a direction dictated by the arrays [127]. Thus, small particles follow the laminar flow streamlines through the chamber, essentially *weaving* around the posts whereas larger particles, above a critical size, are unable to follow the streamlines upon encountering a post, and are instead *bumped* in the direction perpendicular to flow. Using a periodic array of microposts, in which each row of posts is offset by a certain periodic distance, Huang *et al.* showed that smaller cells could more easily traverse between obstacles than larger cells, enabling their separation [128]. The critical sizes of cells and microposts were carefully evaluated

by Inglis *et al.* [129] and have been used to isolate large cells, e.g. cancer cells or leukocytes, from whole blood samples [130–132].

1.3.1.3 Microfluidic centrifugation separation

Centrifugation separation, as it is currently used in bulk cell separation techniques, can also be integrated in microfluidic systems. Such centrifugal microfluidic devices are commonly known as lab-on-a-disk (LOD) [133–135]. Centrifugation approaches for cell separation in LOD include methods that utilize the physical centrifugation process on microfluidic platforms and the centrifugation effects due to Dean flow [136].

Physical LODs are circular-shaped platforms containing a network of microchannels, chambers and other features. As the platform resembles a compact disk (CD), it is referred to as the centrifugal microfluidic CD or lab-on-a-CD [137]. A motor is used to rotate the microfluidic CD, transporting fluid radially outwards through the microfluidic device, and manipulating fluid by means of various microfluidic functions and features on the disc. The spinning disc platform is particularly advantageous in biomedical applications where large samples based on their density are to be separated [138, 139]. Amasia *et al.* demonstrated the separation of plasma from a large sample of whole blood [140]. Similarly, isolation of white blood cells from whole blood using density gradient techniques has also been shown [141, 142].

Physical centrifugation techniques enhance inertial forces. However, inertial forces can also result in curved fluid channels. Typically, inertial forces emanate from boundary effects of fluid flow adjacent to the walls of a microfluidic channel, causing lift. Thus, in curved microfluidic platforms particles can be focused by balancing the inertial lift force and Dean drag force [143]. Di Carlo *et al.* demonstrated that cells could be differentially focused and sorted based on size under laminar flow using a serpentine pattern [144]. A major benefit of this system is its high throughput (e.g.,

1.5 mL/min) without additional sheath flow or sequential cell manipulation, which is useful for processing native biological fluids [145].

As in the case of serpentine patterns, where cells can be focused into a single streamline, a spiral microfluidic channel can sort cells by size [146]. Russom *et al.* created a system with a spiral channel that applied inertial forces to focus and sort cells [147]. Similarly, Hou *et al.* and Nivedita *et al.* utilized a spiral fluid channel to continuously isolate CTCs from blood samples and separate blood cells, respectively [148, 149]. Guan *et al.* and Warkiani *et al.* demonstrated that a channel with a trapezoidal cross section could further enhance the performance of a spiral microfluidic device to focus and sort cells [150, 151].

Inertial forces do not only occur in curved channels, they also play a critical role in straight microfluidic channels [143]. Parichehreh et al. were able to enrich nucleated cell populations in blood using inertial forces in straight microfluidic channels of large aspect ratios [152].

1.3.2 Active particle separation

Figure 1.5 shows the different active manipulation methods and visually depicts the particle size regime to which the different methods have access to, as well as the force range each method can apply.

1.3.2.1 Optical manipulation

Optical manipulation techniques present an effective method for controlling the three degrees of spatial freedom for particles from tens of nanometers in size [154] to tens of microns [155, 156]. Optical forces produced by a highly focused optical beam impose scattering and gradient forces sufficiently large to manipulate micron-sized objects (e.g. cells) [157].

Thus, optical forces have been used for cell manipulation or to trap cells in a liquid

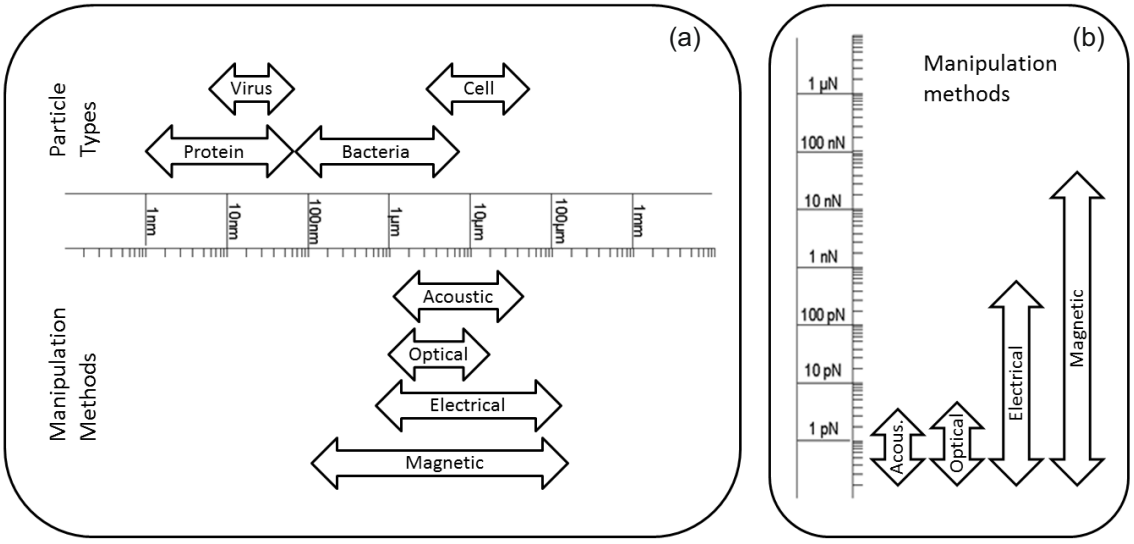


Figure 1.5: Diagrams showing (a) the relative sizes of particles and the associated technologies that provide access to manipulation in these size regimes and (b) the relative forces to which different manipulation schemes have access. Figure reproduced from [153].

due to a mismatch in the refractive index between the cell and its surrounding fluid. Optical manipulation is considered advantageous for biomaterial manipulation due to its preservation of cell functionalities, if the laser intensity is below the level that causes damage [158].

Optics has first being used to levitate and transport individual particles in a fluid by Ashkin in 1970 [159]. Eventually, optical radiation forces were applied to cell sorting by propelling single cells through a microfluidic channel, whereby the long traversal times generally resulted in low throughputs [160]. However, recent innovations in miniaturized optical devices have reinvigorated the use of optics as switches, which have made optics-based methods more feasible for fluorescent label-based cell sorting [161–163]. Several groups have used focused optical beams to impose switchable radiation forces on a continuous stream of focused cells for on-chip sorting and cell characterization [161, 164]. Recently, Wu *et al.* developed a pulsed laser fluorescence-based cell sorter that rapidly forms a stationary bubble due to localized heating to controllably deflect target cells at $20,000$ cells/sec [165].

However, optical techniques have limiting characteristics making them unsuitable for many applications. First, optical manipulation can only exert forces in the order of $O(10^1)$ piconewtons [166], which removes this technique from many force measurement platforms. Second, for many materials lasers often induce charging or heating which is generally detrimental to system performance [167]. Third, sample throughput is limited due to the need to have a focused beam. Finally, optical techniques require the use of expensive, bulky equipment that is currently difficult to integrate into LOC technologies and mobile units.

1.3.2.2 Electrical manipulation

Electrical forces can either be exerted on a particle in a uniform electrical field due to the particle's surface charge (electrophoresis) or on a dielectric particle when it is subjected to a non-uniform field (dielectrophoresis).

Electrophoresis refers to the movement of suspended particles toward an oppositely charged electrode in direct current (DC) fashion. Since most biomaterials have a slight negative net surface charge due to chemical groups on their surface, they migrate toward the positive electrode during electrophoresis [168]. Takahashi *et al.* applied electrophoresis to sort cells on a microchip in which an upstream fluorescence detector identified labelled cells for rapid electrostatic sorting downstream [169]. Yao *et al.* developed a similar device based on gravity that operated in an upright orientation to process cells without convective flow [170]. A more recent example by Guo *et al.* showed electrophoretic sorting with much higher throughput by sorting water-in-oil droplets under continuous flow [171]. In this system, pre-focused cells were encapsulated into droplets such that droplets containing single cells were sorted from droplets containing no cells or multiple cells.

In contrast to electrophoresis, where particles move in a uniform electric field due to their surface charge, dielectrophoresis (DEP) refers to the movement of particles in a

non-uniform electric field due to their polarizability. This force does not require the particle to be charged, but relies on an induced dipole moment across a cell [168]. Once exposed to an AC field, particles migrate either toward or away from the region of strongest field intensity depending on the electrical permittivity of the particle and the fluid. Particles with a higher permittivity than the fluid are attracted toward the field maxima, which is known as positive DEP (pDEP) [82]. The opposite is true for negative DEP (nDEP). The strength of the force depends on the medium and particles' electrical properties, on the particles' shape and size, as well as on the frequency of the electric field [168].

Since cells exhibit a dielectrophoretic force in the presence of an electric field and because integrating electrical systems into a microfluidic device is straightforward (drawing from the highly developed science of chip technology for MEMS) DEP has become a popular choice for cell separation [172].

Huang *et al.* took advantage of the intrinsic dielectric properties of cells and successfully sorted five different cell types based on their individual distinct dielectric properties on a 5×5 microelectronic chip array [173]. Also, Cummings *et al.* designed a microchip containing arrays of insulating posts where the resulting non-uniform electric field across the posts exerted different magnitudes of force on cells as they passed [174]. Later, this principle was used to generate non-uniform electric fields near insulating ridges on a microchip to filter and concentrate cells [175]. Vahey *et al.* introduced an isodielectric separation system for sorting cells without labels [176]. In this system, cells experience dielectrophoretic forces that displace them to their natural equilibrium point across a conductivity gradient to where their net polarization vanishes (i.e. isodielectric point). With this principle, cells with different conductivities are displaced along the gradient for efficient on-chip sorting. Wang *et al.* developed a system using lateral nDEP, whereby a set of interdigitated electrodes aligned along both sides of a microfluidic channel provides repulsive forces

to organize cells at precise distances from the microfluidic channel walls, to enable enhanced on-chip cytometry and sorting across five channels [177]. Doh and Cho developed a microchip to separate viable from non-viable cells due to their dissimilar polarizabilities, resulting in pDEP and nDEP, respectively [178].

An interesting extension of dielectric cell sorting uses field-flow fractionation (FFF), which exploits a combination of approaches (e.g., gravitational, centrifugal, thermal, magnetic, and electrical) to position cells at precise distances from the microchannel floor and thus to distinct regions of the parabolic flow profile for separation by flow [179]. Vykoukal *et al.* first developed a DEP FFF system to isolate stem cells from enzyme-digested adipose tissue [180]. This system contained patterned microelectrodes along the bottom of a microfluidic channel that exerted dielectric forces in the opposite direction to gravity, which let the cell types levitate at different heights based on their weight.

These advances hold promise for creating the next generation of cell sorting devices that could also enhance clinical detection, analysis, and diagnosis using a single microchip. However, the electrical permitivities of solvents are not always tunable, such as in the case of cell media where specific salt concentrations and pH concentrations are required. In addition, electric platforms can have deleterious effects such as charging and heating.

1.3.2.3 Acoustic manipulation

Acoustic standing waves guide particles to regions of higher pressure. This movement of an object in response to an acoustic pressure field is known as acoustophoresis. The method takes advantage of a density and stiffness difference between the particle and the surrounding fluid [181, 182]. Acoustical systems allow for the generation of multiple pressure nodes in a system, without the need for additional structures to create localized distortions to the field, as it is often required in common optical,

electrical, and magnetic systems [99]. Localized pressure nodes can be created using ultrasound sources and signals. Acoustic forces are contact- and label-free and thus biocompatible because they do not affect cellular viability [82].

Acoustic standing waves were first used to sort cells by Johansson *et al.* [183], in which fluorescently labelled cells detected by a camera triggered an ultrasound transducer that moved the cell from its initial streamline toward a pressure node, thereby modifying its trajectory to the target outlet. More recently, an acoustic wave transmitter has been integrated in a microfluidics system. Acoustic microfluidic technologies have provided new areas of development within analytical flow cytometry, including cell sorting [92, 184] or particle trapping [185].

However, pressure nodes tend to be broad, weak, and exhibit higher order effects. These characteristics allow control of large microparticles ($> 10\mu$m), but have reduced effectiveness on smaller particles, which are susceptible to Brownian diffusion. Though this technique has developed into bulk fluid applications of spatial patterning of aggregates [186] and sized-based separation schemes [187], acoustophoresis does not provide for precise, deterministic control of many useful microparticle sizes.

1.3.2.4 Magnetic manipulation

Magnetic separation (immunomagnetic separation) uses either a permanent magnet or electromagnets to apply an external magnetic field to create a force on targeted particles. It is normally facilitated by binding magnetic particles to specific biomarkers. Once the magnetic particle is attached, the biological material inherits the magnetic properties of the magnetic particle. Magnetic forces can also be exerted on magnetically responsive cells or biomaterial suspended in a ferrofluid. Hence, the magnetic biomaterial (labelled or intrinsic) can be effectively manipulated, sorted, captured or separated using an externally applied magnetic field.

Immunomagnetic separation actively applies a strong magnetic field, which can exert

forces into the tens of nanonewtons and over a wide range of different particle sizes (see Figure 1.5) [188, 189]. Most biological materials have a range of magnetic susceptibility and are either diamagnetic or weakly paramagnetic. This separation method has the potential to be selective and a high throughput can be achieved [190–193].

Additionally, magnetism has the practical advantage of being biologically and chemically inert. This is why magnetic separation has shown tremendous promise for biomedical and bioanalytical applications [71, 72].

In the last decade, magnetic separation techniques have been conducted in microfluidic geometries, which combine the advantages of microfluidics and magnetic microparticles. The combination of the two fields, microfluidics and magnetism, is commonly known as magnetophoresis and will be discussed in more detail in the next section (Section 1.4).

1.4 Magnetophoresis

Magnetophoresis is an active separation technique and is the main topic of this thesis. Analogous to the term *electrophoresis*, magnetophoresis describes the behaviour of a magnetic particle (see Section 1.2) moving through a viscous medium under the influence of an external non-homogeneous magnetic field.

The term free-flow magnetophoresis describes the continuous separation of magnetic particles using the means of magnetophoresis while being pumped through a microfluidic system as depicted in Figure 1.6 [194]. The appealing feature of free-flow magnetophoresis is that under well-controlled conditions it provides a means for non-invasive and low-cost particle separation due to its potential to be integrated on a LOC. However, the full control of particle motion in direction and velocity remains complicated, since particle properties and their magnetic response vary quite signif-

icantly depending on the particle manufacturer and its manufacturing processes.

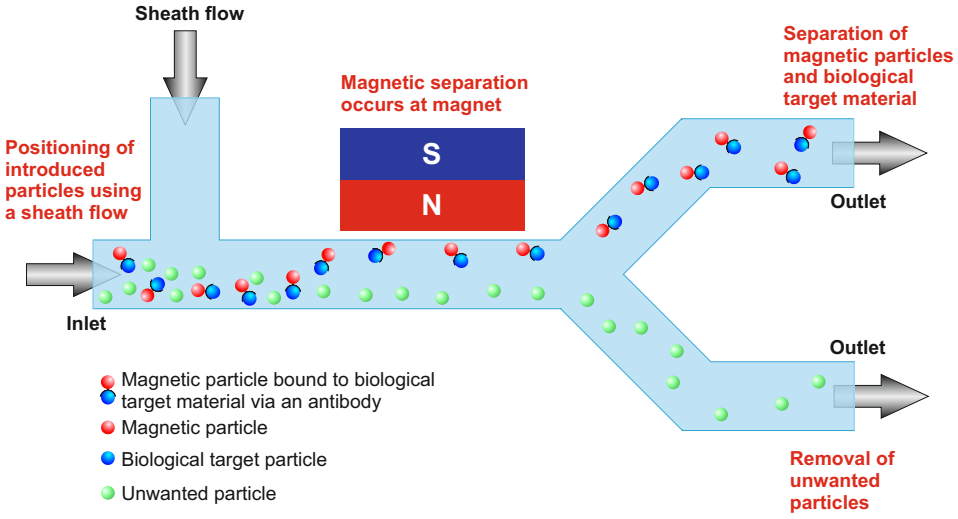


Figure 1.6: A schematic of the magnetic particle separation principle in continuous flow using magnetophoresis. Magnetic particles or magnetically labelled biomaterial are deflected from the direction of laminar flow by the use of an external magnetic field. Figure is not drawn to scale.

Magnetic separation typically uses functionalized magnetic particles with antibody receptors that can recognize and associate with various biological materials by affinity binding. The use of functionalized magnetic microparticles attached to biomarkers lead to a sensitive and relatively inexpensive cell separation method [71, 72] which is a vital component for any magnetic separation device.

Magnetophoresis has gained a lot of attention in recent years due to its potential in bioanalysis systems, e.g. detection of cancerous cells [59]. Numerous configurations have been demonstrated over the course of the last decade including: capturing, isolation and collection of target biomaterial from mixtures of substances [71, 195–197].

Magnetic separation devices use an arrangement of permanent magnets or electro-

magnets in proximity with the fluid handling parts; in its simplest form a test tube is brought into proximity of a permanent magnet. This basic configuration can be further developed into automated devices. In this thesis, magnetic separators will be divided into two categories, namely *batch* (batch mode) and *continuous* (continuous flow) magnetic separators.

1.4.1 Batch mode magnetophoresis

Magnetic cell separation is conventionally achieved using a test-tube arrangement where the magnetically labelled cells are first immobilized using a magnet and subsequently released (batch mode), as schematically shown in Figure 1.7.

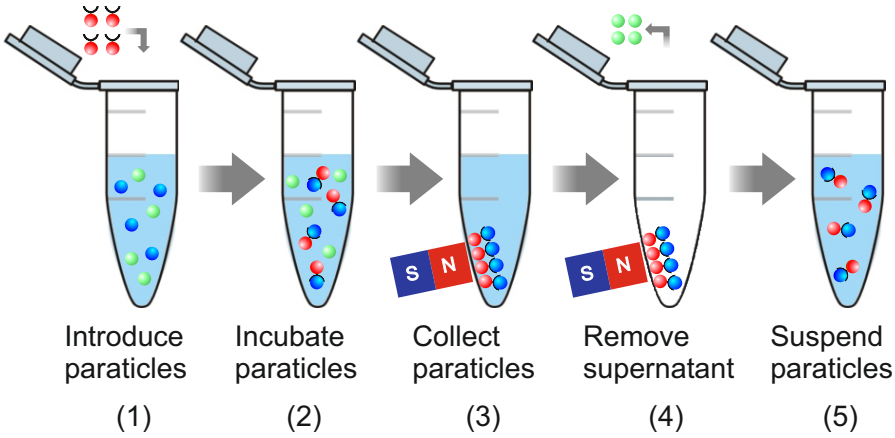


Figure 1.7: A typical reaction or separation using magnetic particles, where (1) the particles are introduced into the sample or reagent solution, (2) they bind to the target analyte/reagent, (3) the particles are collected using an external magnet, (4) the supernatant is removed, and (5) the particles are resuspended in fresh buffer solution. Steps 3-5 may be repeated several times to ensure unbound material is removed from the particle surfaces.

This type of cell separation was commercialised by Miltenyi Biotec in 1990 with the development of magnetic activated cell sorting (MACS) [198]. In MACS, antibody labelled magnetic particles are introduced into a cell suspension, where they bind to the cell of interest. The suspension is then flushed through a high-gradient magnetic separation column. The column contains steel wool that is magnetised by the

presence of an external permanent magnet, which traps the magnetically labelled cells on the wool whilst the unlabelled cells pass through the column, thereby allowing their separation. The magnets can then be removed, allowing the magnetically labelled cells to be eluted from the column (see Figure 1.8). The cell suspension either flows through the column due to gravitational forces or can be enhanced by using a syringe plunger to push the suspension through. Miltenyi Biotec reports the isolation of cells from up to 30 mL of anticoagulated blood in less than 30 minutes [199]. MACS is a well-established platform in both basic research as well as clinical medicine, as a major attraction is its scalability and very low capital costs relative to FACS [200]. Thus, the concept of MACS has been commercially developed by other companies [201].

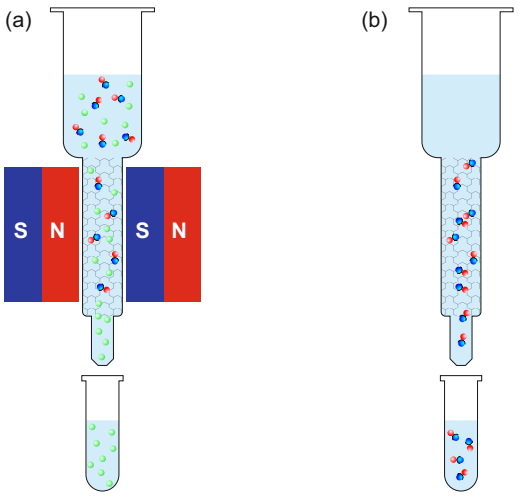


Figure 1.8: Magnetic separation principle of MACS using a magnetic separation column. (a) Unlabelled cells pass through the column, magnetically labelled cells are retained within the high gradient magnetic column. The flow-through can be collected as the unlabelled cell fraction. (b) After the magnetic field is removed, the magnetically labelled cells can be eluted from the column. The magnetically labelled cells can again be collected. Figure reproduced from [199].

However, MACS suffers from lost particles in the system. Due to the remnant field in the magnetized columns it is hard to release all magnetic particles, which negatively impacts the recovery rate. In cases of rare cell populations the recovery

rate should be as high as possible. Additionally, the MACS systems developed by Miltenyi Biotec still requires operator interaction and therefore is in a macroscopic scale range for ease of manipulation. The concept of MACS, however, can be scaled to micrometers and applied in LOCs or μTAS.

Choi and Ahn [202, 203], two of the pioneers in the field of magnetic cell separation in microfluidic systems, investigated the design, fabrication and characterization of a bio-separator composed of micro-machined serpentine and spiral electromagnets in a fluid channel. They successfully immobilized antibody-coated magnetic microparticles ($0.8-1.3$ μm, Bangs Laboratories) from a bio-buffer solution in a 800 μm wide and 250 μm deep channel (see Figure 1.9). They showed that efficient separation can be achieved in a few minutes.

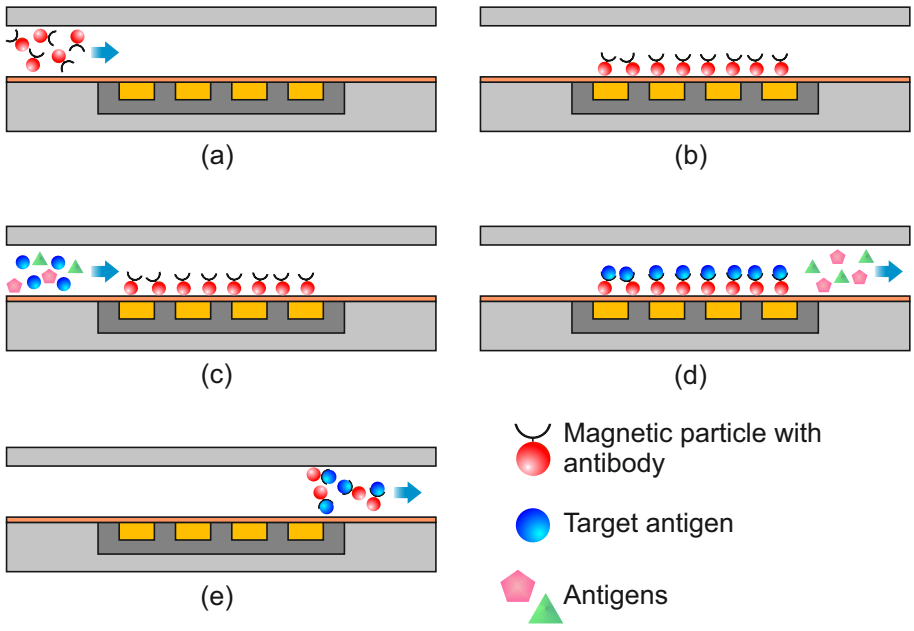
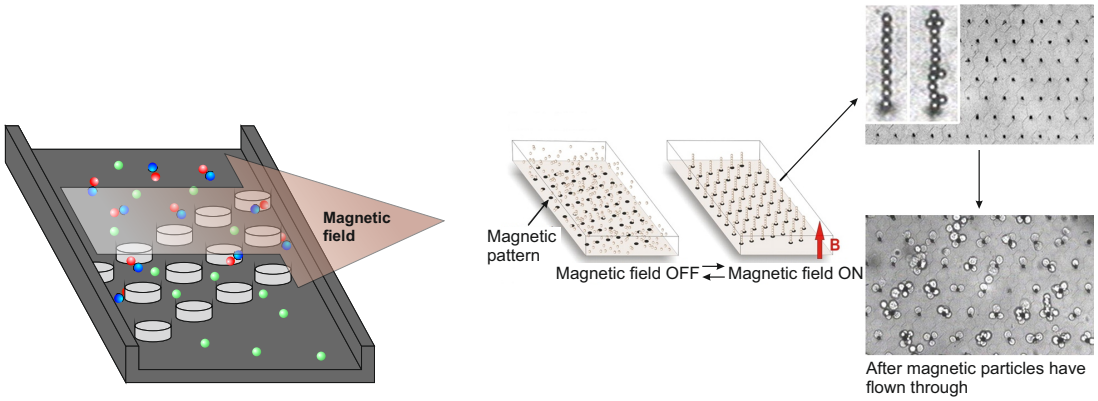


Figure 1.9: Conceptual illustration of bio-sampling procedure. (a) Injection of magnetic particles, (b) separation and holding of particles, (c) flowing samples, (d) immobilization of target antigen, (e) release of magnetic particles to biosensor of bioreactor. Figure reproduced from [202].

Another example of integrated micro-MACS is presented by Deng *et al.* in which arrays of nickel posts are manufactured on the bottom of a 150 μm wide and 50 μm

deep microchannel. The nickel posts are 7 μm in height and a diameter of 15 μm and were magnetized by an external magnetic field to rapidly trap magnetic particles (Figure 1.10a). A high separation efficiency of more than 95% of the 4.5 μm sized magnetic particles (Dynabeads M-450) was achieved when the particle suspension was injected at a flow rate of 2 μL/min ($\bar{u} \approx 4.4$ mm/s) [204].



(a) (b)

Figure 1.10: (a) Schematic outline of the micro-fabricated nickel post arrays using soft lithography. An externally applied magnetic field magnetizes the nickel posts. Cells labelled with magnetic particles are trapped within the post array. (b) Operating principle and practical implementation of the cell sorting system proposed by Saliba *et al.*. A hexagonal array of magnetic ink is patterned on the bottom of a microfluidic channel. The application of an external vertically-aligned magnetic field induces the formation of a regular array of magnetic particle columns localized on top of the ink dots. The particle columns then capture Raji cells. Raji cells are the first continuous human cell line from hematopoietic origin [205]. Images in figure reproduced from [204] and [206].

Saliba *et al.* essintially used the same magnetic trapping principle and magnetic particles as Deng *et al.*, however, invented an unconventional immunomagnetic separation method as shown in Figure 1.10b [206]. Instead of labelling the target cells, antibody conjugated magnetic beads were dynamically assembled into an array of columns in the microfluidic channel with the help of the pre-patterned magnetic traps on the substrate. As a result, when the sample flows through the channel, cells with specific biomarkers are captured by the assembled magnetic particles. A separation efficiency of $> 94\%$ was reported at a flow velocity of $\bar{u} = 100$ μm/s.

This flow velocity corresponds to a cell throughput in the range of ten to hundred cells/s and a flow rate of approximately 150 μL/min in the 500 μm wide and 50 μm high device. Recently, this device has been applied to CTC isolation by Svobodova *et al.* [207, 208] where they achieved a 50% separation efficiency of human breast cancerous cells (ratio of collected particles in target outlet to total collected particles).

However, despite the advantages of using magnetic microparticles for performing assays, these batch mode separation techniques suffer from requiring multiple, sequential reaction and washing steps that render the procedures laborious and time-consuming, and often result in using relatively large volumes of potentially expensive reagents [201]. Therefore, continuous separation, where magnetic particles are continuously pumped through a device and simultaneously sorted, is preferred.

1.4.2 Continuous magnetophoresis

Continuous magnetic separation offers the potential to eliminate some of the inefficiencies of batch separation methods, allowing for an unremitting separation by combining a continuous introduction and guidance of particles through a viscous medium using continuous fluid flow. The problems encountered in the batch separation, where multiple sequential steps are required, do not occur. On the contrary, it allows for multiple staging and recirculation of sorted fractions. In this manner, larger volumes can be processed while allowing continuous monitoring [59].

Various designs of continuous cell separators are reported in the literature. A common design directly integrates an electromagnet by micro-machining a wire in the vicinity of the microfluidic channel. Magnetic particles are deviated via an external magnetic field created by a current passing through the wire [209–212].

Pekas *et al.* [209] fabricated a fully integrated micromagnetic particle diverter in a microfluidic system. The resulting magnetic force deflects particles across a flow

stream into one of the two channels at a Y-shaped junction, as shown in Figure 1.11(a)-(b). At a flow rate of 6 nL/min ($\bar{u} \approx 1$ mm/s), 85% of the micron-sized particles (Bangs Laboratories) flowed down the desired channel, compared to 50% when the diverter was inactive. Derec *et al.* [210] described a similar design for a magnetophoretic bio-diverter, where a copper wire runs either side of the Y-shaped microfluidic channel (see Figure 1.11(c)). One wire was capable of producing a magnetic field between $2 - 7$ mT with a magnetic field gradient ranging from $3 - 70$ T/m within the channel. The dimensions of the etched channel were 100 μm in height and 300 μm in width. 5 μm sized magnetic particles (PMPEG-5.0COOH, Kisker-Biotech) were used to label tumour cells. The device successfully purified a mixture of two different cell types by removing the labelled tumour cells. Only 7% of the initial magnetically labelled tumour cells were obtained in the outlet of the nonmagnetic side, when a withdrawal rate of 0.8 μL/min was applied to both outlets.

Siegel and Shevkoplyas [211, 212] fabricated a microfluidic channel with a 40 μm$\times$ 40 μm cross-section, which has two metal wires either side. Passing an electrical current through one of the two wires generated a magnetic field up to 2.8 mT and a magnetic field gradient up to 40 T/m, which enabled magnetic particles of 6 μm diameter (Bangs Laboratories) to be pulled to either side of the channel. By turning the electromagnets either side of the central microfluidic channel on and off, the particles alternated the direction of their movement. This electromagnetic switch could sort the magnetic particles within $1 - 30$ seconds, depending on the applied current.

Although electromagnets have the advantage of being easily and rapidly switched on and off, offering system flexibility, integrating them into micro-devices often requires numerous and expensive lithography and etching techniques [70, 196]. This makes the fabrication process prone to errors and cumbersome. Electromagnets also

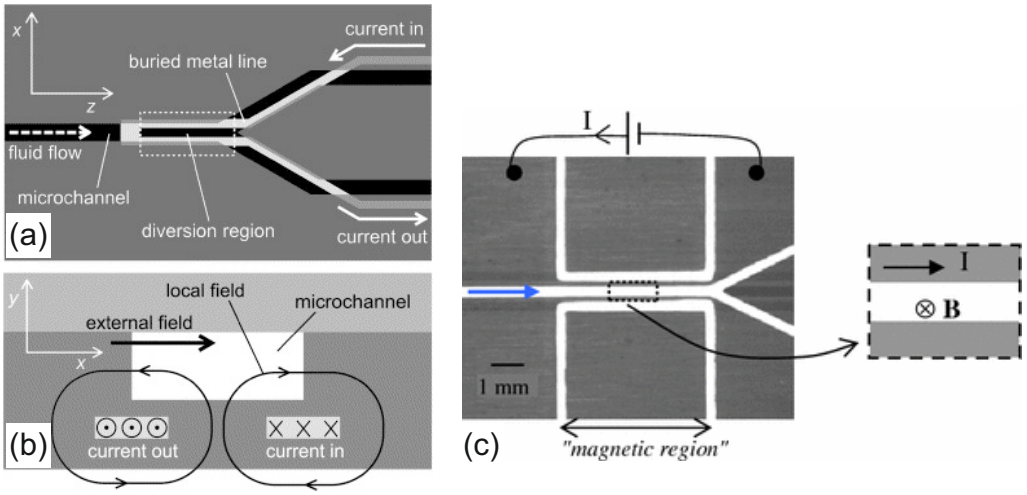


Figure 1.11: (a)-(b) Top and cross-sectional view of a micromagnetofluidic diverter. Magnetic particles in the flow stream are magnetized and deflected by an external magnetic field. The magnetic field is applied by a current passing through one of the inlaid wires. As a consequence, particles are diverted into one of the desired channel. (c) Microfluidic bio-diverter with a Y-shaped junction. The copper appears in grey, and the copper-less channel-like regions appear in white. The central channel is used for the microfluidic flow (shown by the arrow), while the other channels serve to interrupt the copper and generate a narrow copper band framing the central channel. Figure reprinted with permission of Elsevier [209] and Springer [210].

suffer from Joule heating problems that have the potential to damage live cells if too extreme. For this reason, currents may need to remain in the milliamp region, therefore limiting the fields generated to $0.01 - 0.1$ Tesla [213].

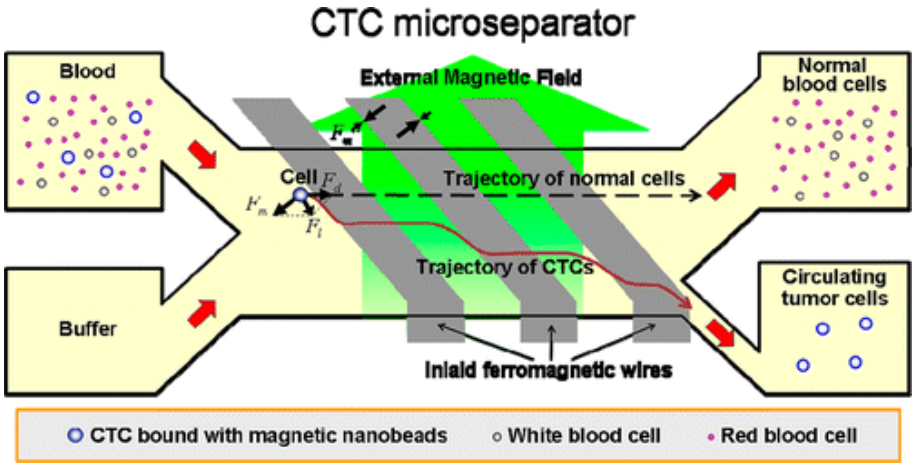
An easy way to avoid these disadvantages is by using soft-magnetic element systems, where external biasing is used to magnetize embedded elements or hard-magnetic element systems that essentially have the same structure but do not require current biasing. Such systems are normally referred to as high gradient magnetic separation (HGMS) devices.

Multiple research groups are working on such HGMS devices. For example, Inglis *et al.* [214, 215] and also more recently Kim *et al.* [216] presented a microseparator where a ferromagnetic wire array had been inlaid in the bottom substrate of the microchannel to continuously isolate magnetically labelled white blood cells and CTCs from peripheral blood, respectively. Both groups labelled their cells with immuno-

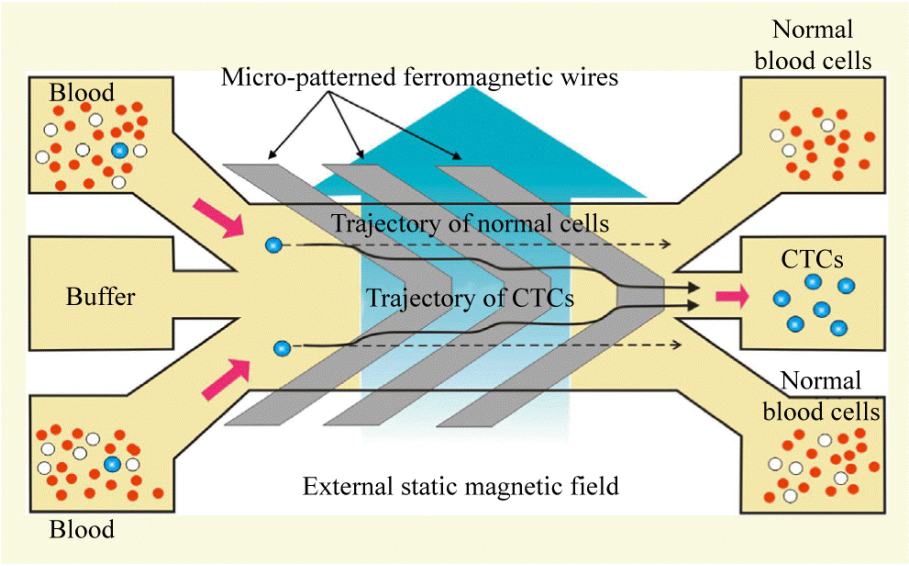
magnetic nanoparticles (50 nm) via specific antibody binding. The microchannel used by Kim *et al.* is an asymmetric Y-junction where the centre channel is 1 mm in width and 50 μm in depth with the two outlet channels being 800 μm and 200 μm wide, respectively (see Figure 1.12a). The externally applied magnetic field of 0.2 T generated a magnetic flux gradient of < 40 kT/m around the microscale ferromagnetic wires. Experimental results showed that under these conditions the microseparator isolated up to 90% of CTCs from human peripheral blood at a flow rate of 5 mL/h ($\bar{u} \approx 27.8$ mm/s). The overall isolation procedure was completed within 15 min for 200 μL of blood. Park *et al.* [217] further developed and improved the design by Kim *et al.*. Instead of having an array of ferromagnetic wires at an angle compared to the flow direction, they fabricated an inlaid array of chevron shaped ferromagnetic wires at the bottom of the microdevice, as shown in Figure 1.12b. A separation efficiency of 93% at a flow rate of 140 μL/min ($\bar{u} \approx 15.6$ mm/s) for the separation of CTCs from human whole blood cells is reported. The time needed to isolate 400 mL of whole human blood only took 10 minutes.

Jung and Han [218] presented a method for the lateral-driven continuous magnetophoretic separation of red and white blood cells from peripheral whole blood, based on their intrinsic magnetic properties. The separation is achieved using a high-gradient magnetic field, caused by a ferromagnetic wire array inlaid on a glass substrate. The wire array creates an even lateral magnetophoretic force on the whole area of the microchannel, which improved the separation efficiency and throughput. When the flow rate and external magnetic flux were 20 μL/h ($\bar{u} \approx 21.3$ μm/s) and 0.3 T, respectively, the microseparator continuously separated out 93.9% of red blood cells and 89.2% of white blood cells from the whole blood.

Earlier, Han *et al.* [219, 220] showed a HGMS microseparators that could separate 93.5% of red blood cells and 97.4% of white blood cells from blood at a flow rate of 5 μL/h ($\bar{u} \approx 77.2$ μm/s). They again only used the native magnetic properties of red



(a)

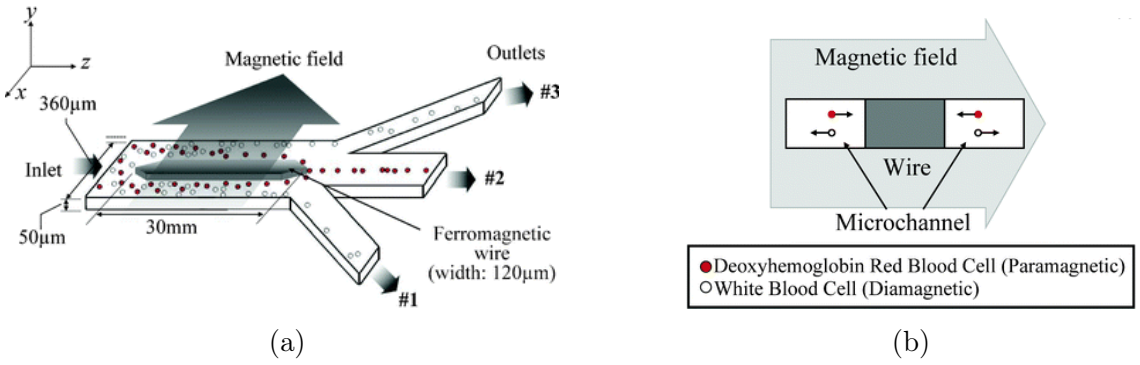


(b)

Figure 1.12: (a) Perspective view of the CTC microseparator, including the inlaid ferromagnetic wire array. The magnetic force acting on the CTCs is induced by a high magnetic field gradient generated near the ferromagnetic wire array with an external magnetic field. (b) Schematic diagram showing the working principles of a microdevice for separation of CTCs using lateral magnetophoresis and immunomagnetic nanobeads. Figure reprinted with permission of American Chemical Society [216] and Electronics and Telecommunications Research Institute Journal [217].

and white blood cells, without additional markers or labelling. The magnetophoretic microseparator incorporated a nickel wire running along the centre of a microfluidic channel, as shown in Figure 1.13a. The channel featured three outlets that were used to separate red and white blood cells from diluted whole blood in continuous

flow. The nickel wire was magnetised by an external magnetic field (0.2 T), such that as the cells passed through the chamber the red cells (paramagnetic) were attracted towards the wire, forcing them towards the centre of the chamber and therefore out of the middle outlet. However, the white cells (diamagnetic) were repelled by the field towards the outer edges of the chamber, exiting the chip via the upper and lower outlets, thereby achieving separation (see Figure 1.13b). Qu *et al.* [221] demonstrated a similar device in which a nickel wire was situated inside the chamber of a microfluidic device and used to separate red and white blood cells by their respective attraction and repulsion.



(a) (b)

Figure 1.13: (a) Illustration of Han and Frazier's magnetophoretic microseparator. The design incorporates a 50 μm wide nickel wire, which is magnetized by a 0.2 T strong external magnetic field. (b) Red and white blood cells were separated based on their intrinsic magnetic properties. Red and white blood cells in a water or plasma behave like paramagnetic and diamagnetic particles, respectively. Figure reproduced from [219].

Xia *et al.* [222] integrated a micro-fabricated comb shaped HGMS geometry on one side of a microfluidic channel. When magnetised by an external permanent magnet they found that the comb structure could locally concentrate the gradient of the applied magnetic field to pull magnetic particles from one laminar flow path to another, and thus selectively remove them from a continuously flowing biological fluid, as depicted in Figure 1.14. The comb structure provided a magnetic field of $0.018 - 0.025$ T and a field gradient of at least 50 T/m ($\approx 55 - 250$ T/m) across the 200 μm wide and 50 μm deep microfluidic channel. This device was used to remove

1.6 μm sized magnetic particles (Bangs Laboratories) as well as magnetically labelled Escherichia coli (*E. coli*) bacteria. In their study, 130 nm magnetic particles were used to label *E. coli* bacteria. Quantification of the separation efficiency for the microfluidic separation device revealed that 92% of the magnetic particles exited the collection outlet at a flow rate of 40 μL/h ($\bar{u} \approx 1.1$ mm/s) when suspended in phosphate buffered saline (PBS), whereas when mixed in isotonic saline with red dye the separation efficiency dropped to 83% at a flow rate of 25 μL/h ($\bar{u} \approx 0.7$ mm/s). *E. coli* cells suspended in PBS were separated with an efficiency of 89% and when suspended in isotonic saline 53% could be isolated for flow rates of 30 μL/h and 25 μL/h, respectively.

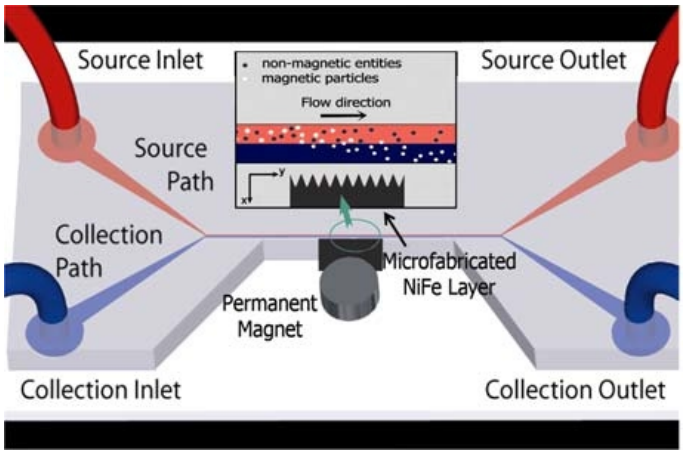


Figure 1.14: Schematic depiction of the combined micromagnetic separation device for separating *E. coli* that contains a microfabricated layer of soft magnetic NiFe material adjacent to a microfluidic channel with two inlets and outlets. Inset shows how magnetic particles flowing in the upper source path are pulled across the laminar streamline boundary into the lower collection path when subjected to a magnetic field gradient produced by the microfabricated NiFe layer located along the lower side of the channel. Figure reprinted with permission of Springer [222].

Afshar *et al.* [223] used multiple sharp tips on either side of the fluid channel (200 μm wide, 100 μm high and 10 mm long) to control, immobilize and release particles in a controlled manner and to continuously separate magnetic particles by size (see Figure 1.15). The magnetic tips that served as field concentrators were powered by an external electromagnet. A coil current of 120 mA generated a magnetic field of

about 5 mT between the open ends of the yoke with an estimated field gradient of approximately 90 mT/mm perpendicular to the flow direction. Two different types of superparamagnetic particles with a diameter of 1.05 μm (MyOne, Dynabeads) and 2.8 μm (M270, Dynabeads) were used to characterize the system. The high field strength around the tips allowed for efficient particle manipulation. In particular, mixtures of 1.05 μm and 2.8 μm sized particles were reported as separated with an efficiency of $70\% - 80\%$ when run under continuous conditions with a flow rate of 22 μL/h ($\bar{u} \approx 0.3$ mm/s).

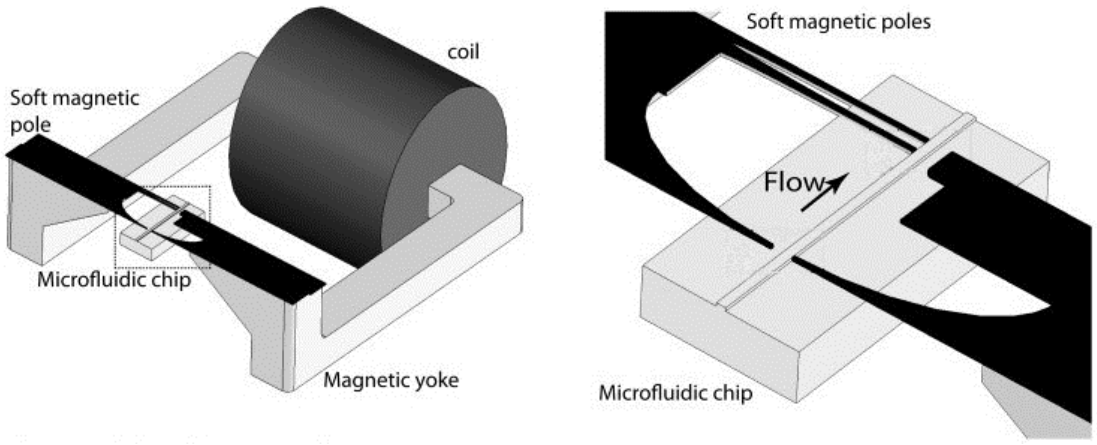
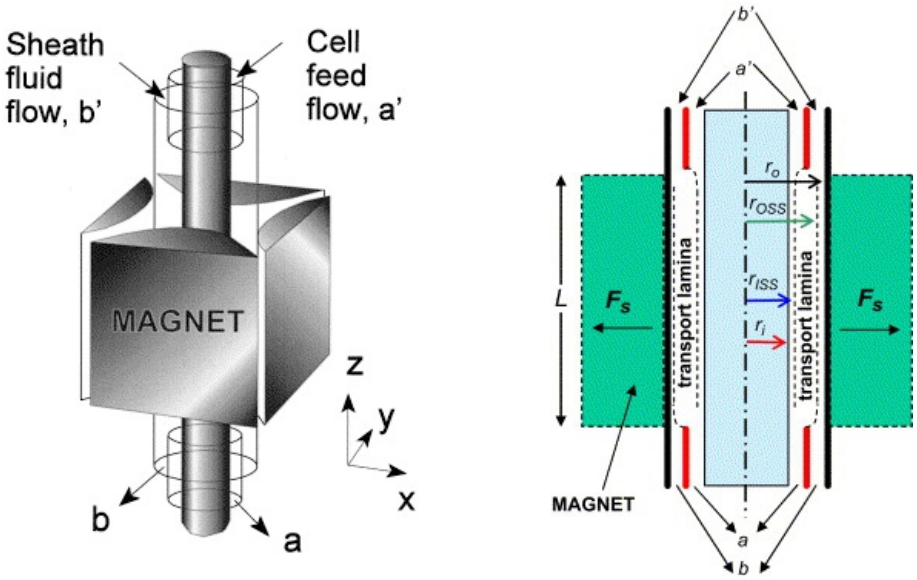


Figure 1.15: (a) Magnetic actuation system comprising an electromagnet (coil), a magnetic yoke and soft-magnetic poles, integrated with the microfluidic chip. Figure reproduced from [223].

HGMS devices, however, can suffer from poor particle recovery because the embedded magnetic elements might retain a residual magnetization which causes particle trapping. Instead of having embedded magnetic elements and structures integrated in the microfluidic device and then magnetized by an external magnetic field, it is possible to generate the required non-uniform magnetic field simply using external permanent magnets. Permanent magnets may not give the flexibility of varying the magnetic strength nor can they be completely switched off, like electromagnets, but they are inexpensive and able to produce a strong magnetic field without being bulky.

One of the earliest adopters to use permanent magnetic elements was Zborowski *et al.* [224, 225]. The group of Zborowski *et al.* has been developing FFF devices that have typically employed quadrupole magnetic fields to provide the lateral forces necessary to radially move magnetic particles in an axial flow [226–228]. The magnetic quadrupole configuration exerted a radially outward force on the magnetically labelled cells within a cylindrical column (see Figure 1.16a). The quadrupole generated a maximum magnetic field of 0.76 T at the channel wall, and a magnetic gradient of 0.17 T/mm in the radial direction. The circular flow splitter (diameter $\approx$ 4 mm) separated labelled CTCs to a purity of 99.6% when started with an initial concentration of 20% at a flow rate for the cell sample of $0.1 - 0.75$ mL/min ($\bar{u} \approx 0.1 - 1$ mm/s). The idea of using a quadrupole arrangement of magnets has been further developed by Kennedy *et al.* [229], where a quadrupole magnetic flow sorting device is modelled, designed, manufactured and tested for the successful sorting and isolation of pancreatic islets. The separation efficiency had not been reported but can be assumed similar to the one described by Zborowski *et al.* as channel geometry and magnetic flux density are similar.

Pamme *et al.* [230, 231] demonstrated the use of a single off-chip permanent magnet to continuously sort magnetic particles of different sizes (2 μm and 4.5 μm sized particles from Micromod and Dynabeads, respectively) from a mixture of both magnetic and nonmagnetic particles (6 μm polystyrene beads, Polysciences Inc.) and also successfully separated magnetically labelled macrophages and tumour cells. The particles were sorted in a rectangular 6×6 mm separation chamber with a depth of 20 μm (see Figure 1.17) based on their different magnetic mobility. The chamber had 16 outlets and depending on how far a particle was deflected by the cylindrical magnet would exit through a different outlet. Different sizes of particles were separated with an efficiency of 75% at a flow rate of 2.5 μL/min, which resulted in a flow velocity of $\bar{u} \approx 0.3$ mm/s in the separation chamber.



(a) (b)

Figure 1.16: (a) Schematic representation of a circular quadrupole flow sorter. The arrows indicate direction of the fluid flow. (b) Simplified cross section of a circular quadrupole flow sorter. The mixed cell/particle suspension is introduced in inlet a' while buffer fluid is introduced in inlet b'. The radially directed magnetic force leads to the movement of the labelled cells in the radial direction towards exit b, while the unlabelled cells are unable to move in the radial direction and leave the channel through exit a. Figure reproduced from [225] and [229]

1.4.2.1 Diamagnetic repulsion

A less commonly used method for particle manipulation exploits diamagnetic repulsion, because diamagnetic repulsive forces are much weaker compared to paramagnetic (superparamagnetic) attractive forces. However, by applying very high magnetic fields and field gradients such as those generated by superconducting magnets, diamagnetic repulsion forces have been used to manipulate large diamagnetic objects [232]. The repulsive effect of diamagnetism, however, can be greatly enhanced by suspending the diamagnetic particles in a paramagnetic solution, which then allows the use of electromagnets and strong permanent magnets, rather than bulky and expensive superconducting magnets.

Kimura *et al.* [233, 234] demonstrated the micro-patterning of cells and particles

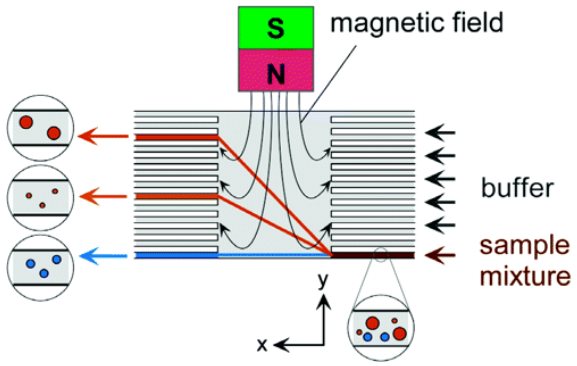


Figure 1.17: Concept of continuous magnetophoresis to separate magnetic particles of different sizes. Magnetic particles are pumped through the flow chamber. The applied magnetic field deflects the particles perpendicular to the direction of flow. Depending on the particle size and magnetic mobility, they exit the chamber through a different outlet. Reprinted with permission from [230].

suspended in aqueous paramagnetic solutions. The suspensions were placed atop a magnetic field modulator constructed from alternating layers of iron and aluminium. By applying an external magnetic field of approximately ≈ 1 T, the field modulator generated a magnetic field, which alternated between 0.2 T and ≈ 1 T every 300 μm. The alternating magnetic field caused the 20 μm sized particles and cells to migrate, forming periodic lines above the iron layers where the field was weakest.

Winkleman *et al.* [235] described the fabrication of a fluidic device for separating diamagnetic particles of different sizes and densities. The basis for the separation is the balance of the magnetic and gravitational forces on diamagnetic materials suspended in a paramagnetic medium. Diamagnetic particles with a wide size range from 5 μm to 5 mm were suspended in a paramagnetic solution and continuously pumped through a funnel shaped fluid device. The funnel was exposed to an inhomogeneous magnetic field, exerted by two permanent magnets (0.4 T at the magnet surface) with their like poles facing. The magnetically exposed particles in the chamber were levitating at different heights depending on their density and thus exited different outlets of the fluidic device.

A similar approach for guiding differently sized particles towards different outlets

based on their varying repelling force was also used by Pamme *et al.* [236–238]. The group reused their initial microfluidic chamber design, which had previously been used to sort superparamagnetic particles, but rather than using superparamagnetic particles, they suspended diamagnetic particles of 5 μm and 10 μm in diameter in a paramagnetic solution. The particles are no longer attracted, but repelled by the magnetic field when continuously passing through the microfluidic chamber. Full resolution of the two particle population was achieved when the flow rate did not exceed 20 μL/h ($\bar{u} \approx 46$ μm/s). The same group also demonstrated the application of simultaneously trapping magnetic and diamagnetic particles [237, 239]. Herein, a mixture of 2.8 μm sized superparamagnetic particles (M270, Dynabeads) and 10 μm sized diamagnetic polystyrene particles (Megabeads) were prepared in a paramagnetic liquid and pumped through a silica capillary (100 μm inner diameter). A magnet assembly of two permanent magnets on either side of the capillary with their opposite poles facing, formed a magnetic *barrier*. The magnetic field, trapped superparamagnetic particles in the area with the highest flux density, whereas diamagnetic particles were pushed towards the area with the lowest flux density, as schematically depicted in Figure 1.18. This led to the formation of two distinct particle plugs. A 100% separation between the two particle types could be achieved at a maximum flow rate of 10 μL/h ($\bar{u} \approx 0.35$ mm/s). At higher flow rates, the drag force on the diamagnetic particles was too large to successfully trap them.

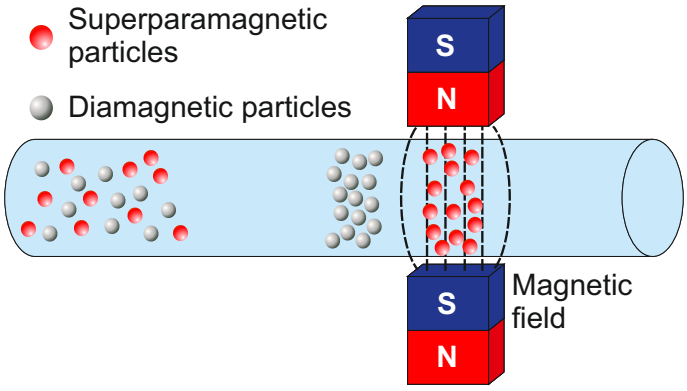


Figure 1.18: Schematic of simultaneously trapping superparamagnetic and diamagnetic particles. Superparamagnetic particles (red) and diamagnetic particles (grey) in a paramagnetic medium are pumped through a capillary and trapped by a pair of magnets. The superparamagnetic particles are attracted to the region between the magnets, while the diamagnetic particles are repelled and unable to pass through this magnetic *barrier*. Figure adapted from reference [239].

Table 1.2: Summary of different continuous magnetophoretic separation techniques. The table compares magnetic field properties, fluid dynamic settings and channel dimensions. The separation performance is given in the column: Separation. If no information could be found to the corresponding property, it is indicated with a hyphen.

Magnet design	Magnet		Fluid Channel				Separation efficiency	Reference
	$\lvert\mathbf{B}\rvert$ [T]	$\nabla\lvert\mathbf{B}\rvert$ [T/m]	Width [μm]	Height [μm]	Flow rate [μL/h]	Velocity [mm/s]		
Electromagnet	0.016	100-1000	18	6	0.36	0.93	85%	[209]
	0.002-0.007	3-70	300	100	48	0.44	93%	[210]
	0.0028	40	40	40	10	1.74	–	[211] [212]
Soft-magnetic element	0.08	5000	–	15	–	–	40%	[214], [215]
	0.2	40000	1000	50	5	0.03	90%	[216]
	–	–	3000	50	8400	15.56	93%	[217]
	0.3	–	360	100	20	0.15	93.9%	[218]
	0.2	–	360	50	5	0.078	$93\% - 97\%$	[219], [220]
	0.3	–	$149 - 287$	73	13.8	0.24	93.7%	[221]
Comb magnet	$0.018 - 0.025$	$55 - 250$	200	50	$25 - 40$	$0.69 - 1.11$	$83\% - 92\%$	[222]
	$0.018 - 0.025$	$55 - 250$	200	50	$25 - 30$	$0.69 - 0.83$	$53\% - 89\%$	[222]
Magnetic tip	$0.013 - 0.016$	25	200	50	25	0.69	20%	[222]
	0.005	90	200	100	22	0.61	$70 - 80\%$	[223]
Quadrupole	0.76	170	9500	9500	$6000 - 45000$	$0.02 - 0.14$	99.6	[225], [226]
	$0.7 - 1.4$	–	15900	63500	–	–	–	[229]
Bar magnet	0.25	$100 - 200$	6000	25	200	0.37	75%	[230], [231]
Superconducting magnet	1	$2000 - 3000$	–	–	–	–	–	[233], [234]
	0.4	20	16000	$6000 - 15000$	–	–	–	[235]
	$7 - 10$	$34.7 - 49.5$	6000	20	–	–	–	[236]
	$7 - 10$	$34.7 - 49.5$	6000	20	$20 - 100$	$0.05 - 0.23$	–	[237]

1.5 Numerical particle trajectory simulation

In this section, the various models for particle trajectory simulation will be discussed. The accurate prediction of the dynamical behaviour of discrete particles released in a contiuous flow of fluid is key for a better understanding and optimisation of several branches of science and technology, e.g. microfluidics, chemical processing, combustion processes or dust precipitation [240–242].

From a theoretical point of view, magnetic particle separation (magnetophoresis) is essentially a two-phase flow problem, where dispersed flow consists of discrete particles (droplets, bubbles, solids, etc.) moving in a continuous phase (air, water, etc.). To model the motion of dispersed particles in a continuous phase, two approaches are generally considered, namely the Lagrangian and Eulerian method.

The Lagrangian method considers particles as a discrete phase and tracks the pathway of each individual particle. The detailed particle motion behaviour, which facilitates a better understanding of the physical phenomena, can be revealed by solving the Newtonian motion equations in Lagrangian coordinates while solving continuity and momentum equations for the continuum phase [243, 244]. By studying the statistics of particle trajectories, the Lagrangian method is able to predict the detailed particle distributions [245, 246]. This requires considerable computational effort, which is why efficient algorithms for Lagrangian particle tracking in fluid flow are an ongoing research topic. To date, a number of algorithms have been implemented in discrete particle simulations. The reader can refer to [247–249] for the historical development of the subject.

Conversely, the Eulerian approach treats the particle phase as a continuum and develops its conservation equation on a control volume basis [250–252]. Individual particle trajectories no longer explicitly appear, but are handled at a conceptual level, where a continuous scalar field (mostly particle concentration) represents the particle positions [245, 246].

The performance of magnetophoretic microsystems for bioapplications can be modelled in advance of fabrication to determine system parameters that optimize the separation or capture efficiency of a target biomaterial. To date, several research groups have studied and modelled magnetic transport and separation at the microscale. Since magnetic separation deals with dilute magnetic particle dispersions, where the particles are only a few micrometres in diameter, the Lagrangian strategy is predominately used to model magnetophoresis [253, 254]. Eulerian particle methods have been explored as an alternative to Lagrangian particle tracking to model the varying particle concentration for sub-micron particles where the Brownian diffusion has a significant impact [255–257].

Furlani *et al.* [258–260] developed magnetic particle transport models based on the Lagrangian approach to study the particle transport of magnetic particles and the continuous separation of white and red blood cells in a magnetophoretic microsystem. The presented microsystem consists of a linear array of permalloy elements embedded beneath a microfluidic channel with a rectangular cross section and dimensions of 30 mm, 1 mm and 120 μm for length, width and height, respectively. They assumed an applied external magnetic field of 0.5 T to magnetize the embedded magnetic elements. Analytical expressions were derived for the field distribution within the microchannel, and the magnetic force on the particles. The model was used to predict the magnetic response of magnetic particles and the separation of red and white blood cells. A successful separation was predicted when the cells had at least 60 seconds to interact with the magnetic structure.

Sinha *et al.* [261, 262] and Nandy *et al.* [263] studied the magnetophoretic transport of magnetic particles in a straight microchannel when a magnetic point dipole is placed adjacent to the microfluidic channel. Explicit mathematical expressions for the fluid velocity and the magnetic force are derived. The model was used to characterize the capture efficiency of the magnetophoretic separator. The analysis

showed that the capture efficiency of the magnetophoretic separator depends on two dimensionless numbers that compare the magnetic force and particle drag. The two numbers incorporate all physical design parameters and operating conditions, such as flow rate, particle size, magnetic strength and microchannel geometry. Sinha *et al.* [262] also validated the model using 1 μm sized particles (PFCM-4056, Kisker-Biotech). The non-uniform magnetic field was established by an electromagnet with a tapered tip, that approximated the point dipole, and an adjustable current coil. The tapered tip was placed in close proximity to the microchannel and could generate a maximum magnetic flux of 30 mT closest to the tip, which reduced to 10 mT at a distance of 1 mm away from it.

Similarly, Modak *et al.* [264], simulated the trajectories of the magnetic particles in a T-shaped microchannel under the influence of a magnetic dipole. The capturing efficiency was found to be a function of different nondimensional parameters, which incorporate dipole strength, residence time, particle launching position, etc.

It is important to note that the aforementioned studies only considered a two dimensional (2D) model and are all assuming one-way coupling between the particles and a prescribed fully developed flow field. Only a few authors have studied magnetic particle transport in microfluidic systems taking into account two-way particle-fluid coupling wherein momentum is transferred from the particles back to the fluid phase. Khashan and Furlani [265, 266] have studied theoretical particle and fluid transport systems comparing the simplified one-way coupling with the two-way coupling model. The model predicts the bead separation dynamics and capture efficiency using a Lagrangian approach and computational fluid dynamics. Their analysis concluded that, while one-way particle-fluid coupling enables rapid calculation, two-way coupling should be modelled whenever more accurate results are needed or particle concentrations are high. Most of the two-way coupling studies, however, have been limited in that they only consider point dipole magnetic

field sources [264, 267, 268].

More recently, multiphysics packages, e.g. ANSYS or COMSOL, have been used to simulate trajectories of magnetic particles in fluid dynamic systems. Finite element methods (FEM) and the increasing computational power make it possible to simultaneously simulate multiple physical effects, such as magnetic and fluid dynamic forces, in highly complex geometries. For example, Tóth *et al.* [269] studied magnetic particle trapping on a Fe-Ni grid by simulating hydrodynamic and magnetophoretic processes in COMSOL Multiphysics. Radulović *et al.* [270] investigated separation methods to separate magnetic microspheres of different sizes with radii between 1 μm and 10 μm. Magnetic field and force on the particles, as well as the fluid dynamics, were simulated in a 2D model in COMSOL.

Haverkort *et al.* [271] performed computational simulations of blood flow and magnetic particle motion to optimise magnetic drug targeting in cardiovascular diseases. For this purpose, they reproduced the complex model of a coronary artery and a carotid artery in ANSYS to investigate the capture efficiency of magnetic particles within the artery when a strong external magnetic field is applied.

Computational simulations make it possible to study the feasibility or performance of magnetic separation devices before starting experiments or entering clinical trials. Simulations are useful to investigate the influence of different factors independently, and for optimisation. However, the multiphysics packages may enable accurate 3D modelling, but are often lacking control over key parameter values and the models often make incomplete assumptions about material properties that result in inaccurate predictions.

1.6 Motivation

This work was initiated after discussions with a research group and clinicians at the John Radcliffe Hospital in Oxford. It was proposed that a continuous flow magnetic separator could be used for the separation and removal of a specific vesicle from a mixed vesicle sample obtained from pre-eclampsia patients. Pre-eclampsia occurs in up to 3% of pregnancies and is one of the leading causes of maternal mortality in both developed as well as developing countries. It leads to the death of approximately $50,000$ women annually [272]. It is a life threatening condition to both mother and child. It results in other symptoms such as high blood pressure, stroke, protein in urine, clotting disorder and a non-functional placenta which would affect the nutritional requirements of the baby [272, 273].

During normal pregnancy, the placenta sheds cellular vesicles into the maternal blood as part of a normal process of turnover and repair, but these vesicles are significantly elevated in pre-eclampsia and it has been hypothesized that the increased levels of cellular micro- and nano-vesicles in human fluids are associated with a wide range of diseases such as pre-eclampsia, cardiovascular disease, cancer, sepsis, HIV and diabetes [274].

The key to managing pre-eclampsia is early detection and diagnosis. In addition to a diagnosis based on patient symptoms, it is also possible to monitor the aforementioned vesicles and biological cells within the body which serve as a biomarker. For example, the variations in the physical structure of the nano-vesicles ($30 - 100$ nm) and micro-vesicles ($0.1 - 1$ μm) found in blood plasma can serve as indicators of a disease [274].

The isolation, detection and characterization of these vesicles will provide more insight on these diseases and help in providing appropriate treatment methods. However, the placental derived vesicles in the maternal plasma samples are found to be less then 1% of the total vesicle population. The pre-dominant vesicle component

are lipoprotein vesicles, which represent 98% of all vesicles and platelet vesicles. The situation is an even greater problem in other diseases where the disease associated particles are of unknown origin and could represent a very small proportion of the vesicle population. The rare occurrence of disease associated vesicles presents a challenge for current established detection methods such as light scattering techniques.

Furthermore, cellular vesicles and lipid vesicles are of the same dimensions. This makes it difficult to use physical based separation method for this application. Currently, ultracentrifugation is used, but the procedure is time consuming and relies on the use of complicated and expensive equipment often handled by specialized and trained personnel.

The separation of such cellular vesicles with the help of magnetic particles and an externally applied magnetic field seems to be a very promising technique to isolate magnetically labelled biomarkers for various reasons given above. The use of external permanent magnets not only allows for portable and automated devices but also makes device manufacturing easier. However, permanent magnets create a unidirectional force causing particles to eventually collide with one of the inner walls of the fluidic channel. Particles being driven towards a surface are likely to be trapped in a region where the fluid velocity is zero because of the no-slip condition at the channel walls, and in some cases experience a binding force if the wall surface is oppositely charged. Such conditions adversely affect the particle throughput and continuous separation; this undesired particle loss is rarely mentioned in the literature.

The separation of placentile derived microvesicles was the initiator of this work on magnetic separation, but not the sole focus. This study extends to the separation of other biological entities including cells which, being significantly larger than microvesicles, require additional factors to be taken into account.

1.7 Aims and objectives

One of the objectives of this project was to understand how magnetic particles move when placed in a non-uniform magnetic field. This will facilitate the design of more efficient biomedical magnetic separators which can separate particles from a continuous flow without a large number of particles getting *lost* in the system. Such designs highly depend on the knowledge of the properties of the magnetic particles. Knowing the magnetic responsiveness of the particles, namely the magnetophoretic mobility, helps to predict their trajectory when suspended in a liquid medium and exposed to a magnetic field. The performance of continuous separation devices can be affected by particle variations and typically requires a different set of system parameters for each particle type in order to achieve the desired separation results. This makes the use of such continuous separation systems complex for clinicians. Therefore, a robust and easy to use separation device is needed that enables the usage of various particle types without compromising the performance of diagnostic assays for clinicians. Additionally, the device should be able to isolate a bio-entity in extremely low concentrations in larger sample volumes such as might be required when screening for disease in samples of urine.

Here, characterization of commercially available magnetic particles has been used to improve the accuracy of the particle trajectory model. The trajectories of magnetic microparticles in a microfluidic separation channel under continuous and pulse flow condition using two novel magnet configurations have been analytically studied. The model incorporated the experimentally found magnetic bead properties in order to represent the magnetic particle response as realistically as possible. Furthermore, the model has been extended to a three dimensional (3D) problem, which allows the simulation of more elaborate magnet designs and offers more flexibility for the trajectory simulations.

Theoretical investigations paired with experimental validation is rare in the liter-

ature. Thus, the new magnetic configurations are simulated and experimentally tested to validate the model and to verify the simulated magnetic field pattern. Confidence in the exact field pattern allows better control of the beads in the region where they are separated by use of an external permanent magnet, and provides accurate field data for calculating the resultant magnetophoretic forces.

The results of this work will help others make more accurate particle separation predictions and the novel magnet designs can be applied to continuous magnetic particle separation in order to contribute to the further development and improvement of inexpensive μTAS or LOC.

It is acknowledged by the author that although previous research has shown promising results, the opportunity for progression is large. For instance, more robust devices need to be developed that do not rely on accurately set flow rates or well known particle mobilities. Ease of manufacturing of such separation devices is also a vital point for the proliferation of this very promising field. Especially, the field of analytical simulation is seen to have a huge potential because it can remove the need to laboriously fabricate and test different microfluidic channels and magnetic separation designs.

1.8 Outline

After an introduction and a literature review of magnetic particle separation and its key features, the theory of magnetophoresis in microchannels as well as the modelling approach is described in Chapter 2. Chapter 3 outlines the materials used in the experiments and describes the experimental procedures. In Chapter 4, the magnetophoretic mobility and susceptibility of five commercially available magnetic bead types are studied. In Chapter 5, the fluid dynamics within a rectangular duct and the hydrodynamic focusing is analytically as well as experimentally investigated.

Chapter 6 presents two new magnetic configurations and the effect on the generated magnetic field by varying key design parameters is identified. Chapter 7 discusses the separation efficiency of the previously introduced magnetic configurations by comparing numerical particle trajectory simulations and experimental results. Chapter 8 summarizes all key findings and gives an outlook for future research.

1.9 Contribution

In this thesis, three key contributions in the field of magnetic particle separations are given. First, the susceptibility of magnetic micron sized beads are characterized using two independent studies and their field dependence has been proven. Second, the results of the susceptibility study have led to the development of a more accurate model for magnetic separation; combining FEM, particle tracking techniques and experimentally determined bead properties. The model serves as a tool for predicting magnetic particle trajectories which will help optimise future magnetic separator designs. Third, with the help of the model, two novel magnet configurations are investigated in detail and experimentally verified. The magnet configurations not only attract superparamagnetic particles but also exhibit a repelling force. This phenomenon has not previously been reported in the literature as a means to guide magnetic particles along specific trajectories. The proposed magnetic separator using the novel magnet configurations is shown to be successful in separating magnetic particles with a separation efficiency of 35% and 80% in continuous and pulsed mode operation, respectively.

Chapter 2

Fundamentals of magnetophoresis and its simulation

2.1 Introduction

In this chapter the fundamentals of microfluidics and magnetism, the two main fields involved in magnetophoresis, will be explained and their basic mathematical models will be derived. Additionally, the numerical methods to simulate the magnetic field using FEM are shown.

This chapter is by no means exhaustive. Further details on fluid dynamics and magnetism, as well as finite element methods, can be found in many published textbooks (e.g. [275–278]).

2.2 Fluid motion in microfluidic systems

In general, the flow field inside a fluid channel can be described by the incompressible Navier-Stokes equations, which represent the conservation of momentum

(Equation 2.1) and conservation of mass (Equation 2.2) [276]:

$$\rho_f \left(\frac{\partial \mathbf{u}}{\partial t} + (\mathbf{u} \cdot \nabla)\mathbf{u} \right) = -\nabla p + \eta_f \nabla^2 \mathbf{u} \tag{2.1}$$

$$\nabla \cdot \mathbf{u} = 0 \tag{2.2}$$

where $\mathbf{u}$, ρ_f, η_f and ∇p are the velocity vector, the fluid density, fluid dynamic viscosity and pressure gradient, respectively. Equation 2.1 assumes the fluid to be incompressible and isotropic (Newtonian fluid), which means the fluid's density ρ_f as well as its viscosity η_f can be approximated as constant. The different terms in Equation 2.1 correspond to the inertial forces, the convection force, pressure forces and diffusion forces applied to the fluid.

The steady-state continuity equation for an incompressible flow (Equation 2.2) reflects the fact that mass is conserved. It states that the rate at which mass enters a system is equal to the rate at which mass leaves the system.

To completely characterise the flow field described by the Navier-Stokes equations (Equation 2.1 and Equation 2.2), also a set of boundary conditions is needed. The boundary conditions need to include the pressure difference on the in- and outlets of the domain as well as the velocities of the bounding surfaces (if these are moving in the frame of reference). In this work, the geometry is assumed to be a rectangular duct with no moving side walls and a *no-slip* condition (Dirichlet boundary condition) with the fluid velocity specified at the inlets and pressure prescribed at the outlets:

$$\mathbf{u} = 0 \qquad \text{on } \Gamma \tag{2.3}$$

where Γ represents the boundaries of the domain, i.e. the channel's side walls. The velocity at the different inlets is assumed to be uniform across the entire area but will be varied in its magnitude.

2.2.1 Steady unidirectional flow in a rectangular duct

On the micro-scale, laminar flow is typically achieved [1]. Whether a flow regime is laminar or turbulent can be determined by calculating the dimensionless Reynolds number, which represents the ratio of inertial force to viscous force [275]:

$$\mathrm{Re} = \frac{\rho_f u_f D_H}{\eta_f} \tag{2.4}$$

Here, u_f is the fluid velocity (in one direction) and D_H is the hydraulic diameter (characteristic length) of the fluid channel. For a rectangular duct, the hydraulic diameter, D_H is given by the ratio between the cross section and the wetted area [279]:

$$D_H = \frac{4A}{W} \tag{2.5}$$

with the cross sectional area A and the wetted perimeter W of the cross section. For a rectangular cross section, A and W can be described as [279]:

$$A = w_0 h_0 \tag{2.6}$$

$$W = 2(w_0 + h_0) \tag{2.7}$$

where w_0 and h_0 are the width and the height of the rectangular fluid channel. In this work the hydraulic diameter is $D_H \approx 0.7$ mm.

Going from a turbulent to a laminar regime, or vice versa, does not occur abruptly but is a continuous transformation process without a clear transition point. In the literature, a transition threshold of $\mathrm{Re} \approx 2300$ is normally given as a rule of thumb [276].

In most circumstances in microfluidics, the Reynolds number is around unity or even one order of magnitude smaller, ruling out turbulent flows in the channel (here, $1.4 \leq \mathrm{Re} \leq 3.7$). At low Reynolds numbers the flow is dominated by viscous drag

rather than inertial forces, and is characterized by a continuous and ordered fluid motion in contrast to turbulent flow which is irregular. [280]. For these conditions the entrance length is defined as the distance between the inlets and the point that the flow becomes fully developed (time invariant or steady). This distance is directly proportional to the Reynolds number and can be estimated by [281]:

$$L_H \approx 0.06 D_H \mathrm{Re} \tag{2.8}$$

The maximum entrance length L_H for the highest Reynolds Number used in this thesis is approximately 155 μm, which is more than 100 times smaller, than the channel length of the devices used in this thesis (see Chapter 3).
For a unidirectional flow that is assumed to be steady-state and fully developed, the inertial force ($\partial \mathbf{u}/\partial t$) and the convective terms ($\mathbf{u} \cdot \nabla \mathbf{u}$) are all equal to zero and thus, can be omitted. Without the nonlinear convection and time dependence, the Navier-Stokes equation (Equation 2.1) can be simplified. The resulting linear equations governing the velocity distribution in the fluid are [276]:

$$\eta_f \nabla^2 \mathbf{u} = \nabla p \tag{2.9}$$

Equation 2.9 together with the continuity equation (Equation 2.2) are known as the Stokes equations. An analytical solution to Equation 2.9 using the Dirichlet boundary conditions given in Equation 2.3 can be found for a number of simple geometries. In the absence of moving beads in the fluid, the hydrodynamics of a rectangular microfluidic channel in the limit of laminar flow is standard textbook material. The solution to Equation 2.9 gives the so called Poiseuille flow for a channel of rectangular cross section and can be mathematically expressed by the following

infinite Fourier series summation [275]:

$$u_f(x,y) = \frac{4h_0^2}{\eta_f \pi^3}\left(-\frac{dp}{dz}\right)\sum_{k=0}^{\infty}(-1)^k \times \left\{1 - \frac{\cosh\left[\frac{(2k+1)\pi x}{h_0}\right]}{\cosh\left[\frac{(2k+1)\pi w_0}{2h_0}\right]}\right\}\frac{\cos\left[\frac{(2k+1)\pi y}{h_0}\right]}{(2k+1)^3} \quad (2.10)$$

where h_0 and w_0 are the height and the width of the fluid channel and dp/dz describes the pressure drop along z. The pressure driven velocity profile across a cross section of a rectangular microchannel is shown in Figure 2.1.

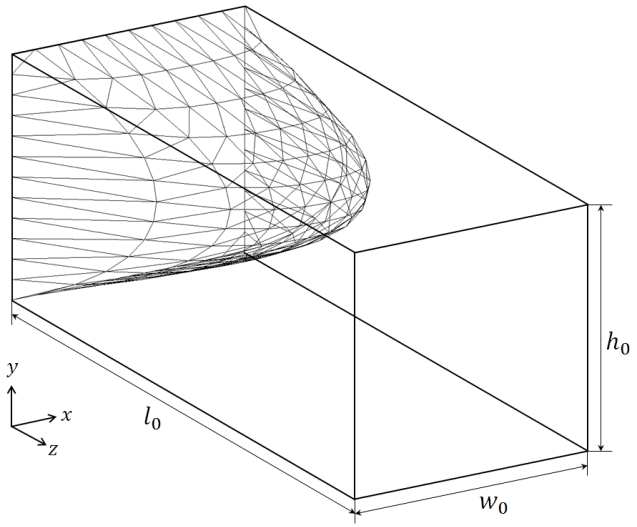


Figure 2.1: Schematic of a 3D velocity profile of a unidirectional flow in a rectangular duct of a viscous fluid. In this analytical calculation the width (w_0) and the height (h_0) of the channel is set to 500 μm and the fluid channel's length (l_0) is set to 10 mm.

2.2.1.1 Hydraulic resistance in microfluidic systems

In Section 2.2.1 the pressure-driven, steady-state flow of an incompressible Newtonian fluid through a straight channel is studied. It is found that a constant pressure drop results in a constant flow rate. This result can be summarised in the Hagen-Poiseuille law [282]:

$$\Delta p = R_H \dot{Q} \quad (2.11)$$

where Δp is the pressure drop along the channel, $\dot{Q}$ the resulting flow rate through the channel and R_H a proportionality factor known as the hydraulic resistance. The hydraulic resistance is due to viscous dissipation of mechanical energy into heat by internal friction in the fluid. For a straight and rigid channel of length l_0 and rectangular cross-section ($w_0 \times h_0$), the hydraulic resistance can be approximated as [282]:

$$R_H \approx \frac{12\eta_f l_0}{h_0^3 w_0 \left[1 - 0.63(h_0/w_0)\right]} \tag{2.12}$$

Equation 2.12 assumes that the fluidic channel is perfectly straight and that its cross section is not changing along its length, which is true for all the microfluidic systems analysed in this work.

Typically, the fluid flow is subject to a no-slip boundary condition at the walls and thus the actual hydraulic resistance will depend on the perimeter as well as the cross-section area. With the miniaturization of microfluidic systems, their surface area to volume ratio increases. This leads to a high hydraulic resistance and thus results in a high back pressure when liquids are pumped through the system. This high back pressure can cause difficulties in the introduction of fluids in microfluidic systems and therefore, should be taken into consideration when microfluidic channels in LOC systems are designed [282].

2.2.2 Particle laden flow in microfluidic systems

Particle laden flows refer to a multiphase flow in which one of the phases is continuously connected and the other phase is made up of small, immiscible, and typically dilute particles. The above discussion on fluid motion in microfluidic systems does not take a discrete phase into account. When particles are added to the flow, they will alter the fluid properties and it is necessary to determine if this effect is signifi-

cant.

Depending on the volume fraction of the dispersed phase, the particle laden flow needs to be modelled differently. The particle volume fraction, υ_p, is described by the ratio [283]:

$$\upsilon_p = \frac{V_{tot}}{V_{unit}} \tag{2.13}$$

where V_{tot} is the total volume of the solid phase in the unit volume V_{unit}. If the concentration of particles is high ($\upsilon_p > 10^{-3}$), the particle-particle interaction and its effect on the fluid (four-way coupling) must be modelled. For intermediate concentrations ($10^{-6} < \upsilon_p < 10^{-3}$), particle-particle interaction may be neglected but the particles still have an effect on their surrounding fluid (two-way coupling). For low concentrations ($\upsilon_p < 10^{-6}$), the fluid flow is not considerably influenced by the particle flow (one-way coupling) [284].

In most microfluidic cases, the particles occur in low concentrations and are very small, hence the dynamics are governed primarily by the continuous phase. The behaviour of the particles in a fluid flow can be characterised by the Stokes number, Stk, which is defined as the ratio of the characteristic time of the particles to a characteristic time of the flow [276]:

$$\mathrm{Stk} = \frac{\tau_p u_f}{D_p} \tag{2.14}$$

where u_f is the velocity of the fluid, D_p is the hydraulic diameter of the particle and τ_p is the relaxation time of the particle, which is given by [276]:

$$\tau_p = \frac{\rho_p d_p^2}{18\eta_f} \tag{2.15}$$

where ρ_p and d_p are the particle's density and diameter.

The Stokes number is a measure of flow tracer fidelity, which means it gives information about how well particles follow the fluid flow. For large Stokes numbers (Stk $\gg 1$), particles will detach from the flow and the particle motion is weakly affected by the flow, whereas for small Stokes numbers (Stk $\ll 1$) the particles follow the streamlines closely, which means the particles are in quasi equilibrium with the surrounding flow.

In the present work, a dilute concentration ($\upsilon_p \leq 10^{-6}$) and a small Stokes number (Stk $\approx 10^{-3}$) can be assumed. Thus, the flow does not depend on the particle dynamics and therefore can be solved in an uncoupled way. This allows calculating the particle laden flow according to Equation 2.9 and independently from other particle movements (see Section 2.4.1).

2.2.3 Hydrodynamic focusing

Hydrodynamic focusing is a widely used technique in microfluidics [285, 286]. It involves the reshaping of a central stream by varying the pressure of the two sheath flows, as schematically shown in Figure 2.2. This way, one can achieve precise control of the focused sample stream width and position, which is of crucial importance to magnetic particle separation because of the non-uniform nature of the magnetic force. Due to the planar nature of most microfluidic devices only two-dimensional hydrodynamic focusing will be considered here. To mathematically express the width of the sample stream the model for hydrodynamic focusing in a rectangular channel by Lee *et al.* [287] will be followed here. The model uses the mass conservation principle for incompressible fluids, which states that the volume flow at inlets and outlets must be the same, i.e. the central inlet channel must equal the volume of fluid passing through the focused stream, and the sum of the volume flows passing through the three individual inlet channels must be the same as the total fluid

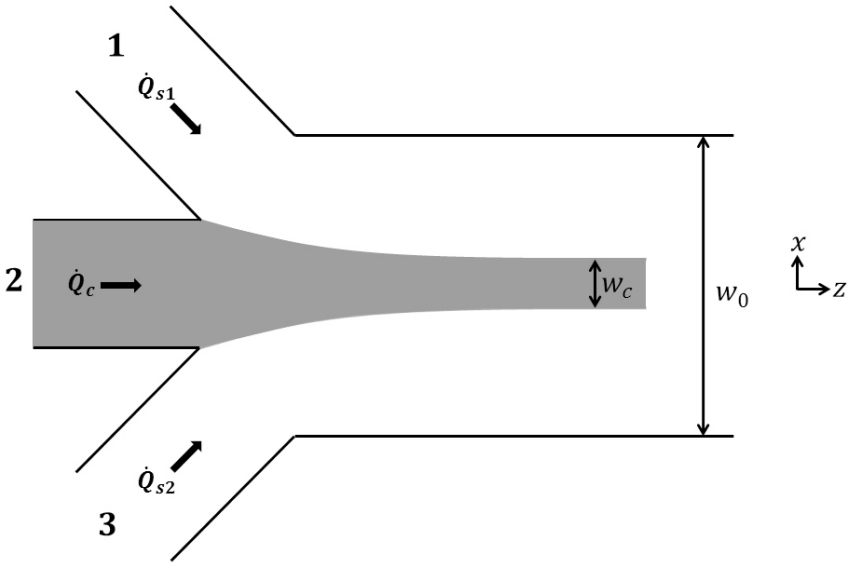


Figure 2.2: A schematic of the three inlet channel of the microfluidic device displaying hydrodynamic focusing of a sample flow $\dot{Q}_c$ by varying the two sheath flows $\dot{Q}_{s1}$ and $\dot{Q}_{s2}$.

passing though the main channel [287]:

$$\dot{Q}_c = w_c h_0 \bar{u}_c \tag{2.16}$$

$$\dot{Q}_c + \dot{Q}_{s1} + \dot{Q}_{s2} = w_0 h_0 \bar{u}_0 \tag{2.17}$$

where $\dot{Q}_c$, $\dot{Q}_{s1}$ and $\dot{Q}_{s2}$ are the volume flow rates of the centre sample stream and the two sheath flows, respectively. The parameter w_c describes the width of the focused sample stream and the two velocities $\bar{u}_c$ and $\bar{u}_0$ are the mean velocity of the hydrodynamically focused flow and the mean velocity in the main channel.

By rearranging the two equations (Equation 2.16 and Equation 2.17) the relationship between the width of the hydrodynamically focused stream and the channel width can be expressed as [287]:

$$\frac{w_c}{w_0} = \frac{1}{\gamma} \cdot \frac{\dot{Q}_c}{\dot{Q}_c + \dot{Q}_{s1} + \dot{Q}_{s2}} \tag{2.18}$$

where the unknown velocity ratio $\gamma = \bar{u}_c/\bar{u}_0$ needs to be found. The two mean velocities, $\bar{u}_c$ and $\bar{u}_0$, can be determined by integrating Equation 2.10 along x and y, and the velocity ratio γ can then be expressed as [287]:

$$\gamma = \frac{\bar{u}_c}{\bar{u}_0} = \frac{1 - \left(\frac{192h_0}{\pi^5 w_c}\right) \sum_{k=0}^{\infty} \frac{1}{(2k+1)^5} \frac{\sinh[(2k+1)\pi w_c/2h_0]}{\cosh[(2k+1)\pi w_0/2h_0]}}{1 - \left(\frac{192h_0}{\pi^5 w_0}\right) \sum_{k=0}^{\infty} \frac{\tanh[(2k+1)\pi w_0/2h_0]}{(2k+1)^5}} \tag{2.19}$$

Based on Equation 2.19, the hydrodynamic focusing effect does not solely depend on the relative flow rates of the sheath and sample flows but is also dependent on the aspect ratio, h_0/w_0, of the microfluidic channel and the width of the hydrodynamically focused stream, w_c. Thus, an implicit formula for w_c can be obtained. For the case where the aspect ratio is close to zero ($h_0/w_0 << 1$), a velocity ratio of $\gamma \approx 1$ can be assumed [288].

2.3 Magnetism

Substances which are magnetized by a magnetic field are called magnetic materials. The term *magnet*, however, is typically used for objects that produce their own persistent magnetic field even in the absence of an external magnetic field. Only certain classes of materials can actually do this. Most materials, however, produce a magnetic field in response to an applied magnetic field. This phenomenon is generally known as magnetism. There are various kinds of magnetism, and all materials exhibit at least one of them [289].

The magnetism of materials originates from the magnetic moment of electrons in the atom; electron momentum gives rise to magnetic dipole moments. The total magnetic moment of the atom is then given by the vector sum of all its electronic moments [290]. In a bulk magnetic material the net magnetization $\mathbf{M}$ is the vector sum of all the magnetic moments of the atoms per unit volume of the material. However, this does not mean that all the magnetic moments in the entire material

will point in the same direction. Rather what happens is the magnetic pattern is a patchwork of different domains with each domain having its own magnetization vector arising from an alignment of atomic moments within the domain as shown in Figure 2.3. Due to this anisotropic alignment of magnetization vectors across different domains, magnetic materials are usually not spontaneously magnetized but exist rather in a demagnetized state, where the overall resultant magnetization vector **M** is normally zero. However, by applying an external magnetic field **H** these domains can align in the direction of the external field and enhance the overall macroscopic magnetic response in the material. How quickly and with what ease the domains align and whether or not their new alignment remains after the external magnetic field has been removed is material dependent and will be discussed in Section 2.3.3.

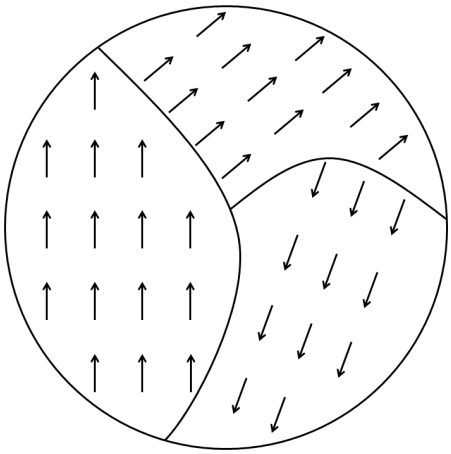


Figure 2.3: Schematic picture of magnetic domains. Arrows represent the direction of the magnetization in the different domains.

2.3.1 Magnetic field

A magnetic field arises whenever there is electrical charge in motion. This can be due to an electrical current flowing in a conductor or produced by a permanent magnet [291, 292]. In the latter case, the magnetization of a material, as discussed

in the previous section (see Section 2.3), is expressed in terms of density of net magnetic dipole moments in the material and can be defined as [292]:

$$\mathbf{M} = \frac{\mathbf{m}}{V} \tag{2.20}$$

where $\mathbf{m}$ and V are the total magnetic dipole moment and volume of the material, respectively. The magnetization can also be described by the following linear relation [292]:

$$\mathbf{M} = \chi \mathbf{H} \tag{2.21}$$

where $\mathbf{H}$ is the applied magnetic field and χ is the susceptibility of the magnetic material. The magnetic susceptibility of a material describes the ease of magnetization in an external magnetic field.

When a magnetic material is placed in a magnetic field, $\mathbf{H}$, the response of the medium is its magnetic induction. The extent to which a medium responds to the magnetic field depends on the relative permeability of the material. In many media the magnetic flux $\mathbf{B}$ can be assumed to be a linear function of $\mathbf{H}$ [292]:

$$\mathbf{B} = \mu_0 \mu_r \mathbf{H} \tag{2.22}$$

where μ_0 and μ_r are the permeability of free space ($4\pi \times 10^{-7}$ N/A^2), relative permeability of the material, respectively. The relationship between the magnetic flux density $\mathbf{B}$, the magnetization $\mathbf{M}$ and the magnetic field $\mathbf{H}$ is given by [292]:

$$\mathbf{B} = \mu_0 (\mathbf{H} + \mathbf{M}) \tag{2.23}$$

If one replaces the magnetization **M** (Equation 2.21) in Equation 2.23 one gets the following expression [292]:

$$\mathbf{B} = \mu_0(1 + \chi)\mathbf{H} \tag{2.24}$$

2.3.2 Magnetic hysteresis and saturation

Considering χ to be a constant in Equation 2.21, even though a good approximation at low fields, is an inappropriate assumption for most magnetic materials. First, the relationship between **M** and **H** is generally nonlinear, approaching a finite saturation magnetization M_S. This represents a condition where magnetic moments within the material are aligned in the direction of the magnetic field **H**. Second, the magnetization **M** is not necessarily a unique function of **H**. The magnetization curve displays a hysteresis loop, because not all domains return to their original orientations when **H** is decreased after the saturation magnetization value is attained. This phenomenon is illustrated in Figure 2.4. Key parameters of the hysteresis loop are

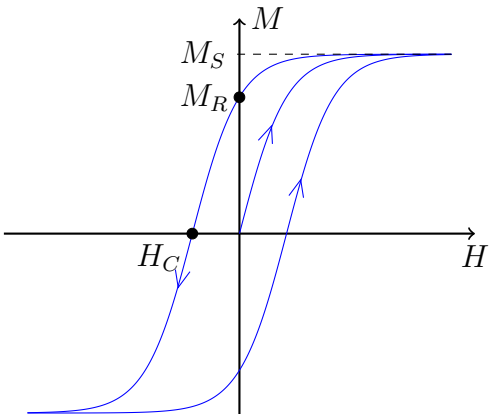


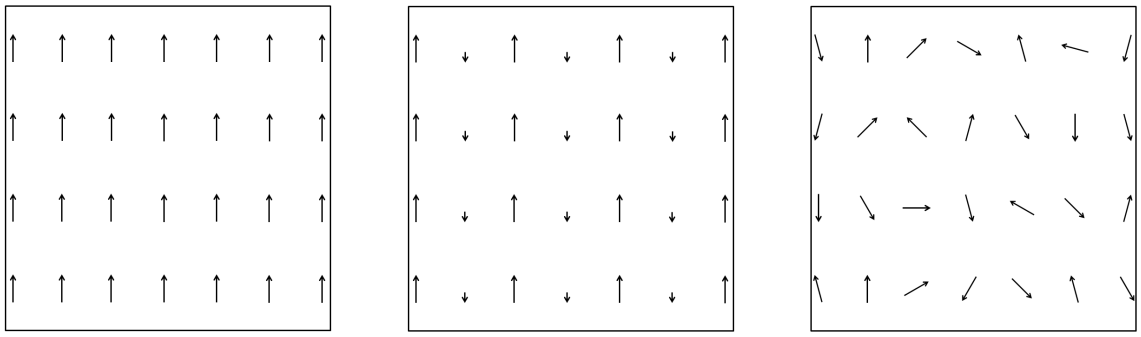
Figure 2.4: Magnetic hysteresis cycle. The magnetic material will retain a magnetic moment, M_R, even in the absence of an external field, which essentially creates a new permanent magnet. Only at a coercive field, H_C, the net magnetic moment of the material will return to zero.

the remanent magnetization or remanence M_R, which is the residual magnetization after the external field is removed and the coercivity H_C, which is the magnitude of

the field that must be applied in the negative direction to bring the magnetization back to zero.

2.3.3 Magnetic materials and properties

Magnetic materials encompass a wide variety of materials and their macroscopic magnetic behaviour can be classified into ferro- or ferrimagnetic, paramagnetic and diamagnetic. They are grouped according to their magnetic dipole orientation and bulk magnetic susceptibility, which is schematically shown in Figure 2.5. The different kinds of magnetism will be briefly discussed in the following subsections.



(a) Ferromagnetism (b) Ferrimagnetism (c) Paramagnetism

Figure 2.5: Overview and comparison of the different types of magnetism. The magnetic dipole orientation defines the magnetic type.

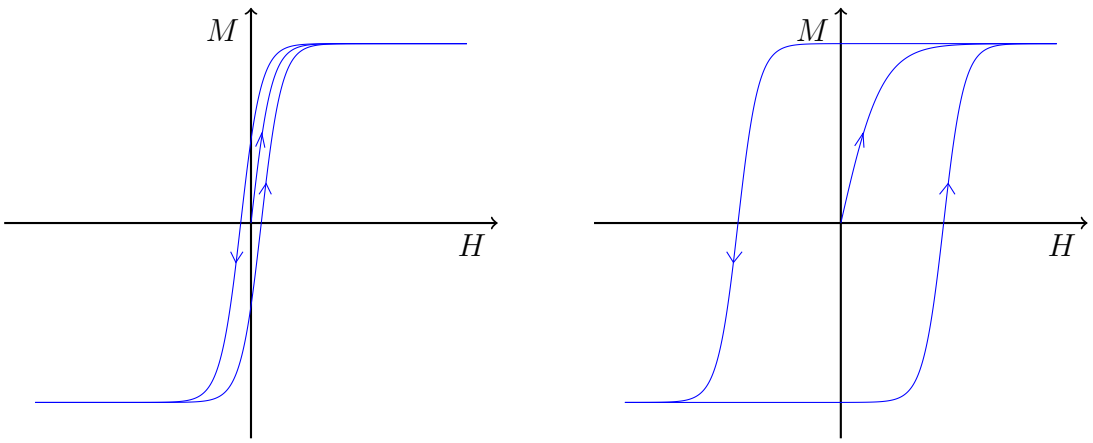
2.3.3.1 Ferromagnetic and ferrimagnetic materials

Ferromagnetic and ferrimagnetic materials are the ones normally thought of as magnetic, because these materials are the only ones that can retain a significant magnetization and become magnets. The magnetic moments interact strongly with an applied magnetic field and their orientation remains stable even after removal of the external field. Thus, ferromagnetic materials exhibit a large and positive magnetic susceptibility ($\chi \gg 0$).

Different classes of spontaneous magnetization have been identified when there are

multiple magnetic moments, whose magnitude and arrangement can be different and arranged anti-parallel. In the case of ferromagnetism, all magnetic moments are aligned parallel to one another, which results in a strong positive interaction between neighbouring moments, whereas in the ferrimagnetic case some magnetic moments are anti-aligned resulting in a weaker net magnetization **M**, as shown in Figure 2.5a and Figure 2.5b [293].

The ease with which the different domains can change their direction differs widely between the different ferro- and ferrimagnetic materials. However, this wide variety of magnetic materials can be rather sharply divided into two groups. If a small applied field suffices to produce saturation, the material is said to be magnetically soft (e.g. iron, iron-silicon alloys or low-carbon steels). Other materials, which require a very large field to saturate are called magnetically hard (e.g. neodymium magnet, Alnico or Strontium ferrite) [290, 293, 294]. The difference can be best seen in their hysteresis loops as depicted in Figure 2.6.



(a) Soft magnetic (b) Hard magnetic

Figure 2.6: Hysteresis loop for ferromagnetic material. (a) A soft magnetic behaviour and (b) a hard magnetic behaviour.

2.3.3.2 Paramagnetic materials

Like ferromagnetic species, paramagnetic materials contain magnetic moments which align when exposed to a magnetic field such that they form a weak net magnetic moment, which means their magnetic susceptibility is small and positive ($\chi > 0$). However, unlike ferromagnetic materials, they do not exhibit magnetic remanence upon removal of the field as the individual magnetic moments of the different domains become randomized due to thermal agitation and do not interact with each other. Thus, paramagnetic materials are only magnetized in the presence of an externally applied field, and once the field is removed the magnetization is lost [289, 293].

2.3.3.3 Superparamagnetic materials

Even if its name suggests a subtype of paramagnetism, superparamagnetism is actually a special form of magnetism with characteristics from both ferromagnetism and paramagnetism. When the length scale of the magnetic material becomes smaller than a critical size ($10 - 20$ nm), the ferro- or paramagnetic grains can essentially be considered as individual magnetic domains and their magnetization is a single magnetic moment [295]. At this scale, the available thermal energy becomes of the same order as the magnetic energy, causing the magnetic moment to immediately align randomly in space, after the magnetic field has been removed. Therefore, the coercivity and remanence is substantially equal to zero and thus, no hysteresis can be observed [296–298].

This behaviour can be described by the Néel relaxation time which describes the time needed for a magnetic moment to change its orientation [299]:

$$\tau = \tau_0 \cdot \exp\left(\frac{\Lambda V}{k_B T}\right) \tag{2.25}$$

where the different parameters Λ, V, k_B and T are the magnetic anisotropy energy density, grain volume, Boltzmann constant and the temperature, respectively. The height of the energy barrier is given by ΛV and $k_B T$ is the thermal energy. τ_0 is the material characteristic time scale, normally in the order of $0.1 - 1$ nanoseconds.
The magnetic susceptibility of these commercially available beads is typically in the range of $0.01 - 1.5$ [194, 300–302].

2.3.3.4 Diamagnetic materials

Diamagnetic materials exhibit a net magnetization which is opposite to the direction of the externally applied magnetic field and thus, are repelled by the applied magnetic field. That means, diamagnetic materials have a small negative magnetic susceptibility ($-1 < \chi < 0$) [290]. Examples for diamagnetic materials are gold, copper or water [294].
The opposed magnetic moment of diamagnetic substances is generally a very weak effect and loses its opposing magnetization after removal of the applied magnetic field.

2.4 Theory of magnetophoresis

Magnetophoresis is the combination of fluid dynamics (Section 2.2) and magnetism (Section 2.3).
A magnetic particle that is in suspension in a liquid and is being exposed to a magnetic field, experiences a set of forces. However, the magnetic force and the Stokes drag force are the most dominant forces relevant to this thesis. Other forces such as, gravity, buoyancy and also Saffman forces can be neglected for the microscopic particles used because of their small size ($1\ \mu$m $-2.8\ \mu$m) compared to the channel dimensions (0.4×3 mm) and the time-scales involved [303–305]. Thus, Newton's

second law of motion can be written as [306]:

$$V_p \rho_p \frac{\partial \mathbf{u}_p}{\partial t} = \mathbf{F}_m + \mathbf{F}_d \tag{2.26}$$

where $\mathbf{F}_m$ and $\mathbf{F}_d$ describe the two dominant forces, the magnetic force and the Stokes drag, respectively. The two parameters V_p and ρ_p describe the particle volume and its density. Thus, the product of the two is the mass of the particle.
The magnetic force on a magnetized object $\mathbf{F}_m$ can be expressed in multiple ways [307]:

$$\mathbf{F}_m = V_p \chi_p (\mathbf{H} \cdot \nabla)\mathbf{B} \tag{2.27}$$

$$= \frac{V_p \chi_p}{\mu_0} \Big(\mathbf{B} \cdot \nabla\Big)\mathbf{B} \tag{2.28}$$

where V_p and χ_p are the volume and the effective susceptibility of the particle, respectively. Equation 2.28 is most commonly used in the literature and will also be used throughout this thesis.
If the particle is suspended in a viscous fluid, Equation 2.28 needs to be slightly modified since the susceptibility of the surrounding medium should be taken into account [59]:

$$\mathbf{F}_m = \Delta\chi V_p \left(\frac{\nabla |\mathbf{B}|^2}{2\mu_0} \right) \tag{2.29}$$

where $\Delta\chi = \chi_p - \chi_f$ describes the difference in relative magnetic susceptibility between the magnetic particle (χ_p) and the surrounding medium (χ_f).
It is important to note here, that Equation 2.27-2.29 assume a constant magnetic field across the volume of the particle and the magnetic media to be linearly polarizable, for which the magnetic susceptibility χ_p is independent of the applied magnetic field. In general, this is a valid assumption for all materials in a sufficiently weak field.

In the case of micrometre sized spherical particles at low Reynolds number, Stokes regime is found to be applicable (see Section 2.2.2) and the Stokes drag force in Equation 2.26 can be assumed as [276]:

$$\mathbf{F_d} = -6\pi\eta_f r_p \Delta u \tag{2.30}$$

where r_p is the particle's radius, η_f the viscosity of the medium the particle is suspended in, and $\Delta u = u_f - u_p$ is the relative velocity between the particle and the fluid.

For micro-sized particles, a terminal velocity is reached in a matter of microseconds, in which case it is appropriate to assume [308]:

$$\mathbf{F}_m = -\mathbf{F}_d \tag{2.31}$$

From this simplified equation of motion (Equation 2.31) and the two equations, Equation 2.29 and Equation 2.30, one obtains the magnetically induced terminal velocity of the particle:

$$\mathbf{u}_p = \underbrace{\frac{\Delta\chi_p V_p}{6\pi\eta r_p}}_{\substack{\text{Material}\\ \text{properties}}} \cdot \underbrace{\left(\frac{\nabla|\mathbf{B}|^2}{2\mu_0}\right)}_{\substack{\text{Magnetic field}\\ \text{properties}}} \tag{2.32}$$

An interesting interpretation of the expression given in Equation 2.32, is that it depends on a purely material related term and a field related term; it is a product of particle and suspending viscous medium properties and the applied magnetic field properties. The two factors of this product can be defined as the magnetophoretic

mobility of the particle ν_p and the magnetophoretic driving force S, given by:

$$\nu_p = \frac{\Delta\chi V_p}{6\pi\eta r_p} \tag{2.33}$$

$$S = \frac{\nabla|\mathbf{B}|^2}{2\mu_0} \tag{2.34}$$

The magnetically induced terminal velocity (Equation 2.32) can be used to model the trajectory of a single magnetic particle in a magnetic field with the help of the Lagrangian particle tracking scheme, which will be discussed in the next section.

2.4.1 Lagrangian particle tracking

The Lagrangian tracking scheme is based on Newton's equation of motion (Equation 2.26) and maps the positions of a single particle at discrete time steps. The mathematical expression for the tracking scheme can be given by:

$$\mathbf{x}(t+\delta t) = \mathbf{x}(t) + \mathbf{u}_p\delta t \tag{2.35}$$

in which $\mathbf{x}(t)$ is the location vector of the particle at time t, $\mathbf{u}_p$ is the instantaneous particle velocity vector (see Equation 2.32) and δt is an incremental time interval, small enough so that the particle velocity vector $\mathbf{u}_p$ is essentially constant during the finite time step δt. In solving the equation of motion (Equation 2.31) in a Lagrangian approach, the trajectory of single magnetic particles can be simulated. Thereby, time step, δt, needs to meet the Courant-Friedrich-Lewy (CFL) condition to guarantee accuracy and computational stability of the particle trajectory solution [309]:

$$\frac{\mathbf{u}_p^i\delta t}{\omega} \leq 1 \tag{2.36}$$

where $\mathbf{u}_p^i$, δt and ω are the velocity vector of the i^{th} particle, the time marching step and the grid size of the simulated magnetic field, respectively. The simulation of the

magnetic field, using FEM, is the subject of the next section.

2.5 Mathematical formulation of finite element equations for magnetostatic problems

All macroscopic electromagnetic phenomena are governed by a set of equations, known as the Maxwell's equations. For the magnetostatic problem, where the magnetic field is time-invariant and the electric field can be neglected, the magnetic field must satisfy the following differential equations [310]:

$$\nabla \times \mathbf{H} = \mathbf{J} \tag{2.37}$$

$$\nabla \cdot \mathbf{B} = 0 \tag{2.38}$$

$$\mathbf{B} = \mu_0 \mu_r \mathbf{H} \tag{2.39}$$

where $\mathbf{H}$, $\mathbf{B}$ and $\mathbf{J}$ are the magnetic field intensity, the magnetic flux density and the current density, respectively. The magnetic flux density can be expressed in terms of its vector potential $\mathbf{\Phi}$ [310]:

$$\mathbf{B} = \nabla \times \mathbf{\Phi} \tag{2.40}$$

Substituting Equation 2.40 into Equation 2.37 with the aid of Equation 2.39 yields the second-order differential equation [310]:

$$\nabla \times \left(\frac{1}{\mu_0 \mu_r} \nabla \times \mathbf{\Phi} \right) = \mathbf{J} \tag{2.41}$$

Assuming the magnetic permeability is isotropic and independent of the magnetic field, Equation 2.41 can be written as Poisson's equation [310]:

$$\nabla^2 \mathbf{\Phi} = \Delta \mathbf{\Phi} = \mu_0 \mu_r \mathbf{J} \text{ in } \Omega \tag{2.42}$$

where Δ is the Laplace operator and the vector potential $\mathbf{\Phi}$ needs to be a real function in the problem domain Ω with boundary $\partial\Omega$. This boundary value problem can be further formulated as a variational expression [311]:

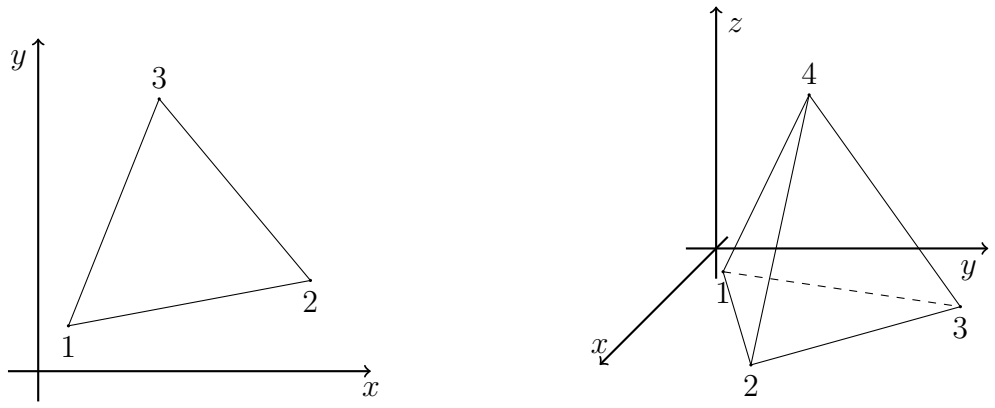
$$E(\mathbf{\Phi}) = \frac{1}{2} \int_{\Omega} \left(\frac{\nabla \mathbf{\Phi} \cdot \nabla \mathbf{\Phi}}{\mu_0 \mu_r} - \mathbf{\Phi} \cdot \mathbf{J} \right) d\Omega \tag{2.43}$$

However, the vector potential $\mathbf{\Phi}$ in Equation 2.43 is formulated as a continuous function, which FEM cannot deal with. Therefore, the continuous problem in Equation 2.43 is broken into a discrete physical representation consisting of a finite number of regions or finite elements.

The discretization of the domain Ω is normally the first step in FEM. One of the most commonly used approaches for two-dimensional (2D) and three-dimensional (3D) problems, is to divide the domain into a mesh of triangles or tetrahedra, respectively. These basic building blocks, triangle or tetrahedral, are called elements and are depicted in Figure 2.7. In each element the unknown function $\mathbf{\Phi}$ is represented by a trial function $\tilde{\mathbf{\Phi}}$, where the desired field in each element is approximated with a 2^{nd} order quadratic polynomial [311]:

$$\tilde{\mathbf{\Phi}}(x, y, z) = a_0 + a_1 x + a_2 y + a_3 z + a_4 xy + a_5 yz + a_6 xz + a_7 x^2 + a_8 y^2 + a_9 z^2 \tag{2.44}$$

The parameters a_i are unknown values, which need to be found. In order to obtain these values, field quantities are calculated for 10 points of each element, shown in Figure 2.8. The solution to these points, which solves Equation 2.42, can then



(a) Triangular (b) Tetrahedral

Figure 2.7: Typical finite elements: (a) triangular element and (b) tetrahedral element.

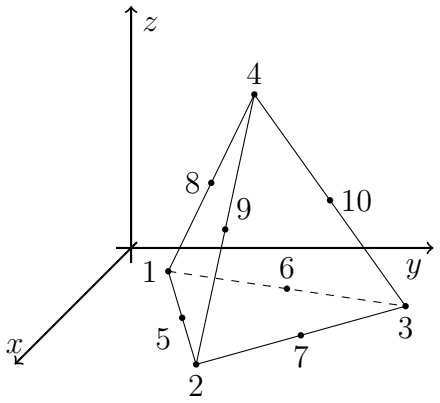


Figure 2.8: Points for which the magnetic vector potential will be calculated in the FEM. Field quantities inside the tetrahedral are calculated using a 2^{nd} order quadratic interpolation scheme.

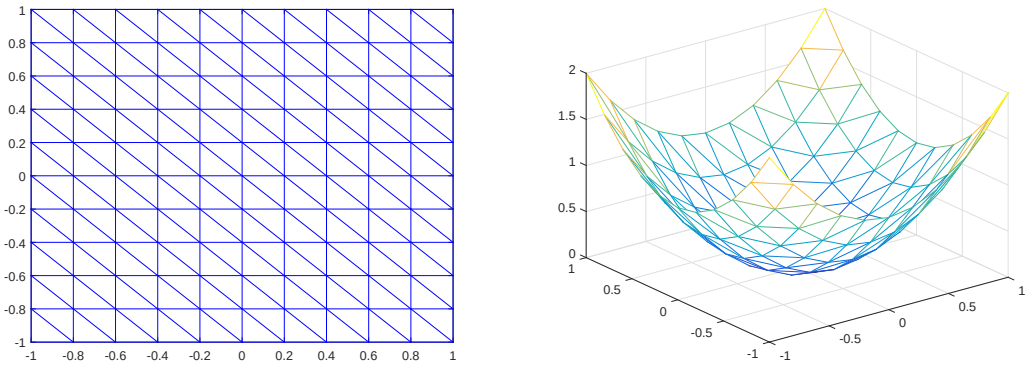
be obtained by minimizing the energy functional (Equation 2.43) with respect to the values a_i and subject to the given boundary conditions and user defined initial conditions. This calculation is done at each node in every tetrahedral which results in a large, sparse matrix equation, which can be solved using standard matrix solution techniques. Proof can be found in [312].

2.5.1 Error estimation of the finite element method

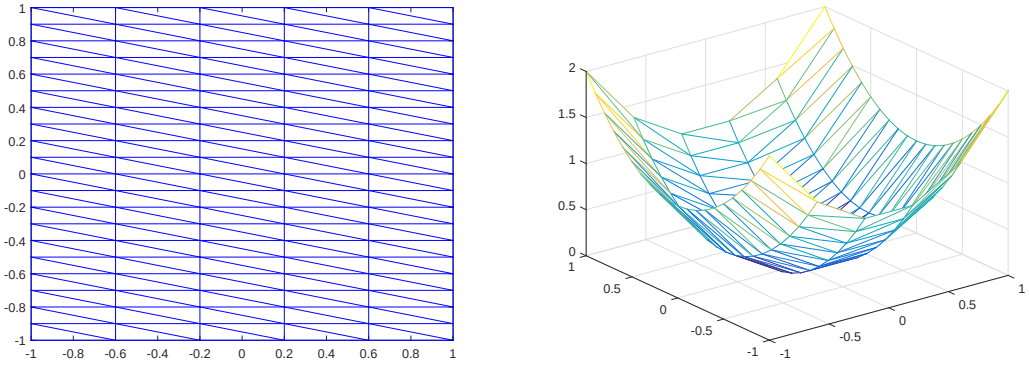
Even though FEM has evolved into one of the most widely used techniques for finding approximate solutions to differential equations it suffers from one major problem. The very act of subdividing the domain Ω provides the opportunity for *discretization errors*. First, discretization errors occur because the *finite* element model is, by definition, incapable of reproducing every one of the *infinite* solution patterns that the problem domain can assume. Second, the construction of these subsets of the domain is not a trivial task, since the mesh must satisfy nearly contradictory requirements: it must conform to the shape of the object or simulation domain; its elements must be neither too large nor too numerous; it may have to grade from small to large elements over a relatively short distance; and it must be composed of elements that are of the right shapes and sizes. Such a mesh is known as a *regular mesh* and is achieved by keeping the aspect ratio of its elements below a positive constant ϑ [278]:

$$\theta = \frac{\varrho_{out}}{\varrho_{in}} \leq \vartheta \tag{2.45}$$

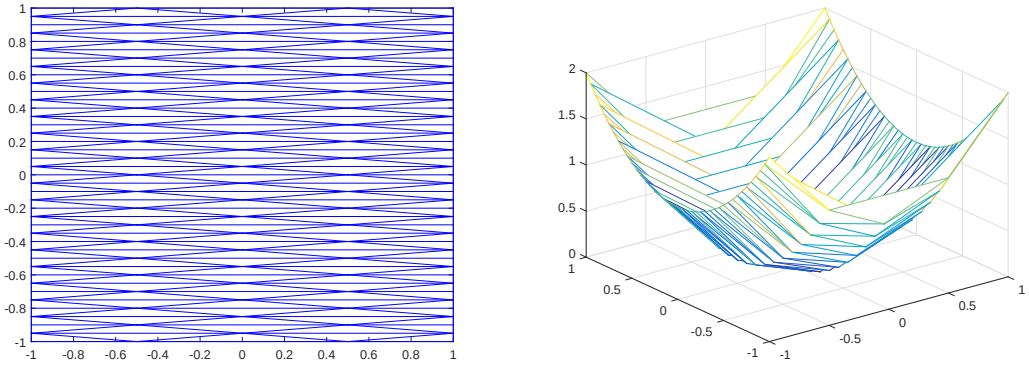
where ϱ_{out} and ϱ_{in} are the outer and inner diameter of the element (triangle or tetrahedral), respectively. If ϑ is small, normally $\vartheta \leq 5$, the mesh quality is considered to be sufficient. The literature demonstrates that the accuracy of finite element solutions on triangular meshes degrades as angles are allowed to approach 180° [278]. Figure 2.9 visually illustrates these effects. The three triangulations are each using 200 triangles to render a paraboloid. It can be seen that the mesh of Figure 2.9b, where the mesh is composed by long thin triangles with no angle greater than 90°, only performs slightly worse than the isotropic triangulation in Figure 2.9a. However, when the angles approach 180° as shown in Figure 2.9c, the solution gets more distorted.



(a) Isotropic triangles



(b) Sharp angle triangles



(c) Obtuse angle triangles

Figure 2.9: Visual illustration of how large angles negatively effect the result of the FEM solution. The left hand side of each subfigure shows the mesh used to render the 2D parabolic function (right hand side). Each mesh has exactly 200 triangles where a) contains isotropic triangles, b) has sharp angle triangles and c) is made of obtuse angle triangles.

2.5.1.1 Adaptive mesh refinement algorithm

The difference between the exact solution $\mathbf{\Phi}$ and the nummerical approximation $\tilde{\mathbf{\Phi}}$ is the discretization error [313]:

$$\epsilon = \|\mathbf{\Phi} - \tilde{\mathbf{\Phi}}\|_\star \tag{2.46}$$

The discretization error can be given in any given norm, which is indicated by the asterisk, but always depends on the number of elements in the mesh; i.e. the finer the mesh, the smaller the discretization error. Adaptive mesh refinement is an approach to minimise the discretization error by locally refining the mesh where errors are particularly high. This process is then repeated until an end criteria is reached, e.g. the required accuracy is met or the maximum number of iteration steps is reached. Figure 2.10 schematically illustrates the adaptive mesh refinement algorithm. Mul-

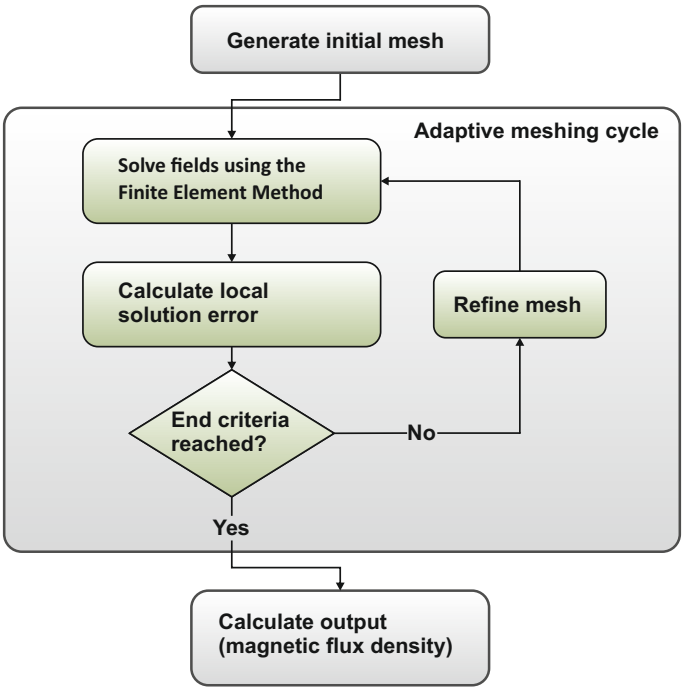


Figure 2.10: Box flow diagram of an adaptive mesh refinement algorithm used in various FEM programs.

tiple adaptive mesh refinement algorithms are described in the literature [313, 314];

e.g. more mesh points are placed in areas where the gradient of the solution is highest or the mesh is refined according to the change in the derivative at the element boundaries [315, 316]. Another approach, which will be used in this thesis, is using the residuals in the elements [317]:

$$\varepsilon_e = \Delta\tilde{\mathbf{\Phi}} - \mathbf{J} \tag{2.47}$$

The parameter ε_e indicates how well the original equations are locally satisfied by the approximate solution. The generated mesh is required to meet acceptable energy error estimate [311]:

$$\xi_e = \frac{|\varepsilon_e|}{E(\tilde{\mathbf{\Phi}})} \tag{2.48}$$

where ξ_e is the local energy error in element e and $E(\tilde{\mathbf{\Phi}})$ describes the total energy in the discrete system, which for the FEM approximate solution can be formulated as the following (also see Equation 2.43) [311]:

$$E(\tilde{\mathbf{\Phi}}) = \frac{1}{2}\int_{\Omega}\left(\frac{\nabla\tilde{\mathbf{\Phi}}\cdot\nabla\tilde{\mathbf{\Phi}}}{\mu_0\mu_r} + \tilde{\mathbf{\Phi}}\cdot\mathbf{J}\right)d\Omega \tag{2.49}$$

The ξ_e values act as an energy error estimate criteria and are used for adaptive mesh refinement. Summing the local errors in each element and dividing the sum by the total energy leads to a global percentage error energy [311]:

$$\xi = \frac{\sum_{e=1}^{n}|\varepsilon_e|}{E(\tilde{\mathbf{\Phi}})} \times 100 \tag{2.50}$$

Equation 2.50 is used as a stopping criteria in order to terminate the refinement process.

2.6 Statistical data analysis

Part of the analysis in this thesis includes statistical testing. The basis and the concepts of the analysis are introduced here, but will be used later in the thesis.

In general, all processes are affected by *chance* to a certain degree. Thus, every single measurement will be affected by small variances because of experimental errors. These random effects also occur in engineering problems because fabrication and other procedures are prone to small variations. The magnetic particles are not immune to these random variations due to small uncontrollable differences in their composition or shape.

A common aim of statistical analysis is to produce information (e.g. mean or variance) about a certain population. A *population* is any well defined collection or set of values. This sense of the term population differs from the sense in which most social scientists use the term, as social scientists tend to view collections of people or objects as defining a population.

Since testing an entire population can be very lengthy, one often makes inferences (generalizations) where a subset of the population (statistical data sample) is chosen to represent the population. This process is also known as *statistical interference* [318]. Selecting a statistical sample has its pitfalls, but the challenges of sampling will not be discussed here. There is a large body of work on sampling in the literature which the interested reader can consult [318–321].

The sample mean (Equation 2.51) and the sample variance (Equation 2.52) for a sample with N observations can be expressed as [318]:

$$\bar{x} = \frac{1}{N}\sum_{j=1}^{N} x_j = \frac{1}{N}(x_1 + x_2 + \cdots + x_N) \tag{2.51}$$

$$s^2 = \frac{1}{N-1}\sum_{j=1}^{N}(x_j - \bar{x})^2 = \frac{1}{n-1}\left[(x_1 - \bar{x})^2 + \cdots + (x_N - \bar{x})^2\right] \tag{2.52}$$

The variables x_j are considered independent random variables, each corresponding to one randomly selected observation. Note that the sample mean (Equation 2.51) and sample variance (Equation 2.52) are estimates of the population mean and population variance. With increasing sample size N the difference between the sample and the population moments can be neglected. In this work, the statistical samples are the different particle types. Every observation of a single particle is assumed to be an independent random variable, which means the occurrence of one observation does not affect the probability of occurrence of another observation [322].

2.6.1 Significance testing

Once sample data has been gathered through an observational study or quantitative research, statistical inference allows evidence in favour of a claim or hypothesis about a population statistic from which the sample has been drawn to be tested. The methods of inference used to support or reject claims on a sample data are known as significance tests.

Every significance test begins with a *null hypothesis* H_0. The null hypothesis represents a theory that has been assumed, either because it is believed to be true or because it is to be used as a basis for arguments.

The *alternative hypothesis* H_a is a statement of what a statistical hypothesis test aims to establish.

The conclusion once the test has been carried out is always given in terms of the null hypothesis. Either H_0 is accepted (which does not necessarily mean that the null hypothesis is true) except for a small error probability α, called the *acceptance level*, or H_0 is rejected in favour of H_a. Hence α is the probability of rejecting a hypothesis although it is true (Type I error). The choice of α is up to the person who performs the test. Common values are $\alpha = 5\%$ or $\alpha = 1\%$.

In deciding which test is appropriate to use, it is important to consider the type

of variables, i.e. whether the variables are categorical, ordinal or interval and what distribution the variables have [306, 323]. In this study, the mean values of different magnetic particle samples will be tested using a *one-way analysis of variance* (ANOVA) with an acceptance level $\alpha = 5\%$. The one-way ANOVA is used to determine whether there are any statistically significant differences between the means of three or more independent groups. Specifically, it tests the null hypothesis H_0:

$$H_0 : \mu_1 = \mu_2 = \cdots = \mu_n \tag{2.53}$$

where the different μ_i are the different means of the separate groups and the index n the number of groups. If, however, the one-way ANOVA returns a statistically significant result, the alternative hypothesis H_a is accepted, i.e. there are at least two group means that are significantly different from each other. At this point, it is important to state that the one-way ANOVA cannot tell which specific groups are significantly different from each other, only that there are at least two. To determine which specific groups differ from each other, a post-hoc test needs to be performed. Whenever the one-way ANOVA is used the following assumptions are made:

- The sample means $\bar{x}$ in each group are normally distributed. A normal distribution can usually be assumed for samples where the number of observations is large ($N \geq 30$) due to the central limit theorem [306, 324].

- There is homogeneity of variances, meaning the variances in each group are equal.

- Independence of observations, which is already assumed when using Equation 2.51 and Equation 2.52.

In this work, the ANOVA test will be used to compare the susceptibility values at different magnetic field strengths of two groups of magnetic beads. The two groups

use different measurement approaches to determine the susceptibility of the bead population.

Chapter 3

Experiments and simulations

3.1 Introduction

This chapter describes the setups and procedures used for the experiments and MATLAB simulations in this thesis. A detailed description of the particle suspensions, microfluidic channels and chambers will be given here, such that the experiments can be repeated.

3.2 Particle suspension

Commercially available superparamagnetic SiMAG-Silanol and ScreenMAG-Silanol beads of 1 μm in size were obtained from Chemicell [325]. Dynabeads MyOne, M270 and M280 were purchased from Thermo Fisher Scientific, UK. MyOne beads have a nominal diameter of 1.05 μm, whereas M270 and M280 beads have a nominal diamter of 2.8 μm [326]. Both manufacturers (Chemicell and Dynabeads) ship their beads already in suspension with an initial starting concentration as given in Table 3.1. Prior to the suspension preparation, the Dynabeads were washed three times following the protocol by Thermo Fischer. The washing solution used was phosphate buffered saline (PBS) with 0.01% w/v BSA and 0.01% v/v Tween-20. First, 1 mL

Table 3.1: List of all bead types used in the experiments. The bead diameter and bead concentration listed is as given by the manufacturer.

Bead Type	Size [μm]	Supplier	Concentration [beads/mL]
ScreenMAG-Silanol	1.0 ± 0.15	Chemicell GmbH	9×10^{10}
SiMAG-Silanol	1.0 ± 0.15	Chemicell GmbH	9×10^{10}
Dynabeads MyOne	1.05 ± 0.05	Thermo Fisher Scientific	$7 - 10 \times 10^{9}$
Dynabeads M280	2.8 ± 0.08	Thermo Fisher Scientific	$6 - 7 \times 10^{8}$
Dynabeads M270	2.8 ± 0.08	Thermo Fisher Scientific	$6 - 7 \times 10^{8}$

of bead suspension was added to an equal volume of washing solution in an Eppendorf tube and vortexed for 5 seconds. Next, the Eppendorf tube was placed on a Neodyminum magnet (25 mm $\times$ 25 mm $\times$ 5 mm) for at least 1 minute to pellet the beads. With the beads pelleted, the supernatant was removed. Next, the magnet was removed from the Eppendorf tube and the washed Dynabeads were re-suspended in deionized water. This procedure was repeated twice more.

To prepare the different bead suspensions, 1 mL of washed bead suspension was diluted either by 8 mL, 7.5 mL or 5.5 mL of deionized (DI) water, depending on the initial bead concentration, to approximately produce whole number multiples of ten in concentration. From this concentrated bead suspension 1 mL was taken and diluted with 9 mL of DI water. This subsequent dilution step was performed multiple times in order to achieve concentrations which differ by one order of magnitude, ranging from 10^5 to 10^9 beads/mL. Between every dilution step, the suspension was vortexed for at least 30 seconds to make sure the beads were fully suspended and evenly dispersed. Note that the volume of the beads was assumed to be negligible in this dilution process. This is a valid assumption because the volume fraction of beads in the as-supplied bead suspension is in the order of $O(10^{-4})$. Finally, 0.1% w/v of Pluronic F-127 and 0.01% v/v of Tween-20 was added to prevent the beads from sticking together and adhering to the microfluidic channel surface. All the chemicals used to make the suspensions are listed in Table 3.2 and are all commonly

used in the literature for particle separation and sample preparation [204, 223, 231, 237, 239, 327, 328].

Table 3.2: List of the chemicals used in the experiments to prepare the particle suspension.

Chemical	Supplier
PBS	Life Technologies
Tween-20	Thermo Fisher Scientific
Pluronic F-127	Sigma-Aldrich

3.2.1 SEM imaging of magnetic beads

To visualize the beads and to verify their size distribution, the particles were imaged using Scanning Electron Microscope (SEM) in the secondary electron mode. In this study an FEI™ Quanta™ 600 SEM was used; the accelerating voltage was set to 10 kV to minimise charging effects during imaging.

The samples for the SEM analysis were prepared as follows: 20 μL of bead suspension with a concentration of 10^6 beads/mL was pipetted on a 15 cm silicon wafer, that had prior to the experiment been oxygen plasma treated to make its surface hydrophilic. The wafer was spun at 2000 rpm for 30 seconds, leaving a distribution of beads on the surface of the silicon wafer. Then, a 5 nm thick gold layer was vapour deposited to enhance conductivity.

3.3 Microfluidic devices and chambers

Four different fluid devices are used throughout the work described in this thesis. The different devices are either channels, which allow a flow, or hydrostatic chambers. Each device will be described here and referenced back in the various chapters.

3.3.1 Microfluidic hydrodynamic focusing device

The device used for the hydrodynamic focusing was produced at Pusan National University in South Korea (PNU), using standard microfabrication techniques (soft lithography). The device comprised two fluid channels with three inlets and three outlets, as shown in Figure 3.1. These channels will be referred to as PNU 3in3 throughout this thesis. The main channel section had length of 35 mm and width of 500 μm. The three inputs had width of 200 μm. By having three input channels, hydrodynamic focusing is possible, which allows for precise control of the middle inlet stream (sample stream).

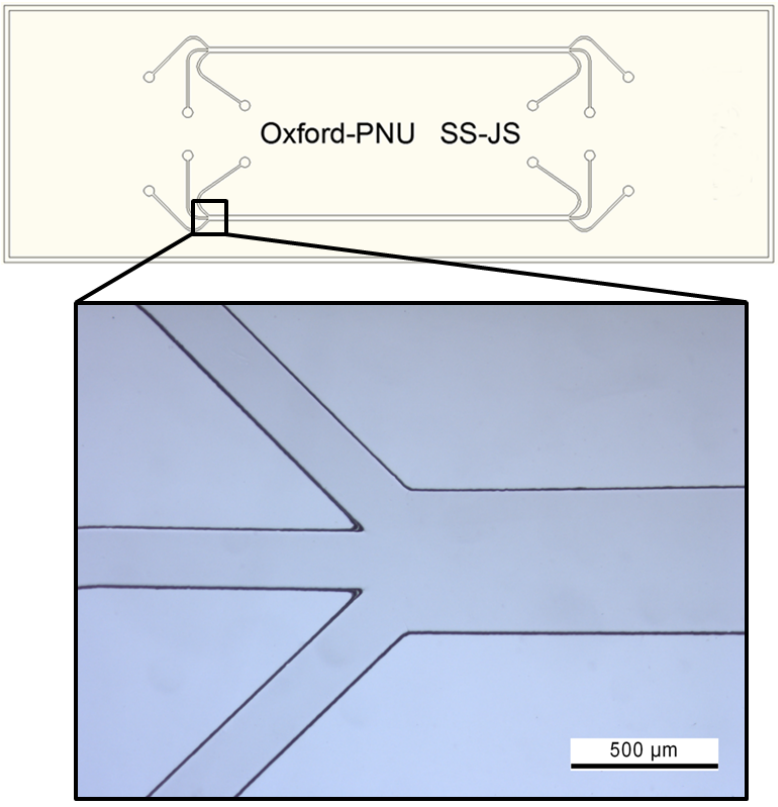
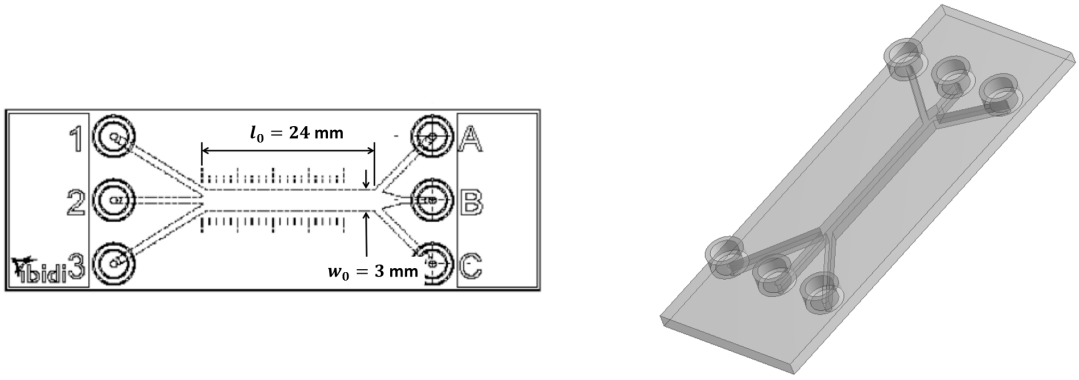


Figure 3.1: Schematic view of the microfluidic hydrodynamic focusing device, produced at Pusan National University using soft lithography. The design is symmetric with three inlets and outlets on either end. The three inlet channels allow for hydrodynamic focusing.

3.3.2 Microfluidic separation device

In addition to the PNU 3in3 device another microfluidic device was obtained which was better suited for bead separation studies. A custom designed microfluidic channel was manufactured by iBidi GmbH in PDMS, to be more convenient for bead separation and hydrodynamic focusing of the injected beads. The design was based on a standard iBidi geometry of μ-Slide III 3in1 modified to a μ-Slide III 3in3 with three inlets and three outlets. The device had the following dimensions: length 24 mm, width 3 mm and depth 0.4 mm. The three inlets and three outlets allowed for hydrodynamic focusing at the inlet, and collection of the three separate fluid streams at the outlet. A schematic of the customized iBidi device is shown in Figure 3.2.



(a) (b)

Figure 3.2: A schematic of the customized iBidi μ-slide, with a length of 24 mm, a width of 3 mm and a depth of 0.4 mm. (a) Top view of the microfluidic separation device. (b) 3D model of the iBidi μ-Slide III 3in3.

3.3.3 Microfluidic counting slide

To observe beads, a FastRead 102 microscope counting slide (Immune Systems, UK) was used. The FastRead 102 is a disposable plastic device composed of a set of 10 easy-to-fill fluid *observation chambers*, as depicted in Figure 3.3. Each observation chamber has a depth of 100 μm and a counting grid etched into its

surface, as illustrated in the magnification section of Figure 3.3. The counting grid has a dimension of 5 mm × 2 mm and is divided into 10 squares. Each square is further divided into 16 smaller squares.

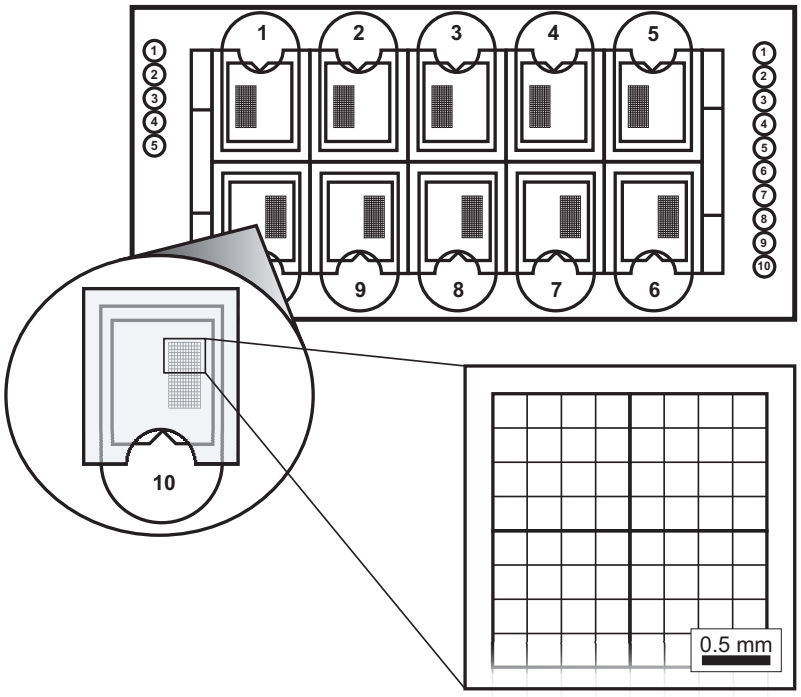


Figure 3.3: Schematic illustration of a FastRead 102. The magnifying glass shows a close up view of a single observation chamber.

3.3.4 Hydrostatic fluid chamber

It is convenient to use a single observation chamber for easy access by the permanent magnet. Either a FastRead 102 slide can be cut down or a simple hydrostatic fluid chamber can be constructed from simple components. The hydrostatic fluid chamber shown in Figure 3.4 was assembled from standard glass microscope slides and No. 1.5 glass cover slips, purchased from Agar Scientific Ltd. To create the chamber, two thin strips of cover slip were first cut using a diamond-tipped scribe and then bonded to the face of the bottom microscope slide using varnish (Rimmel London, 60 seconds). The top microscope slide was then bonded before leaving the device to

cure for a minimum of two hours. Once the device was cured, the aqueous suspension of magnetic beads was drawn into the channel via capillary action and then sealed around all edges with varnish to ensure that it was water-tight.

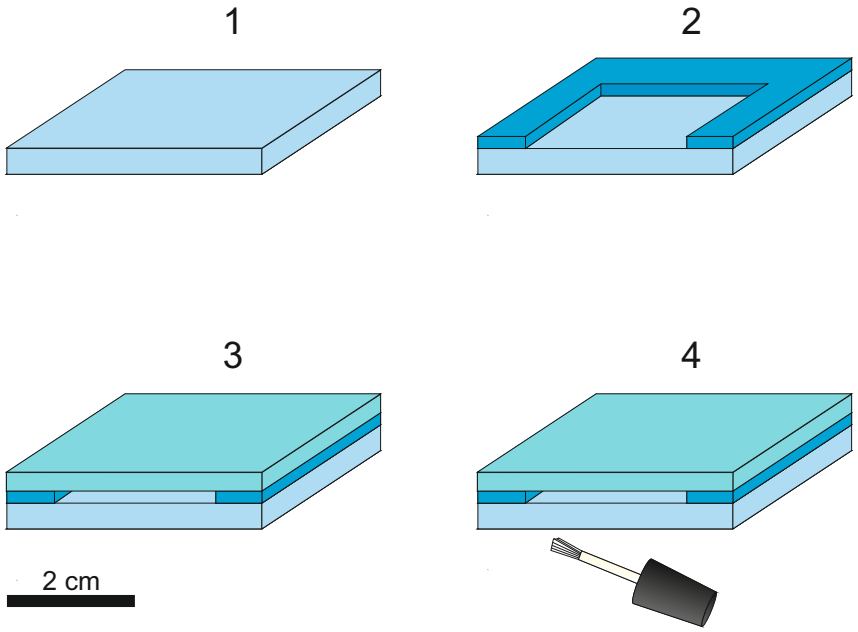


Figure 3.4: Fabrication procedure of the hydrostatic fluid chamber. (1) Glass microscope slides are cut in squares. (2) Standard glass cover slips are cut in thin strips and glued to the bottom microscope slide using varnish. (3) Another cut microscope slide is bonded to the top of the structure. (4) After the chamber is filled with a particle suspension, the chamber is sealed around all edges and openings with varnish.

These single chambers could be rapidly and reproducibly made and used minimal amounts of the suspension, making them suitable for use in the equilibrium position experiments (see Section 3.9). The only drawback, compared to the FastRead 102 slides, was that there is no patterned grid for counting or locating beads.

3.4 Magnetic field measurement

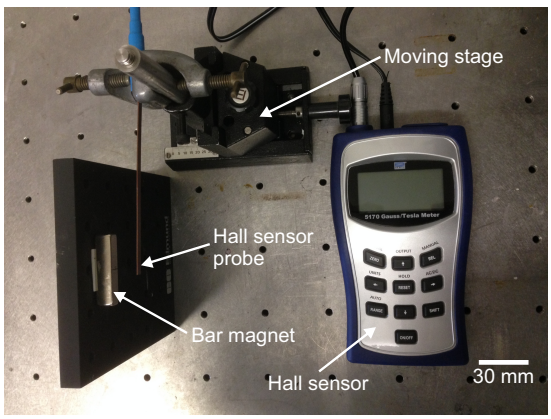
The magnetic flux density of a N42 neodymium bar magnet with dimensions 42 mm $\times$ 8 mm $\times$ 10 mm (Magnets4U, UK) was measured using a hand-held Hall sensor (5170 Gauss/Tesla Meter, F.W. Bell). The Hall probe was constructed from a thin

sheet of semiconductor with output connections perpendicular to the direction of current flow. When subjected to a magnetic field, the Hall probe responds with an output voltage proportional to the magnetic flux density.

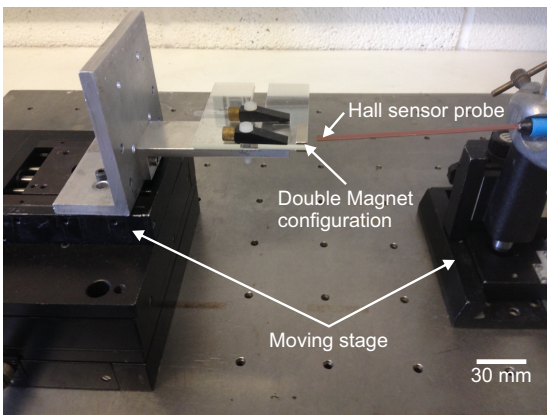
The flux density of the bar magnet was measured by moving the transversal Hall probe away from the magnet along its centreline to 48 mm from its surface. The Hall probe was mounted on a precision translational moving stage and was manually moved in step sizes of 0.1 mm. The Hall probe was maintained perpendicular to the flux lines in order to maximise the output signal.

The Double Magnet configuration was measured in the same way. For the Double Magnet configuration two rectangular N42 Neodymium magnets (20 mm × 6 mm × 1.5 mm) were arranged on top of each other, leaving an air gap of 2 mm in between. The Hall probe was kept in the centre plane between the two magnets. The probe was moved from the centre point between the two magnets up to 17 mm away from the outer edge of the two magnets with a step size of 0.5 mm.

Prior to each measurement, the Hall sensor was re-calibrated inside a zero flux chamber. Photographs of both measurement setups, for the single bar magnet as well as the Double Magnet configuration, are presented in Figure 3.5.



(a) Single bar magnet setup measurement



(b) Double Magnet configuration measurement

Figure 3.5: Setup to measure the magnetic flux density of different magnet configurations: (a) single bar magnet. (b) double magnet configuration.

3.5 Magnetophoretic mobility experiment

To compare the mobility of individual magnetic microparticles, a cell tracking velocimetry (CTV) setup was assembled to enable measurements of the magnetophoretic velocity of single beads in stationary liquid (DI water) within a region of known magnetic field. The magnetic beads were optically observed in a FastRead 102 microscope counting slide (see Section 3.3.3). The rectangular grid structure, which is etched onto each observation chamber, allows determination of the exact view location within the chamber and thus the precise distance between the magnet and the currently observed bead. The magnetic beads moving towards the magnet were video recorded using an inverted microscope (Leitz Wetzlar, Germany) with a long working distance 20× objective lens (Comar Optics, Cambridge, UK) and a CCD camera (μEye Imaging Development Software, Germany). The resolution of the inverted microscope system allowed the clear viewing of individual beads of 1 μm to 2.8 μm in diameter. The recorded trajectories of individual beads moving towards the magnet were analysed off-line using the freely available software *ImageJ*. The magnetically induced velocity was calculated using the open source particle tracking plug-in *MTrackJ*.

Prior to the measurement, the beads had been diluted to a suspension of $0.9 - 1.4 \times 10^5$ beads/mL as described in Section 3.2. The concentrations were confirmed by observing the number of beads on the counting grid of the observation chamber. Visual inspection of previous experiments had shown that such low concentrations successfully avoid bead interaction [329]. Before each experiment, bead suspensions were sonicated in an ultrasonic bath for at least five minutes to break up aggregates and fully suspend the beads. A volume of 20 μL of the sonicated suspension was pipetted into an observation chamber assisted via capillary action. Once the beads had become stationary, an external magnetic field was applied by accurately positioning an N42 neodymium (NdFeB) magnet (42 mm × 8 mm × 10 mm) adjacent

to the FastRead 102 counting slide. The FastRead 102 counting slide was cut down in size in order to be placed at a minimum distance of 10 mm from the magnet. When the magnet was moved 40 mm away from the chamber's edge the motion of the beads was observed to be negligible and was thus used as the magnet *parking* position. The permanent magnet was attached to a high precision translation stage, which allowed accurate movement of the magnet to different positions from the counting grid, while keeping the view location within the chamber stationary. This configuration enabled the magnetic field experienced by the beads to be accurately adjusted. A photograph of the CTV setup is shown in Figure 3.6.

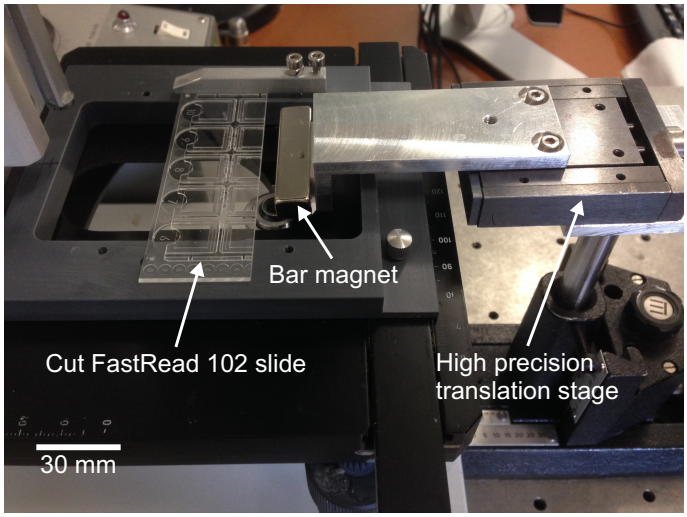


Figure 3.6: Setup to measure the magnetically induced velocity. The magnet (42 mm × 10 mm × 8 mm) is mounted on a high precision translation stage to move the magnet with respect to the observation chambers.

3.6 SQUID measurement

For the purpose of simulating the bead trajectories accurately, it is necessary to know their magnetic susceptibility. The susceptibility of magnetic beads was independently measured using a SQUID measurement system (Quantum Design Magnetic Property Measurement System MPMS-XL). A sample ($1 - 30$ mg) of the

different magnetic bead types listed in Table 3.1 was dried in an oven at 65° C. The dry beads were placed in a sample capsule. The sample capsule was put in a *straw* (sample holder) and both ends were filled with empty capsules in order to keep the sample capsule at an appropriate height within the holder. The sample holder was sealed and attached to the SQUID probe. The probe is lowered into the SQUID measurement system where a magnetic field up to ±5 Tesla was applied at a stabilised temperature of 300 K. The different sample preparation steps are depicted in Figure 3.7. The results of the SQUID measurements and discussion are in Section 4.4.

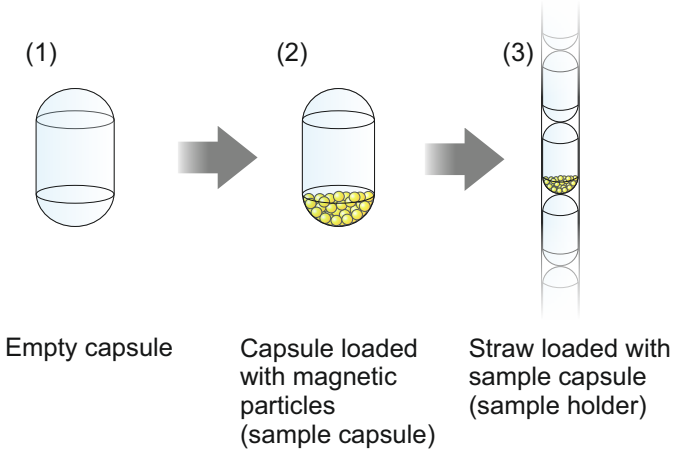


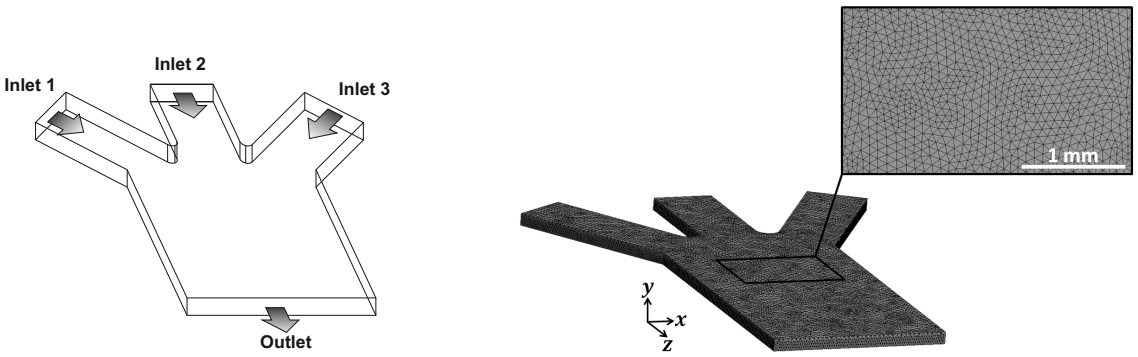
Figure 3.7: Different steps to prepare the SQUID sample. (1)-(2) The dried particles are placed in an empty capsule, which will be the sample capsule. (3) The sample capsule is then put in a *straw* (sample holder). To have the sample capsule at a fixed height within the straw, both ends are filled with empty capsules and sealed with tape. The straw is attached to a SQUID probe and then lowered into the SQUID measurement system. Figure is not drawn to scale.

3.7 Hydrodynamic focusing

The hydrodynamic focusing was numerically simulated and experimentally verified. A detailed description of the numerical and experimental setup is given here.

3.7.1 Hydrodynamic focusing simulation

In order to simulate the fluid dynamics in the microfluidic channel, a three dimensional (3D) symmetric geometry, representing the entrance of the iBidi μ-slide microfluidic channel (see Section 3.3.2), including the three inlets, was modelled in ANSYS Design Modeller (see Figure 3.8a). The model was meshed by a fine hexahedral mesh with $464,558$ elements and $91,424$ nodes. Increasing the number of points beyond this was found to have no noticeable impact on the output of the model (i.e. grid independence). Figure 3.8b shows the top half of the meshed model. Only the top half of the channel is computed due to symmetry, which is equivalent to a symmetry boundary condition at $y = 0$.



(a) (b)

Figure 3.8: 3D model of the entrance of the microfluidic iBidi channel used for the simulation of the hydrodynamic focusing. (a) Modelled entrance of the channel including the three inlet channels. The arrows indicate the simulated direction of flow. (b) 3D mesh model used for the finite element method simulations of the hydrodynamic focusing effect. The model was hexahedral meshed with $464,558$ elements and $91,424$ nodes. The model represents only the upper half of the entrance ($y > 0$), with the bottom half simulated using a symmetry condition.

All liquids were modelled as water at room temperature with *no-slip* boundary conditions applied to all side-walls. Thus, all walls were set to no flux and the diffusion constant to 2.2×10^{-11} m^2/s (self-diffusion of water). Only the continuous liquid phase was modelled and the effect of the suspended particles was neglected due to their size and low concentration ($\upsilon_p < 10^{-6}$). This allowed solutions of the

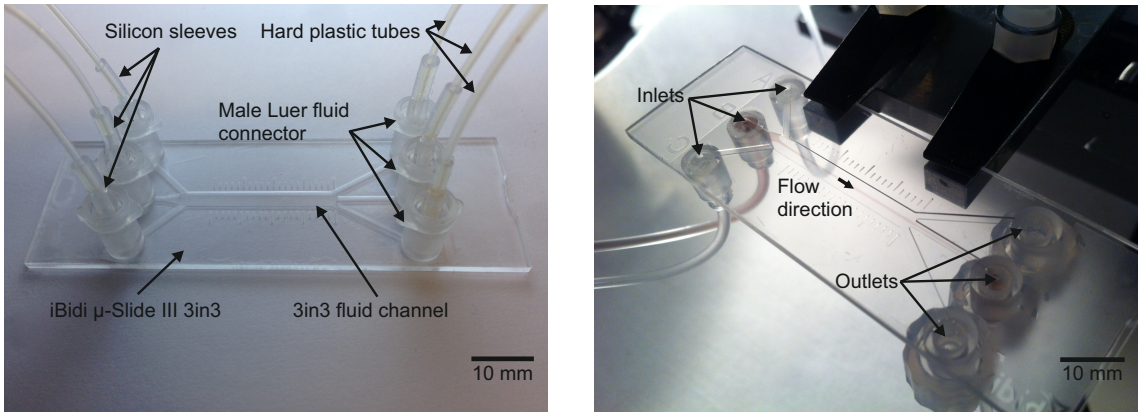
flow in the microfluidic channel in an uncoupled manner (see Section 2.2.2), i.e. only the fluid phase was simulated using an Eulerian approach. The three inlets were treated as laminar inflows with a set flow rate. The outlet is pressure controlled and set to atmospheric pressure. The model equations were solved by finding a steady solution for the velocity field of all flows.

3.7.2 Hydrodynamic focusing experiment

The hydrodynamic focusing experiments were performed to test the viability to accurately focus the inlet sample stream in two different fluid channel designs; PNU 3in3 and iBidi μ-Slide III 3in3. Both designs are described in Section 3.3.1 and Section 3.3.2 and used in the study described below.

The three inlets were connected to three 1.0 mL glass syringes (BD Biosciences, UK) using 0.5 mm inner diameter flexible hard plastic (PTFE) tubing (Microfluidic ChipShop) to introduce the flows to the device. Silicone tubes with an inner diameter of 0.76 mm (Microfluidic ChipShop) were used as a sleeve to connect the hard plastic tubes with the syringe and microfluidic device via its respective interface. The interface of the two devices either required an intermediate tube or a Male Luer fluid connector (Microfluidic ChipShop). Figure 3.9a shows the interface and tubing connections of the iBidi μ-Slide III 3in3. Syringes were mounted on Harvard Apparatus syringe pumps (Harvard Apparatus, Standard Infuse/Withdraw Syringe Pump 11 Plus).

The outlet channels were either connected by tubing to a single external collection pot or directly connected to separate 500 μL collection tanks (Microfluidic ChipShop) mounted on the iBidi μ-Slide III 3in3 device. In the case where tubing was used, to avoid siphoning effects care was taken to keep the ends of the tubes below height of the microfluidic device while having the tubing ends submerged in water at all times, as shown in Figure 3.9b.



(a) (b)

Figure 3.9: (a) Connections and tubing for the μ-Slides III 3in3. Flexible hard plastic tubes were used to introduce the fluid to the device. Silicone sleeves were mounted on a Male Luer fluid connector to interconnect the hard plastic tubes. (b) Setup of the hydrodynamic focusing experiment. Fluid is introduced through the three inlets and leaves the device through the three outlets. The ends of the outlet tubes were submerged in a single collection pot to avoid siphoning effects at low flow rates.

The three syringe pumps allowed independent control of the sheath and sample sample flow rate. In order to make the focusing effect visible, DI water was used as the sheath flow and ink (Pelikan, Royal Blue 4001) diluted in water was used as the inlet sample stream. The DI water was filtered prior to the experiment using a Millipore syringe filter (Whatman GE Healthcare) with a pore size of 1.0 μm to reduce the risk of blocking the channels during the experiment.

Prior to any experiments it was necessary to coat the inside walls of the microfluidic device with a surfactant. This step was absolutely crucial to reduce the risk of air bubbles getting stuck in the device. A 10% w/v ratio (with water), of Sigma-Aldrich F-127 non-ionic surfactant was used for this purpose (Sigma-Aldrich). This solution was flushed through the device before each experiment for 10 minutes at a flow rate of 1 mL/min. The microfluidic device was then filled with DI water, assuring no air bubbles were trapped. Trapped air bubbles could be conveniently flushed using higher flow rates.

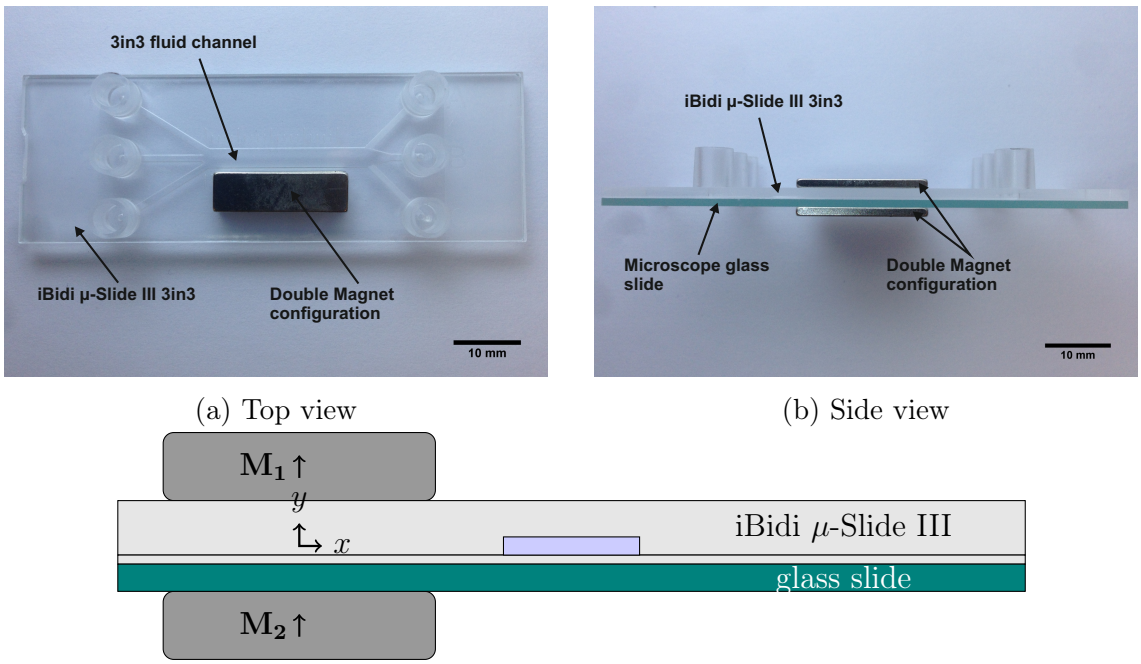
Before images of the hydrodynamic focusing effect were taken, the experiment was run for at least 30 seconds, in order to establish steady state. Images were taken with a CCD camera (μEye Imaging Development Software, Germany) mounted on a stereo microscope (Optika SZM-1 LED stereo microscope) with a 4× magnification.

3.8 Magnet configurations

Two magnet configurations, Double Magnet and Quadrupole, were used for magnetic bead enrichment. All configurations used N42 Neodymium (NdFeB) magnets (First4Magnets®,UK) with a dimension of 20 mm × 6 mm × 1.5 mm.

3.8.1 Double Magnetic configuration

The Double Magnet configuration shown in Figure 3.10 consisted of two NdFeB magnets. Both magnets were placed on the same side of the microfluidic separation device such that the edge of the magnets was 1.65 mm away from the microfluidic channel edge. The two magnets were arranged in an attractive configuration, with both magnetizations pointing in the same direction, while having the microfluidic separation device clamped in between. The vertical separation between the two magnets was adjusted to be 2.6 mm. In order to have a 2.6 mm vertical separation and thus have the centre of the fluid channel along the y direction, a microscope slide was inserted as a spacer between the iBidi μ-Slide and the bottom magnet. The two magnets were conveniently aligned by eye, being held in place by the attractive magnetic force. The magnets and the spacer were robustly held in position with respect to the microfluidic channel, as shown in Figure 3.10b.



(a) Top view

(b) Side view

(c) Cross section schematic

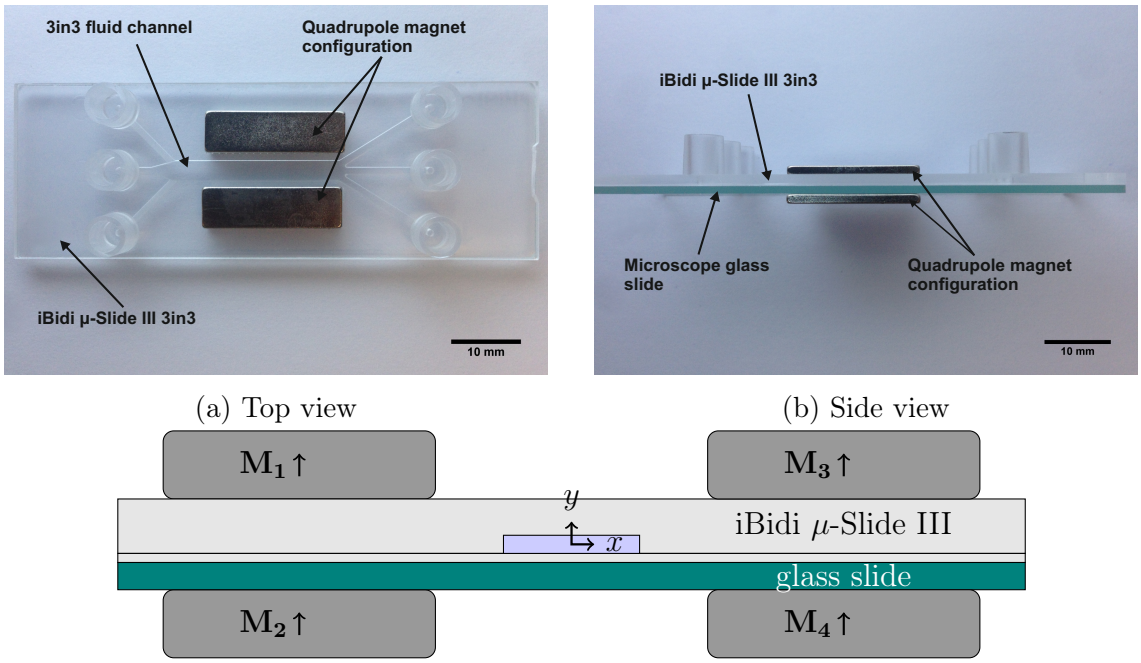
Figure 3.10: Experimental setup of the Double Magnet configuration. Two permanent magnets (20 mm × 6 mm × 1.5 mm) were located adjacent to the 3in3 fluid channel with the iBidi μ-Slide III 3in3 held in between. (a) Top view of the Double Magnet configuration. (b) Side view of the Double Magnet configuration (c) 2D slice diagram ($z = 0$) of the Double Magnet configuration. The permanent magnets (grey) were configured in attraction, with their magnetization vectors $\mathbf{M}$ pointing in the same direction. The microfluidic channel (light blue) was located to the right of the dipole configuration and was centred along y by using a microscope glass slide (turquoise) as a spacer.

3.8.2 Quadrupole configuration

The Quadrupole configuration shown in Figure 3.11 featured four NdFeB magnets, basically two Double Magnet configurations on either side of the 3in3 fluid channel. Each Double Magnet had its magnetization in the same direction (i.e. in attraction), but the two Double Magnets were configured repelling each other. In order to overcome the repelling force and to have a horizontal separation of 3.5 mm, an acrylic glass frame was made to keep the magnets in place (not shown in Figure 3.11).

As for the Double Magnet configuration described above (see Section 3.8.1), a microscope glass slide was inserted between the iBidi μ-Slide III 3in3 and the two bottom

magnets in order to keep the 3in3 microfluid channel centred along the y direction, as shown in Figure 3.11b.



(a) Top view

(b) Side view

(c) Cross section schematic

Figure 3.11: Experimental setup of the Quadrupole configuration. Four permanent magnets (20 mm × 6 mm × 1.5 mm) were located next to the 3in3 fluid channel with two magnets on either side of the 3in3 fluid channel and with the iBidi μ-Slide III 3in3 clamped in between. (a) Top view, (b), side view and (c) 2D slice diagram ($z = 0$) of the Quadrupole configuration. The permanent magnets, iBidi μ-Slide III 3in3 and spacer, to keep the channel centred in y direction, are indicated by different colours; i.e. grey, light blue and turquoise, respectively.

3.9 Static gathering points experiments

To verify the magnetic field pattern of the Double Magnet configuration and the existence of the static gathering point beyond the magnets, a specially made setup was built, as shown in Figure 3.12. The setup had several degrees of freedom for flexibility, allowing the magnet height (Section 3.9.1) and the vertical separation between the two magnets (Section 3.9.2) to be varied.

In these experiments, two N42 NdFeB magnets (First4Magnets®,UK) with a length,

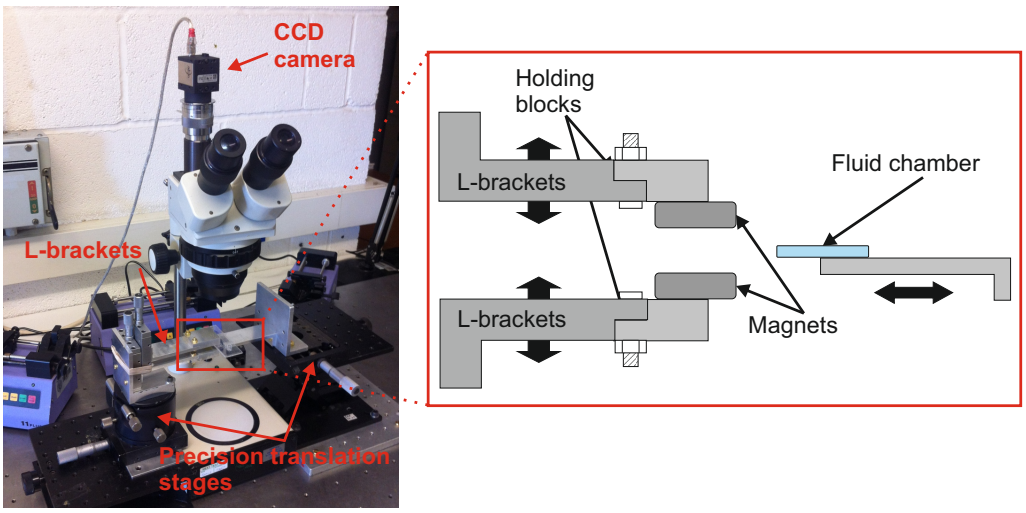


Figure 3.12: Experimental setup to verify the static gathering points of the Double Magnet configuration. Magnets and microfluidic chamber are mounted onto L-brackets which can be accurately adjusted using precision lateral translation stages. The degrees of freedom of the setup are shown in the close up schematic. The schematic is not drawn to scale.

width and height of 20 mm, 6 mm and 1.5 mm, respectively, were mounted onto aluminium holding blocks using Araldite® adhesive. The holding blocks were screwed onto L-brackets and could be removed to change the magnets. The L-brackets were mounted onto precision linear translation stages for accurate control of the vertical gap and height of the Double Magnet configuration, as shown in Figure 3.12. Nonmagnetic materials were used to minimise the distortion of the magnetic field; the holding blocks and L-brackets were fabricated from aluminium and the fasteners were brass. The holding blocks and L-brackets were manufactured by the Oxford University workshop based on schematics drawn by the author. The schematic diagram in Figure 3.12 shows the Double Magnet configuration and illustrates the direction of movement of the magnets as well as the location of the fluid chamber.

In all experiments, a hydrostatic chamber was chosen to visualize the beads' static gathering positions, because these experiments did not require continuous sample flows. The hydrostatic chambers were prepared according to Section 3.3.4 and then filled with bead suspensions before being mounted onto the L-bracket. Suspensions

of all considered bead types (see Table 3.1) were used in the experiments, where the concentration was varied between $\approx 10^6$ beads/mL to $\approx 10^8$ beads/mL ($\upsilon_p \approx 10^-8 - 10^-4$). These high concentrations were chosen, in order to make the gathering positions clearly visible.

Initially, the L-bracket, with the hydrostatic cover slip chamber, was positioned away from the magnets so that the beads within the chamber did not have any significant interaction with the field. The cover slip chamber was then slowly moved towards the magnets using the horizontal positioning stage. Moving the chamber slowly caused the beads to be repelled away from the magnets towards the position of static equilibrium, therefore increasing the concentration along the equilibrium line. When the chamber was correctly placed, the setup was left for two minutes to ensure the beads have reached their static gathering point and no further observable growth in particle agglomeration could be seen. A microscope (Optika SZM-1 LED stereo microscope) with a lower magnification (maximum magnification of 4×) gave a better visualisation of the overall structure of the formed band.

Pictures were taken with the CCD camera (μEye Imaging Development Software, Germany) attached to the microscope (Optika SZM-1 LED stereo microscope) and the gathering position was measured as being the distance from the centre axis of the equilibrium band to the edge of the magnets. The experiment could be repeated with the same chamber after 5 minutes of sonication to break up agglomerations.

3.9.1 Magnet height variation

In order to increase the height of the magnet, multiple N42 neodymium magnets with dimensions 20 mm × 6 mm × 1.5 mm were stacked on top of each other on both sides of the L-brackets. In this manner, the assembled magnets can increment in height between 1.5 mm and 6.0 mm.

The vertical separation between the two magnet stacks was kept at 2 mm and only

the height of each magnet stack was varied. In order to ensure the 2 mm gap, microscope cover slips were used as spacers because the attractive force between the two magnet stacks was sufficient to close the gap without spacers, which would make the separation distance uncertain when the attractive force was significant.

3.9.2 Magnet vertical separation variation

The vertical magnet separation was increased from 2.6 mm to 5.8 mm in 0.2 mm intervals, by adjusting the L-brackets using the precision linear translation stages. At every separation the particles were left for at least two minutes allowing them to reach their new position of static equilibrium.

3.9.3 Magnet geometry

The Double Magnet configuration described in Section 3.8.1 was also investigated with tapered magnets such that the magnet flux density varies along the length of the magnet. For this experiment two 20 mm $\times$ 6 mm $\times$ 1.5 mm N42 NdFeB magnets were tapered by manually grinding and polishing down the 1.5 mm dimension, beginning halfway along the length of the magnet as shown in Figure 3.13. The thickness of the magnet at the end of the taper was approximately half the non-tapered thickness ($\approx$ 0.75 mm). The magnet tapering was carried out by removing material by filing and polishing by hand whilst the sample was supported between steel templates to achieve the desired angle and shape; manufactured by the Department of Engineering Science Mechanical Engineering workshop, University of Oxford. The results of the magnet configuration variations are presented in Section 6.2.

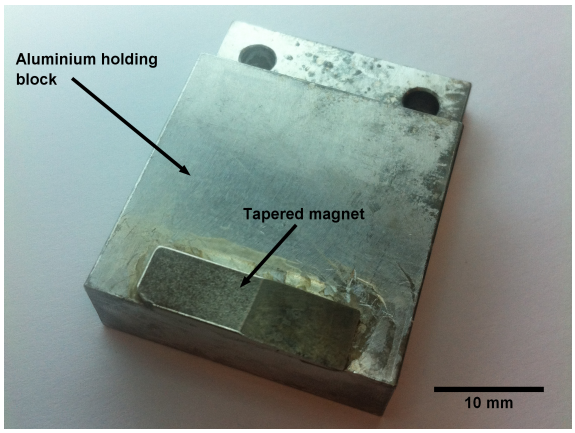


Figure 3.13: Tapered magnet attached to an aluminium holding block

3.10 Magnetic particle trajectory simulation

The trajectory of a magnetic bead when being exposed to a magnetic field was simulated in two steps. First the magnetostatic field of the two magnet configurations used in this thesis (i.e. Double Magnet configuration and Quadrupole configuration, see Section 3.8) was modelled and simulated using the commercially available FEM software package ANSYS Maxwell. The simulated magnetic field was exported to a uniform mesh, stored in a 3D array in which the position and values in the array represent the localised magnetic flux density. The box flow diagram in Figure 3.14 shows the modelling process and where data was exchanged between different software packages.

3.10.1 Magnetic field simulation

The magnetic **B** field of the two magnet configurations was numerically simulated using ANSYS Maxwell. Maxwell uses FEM to solve the Maxwell's equations (see Equation 2.37-2.39 in Section 2.5). A boundary box, surrounding the magnet configuration, is used to limit the simulation domain, Ω, i.e. the region over which the set of equations was solved. The box was assumed to be filled with air and was sufficiently large that no boundary effects influenced the results.

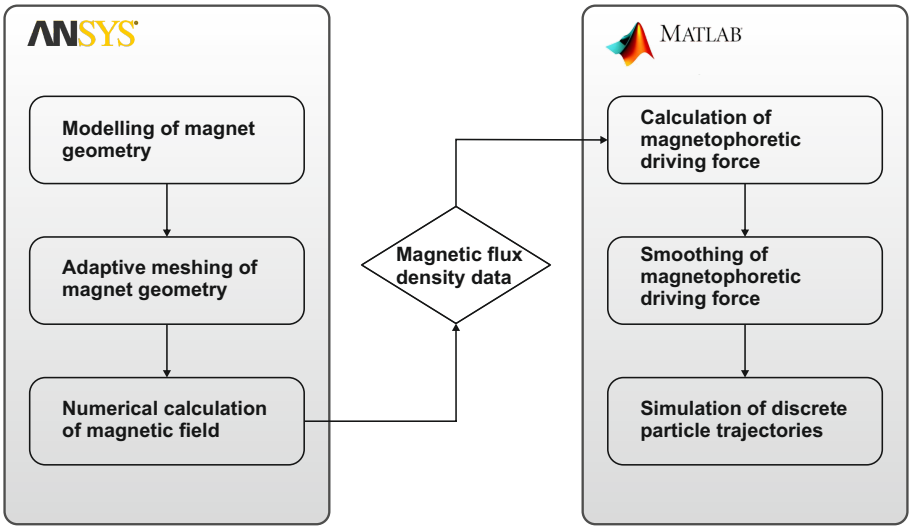


Figure 3.14: Box flow diagram of the modelling and simulation process. The magnetic flux density was calculated using ANSYS FEM solver. Based on the FEM results, the discrete particle trajectories were then simulated in MATLAB.

The simulated domain was first divided into tetrahedral sub-domains (elements) to form the mesh for the FEM analysis. ANSYS Maxwell employs multiple automated meshing algorithms using default physics controls to ensure a high quality mesh suitable for the defined simulation. It also has an adaptive mesh refinement algorithm built in, which automatically refines the mesh as described in Section 2.5.1.1. In this work, a global percentage energy error (see Equation 2.50) of 0.1% was normally chosen as a stopping criteria for the adaptive refinement algorithm; setting a lower value did not show a significant improvement in the computed solution and grid independence was observed. As further confirmed, the corresponding mesh met the mesh regularity criteria ($\theta \leq 5$) as set in Equation 2.45, where the elements' mean aspect ratio was $\bar{\theta} = 4.6$.

3.10.2 Discrete particle trajectory simulation

After the magnetic field of the magnet configuration had been simulated in ANSYS Maxwell, the trajectories of the beads were calculated in MATLAB. The trajectory calculation was split into two steps; calculation of the magnetophoretic driving force

(see Equation 2.34) and discrete particle simulations using the Lagrangian particle tracking scheme (see Equation 2.35).

3.10.2.1 Magnetophoretic driving force calculation

The computed magnetic flux density was imported into MATLAB (see Figure 3.14). Since FEM computes the magnetic field values on discrete nodes of a tetrahedral mesh, the values were mapped onto a regular equispaced 3D grid in MATLAB for further processing. In the MATLAB model, the distance between neighbouring grid points was kept fixed in all directions and was chosen to be equal to the smallest element of the mesh in the FEM analysis. This ensured that the detail in the magnetic field simulation was accurately captured. It was found that the smallest elements were normally in the order $O(10^{-5})$ m. Values of grid points which did not fall on the mesh directly, were interpolated using a second order polynomial interpolation method. Based on the numerically simulated magnetic flux density $\mathbf{B}$, the magnetophoretic driving force for both magnet configurations was calculated at every single point of the imported grid. In order to numerically calculate the magnetic driving force, the derivative of the FEM results was taken by applying the forward numerical differencing approximation [330].

Since the gradient was taken on a finite grid, the computed magnetophoretic driving force suffered from numerical irregularities, as depicted in Figure 3.15. These irregularities were reduced by applying a total variance denoising smoothing algorithm. This algorithm was found to be the most appropriate and effective smoothing algorithm given the variance of the magnetic field and the noise level.

3.10.2.2 Lagrangian particle tracking

Based on the numerically simulated magnetophoretic force, individual particle trajectories were simulated using a Lagrangian bead tracking scheme. The time step,

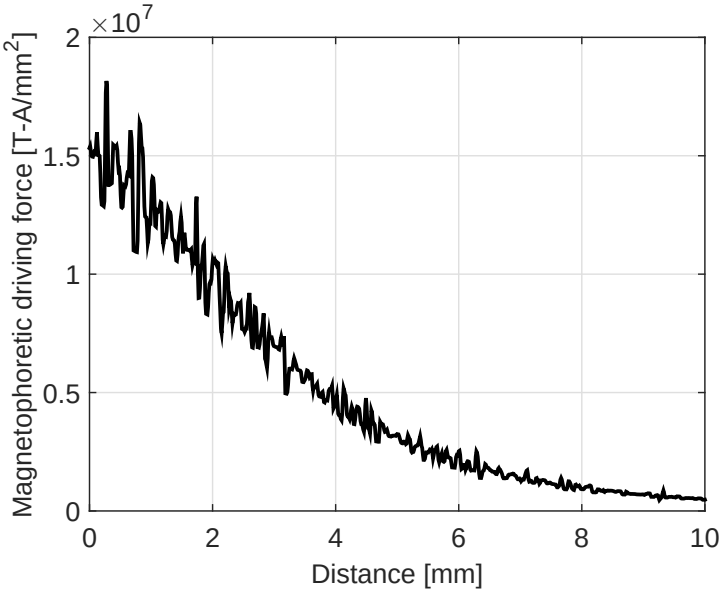


Figure 3.15: Simulation of the magnetophoretic driving force suffered from numerical irregularities due to the finite differentiation of the magnetic flux density (prior to smoothing).

δt in Equation 2.35, needs to be smaller than 10 ms in order to meet the CFL condition (see Equation 2.36) because of the chosen grid length ($O(10^{-5})$ m) and fluid velocity ($O(10^{-3})$ m/s). Here, the time step was set to 1 ms for accuracy.

At every time step, the bead's terminal velocity (see Equation 2.32) was recalculated. In order to increase computing efficiency, the initial magnetophoretic driving force matrix was pre-conditioned. The pre-conditioning reduced the dimension of the initial magnetophoretic driving force matrix to a $5 \times 5 \times 5$ matrix (minimum dimension for spline interpolation), which improved the speed of the interpolation algorithm. This dimension reduction reduced the computing time by a factor of ≈ 5.

3.11 Magnetic separation efficiency

3.11.1 Separation efficiency simulation

The separation efficiency of the two magnet configurations described above (see Section 3.8) was evaluated using a Monte Carlo method where 400 single bead trajectories were simulated. Each bead trajectory was sampled as described in Section 3.10. The sample size was estimated by using a maximum variance scheme where an underlying binomial distribution of the outcome was assumed and a confidence interval of 95% was used [306].

Due to symmetry, the beads were randomly distributed across the upper half of the fluid channel. Depending on the magnetic configuration the beads were assumed to be introduced through the centre inlet (inlet 2) or one of the sheath flow inlets (inlet 1 or inlet 3) for the Double Magnet or Quadrupole configuration, respectively (see Figure 3.16). The starting point of the bead was along the streamlines of the corresponding inlet in a region where the magnetophoretic driving force had dropped to 10% of its maximum possible value. This occurred at a distance $c = 15$ mm away from the $x-y$ plane ($z = 0$). The starting positions of the beads for the two different magnet configurations are depicted in Figure 3.16.

For the simulation, the vertical magnet gap (see Figure 6.1) was set to $a = 2.6$ mm for both magnet configurations. The Double Magnet configuration was simulated to be placed 4.6 mm away from the centre of the fluid channel ($y = 4.6$ mm), such that the gathering points aligned within the fluid channel but 0.5 mm away from the channel's side wall pointing to one of the sheath flow exits. In the case of the Quadrupole configuration, the magnet pairs were symmetrically placed around the fluid channel, with a horizontal gap of $b = 3.5$ mm.

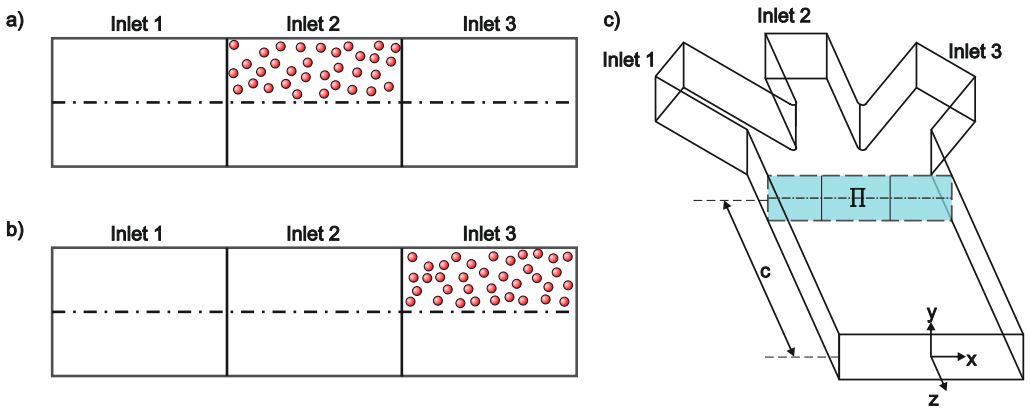


Figure 3.16: Schematic showing where beads are introduced and released from in the magnetic particle separation simulation for the two magnet configurations: (a) and (b) show the release position of the beads for the Double Magnet and Quadrupole configuration, respectively. The beads were assumed to be released downstream of one of the three inlet at a distance $c = -15$ mm in the z direction across the highlighted plane Π shown in (c). The hydrodynamic focusing ratio between the three inlets was assumed to be 1. Due to symmetry around the y axis, bead trajectories were only simulated in the upper half of the fluid channel's cross section.

3.11.1.1 Continuous mode simulation

Devices can be operated in continuous flow or pulsed flow. The advantage of using a pulsed mode is to flush beads that are trapped in the channel, but this mode increases the complexity of the system. When simulating continuous mode operation, bead trajectories were aborted as soon as the bead touched any inner side wall and the next trajectory iteration was started. The beads touching the inner surface of the channel were considered as trapped and thus *lost*, as they were not expected to exit the system; these beads will have an impact on the separation throughput.

The flow rates were varied, ranging from 3.3 μL/min ($\bar{u} = 0.046$ mm/s) to 125 μL/min ($\bar{u} = 1.74$ mm/s) at each inlet, whilst the ratio between all inlet flow rates was kept at 1.

3.11.1.2 Pulse mode simulation

In the pulse mode simulation, beads in close proximity to the inner surface were regarded as trapped (due to their small velocity), but could still move along the surface because of magnetophoresis. Therefore, bead trajectories were not aborted, but were simulated for different time intervals (60 seconds, 100 seconds and 200 seconds). At the end of each time interval, the beads were assumed to leave the system along their streamlines. This was considered a simulation of *flushing*, which will recover the trapped beads. Pulse mode is only applied for the Quadrupole configuration.

3.11.2 Separation efficiency experiment

The magnetic separation efficiency of the Double Magnet and Quadrupole configuration in continuous mode, and in the case of the Quadrupole configuration in pulse mode, was experimentally verified. The geometry parameters of the two magnet configurations described in Section 3.8 were set as stated above in this section (Section 3.11.1).

The inlets of the iBidi μ-Slide III 3in3 microfluidic device were connected to three 1 mL glass syringes (BD Biosciences, UK) mounted on Harvard syringe pumps using 0.5 mm inner diameter flexible tubing to introduce the flows to the device. The syringes were connected to the interface of the device as shown in Figure 3.9a in Section 3.7.2. The outlet channels were connected to three 0.5 mL collection pots (Microfluidic Chip Shop, Germany) mounted on the fluid device, which were capped after each experiment and removed for further analysis (i.e. bead concentration measurement).

To demonstrate the separation efficiency of magnetic beads from a sample, a bead suspension of 1 μm sized magnetic beads (SiMAG-Silanol, Chemicell) with a bead concentration of 10^6 beads/mL ($\upsilon_p \approx 10^-7$) was prepared. The suspension was dyed

with blue ink (Pelikan, Royal Blue 4001) such that the sample liquid was coloured blue to enable the hydrodynamic focusing to be viewed clearly. The surfactant Pluronic F-127 (Sigma-Aldrich) at 0.1% weight to volume ratio was added to the bead suspension to prevent adhesion of beads to the fluid channel surfaces and also a mixture of DI water and 0.1% of F-127 was used to flush the channel for 5 minutes prior to each experiment. The two sheath flows, used to focus the bead containing sample flow, was also a mixture of DI water and 0.1% of F-127.

The bead suspension was injected through the centre inlet or one of the sheath flow inlets of the device for the Double Magnet configuration or Quadrupole configuration, respectively. The flow rates at each inlet were adjusted in order to fill, but not overspill, their respective exit channel. Thereby, the inlet flow rate ratios were kept as close to $1:1:1$, whilst maintaining the hydrodynamic focusing. The inlet and outlet channels of the device were observed with a CCD camera (μEye Imaging Development Software, Germany) mounted on a low magnification microscope to observe the hydrodynamic focusing.

In the continuous mode, the experiment was run for at least five minutes, to achieve steady state and collect enough sample volume. For the pulse mode operation, magnetic beads in suspension were introduced for 30 seconds followed by a 60 second pause, where all flows were stopped and the beads given sufficient time to gather. This cycle was repeated 10 times, before flushing the microfluidic channel with a flow rate of 1 mL/min for 10 seconds.

The bead concentrations for the collected samples for the separation experiments were measured using a BD Accuri C6 flow cytometer. A volume of at least 30 μL was analysed with a flow rate of 8 μL/min. The cytometer flow rate was verified to be constant by analysing a DB Trucount tube at the beginning and at the end of the measurement. The findings and discussion are presented in Chapter 7.

Chapter 4

Magnetophoretic mobility

4.1 Introduction

In Chapter 2, the concept of magnetophoretic mobility was introduced as a fundamental property of a particle or cell and is equally applicable to materials that are diamagnetic, paramagnetic, or ferromagnetic, depending on the relationship between the applied field and the particle's susceptibility. Magnetophoretic mobility is the basic concept which enables the design of magnetic separation systems and provides a tool for the operation and evaluation of the magnetic separation process.

The increasing interest in using magnetic beads as carriers to perform cell separation tasks has also fuelled the industry of magnetic particles. Different low cost and easily functionalizable microbeads are now commercially available from various manufacturers. However, depending on their fabrication process, and the variability in these processes, the magnetic beads can vary significantly in respect of their material properties (e.g. size distribution or iron content). The extend to which beads deflect when being exposed to an external nonhomogeneous magnetic field highly depends on these properties (see Equation 2.32). This makes the full control of single bead trajectories in free-flow magnetophoresis highly sensitive to small variations

of intrinsic parameters. In order to have a separation device with high collection efficiency and discrimination it is essential to know the *magnetic responsiveness* of the magnetic beads.

As explained in Section 2.4, Equation 2.32 can be split into two independent terms, magnetophoretic mobility ν_p and magnetophoretic driving force S, given in Equation 2.33 and Equation 2.34. Previous work on free-flow magnetophoresis attempted to keep S constant over the distance the particle travelled in order to have a constant magnetic migration velocity $\mathbf{u}_p$ and thus improved control of the particle movement [225, 331, 332]. A challenging task, however, is to find the exact value of the particle's magnetophoretic mobility ν_p, since it depends on multiple material properties and is therefore highly dependent on the particle manufacturer. Different values for the magnetic susceptibility of iron oxide particles can be found in the literature [333–335]. Researchers have attempted to characterize the magnetic properties of the micron-sized beads directly; Fonnum *et al.* [300] as well as Shevkoplyas *et al.* [212] determined the beads' magnetic response based on their magnetization curves (hysteresis loops). A different approach was used by Zborowski [331] and also Häfeli [301], where they measured the magnetophoretic velocity, using cell tracking velocimetry (CTV), to then work out the magnetophoretic mobility of single magnetic beads and their magnetic susceptibility. Yet, it is highly desirable to arrive at a definition of the magnetophoretic mobility as a property that is independent of a particular magnetic system and provides means of calculating motion of a magnetic particle for any field geometry.

Given the importance of the magnetophoretic mobility, the following chapter will describe a method to experimentally evaluate the magnetophoretic mobility of single superparamagnetic beads using a CTV system. Additionally, the magnetic susceptibility of the beads is measured using a superconducting quantum interference device (SQUID). In this study, five different types of magnetic beads from two different

manufacturers (Table 4.1) are investigated and representative measures including mathematical relationships will be provided.

Table 4.1: Physical characteristics of magnetic beads: density, iron content and diameter (d_M) as stated by the manufacturer [326, 336]. The diameter (d_p) is independently measured for comparison, by dynamic light scattering$^{(1)}$ or by analysing scanning electron microscopy$^{(2)}$ images.

Bead type	Manufacturer	Density $[g/c\mathrm{m}^3]$	Iron content [wt. %]	Diameter d_M [μm]	d_p [μm]
ScreenMAG	Chemicell	2.25	40	1.0	$0.77 \pm 0.42^{(1)}$
SiMAG	Chemicell	2.25	40	1.0	$1.12 \pm 0.97^{(1)}$
MyOne	Dynabeads	1.8	26	1.05	$1.05 \pm 0.03^{(2)}$
M280	Dynabeads	1.4	12	2.8	$2.79 \pm 0.05^{(2)}$
M270	Dynabeads	1.6	14	2.8	$2.75 \pm 0.07^{(2)}$

4.2 Magnetophoretic mobility of superparamagnetic beads

To compare the mobility of different single beads, their drift velocities in stationary fluid (deionized water) is observed, similar to the work of Häfeli *et al.* [337]. Unlike Ref [337] where beads were kept at a constant distance from the magnet, in this work the magnetophoretic velocity was optically measured at different distances away from the magnet. This new approach allows evaluation of magnetic field dependence of the bead's properties.

The magnetophoretic movements of single magnetic beads in an observation chamber are observed under an optical microscope. The observation chamber used (see Section 3.3.3), had a counting grid etched to its surface, which helped determine the viewing location of the beads within the observation chamber as well as the distance to the magnet. The distance d_m between the bar magnet and the counting chamber could be adjusted and the magnetically induced velocity was measured for the

magnet positioned at 10 mm, 12 mm, 14 mm and 16 mm away from the counting grid. These four positions will also be referred to as A, B, C and D, respectively. Note, that d_m describes the distance to the magnet's surface. A schematic diagram of this experimental setup is depicted in Figure 4.1. For a more detailed description of the experiment see Section 3.5 in Chapter 3.

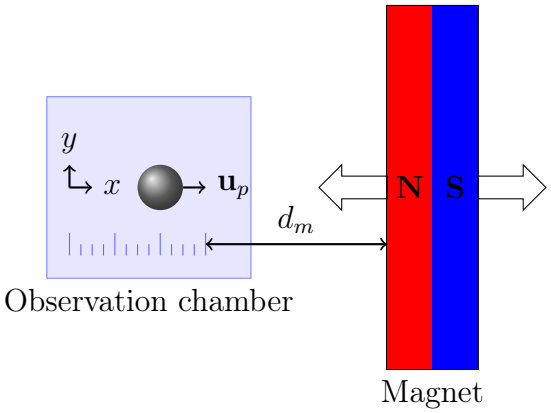


Figure 4.1: Schematic drawing showing the experimental setup used to determine the magnetically induced velocity of magnetic particles. The distance d_m is varied step wise from 10 mm to 16 mm with a step size of 2 mm. The figure shown here is not drawn to scale. The experimental setup can be seen in Section 3.5.

The beads were tracked moving in the x direction towards the magnet over a distance of 55 μm, which was equivalent to one traverse of the field of view of the microscope camera. The magnetically induced velocity of single beads was measured for each bead type in Table 4.1 and for all four magnet positions. Beads travelling at the top or the bottom of the observation chamber were discarded in the measurement, to avoid including data from beads that were clearly interacting with the chamber surface. Also bead agglomerations were ignored from this particular analysis.

The magnet dimensions were much larger than the observation chamber. Thus, a uniform magnetic field along the width (y direction) and height (z direction) of the observation chamber was assumed and edge effects could safely be neglected. The magnetic field of the bar magnet was investigated, as outlined in the next section.

4.2.1 Properties of the static magnetic field

The magnetic flux density of the bar magnet, under which the particles are influenced in the observation chamber, was simulated and measured to confirm its magnetic field (see Section 3.4). The magnetic flux density map of the bar magnet is shown in Figure 4.2.

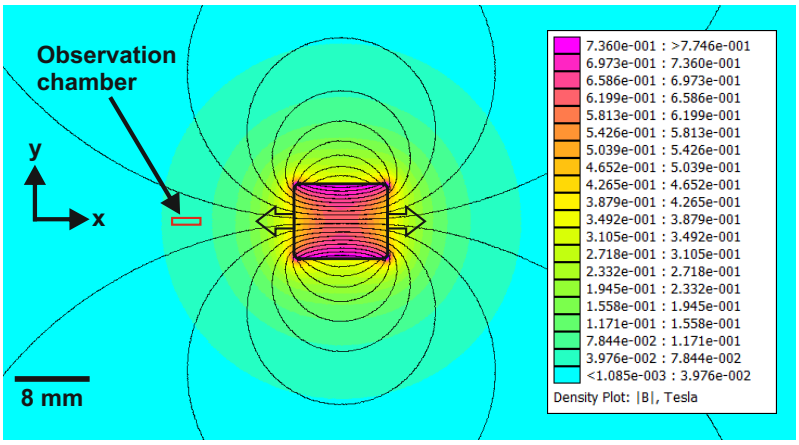
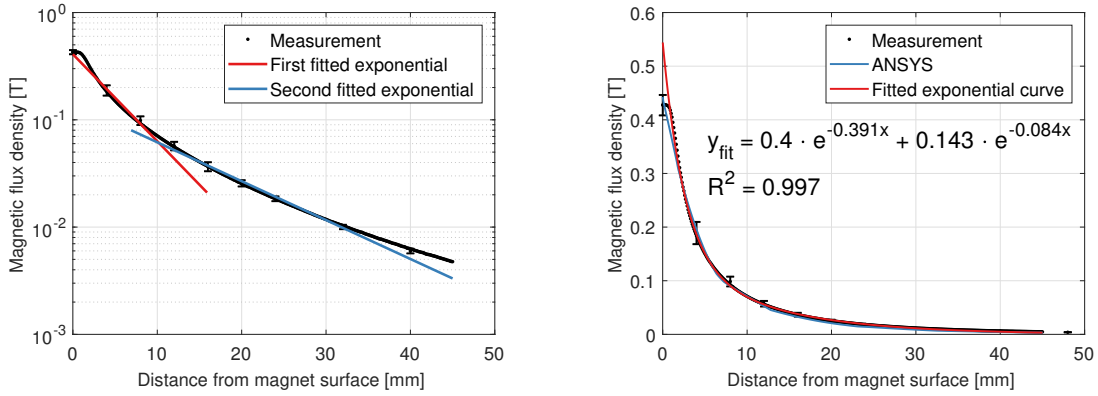


Figure 4.2: Modelling of the magnetic field generated by a N42 Neodymium magnet ($42 \times 8 \times 10$ mm) simulated in FEMM. The red box shows the position of the observation chamber and the two (open) arrows indicate that the magnet was attached to a movable stage.

Figure 4.3 shows how the magnetic flux density decayed when moving away from the magnet surface along its centre line. The magnetic flux density was measured using a Hall probe and plotted on a log-linear graph to determine if the behaviour was exponential. The two straight line fits in Figure 4.3a revealed that the data points were best modelled as two separate exponential functions, as determined by the gradient of the two straight lines. From this observation an empirical formula was derived and compared to the ANSYS model. All three curves showed a good agreement, as given in Figure 4.3b, and confirmed that the more computationally convenient empirical formula was a good approximation to the magnetic field.

In the region of interest, which was within a distance of $d_m = 10$ mm to $d_m = 16$ mm away from the magnet surface, the flux density was found to drop from 70 mT to



(a) (b)

Figure 4.3: Characterization of the magnetic flux density of a N42 Neodymium bar magnet (42 × 8 × 10 mm) in logarithmic and linear form. (a) The flux density measurement is fitted with two individual exponential curves and plotted on a logarithmic scale. (b) The flux density measurement is compared to the ANSYS simulation and a fitted function with two exponential terms and plotted on a linear scale. The measurement is taken along the centre line of the magnet, starting at the surface of the magnet to 48 mm away, with a step size of 0.1 mm. The error bars are calculated by taking the standard deviation of 14 independent measurements at specific distances away from the magnet surface.

38 mT and the corresponding flux gradient was found to change from 8.3 mT/mm to 3.4 mT/mm, respectively. Within this region of interest, the fitted exponential curve was a good approximation to the measurements, as shown in Figure 4.4. The difference between the measurement and the fitted line in the area of interest was found to be no more than 0.6%. The different positions of interest are labelled with A, B, C and D. The labels correspond to $d_m = 10$ mm, $d_m = 12$ mm, $d_m = 14$ mm and $d_m = 16$ mm, respectively.

Ideally, the magnetophoretic driving force S (see Equation 2.34), which is the product of the magnetic $\mathbf{B}$ field and the field gradient $d\mathbf{B}/dx$, would be constant since this implies that the velocity of the magnetically attracted beads will be constant too. This was not possible with the setup used here, due to the shape and small size of the magnet. However, the magnetophoretic driving force could be approximated to be constant across the field of view (55 μm) since the maximum change in the

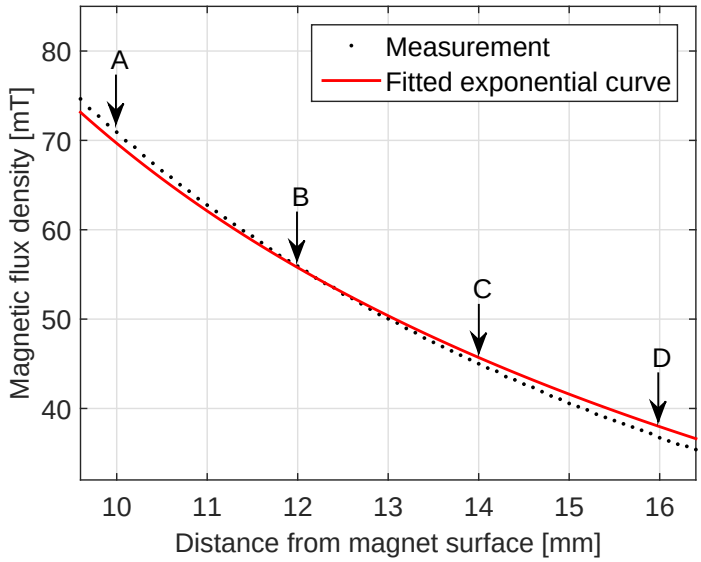


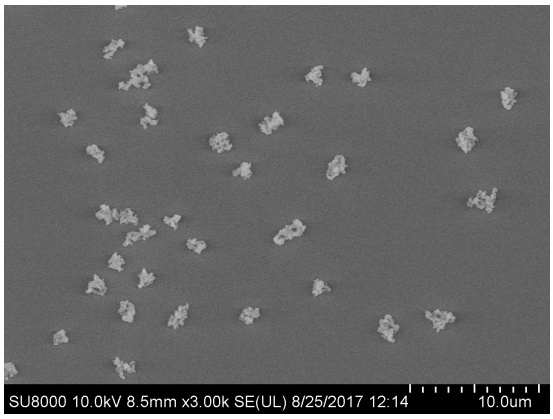
Figure 4.4: Characterization of the magnetic flux density of a N42 Neodymium magnet ($42 \times 8 \times 10$ mm) between 10 mm and 16 mm away from the magnet surface. The letters A, B, C and D indicate the positions at which the magnetophoretic velocity of the particles are measured. The four positions are equivalent to $d_m = 10$ mm, $d_m = 12$ mm, $d_m = 14$ mm and $d_m = 16$ mm, respectively.

magnetic field strength at the different magnet positions d_m was only 1.5%, and could thus be neglected.

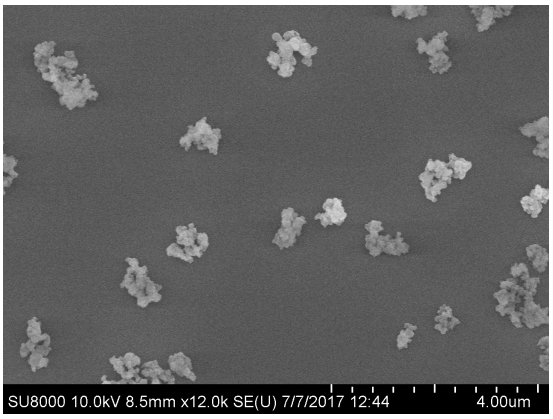
4.2.2 Size characterization of superparamagnetic beads

The magnetophoretic mobility highly depends on the particle size. Therefore, the superparamagnetic beads were all imaged using standard SEM techniques (see Section 3.2.1 in Chapter 3). The SEM images allowed for a clear inspection of the beads' shape and size distribution. Figure 4.5 shows SEM images of each of the bead types used in this thesis. Further SEM images of the different bead types can be found in Appendix A.

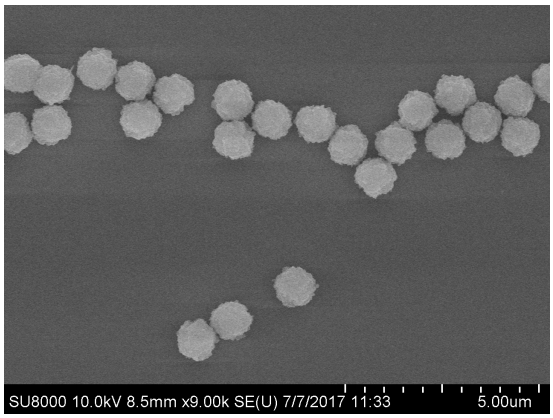
A clear visual difference between the two manufacturers can be seen in Figure 4.5. While all Dynabeads particles (see Figure 4.5c-4.5e) were approximately spherical in shape with a highly uniform size distribution, the Chemicell particles (see Fig-



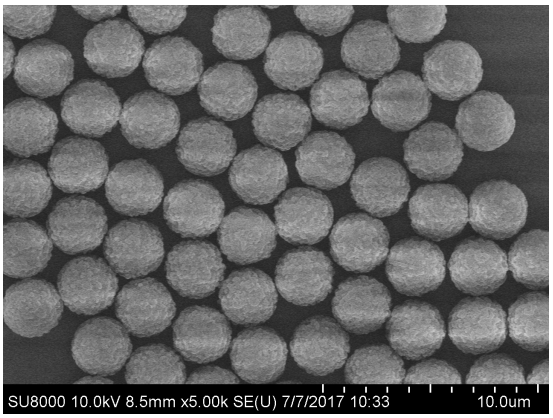
(a) Chemicell ScreenMAG



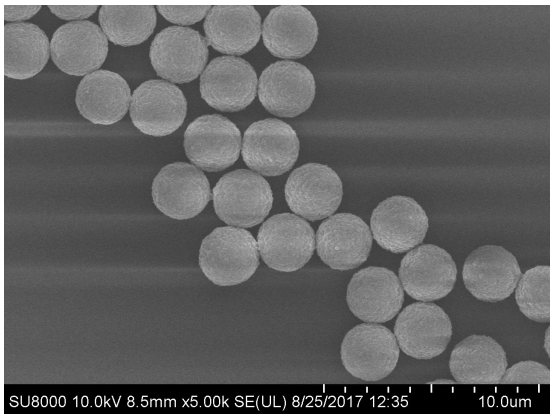
(b) Chemicell SiMAG



(c) Dynabeads MyOne



(d) Dynabeads M280



(e) Dynabeads M270

Figure 4.5: SEM images of superparamagnetic particles of different types and from different manufacturers. (a) and (b) show 1 μm sized ScreenMAG and SiMAG beads by Chemicell. (c), (d) and (e) show 1 μm MyOne, 2.8 μm M280 and 2.8 μm M270 Dynabeads, respectively, from Thermo Fisher Scientific. Note the irregular shape of the Chemicell beads compared to those supplied by Dynabeads.

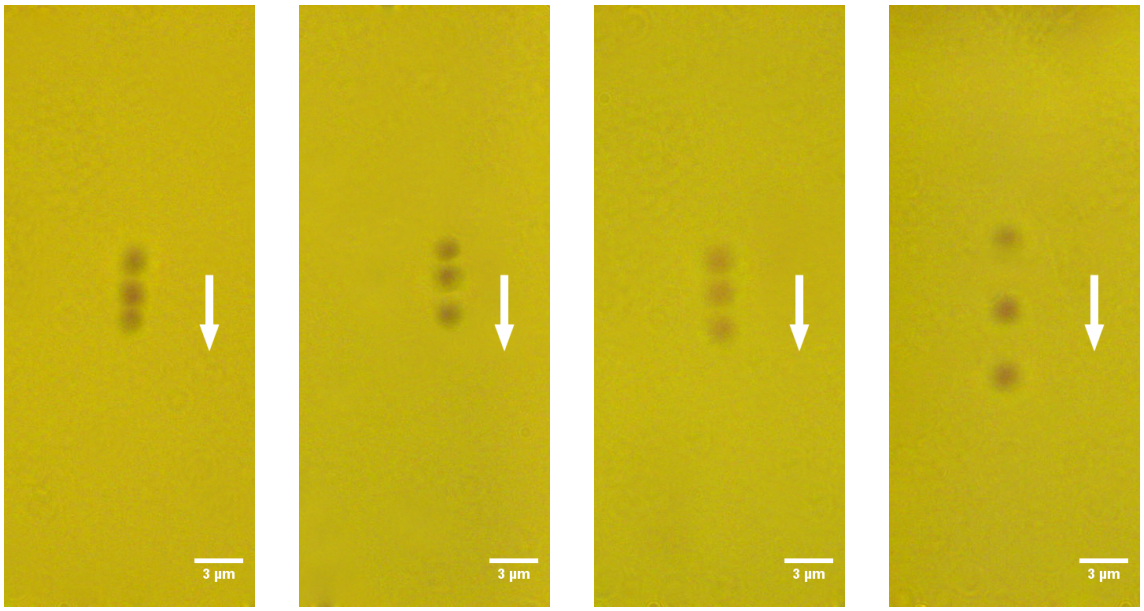
ure 4.5a-4.5b) did not show monodispersity nor did they have a spherical shape. Similar SEM images of Chemicell SiMAG particles can also be found in a paper by Herrasti et. al. [338]. In order to determine the mean diameter of the Chemicell particles, their size was measured using dynamic light scattering (DLS). The measured mean diameter and standard deviation of the particles are listed in Table 4.1. The measured values for the Dynabeads particles are consistent with those stated by the manufacturer and found in the literature [300, 326]. Additionally, Dynabeads particles showed a narrower size distribution compared to their Chemicell counterparts. The coefficient of variation of the measured size distribution of Dynabeads particles (see Table 4.1) was below the value given by the manufacturer, i.e. $< 3\%$ for the M280 and M270 beads and $< 5\%$ for the MyOne beads. The measured size variation for the Chemicell particles was 55% and 87% for ScreenMAG and SiMAG particles, respectively, i.e. higher than the $10\% - 20\%$ stated by Chemicell GmbH [336]. Measuring the diameter of the Chemicell particles, however, depends on the particle orientation in the DLS instrument due to their non-spherical shape. This may lead to a larger size variation.

4.2.3 Magnetically induced velocity on superparamagnetic beads

In Figure 4.6-4.10 the movement of the different bead types for all four magnet positions (A, B, C and D) is shown. The various pictures show a sequence of superimposed images of a single bead travelling towards the magnet. The direction of the particle movement is indicated by the arrow. The time interval, Δt_p, between each particle position was 0.3 s, except for the Chemicell's ScreenMAG particles where a larger interval of 0.6 s was chosen due to their lower mobility. These time intervals allowed a clear visualization of the different bead positions in a weak magnetic field, while keeping the particles within the viewing region at stronger

magnetic fields.

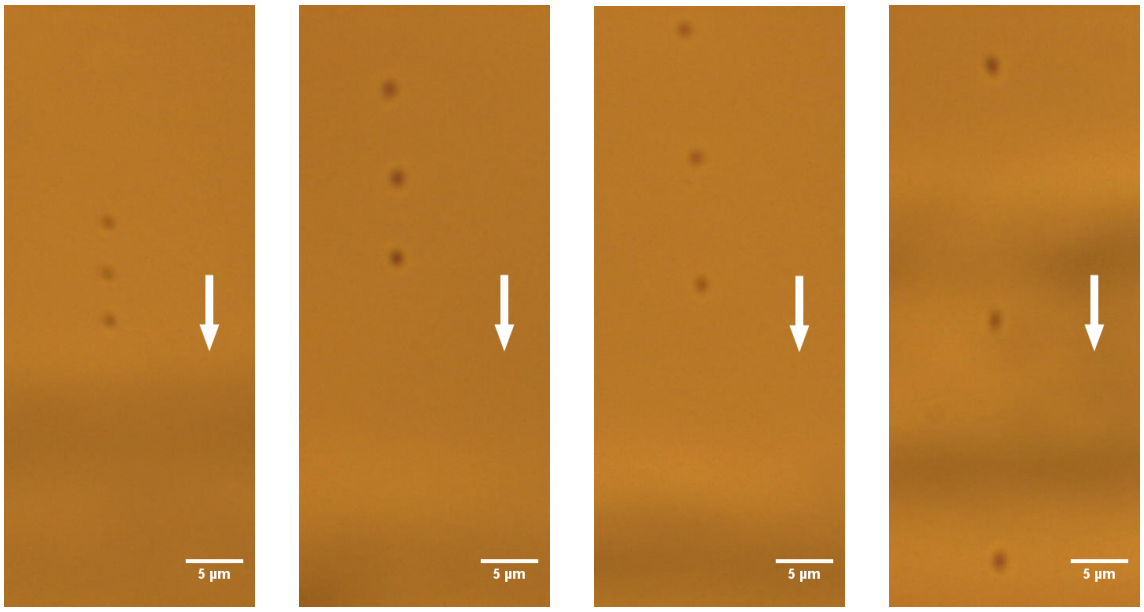
It can be seen, that the beads travelled larger distances in equal time intervals as they got closer to the magnet (d_m decreased). All beads were equidistant for the given time interval and discrete magnet position, which confirmed the assumption that the change in the magnetic field across the field of view of the microscope (55 μm) could be neglected.



(a) Position: D (b) Position: C (c) Position: B (d) Position: A

Figure 4.6: Image superposition of the magnetically induced velocity of Chemicell's ScreenMAG beads measured at discrete distances away from the magnet. The time interval between different superimposed images was 0.6 s. The distance between the magnet and the observation chamber was incrementally reduced (from left to right) to d_m = 16 mm, d_m = 14 mm, d_m = 12 mm and d_m = 10 mm. These distances corresponded to the four magnet position D, C, B and A, respectively. At each magnet position, the same bead was being tracked, but varied between magnet position.

Figure 4.11 shows the magnetically induced drift velocities of the five bead types at the discrete magnet positions A, B, C and D plotted against the distance to the magnet surface d_m. For comparison, the five bead types ScreenMAG, SiMAG, MyOne, M280 and M270 experienced a gravity induced velocity of 0.2 μm/s, 0.5 μm/s, 0.3 μm/s, 1.8 μm/s and 2.1 μm/s, respectively. On average, the magnetically



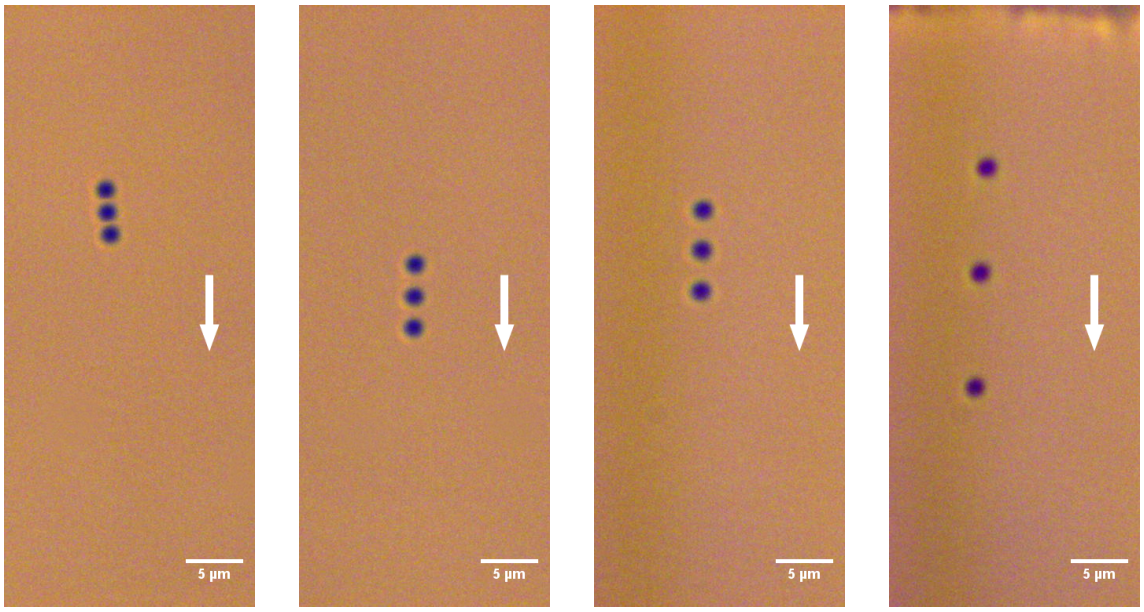
(a) Position: D (b) Position: C (c) Position: B (d) Position: A

Figure 4.7: Image superposition of the magnetically induced velocity of Chemicell's SiMAG beads measured at discrete distances away from the magnet. The time interval between different superimposed images was 0.3 s. The distance between the magnet and the observation chamber was incrementally reduced (from left to right) to $d_m = 16$ mm, $d_m = 14$ mm, $d_m = 12$ mm and $d_m = 10$ mm.

induced drift velocity was at least one order of magnitude larger than the gravity induced velocity. As also seen in Figure 4.6-4.10, the particles' velocity increased when moving the magnet closer.

The magnitude of the magnetophoretic mobility, ν_p, was calculated according to Equation 2.33. The magnetophoretic driving force at the various positions of the magnet was estimated by using the fitted exponential curve to the measured magnetic flux density. The magnetic mobilities of each bead type was determined for the discrete magnet positions (A, B, C and D) and are depicted in Figure 4.12.

Despite the fact that the drift velocity in Figure 4.11 showed an increase as the magnetic microparticles approached the magnet, their mobility in Figure 4.12 appeared to be less sensitive to distance d_m from the magnet and one can assume that the beads did not reach their magnetic saturation (see Figure 4.16 in Section 4.4). Figure 4.13 shows the histograms of the measured mobilities for all particle types.



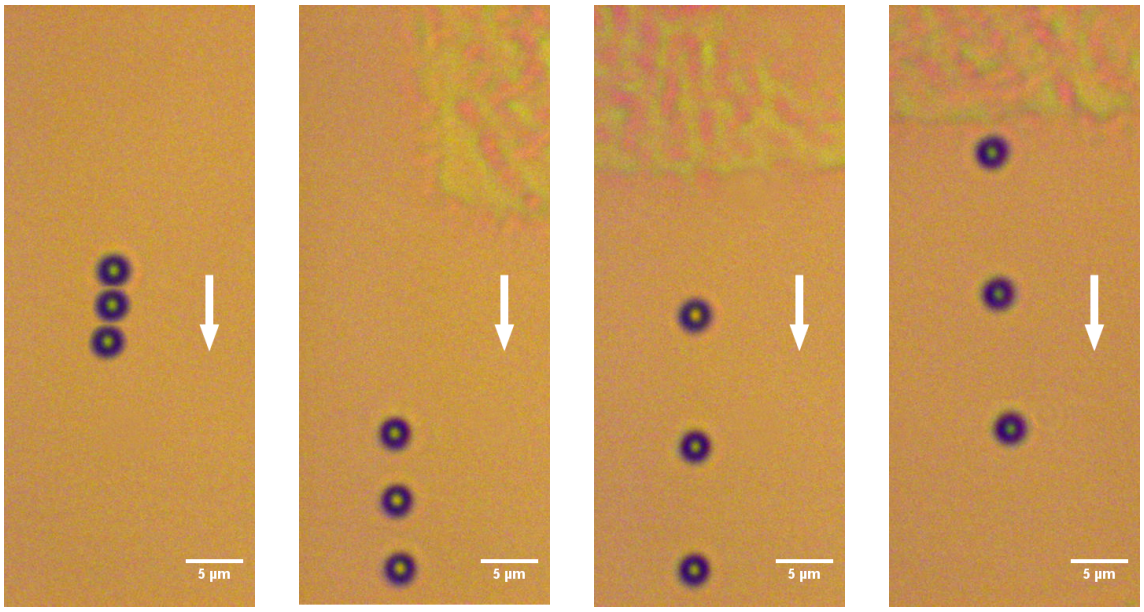
(a) Position: D (b) Position: C (c) Position: B (d) Position: A

Figure 4.8: Image superposition of the magnetically induced velocity of Dynabeads' MyOne beads measured at discrete distances away from the magnet. The time interval between different superimposed images was 0.3 s. The distance between the magnet and the observation chamber was incrementally reduced (from left to right) to $d_m = 16$ mm, $d_m = 14$ mm, $d_m = 12$ mm and $d_m = 10$ mm.

Except for Dynabeads' M270 (Figure 4.13e), all histograms have a clearly defined peak, but they also show a large variance in magnetic mobility. The averaged magnetophoretic mobilities for each of the five bead types, as well as their averaged particle diameter, was used to derive the magnetic susceptibility, tabulated in Table 4.2.

4.3 Magnetophoretic mobility of superparamagnetic bead agglomerates

As soon as superparamagnetic microparticles are exposed to an external magnetic field they become magnetized, which causes them to form chains if they are in close proximity to each other. This chain formation could be seen during the magnetophoretic mobility study of single beads described in the previous section (see



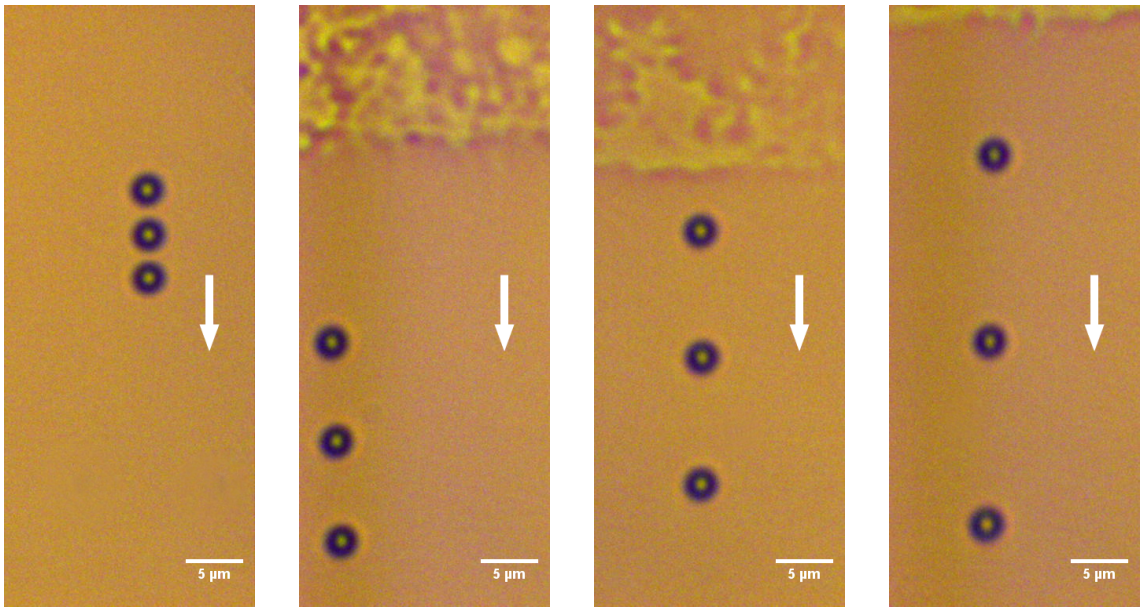
(a) Position: D (b) Position: C (c) Position: B (d) Position: A

Figure 4.9: Image superposition of the magnetically induced velocity of Dynabeads' M280 beads measured at discrete distances away from the magnet. The time interval between different superimposed images was 0.3 s. The distance between the magnet and the observation chamber was incrementally reduced (from left to right) to $d_m =$ 16 mm, $d_m = 14$ mm, $d_m = 12$ mm and $d_m = 10$ mm.

Section 4.2). These bead agglomerations have a different magnetophoretic mobility compared to single beads due to their increased magnetic force and change in Stokes' drag. The change in mobility also has an effect on the magnetic separation process and thus needs to be treated differently in magnetic separation simulations that consider agglomerates.

Chains of magnetic beads are evaluated for their velocity as they pass through the observation chamber. As the chains self-assemble along the direction of the magnetic field lines, it is possible to establish drift with either orientation of the chain, by using a different configuration of the permanent magnet.

The orientation of the chain is in the same direction as the pole axis of the magnet and the magnetic field lines, but drift is in the direction of increasing magnetic energy density, i.e. towards the magnet. The magnetic field lines and magnetic energy density gradient do not necessarily point in the same direction, as illustrated



(a) Position: D (b) Position: C (c) Position: B (d) Position: A

Figure 4.10: Image superposition of the magnetically induced velocity of Dynabeads' M270 beads measured at discrete distances away from the magnet. The time interval between different superimposed images was 0.3 s. The distance between the magnet and the observation chamber was incrementally reduced (from left to right) to $d_m =$ 16 mm, $d_m = 14$ mm, $d_m = 12$ mm and $d_m = 10$ mm.

in Figure 4.14.

The hydrodynamic drag force on a chain depends on its length and orientation. The hydrodynamic resistance of elongated bodies, however, is more complicated to determine than for a simple sphere. No exact solutions for bead chains have been reported in the microfluidic literature to the author's knowledge and therefore approximate methods were employed here for elongated bodies. Since the hydrodynamic drag mainly depends on the body aspect ratio or, in this case the number of beads, the chain of beads moving in axial or lateral direction in low Reynolds number flow can be adapted as a longitudinal elliptic body, with a circular cross-section equal to the diameter of the spherical bead, $2r_p$, and the long axis equal to the length of the number of beads in the chain, $n \times 2r_p$. Using this approximation the hydrodynamic resistance acting on a chain of particles moving in parallel or orthogonal to its long

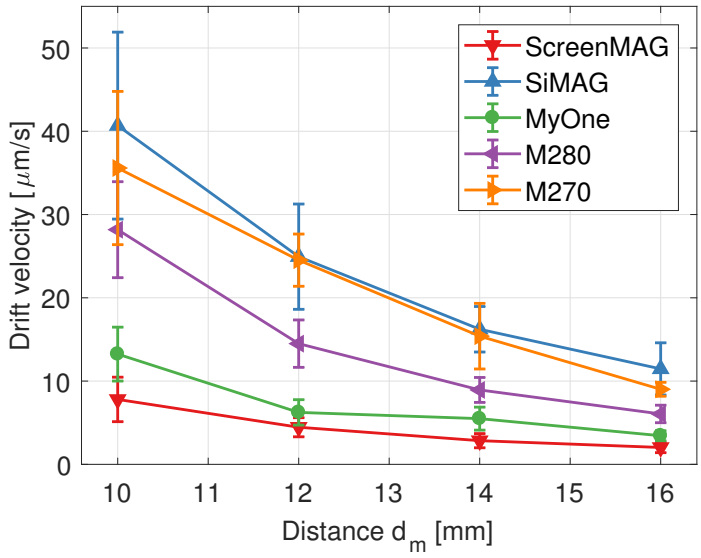


Figure 4.11: Magnetically induced drift velocities of each of the five investigated bead types measured at four different distances d_m from the magnet face.

axis can be approximated as follows [276, 339]:

$$F_{\parallel} = 4\pi\eta_f r_p u \left[\frac{n^2-1}{\left(\frac{2n^2-1}{\sqrt{n^2-1}}\right) \cdot \ln\left(n+\sqrt{n^2-1}\right) - n} \right] \tag{4.1}$$

$$F_{\perp} = 8\pi\eta_f r_p u \left[\frac{n^2-1}{\left(\frac{2n^2-3}{\sqrt{n^2-1}}\right) \cdot \ln\left(n+\sqrt{n^2-1}\right) + n} \right] \tag{4.2}$$

where $F_{\parallel}$ and $F_{\perp}$ describe the drag force of the chain when its long axis is aligned

Table 4.2: The experimentally found mean magnetophoretic mobility ($\bar{\nu}_p$) and average susceptibility ($\bar{\chi}_p$) obtained for the five observed types of superparamagnetic microparticles using magnetophoresis. Experiments were performed in deionized water over a magnetic field range of 38 mT to 70 mT.

Particle type	Number of particles analysed	$\bar{\nu}_p$ [mm^3/T·A·s]	$\bar{\chi}_p$ [−]
ScreenMAG	238	0.017 ± 0.01	0.51 ± 0.11
SiMAG	359	0.091 ± 0.03	1.53 ± 0.56
MyOne	46	0.028 ± 0.01	0.46 ± 0.13
M280	248	0.053 ± 0.01	0.12 ± 0.02
M270	92	0.082 ± 0.02	0.19 ± 0.04

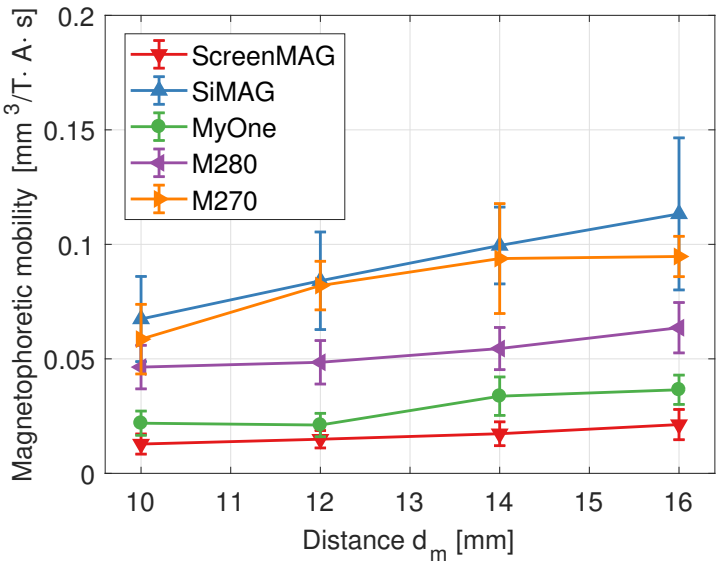
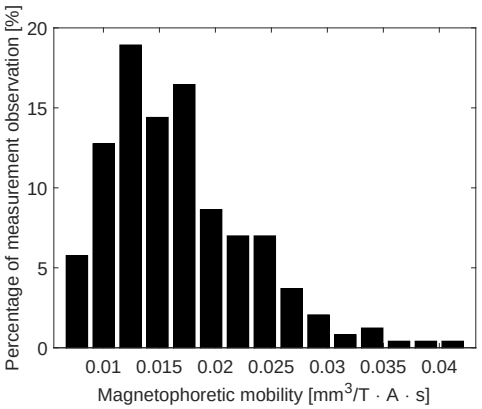


Figure 4.12: Magnetophoretic mobility of each of the five investigated bead types measured at four different distances d_m from the magnet face (10 mm, 12 mm, 14 mm and 16 mm).

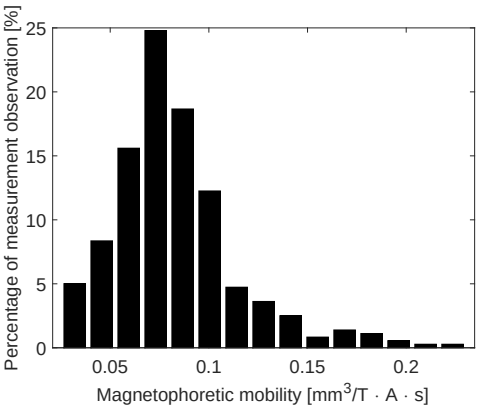
in parallel or orthogonally to its moving direction, respectively. The parameter η_f describes the dynamic viscosity of the fluid. The two equations above, Equation 4.1 and Equation 4.2, only apply for $n \geq 2$.

By using Equation 4.1 or Equation 4.2 in the proposed magnetophoresis model one can estimate the magnetophoretic mobility of chains with different lengths. In a first approximation, it was assumed that the total magnetic moment of a chain is given by the summation of all magnetic moments of the beads in the chain. In other words, dipole interaction between neighbouring beads was considered to be negligible compared to changes in the drag force.

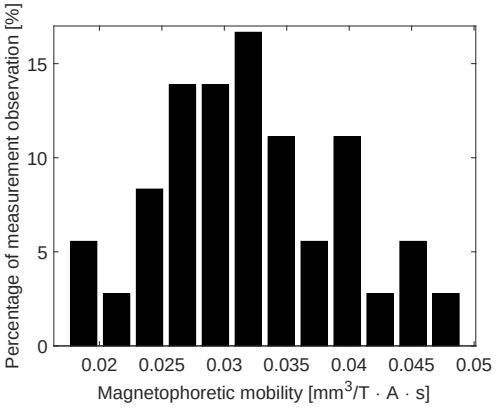
In order to explore the effect of Stokes' drag upon the mobility of chains of microbeads and to demonstrate the models proposed, two magnetic orientation configurations were investigated experimentally. Videos of beads that had formed chains were recorded and their magnetically induced velocity was measured. The bead concentration was increased (1.8×10^7 beads/ml) compared to the measurements aiming to study isolated beads in order to increase the number of agglomeration



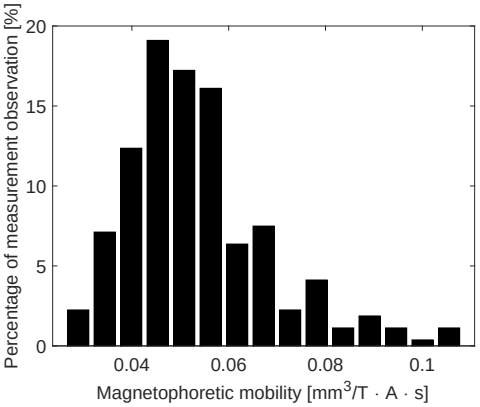
(a) Chemicell ScreenMAG



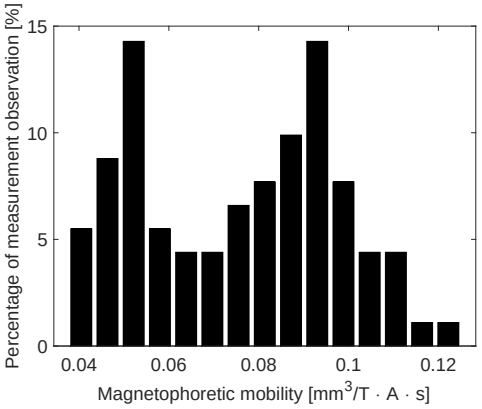
(b) Chemicell SiMAG



(c) Dynabeads MyOne

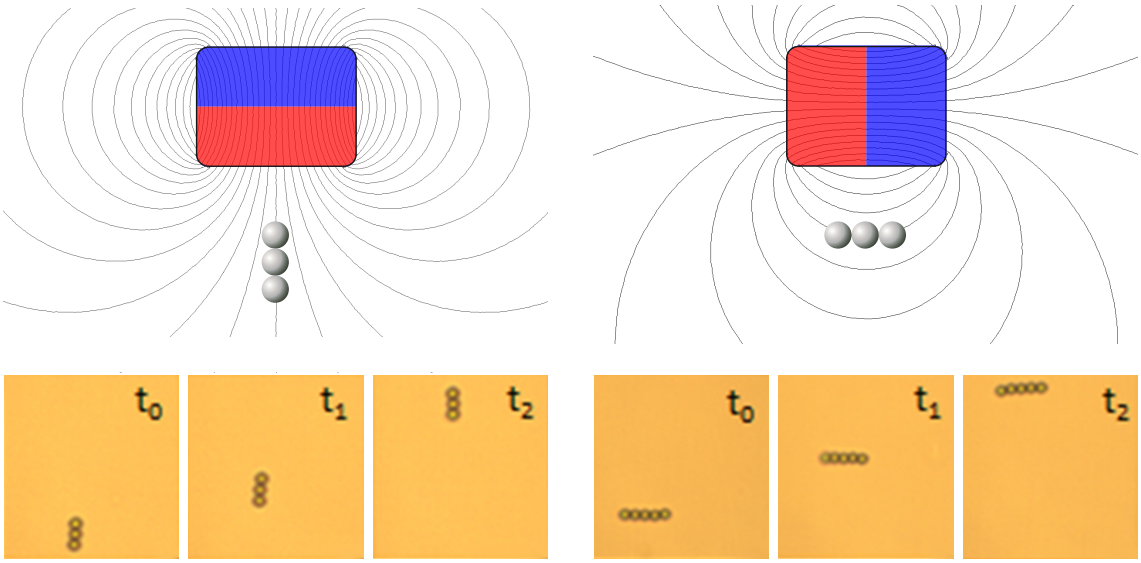


(d) Dynabeads M280



(e) Dynabeads M270

Figure 4.13: Histogram of the magnetophoretic mobility distribution of the five investigated bead types. The histograms show the mobility distribution of all bead measurements taken at A, B, C and D. The number of observations vary for the different bead types, see Table 4.1. The medians of the distributions is estimated at 0.017 $\mathrm{mm}^3/\mathrm{T}\cdot\mathrm{A}\cdot\mathrm{s}$, 0.091 $\mathrm{mm}^3/\mathrm{T}\cdot\mathrm{A}\cdot\mathrm{s}$, 0.028 $\mathrm{mm}^3/\mathrm{T}\cdot\mathrm{A}\cdot\mathrm{s}$, 0.053 $\mathrm{mm}^3/\mathrm{T}\cdot\mathrm{A}\cdot\mathrm{s}$ and 0.082 $\mathrm{mm}^3/\mathrm{T}\cdot\mathrm{A}\cdot\mathrm{s}$ for the ScreenMAG, SiMAG, MyOne, M280 and M270 particle type, respectively.



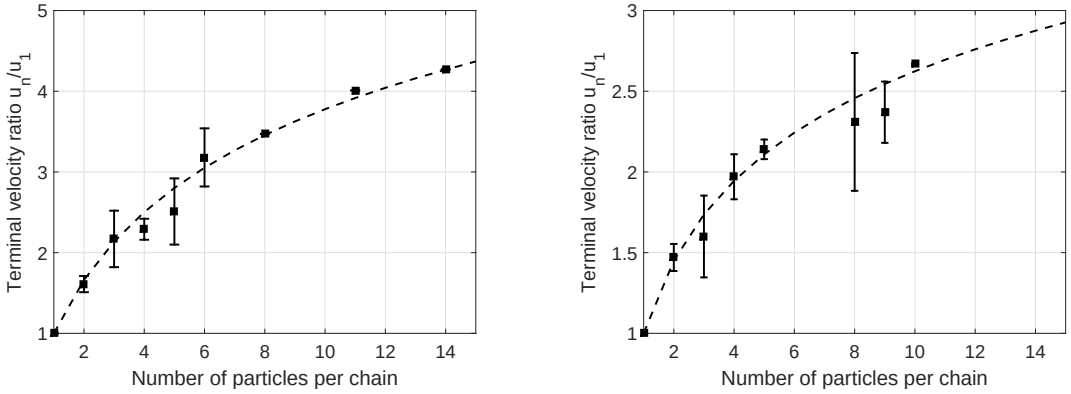
(a) Parallel alignment (b) Perpendicular alignment

Figure 4.14: A schematic and photographs of magnetic bead agglomerates travelling towards a permanent magnet. In configuration (a) the magnetic field lines are parallel to the direction of the magnetically induced velocity. Bead chains are formed along the direction of the magnetic field lines and the chain drifts in the direction of increasing magnetic energy density. In configuration (b) the long axis of the magnet is rotated by 90 degrees, perpendicular to the observation chamber, and the magnetic pole axis is rotated. The field lines and travelling velocity are perpendicular to each other. The microbead chains form along the magnetic field lines but drift orthogonally to the long axis of the chain. The sequential images at the bottom of (a) and (b) show a bead chain at three time intervals ($t_0 < t_1 < t_2$) travelling towards the magnet.

examples.

To compare the mobility of chains of different length with the model described above it was sufficient to only consider a normalized terminal velocity. The normalized velocity was obtained by dividing the chain velocity by the magnetic drift velocity of a single bead. Due to this normalization the different bead types, given in Table 4.1, could be directly compared to each other.

Figure 4.15 shows the experimental data compared to the model for both magnet orientations, and confirms that the longitudinal elliptical body approximation is a sufficiently accurate predictor of the drift velocity for chains of different bead lengths.



(a) Parallel alignment (b) Perpendicular alignment

Figure 4.15: The normalized ratio of the magnetophoretically induced velocity per chain of magnetic beads to the magnetophoretically induced velocity of a single magnetic bead travelling towards a magnet (a) parallel and (b) perpendicular to the field lines. The dotted curves represent the data calculated from the proposed model.

Table 4.3 lists the number of chains observed for each chain length. The longer the chain the smaller the number of observations since chains of longer length occurred less often.

Table 4.3: Number of chain observations for each integer chain length.

Chain length	Parallel alignment	Perpendicular alignment	Chain length	Parallel alignment	Perpendicular alignment
1	84	11	8	1	7
2	29	8	9	0	3
3	22	8	10	0	1
4	9	8	11	1	0
5	5	7	12	0	0
6	3	0	13	0	0
7	0	0	14	1	0

4.4 Magnetization of superparamagnetic beads

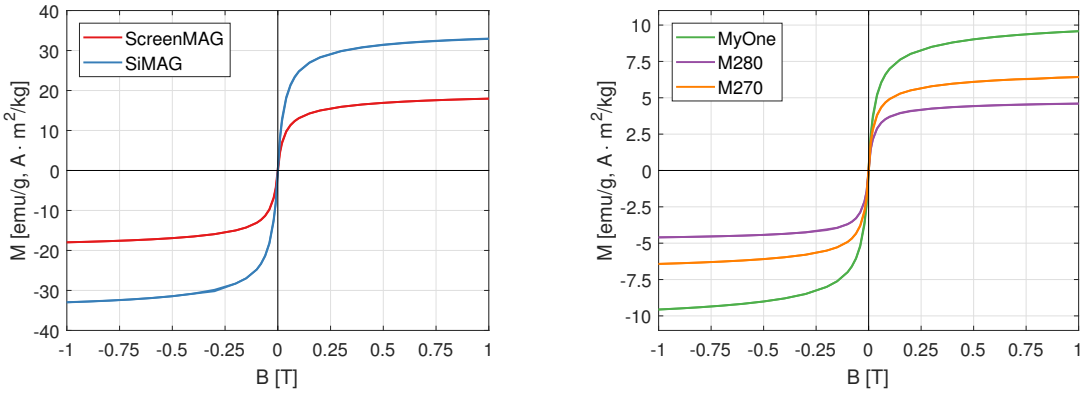
In order to obtain independent and consistent magnetic information for all bead types given in Table 4.1, their magnetization curve was measured using a SQUID.

The SQUID has become a widely used instrument for determining moment of magnetization as a function of an externally applied magnetic field and is also used for studying the magnetic properties of superparamagnetic particles such as the magnetic susceptibility and saturation magnetization [290]. The SQUID relaxometry technique and the apparatus used for the measurements reported have been described in detail in other literature [290, 340, 341]. Thus, only a brief explanation is given here. The SQUID sensor measures the magnetic moment by magnetizing the sample using an applied magnetic field pulse ranging from -5 T to 5 T in amplitude and with a frequency of $0.5 - 4$ Hz. Further details of the use of the SQUID sensor and sample preparation is given earlier in Section 3.6.

Figure 4.16 and Figure 4.17 show the hysteresis loops for the different bead types for various applied magnetic fields, ranging from ± 75 mT up to ± 1 T. The hysteresis loops directly give the magnetization of each of the five types of beads at a specific applied magnetic field and incorporate all magnetic properties of the bead sample. From these curves the saturation magnetization, M_S, as well as the remanence, M_R are estimated. Additionally, the magnetic susceptibility of the bead sample, χ, can be obtained by taking the ratio of the sample magnetization and the applied magnetic field. In the magnetization study the subscript p in the susceptibility parameter χ is dropped, since the magnetic response is measured not only on a single bead but rather on a sample which contains a large number of beads.

Figure 4.16 shows that the samples started saturating at a magnetic flux density of ≈ 0.1 T. The difference in saturation magnetization for each type originates from the different iron oxide content.

In order to get a more accurate resolution at a lower flux density range, another set of hysteresis loops was recorded, where the applied magnetic flux density reached from -75 mT to 75 mT, as shown in Figure 4.17a-4.17b. This range was chosen because the beads in the mobility study described above (see Section 4.2.3) were



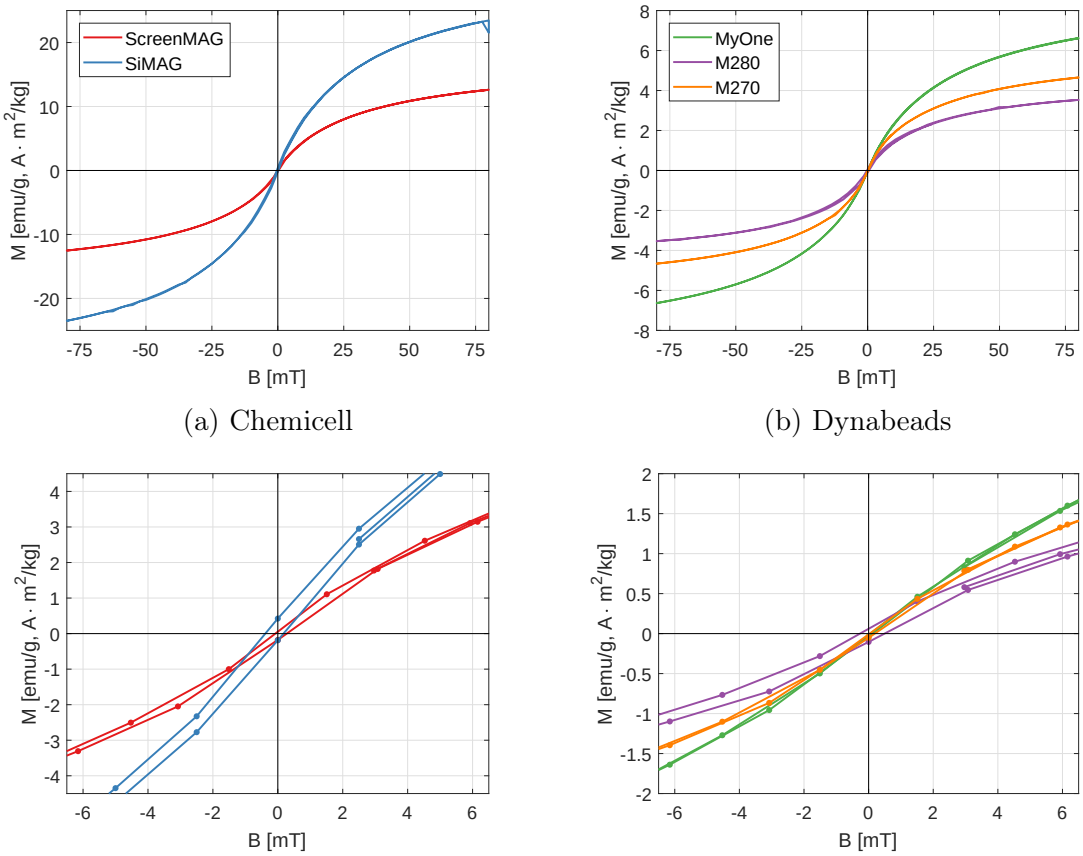
(a) Chemicell (b) Dynabeads

Figure 4.16: Magnetization curves of the different bead types within an applied magnetic field range of ±1 T. (a) Magnetization curves of Chemicell bead types. (b) Magnetization curves of Dynabeads bead types. The curves were measured with a Quantum Design MPMS-XL SQUID magnetometer at room temperature (300 K).

also exposed to the same magnetic flux densities.

In Figure 4.17c and Figure 4.17d a closer view of the same magnetization curves presented in Figure 4.17a and Figure 4.17b is shown, where the magnetic field range was ±6 mT. From these figures, the remanence was observed to be no more than 953 A/m, which is a value comparable to what is found in the literature; i.e. Shevkoplyas *et al.* [212] or Hien *et al.* [342]. It was assumed that the SQUID system had no significant measurement offset, such that the values obtained for sample remanence are reliable. To verify this assumption, an empty sample (i.e. air) was measured for the purpose of calibration. The hysteresis loop of the *air* sample is shown in Figure 4.18. One can see that the magnetic response was of the order of $O(10^{-5})$, i.e. at least five orders of magnitude smaller than the magnetic response of the bead samples. Therefore, the impact of potential offset errors when determining remanence of the beads could be neglected.

Magnetic remanence stems from thermally blocked magnetic moments of the incorporated iron oxide nano-sized particles [300]. Research papers on magnetic separation frequently discard the remanence of the magnetic particles, because its value



(a) Chemicell (b) Dynabeads

(c) Chemicell (d) Dynabeads

Figure 4.17: Magnetization curves of the five different bead types. The curves were measured with a Quantum Design MPMS-XL SQUID magnetometer at room temperature (300 K). (a) Magnetic response of the Chemicell particles in applied magnetic fields ranging from ±75 mT. (b) Magnetic response of the Dynabeads particles in applied magnetic fields ranging from ±75 mT. (c)-(d) Magnified view of the magnetization curves ranging from −6 mT to 6 mT.

is assumed to be significantly smaller than the applied magnetic field. However, not taking remanence into account may compromise the susceptibility parameter as concluded by Shevkoplyas et. al. [212]. Using all data points along the hysteresis loop to determine the susceptibility as a function of the applied magnetic field takes all magnetic parameters and conditions into account, including remanence.

Using the measured hysteresis loops given in Figure 4.17 the susceptibilities were determined at four different magnetic fields over the range of $38 - 70$ mT, corresponding to the magnetic flux density at positions A, B, C and D of the mobility

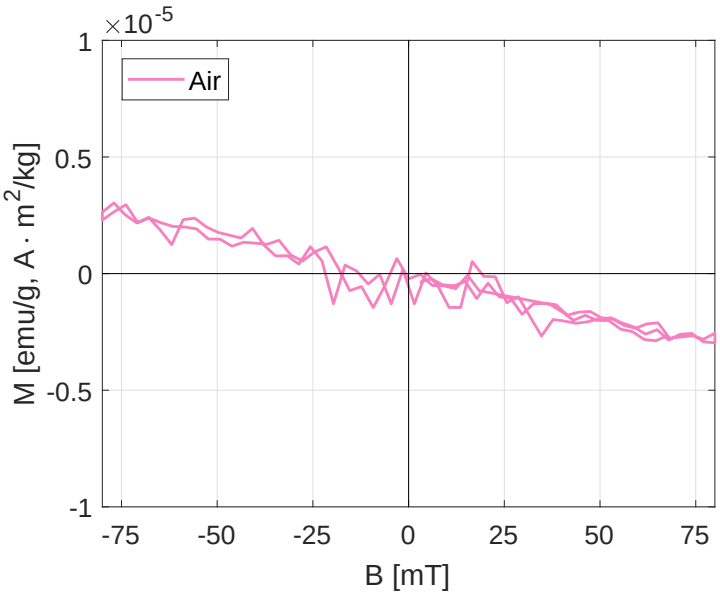


Figure 4.18: Magnetization curve of an air filled sample in the range of ±75 mT. Air shows a diamagnetic behaviour with no remanence. This calibration measurement confirms that the measured remanence of the magnetic bead is no artefact.

measurement for single beads reported in Section 4.2. From these four values the mean was calculated for comparison with the average susceptibility values reported in Table 4.2. The magnetic properties such as susceptibility and the saturation magnetization, obtained from the SQUID data are summarized in Table 4.4.

Table 4.4: Measured magnetic susceptibility of the different bead types using SQUID.

Particle type	M_R [emu/g] ($\lvert\mathbf{B}\rvert \approx 0$ T)	M_S [emu/g] ($\lvert\mathbf{B}\rvert \geq 1$ T)	$\bar{\chi}$ [−] ($\lvert\mathbf{B}\rvert < 70$ mT)
ScreenMAG	0.05	19.2	0.66 ± 0.12
SiMAG	0.42	34.7	1.22 ± 0.21
MyOne	0.02	10.1	0.27 ± 0.06
M280	0.06	4.7	0.12 ± 0.02
M270	0.01	6.9	0.18 ± 0.04

The mean susceptibility values and the saturation magnetization found here, compare well with the results found in Section 4.2 and also what has been stated in the literature [300–302, 331]. Additionally, they show that the magnetophoretic mobility

measurement is a promising technique to determine the susceptibility of magnetic particles.

4.5 Comparison of the susceptibility based on the mobility and magnetization study

Two independent results for the susceptibility of the magnetic particles were obtained by the two studies described in Section 4.2 and Section 4.4.

Figure 4.17 reveals that assuming a linear relationship between magnetization and applied field is only a simplified model, even at weak magnetic fields. The observed monotonic increase in magnetophoretic mobility with increasing distance from the magnet (see Figure 4.12) implies that the mobility is a function of the externally applied magnetic field due to the susceptibility dependence. This dependence is not accounted for in a simplified model, where the susceptibility is assumed constant, and in some circumstances might need to be taken into consideration. Table 4.5 and Table 4.6 compare the different susceptibilities for both measurement approaches at all four magnet positions A, B, C and D. It can be seen that for every bead type the susceptibility increased when the magnetic field decreased, which is equivalent to moving from magnet position A to magnet position D.

The susceptibility values of the two measurement approaches (magnetophoresis and SQUID) were compared pairwise at each magnetic field strength. In Table 4.5 and Table 4.6 it can be seen that most susceptibility values were within one standard deviation of the values obtained by the magnetophoresis study at the same B-field. This suggests that the samples are from a population with similar mean. However, the susceptibility values of the MyOne beads consistently overestimated the susceptibility by more than one standard deviation compared to their corresponding values from the SQUID measurement. In order to have reliable susceptibility esti-

Table 4.5: Measured bead susceptibility obtained from the magnetophoretic mobility study (Section 4.2). For each bead type, four susceptibility values for different magnetic fields are listed. The magnetic fields correspond to the four observed magnet positions A, B, C and D, or equivalently to a distance 10 mm, 12 mm, 14 mm and 16 mm away from the magnet surface, respectively. Additionally, one standard deviation of the observed measurements is given. $\bar{\chi}_p$ indicates that the values are averaged over all particle measurements at a specific location.

Bead type	$\bar{\chi}_p$			
	70 mT	56 mT	46 mT	38 mT
ScreenMAG	0.39 ± 0.13	0.45 ± 0.12	0.53 ± 0.16	0.65 ± 0.20
SiMAG	0.98 ± 0.27	1.22 ± 0.31	1.44 ± 0.24	1.64 ± 0.48
MyOne	0.34 ± 0.09	0.33 ± 0.08	0.54 ± 0.14	0.58 ± 0.10
M280	0.11 ± 0.02	0.11 ± 0.02	0.13 ± 0.02	0.15 ± 0.03
M270	0.14 ± 0.04	0.19 ± 0.03	0.21 ± 0.06	0.22 ± 0.02

Table 4.6: Measured particle susceptibility obtained from the magnetization study (Section 4.4). The susceptibility is measured at four different magnetic fields for each bead type, similar to Table 4.5.

Bead type	χ			
	70 mT	56 mT	46 mT	38 mT
ScreenMAG	0.52	0.62	0.71	0.81
SiMAG	0.96	1.14	1.31	1.48
MyOne	0.22	0.26	0.30	0.34
M280	0.09	0.11	0.13	0.15
M270	0.14	0.16	0.19	0.22

mates, more beads would need to be observed. The comparison of the susceptibility values of the two measurement approaches made it evident that the CTV system is a sensitive approach to determine the susceptibility of magnetic beads within an environment (i.e. fluidic channel) relevant to their intended application.

Across all particle types, an increase in susceptibility could be seen when decreasing the magnitude of the magnetic field. The observed increase in susceptibility, however, could be due to simple statistical variation. Therefore, the change in susceptibility at each magnet position would need to be tested for significance.

In order to compare the four measured susceptibility values of one particle type with each other, two approaches were used. The first analysis tested whether or not there was a significant change in susceptibility using an analysis of variance (ANOVA). The second analysis tested for the likelihood of susceptibility being constant by applying a regression analysis. Additionally, a scaling analysis was performed in Section 4.5.3 to see the impact of the various parameters influencing the particle's mobility and to compare the simplified model, where the susceptibility was assumed constant with a variable susceptibility model.

4.5.1 Analysis of variance

A difference between the mean susceptibility of magnetic beads in varying magnetic fields was observed. The aim of the experiments described in this section was to determine if these differences in susceptibility within each bead type were statistically significant. In order to test for equality of the measured susceptibility means, a balanced one-way analysis of variance test was performed on the data of the magnetophoresis study (see Section 4.2.3). The null hypothesis of the test assumed that all measured susceptibility means at the four magnet positions and within each bead type are equal at a significance level of 5%. The alternative hypothesis assumed that at least one susceptibility mean was different from the others. Whenever more than two sample populations are compared, the ANOVA test is a more conservative approach, as it results in fewer false positives (Type I error) compared to multiple two-sample t-tests. The ANOVA test assumes a normal distribution of the different sample groups [343].

The p-values of the analysis were all in the order of $O(10^{-7})$ or less (p-value $\leq 7.6 \times 10^{-7}$); this suggests a rejection of the null hypothesis for all particle types. In general, the low p-value implies that at least one mean value differs from the others but no information on which one. In order to determine which pairs of suscepti-

bility means were statistically significantly different, the confidence intervals of the different susceptibility sample groups had to be compared. Figure 4.19 shows the box plot diagrams for all five bead types where the notches (angled lines) represent the upper and lower bound of the 95% confidence interval. If the notches of the different boxes are not overlapping, one can conclude with 95% confidence that the true medians do differ.

In most cases, as seen in Figure 4.19, the confidence intervals did not overlap when comparing two successive susceptibility values, e.g. $\bar{\chi}_p^A$ with $\bar{\chi}_p^B$ or $\bar{\chi}_p^B$ with $\bar{\chi}_p^C$. This implies that the two susceptibility values do not significantly differ and the null hypothesis is accepted. However, when comparing $\bar{\chi}_p^A$ with $\bar{\chi}_p^D$ all bead types showed a statistically significant difference, which means the null hypothesis was rejected in favour of the alternative hypothesis. Therefore, the detected increase of the beads' susceptibility is with 95% certainty due to the change in susceptibility when the beads are exposed to a weaker magnetic field and not simply a statistical phenomena.

4.5.2 Regression analysis

In this analysis two models, a linear model and a constant, are fitted to the measured susceptibility data using an ordinary least square regression. This way it is possible to see if an increasing trend in susceptibility is more likely compared to a constant susceptibility. Figure 4.20 shows the two fitted models for all bead types.

Considering Figure 4.20, the linear model (green lines) more accurately captures the trend of the increasing susceptibility when the distance to the magnet surface, d_m, in the magnetophoresis study is increased. In order to confirm this, the residuals of both regressions were plotted on a normal probability plot, as shown in Figure 4.21. The residuals deviated more strongly from a normal distribution for the constant susceptibility model than for the linear model. This does, by no means, imply

that the linear model is the correct model to use in order to predict the particles' susceptibility at weak magnetic fields, but it is a strong indication that the positive trend of the susceptibility is not just an *artefact* of the large variation of measured magnetophoretic mobilities.

4.5.3 Numerical scaling analysis

Based on Equation 2.32 it is intuitive that r_p, χ_p, η and $\mathbf{H}$ or $\mathbf{B}$ all influence the magnetically induced velocity.

If the bead is sufficiently far away from the magnet, meaning d_m is large compared to the relevant magnet dimension, the magnetic field can be approximated as $\mathbf{H} \approx l_m w_m h_m M/d_m^3$. Thus, the derivative of $\mathbf{H}^2$ with respect to d_m can be approximated as $\frac{d\mathbf{H}^2}{dx} \approx (l_m w_m h_m M)^2/d_m^7$.

By multiplying the induced drift velocity described in Equation 2.32 with $\Delta t_p/r_p$ one obtains a dimensionless normalized travelling distance $\hat{X}_p$ for a certain time interval Δt_p. The travelling distance is scaled by the bead radius and can also be expressed as a linear function, using a dimensionless design parameter, Θ:

$$\hat{X}_p = |\mathbf{u}_p| \times \frac{\Delta t_p}{r_p} = \kappa\Theta \tag{4.3}$$

where κ is a dimensionless scaling constant and the design parameter, Θ, can be described as follows, using the analytical expression for the magnetic field described above:

$$\Theta = \frac{\mu_0 \chi_p V_p \Delta t_p}{12\pi\eta r_p^2} \times \frac{(l_m w_m h_m M)^2}{{d_m}^7} \tag{4.4}$$

Equation 4.3 describes how far a certain bead moves, measured in bead radii, in a given time interval. A linear dependence between the dimensionless normalized magnetically induced travelling distance and the design parameter, Θ, can be seen.

Furthermore, Equation 4.3 also shows the impact of different parameters, e.g. magnetic beads travel further when their susceptibility is increased whereas the distance from the magnet has a significant opposite effect. Thus, Equation 4.3 agrees qualitatively with what has been observed experimentally (see Section 4.2.3).

Due to the linear dependency between $\hat{X}_p$ and Θ, all points should collapse onto a straight line, when the measured bead properties are inserted into Equation 4.4. Figure 4.22 compares the dimensionless normalized magnetically induced travelling distance of the scaling law with the experimental results. In Figure 4.22a a constant susceptibility was assumed (see Table 4.2) whereas in Figure 4.22b the susceptibility was adjusted according to the magnetic field (see Table 4.5). Figure 4.22b shows a stronger linear trend compared to Figure 4.22a. This makes it evident, that over the analysed distance of 6 mm, the susceptibility is influenced by the magnetic field magnitude and should be adjusted accordingly.

4.6 Discussion

A clear difference in magnetophoretic mobility could be seen between the analysed magnetic particle types (see Figure 4.12). In the case of single magnetic beads, Chemicell SiMAG beads exhibited the largest magnetophoretic mobility, followed by the Dynabeads M270, Dynabeads M280, Dynabeads MyOne and Chemicell ScreenMAG beads. The different magnetophoretic mobilities for the Dynabeads was attributed to their different size and iron content (see Table 4.1). The two types of Chemicell beads supposedly have the same magnetic properties, given their size and iron content stated by the manufacturer. The difference in mobility certainly arises from their measured size difference. In the case of Chemicell beads, additional factors, such as their non spherical shape, helps to explain the discrepancy between the two manufacturers.

The variation in magnetically induced velocity, and thus mobility, of one bead type from the same manufacturer cannot be attributed to variation in bead diameter alone because the measured size distribution of Dynabeads particles ($< \pm 3\%$) resulted only in a drift velocity variation of $\pm 6\%$. However, velocity variations of $17\% - 33\%$ were measured. This conclusion is in contrast to the findings of Xu et al. where the spread of the different magnetically induced velocities was mostly attributed to the bead size distribution [344]. Another factor that could have added to the velocity variation are measurement errors. The dominant error in the experimental measurements can be attributed to uncertainty in determining the exact position of the beads when observed with the video camera. Measurement errors, however, are considered to be insufficient to account for the variation. Measurement errors do increase when the magnetic force is weak, because errors in determining distance have a more significant effect when the total distance travelled by the particle is small, but estimates predict that this measurement error should not exceed 1%. Thus, the observed variation in magnetic mobility reported is significantly attributed to varying iron content in this study. The variation in iron content was estimated to be between 12% and 25% based on the measurements. In the literature, iron content of 11.8% and 25.5% for Dynabeads' M280 and Dynabeads' MyOne, respectively, are reported [300]. However, data on statistical variation in iron content between single magnetic beads is not available and might differ between different manufactured batches [345]. Due to the complex structure of the magnetic particles it is unlikely that every particle will exhibit the exact same magnetic responsiveness. The different uncertainties and variations make the accurate prediction of bead trajectories more challenging, which has a negative effect on the separation efficiency for continuous separation. For separation performed in test tubes, these uncertainties only weakly influence the separation efficiency, as they only have an effect on the separation time.

In this study, sedimentation of the magnetic beads due to the action of gravity was neglected without introducing measurement error. This is because the forces due to magnetism and gravity were configured to be orthogonal in the experiments. The drift velocity of the beads due to the magnetic force was determined over a tracking distance of 55 μm using a microscope and imaging camera. Calculations of the sedimentation rate of different bead types predicted the beads sediment between $2-16$ μm whilst being observed, which is consistent with observations made with the captured video of bead transport. Only data from beads that were clearly suspended in the channel was used. Additionally, if the beads were to sink towards the bottom of the counting slide (of channel thickness 100 μm) then the drag on the beads would approximately triple (see Section 7.3) and thus reduce the magnetophoretic velocity by the same factor. However, velocity variations of less than 33% were measured. Therefore, interactions between the magnetic beads and the bottom surface of the counting slide could be discounted in these measurements.

The susceptibility for the analysed bead types of the two measurement methods, magnetophoresis study and SQUID measurements, showed similar trends with decreasing applied magnetic field. The determined susceptibility values also showed a good agreement with values stated by the manufacturer and in the literature. In the literature, the susceptibility ranges between 0.26 and 1.4 for MyOne beads [300, 346], between 0.14 and 0.76 for M280 beads [300, 347, 348] and a value of $\approx$ 0.17 for the M270 beads [346, 349]. The susceptiblity of Chemicell beads is less frequently reported in the literature, but susceptibilty is quoted between 0.03 and 1.5 [301, 302, 329, 350]. Also the susceptibilities of other bead types stated in the literature appear to be in the same range [212, 262, 351], i.e. the susceptibility values determined in this study are consistent with those previously published in the literature. One further explanation for the variation in particle susceptibility is potential variability in the manufacturing process. It is reported in [212] that mag-

netization curves are not routinely measured by the manufacturer for each batch of superparamagnetic beads produced. This might be because magnetic separation is conventionally performed in test tubes with strong permanent magnets and consistent susceptibility is not necessary.

The monotonic increase of susceptibility with decreasing magnetic field can be seen across all particle types and in both measurement methods (magnetophoresis study and SQUID measurements) and has been found to be a consequence of a magnetic field dependent magnetization of the magnetic particles. The magnetization curves in Figure 4.17 reveal that the linear relationship $\mathbf{M} = \chi\mathbf{H}$ between magnetization and applied field is a simplification and might only be a valid approximation for magnetic fields $|\mathbf{B}| \leq 6$ mT, based on the observations in Figure 4.17c and Figure 4.17d. In addition, the remanence of the magnetic particles may contribute to the behaviour of the beads at even lower magnetic fields and should not be neglected as discussed by Shevkoplyas et. al. [212]. At larger magnetic fields, the data presented in Figure 4.16 should be considered to account for the non-linear behaviour of the susceptibility. Many publications in the literature [59, 230], however, neglect remanence and the magnetic field dependence of the susceptibility, which can lead to modelling errors.

4.7 Conclusion

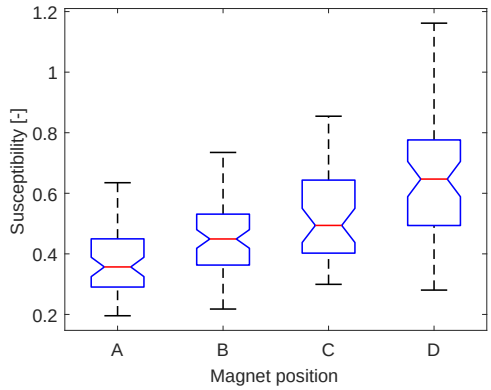
In this chapter, the magnetic responsiveness of five different magnetic bead types were tested using two different approaches. The magnetophoretic drift velocity of single magnetic beads as well as bead complexes was studied using a simple particle tracking system and the magnetization of the same beads measured using SQUID relaxometry. Based on the observed drift velocity one can determine the overall magnetic responsiveness of the particles. The consistent values of the suscepti-

bility obtained between the magnetophoresis analysis and those from the SQUID measurement suggest that particle tracking is a viable technique for determination of susceptibility of superparamagnetic microspheres over a range of magnetic flux densities. Unlike average magnetic susceptibility data obtained from SQUID, the particle tracking system can characterize the magnetic properties of single particles. Additionally, the particle tracking system is also capable of validating drift velocities of assembled bead chains being aligned in parallel or perpendicular to their direction of movement.

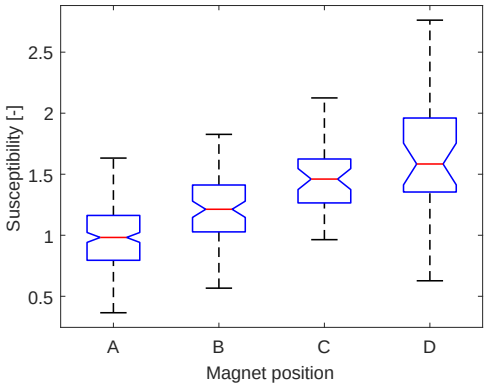
The magnetophoretic mobility of individual particles was measured over a range of $38 - 70$ mT using a permanent magnet. The monotonic reduction in mobility of the magnetic particles as they approached the permanent magnet was attributed to a reduction in susceptibility with increasing magnetic field strength. The same negative correlation between the magnitude of the magnetic field and the susceptibility of the magnetic particles was observed by analysing hysteresis curves of particle samples, obtained from SQUID measurements. The change in mobility results from the non-linearity of the magnetic susceptibility with respect to the applied magnetic field. In cases where the trajectory of magnetic particles needs to be determined accurately, the observations in this study conclude that a constant susceptibility does not lead to accurate calculations and instead the non-linear behaviour of the susceptibility should be taken into account. A constant susceptibility can only be assumed when the magnetic particles interact over a narrow magnetic field regime, but the susceptibility value should still account for the magnitude of the applied magnetic field.

The comparison of the commercially available magnetic beads also highlights the differences of their physical properties and make it evident that some magnetic particle types are potentially more suitable for continuous magnetic separation. A high magnetic mobility with a narrow distribution is desirable because separation time

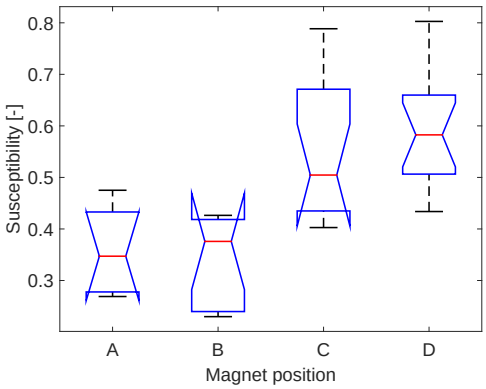
and reproducibility are often limiting factors in continuous magnetic separation. A high magnetophoretic mobility ensures that even at short interaction time the particles separate. A narrow magnetophoretic mobility distribution allows for accurate magnetic bead trajectory predictions and will enhance separation efficiency. Dynabeads M270 magnetic microspheres meet the above criteria and are therefore the best choice for magnetic particle separation based on this study. Chemicell beads, on the other hand, do not have a uniform size distribution, nor are they spherical in shape. This would make cell separation prone to error, because a large distribution in bead diameter and shape not only varies their magnetophoretic mobility but also influences the number of cells each particle can have attached.



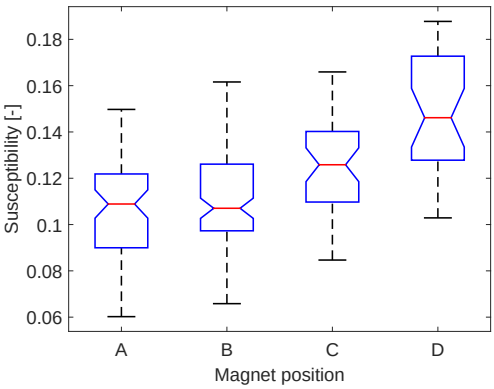
(a) Chemicell ScreenMAG



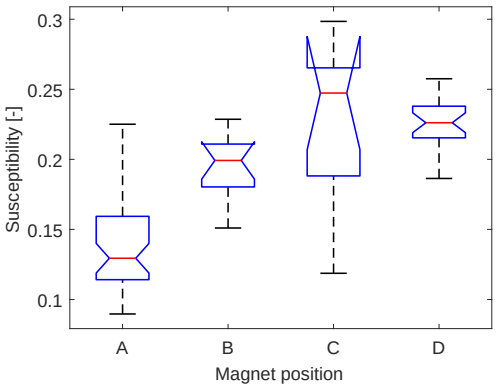
(b) Chemicell SiMAG



(c) Dynabeads MyOne

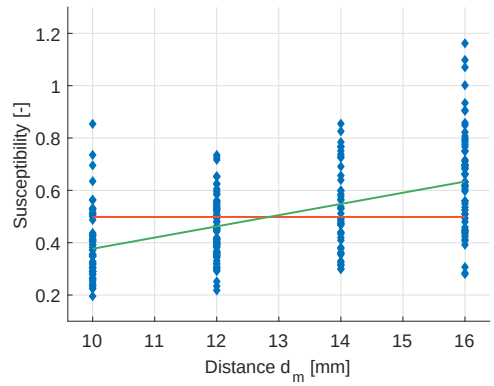


(d) Dynabeads M280

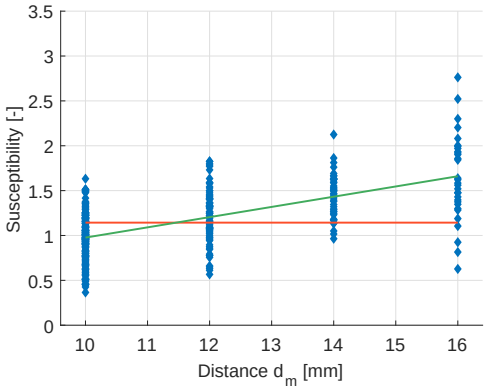


(e) Dynabeads M270

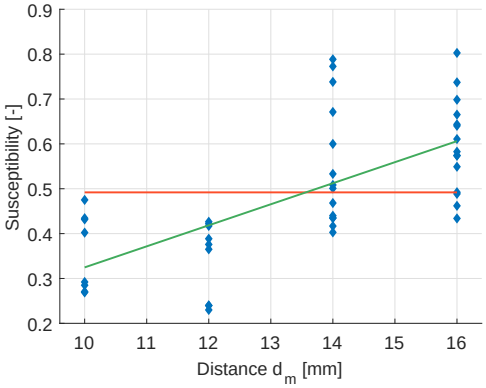
Figure 4.19: The different box plots show the susceptibility distribution at different magnet positions for all particle types. The distribution arises from the fact that the susceptibility is calculated based on the data from the magnetophoretic mobility study. The central mark (red line) indicates the median, the bottom and top edges of the box indicate the 25th and 75th percentiles and the whiskers extend to the most extreme data points of the susceptibility sample distribution. The notches (in blue) represent the upper and lower bound of the 95% confidence interval. An overlap of one or multiple notches indicate that the medians of those specific susceptibility sample groups are considered to be statistically identical within a confidence level of 95%.



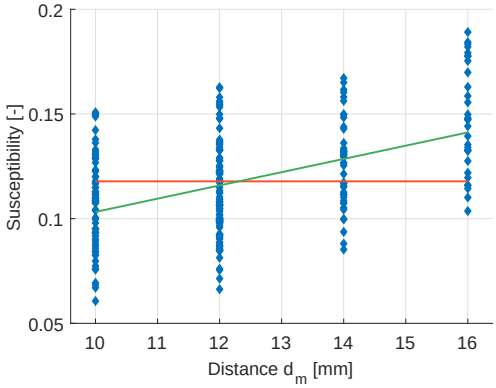
(a) Chemicell ScreenMAG



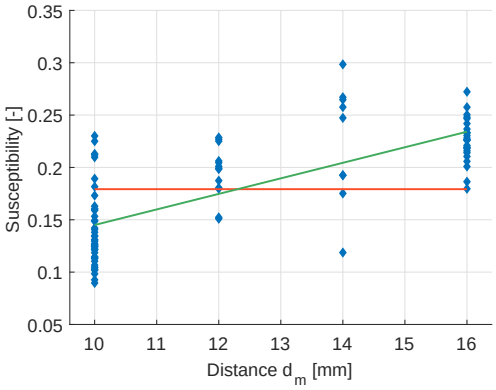
(b) Chemicell SiMAG



(c) Dynabeads MyOne



(d) Dynabeads M280



(e) Dynabeads M270

Figure 4.20: Regression analysis for the calculated susceptibility data. The black circles shows the individually determined susceptibility values at the different distances away from the magnet. The data is regressed against two models. A constant model $y = C$ where parameter C is estimated (red line) and a linear model $y = mx + b$ where parameter m and b are estimated (green line). The regression is done using an ordinary least square estimator.

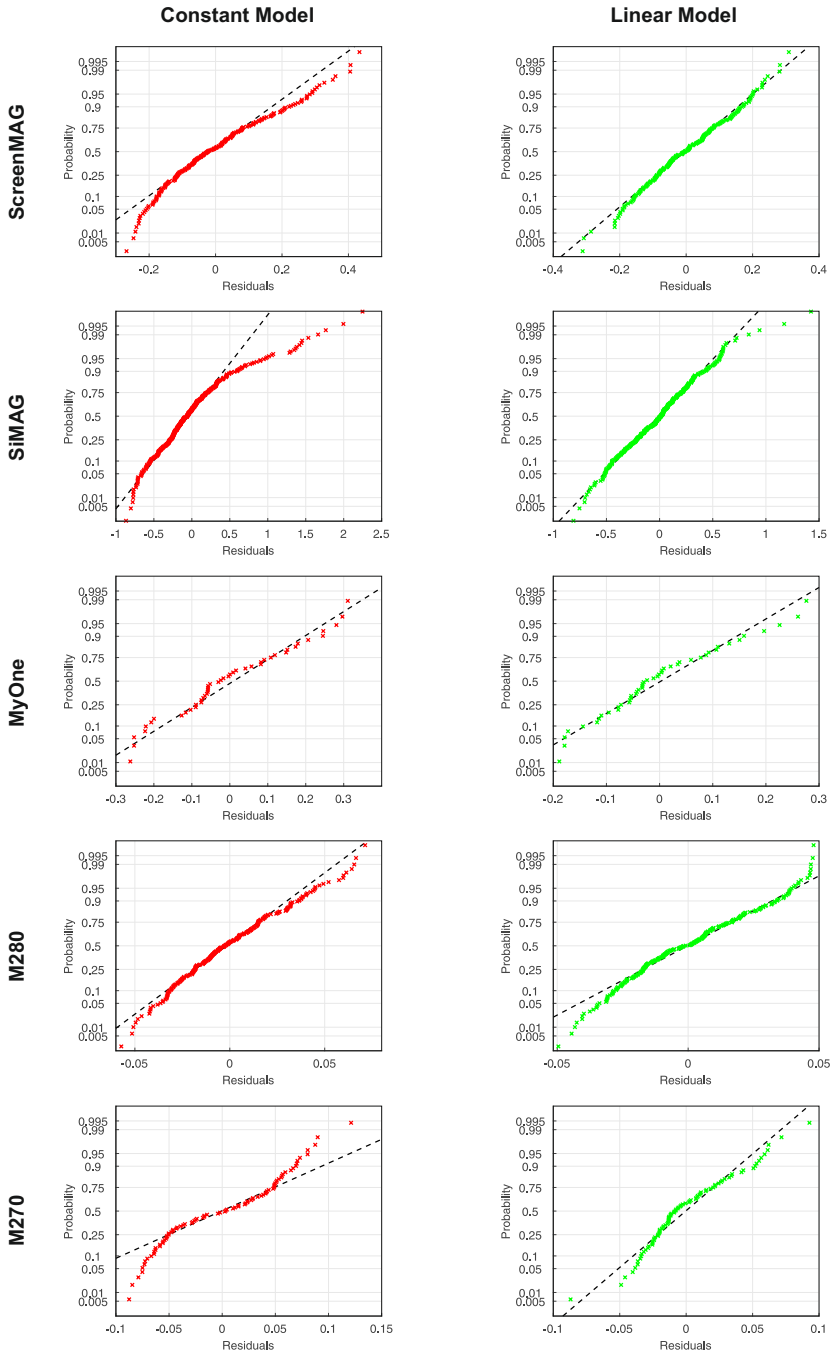
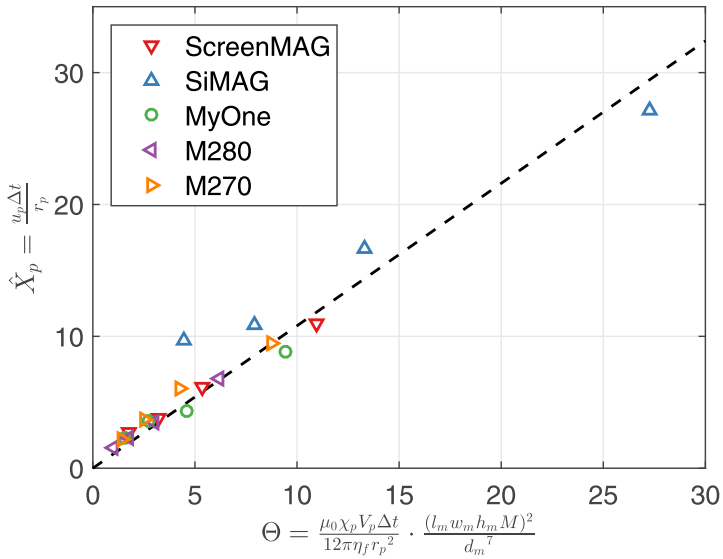
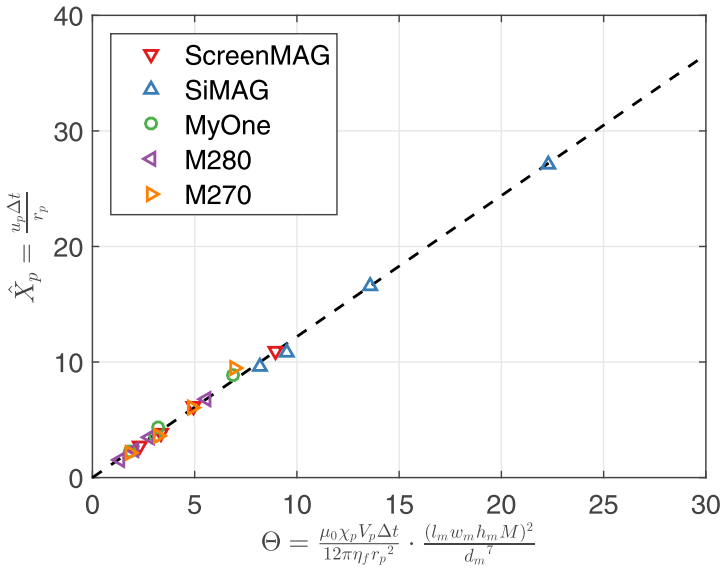


Figure 4.21: Residuals of the regression analysis for two assumed models. The first model assumes the susceptibility to be constant (constant model) whereas the second model assumes the susceptibility to be a linear function (linear model).



(a) Constant susceptibility



(b) Magnetic field adjusted susceptibility

Figure 4.22: Dimensionless normalized magnetically induced travelling distance plotted against the dimensionless design parameter Θ. In (a) the susceptibility is assumed to be constant (Table 4.2). In (b) the susceptibility is assumed to be magnetic field dependent and adjusted accordingly (Table 4.5). The dimensionless scaling constant κ is found by fitting a straight line using an ordinary least square algorithm. Here κ is set to 1.1 and 1.2 in (a) and (b), respectively. The time interval Δt_p is set to 0.6 s for the Chemicell ScreenMAG particles. For all other particle types a time interval of 0.3 is chosen.

Chapter 5

Hydrodynamic flow in a microfluidic device

5.1 Introduction

The hydrodynamic flow in the two microfluidic devices described in Section 3.3.1 and Section 3.3.2 was numerically modelled using the simulation software ANSYS Fluent and experimentally tested and verified. Here, only results for the microfluidic separation device (see Section 3.3.2) are presented, since this device will be used further throughout this thesis.

5.2 Hydrodynamic flow in a microfluidic separation device

The solution to the Stokes equation (Equation 2.9) in a straight and rigid channel is the pressure-driven, steady-state flow, also known as Poiseuille flow. Figure 5.1 shows the 3D velocity profile of the Poiseuille flow across the rectangular cross section of the microfluidic separation device at a Reynolds number of approximately

Re ≈ 0.3. The dimensions of the fluid channel in the simulation were set equal to the actual dimensions of the microfluidic separation device (iBidi μ-Slide III 3in3) as described in Section 3.3.2. In Figure 5.1 the analytical solution based on Equation 2.10 as well as the numerical simulation is shown. For the numerical simulation, however, only half of the channel height was computed.

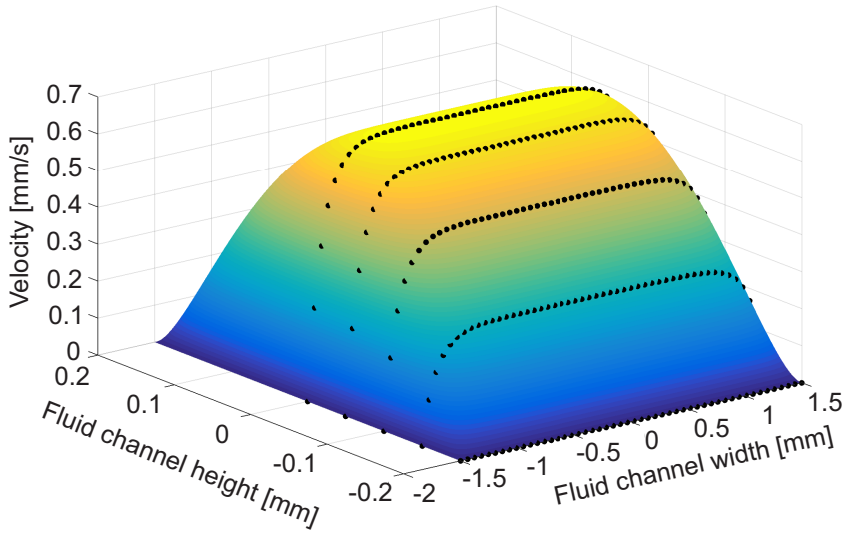


Figure 5.1: Velocity profile across half the cross-section of the microfluidic separation device at Re ≈ 0.3. The continuous profile shows the analytical solution. The black dots are the results of the numerical solution computed with ANSYS Fluent. For the numerical simulation, only half of the channel height is simulated due to symmetry. The channel dimensions are representative of the microfluidic separation device (iBidi μ-Slide III 3in3) described in Section 3.3.2. Note, that the cross section of the microfluidic separation device has a large aspect ratio, which the illustration does not represent accurately.

This particular flow profile is of major importance for the understanding of liquid handling and thus particle manipulation in suspension in microfluidic systems. A main characteristic of the fluid dynamics is the parabolic flow through a rectangular channel and the resultant zero velocity at the internal surfaces of the channel (no-slip) as described in Chapter 2. The flow profile in the rectangular case remains constant along a large part of the channel's wide width, but parabolic across the short height. The shape of the velocity profile, and whether it has a parabolic shape

in all directions or tends towards a plug-like form (similar to the electroosmotic flow [352]), depends on the aspect ratio (h_0/w_0) of the channel [287]. The plug-like flow profile seen here is also well documented in the literature for different channel cross sections [275, 282].

The magnetic beads experience a force from the magnetic field and a force from the fluid. The pull towards the magnet must be sufficient for the magnetic beads to be separated from the main sample flow and drawn into the sheath flow, whilst beads should be prevented from arriving at the internal surfaces of the fluidic channel. Beads at the channel surfaces will experience almost zero drag and thus will not flow out of the fluidic device. Such beads will be considered as *lost*, as they are difficult to recover using continuous flow at low flow rates. In order to minimise beads arriving at an internal surface and to control their path through the device, the fluid stream can be manipulated using hydrodynamic focusing as described in the next section.

5.3 Hydrodynamic focusing in a microfluidic separation device

The hydrodynamic focusing effect was simulated and experimentally tested for different flow rates as well as different inlet flow rate ratios. The inlet flow rate ratio describes the ratio between the inlet flow rate of one of the sheath flow channels to the inlet flow rate of the centre channel. In this work, the two sheath flows were always identical.

Figure 5.2 shows a comparison of the numerical simulations and the experiments of the hydrodynamic focusing for different flow rates. In order to make the sample stream visible, the water was dyed with black ink. It can be seen that the simulations accurately represent the experimentally found results for different aspect ratios,

which also verifies the results of the numerical simulation.

It was found that higher flow rates and thus also higher Reynolds numbers, produced a more narrowly focussed sample stream. This effect is also visible in the numerical simulation.

Table 5.1 lists the measured sample stream width determined by experiment result and the corresponding flow conditions. The Reynolds numbers ranged within two orders of magnitudes ($O(10^{-1}) - O(10^{1})$). It was assumed that the range of values of Reynolds number were sufficiently low to provide laminar flow conditions. In general, all values of Reynolds number relevant to this thesis could be considered as sufficiently low to provide laminar flow.

The data in Table 5.1 is also visually shown in Figure 5.3. Figure 5.3 shows the width ratio between the sample stream width and the width of the fluid channel for four inlet flow rate ratios at various sample flow rates. As predicted by the model described in Equation 2.18, a non-linear relationship was observed where the focus width of the sample flow decreased rapidly with increasing flow ratio. The experimental results, as well as the simulation, compare well with the theoretical values.

From the experimental results presented in Table 5.1 and Figure 5.3, as well as Equation 2.18, it can be seen that the width of the focused stream mainly depends on the inlet flow rate ratio but not the overall volumetric flow rate.

5.3.1 Entrance length

Where a fluid enters a channel, or where several flow streams are brought together at the entrance region of a microfluidic device, as it is the case in hydrodynamic focusing, the following question arises: At which distance L_H down-stream from the entrance point is the laminar flow a fully developed steady-state Poiseuille flow profile as described in Section 5.2. The entrance length L_H is calculated according to

Table 5.1: Experimentally measured width of the hydrodynamically focused sample stream and the corresponding flow conditions, such as flow rates, Reynolds number and back pressure, calculated for the iBidi separation device geometry. The flow rate of the two sheath flows are kept the same. The Reynolds number and back pressure are calculated according to Equation 2.4 and Equation 2.11, respectively.

Sample flow rate [μL/min]	Sheath flow rate [μL/min]	Reynolds number [−]	Back pressure [Pa]	Sample stream width [mm]
10	10	0.29	0.96	1.20
10	20	0.49	1.59	0.72
10	30	0.68	2.23	0.54
10	40	0.88	2.87	0.44
20	20	0.59	1.91	1.04
20	40	0.98	3.19	0.65
20	60	1.37	4.47	0.48
20	80	1.76	5.74	0.38
50	50	1.47	4.78	1.02
50	100	2.44	7.97	0.61
50	150	3.42	11.16	0.44
50	200	4.40	14.35	0.36
100	100	2.93	9.57	0.93
100	200	4.88	15.94	0.61
100	300	6.84	22.33	0.45
100	400	8.79	18.70	0.36
200	200	5.86	19.14	0.94
200	400	9.77	31.89	0.62
200	600	13.67	44.65	0.44
200	800	17.58	57.41	0.40

Equation 2.8 (see Chapter 2). In the microfluidic iBidi separation device, where the hydrodynamic diameter was calculated as $D_H \approx 0.7$ mm, the entrance length L_H did not exceed 0.7 mm for all the flow rates tabulated in Table 5.1. For lower flow rates this entrance length was also smaller. Typically used flow rates in this thesis were between 50 μL/min and 400 μL/min which results in an entrance length of $L_H \approx 21$ μm and $L_H \approx 165$ μm, respectively. Thus, the velocity profile was fully developed and remained steady a short distance from the entrance of the fluid separation device, which had a total length of 24 mm. Also particles in suspension could be assumed to

travel at a constant velocity down-stream when being magnetically manipulated, as long as the magnet was located 0.7 mm or further down-stream from the entrance.

5.4 Conclusion

The micromachined microfluidic iBidi separation device, designed and fabricated on a plastic susbstrate, which met the requirements for hydrodynamic focusing as well as for particle separation, was validated based on its fluid dynamic properties.

The flow field inside the microfluidic device was modelled numerically. The simulated velocity profile inside the rectangular duct met the theory and was in line with the vast literature published on this topic. Due to the straight shape and the rigid rectangular cross section of the channel, analytical results would have been sufficient for the analysis presented in this chapter. The numerical model approach adopted, however, gives more flexibility for future analysis and can easily be extended to consider more complex channel designs.

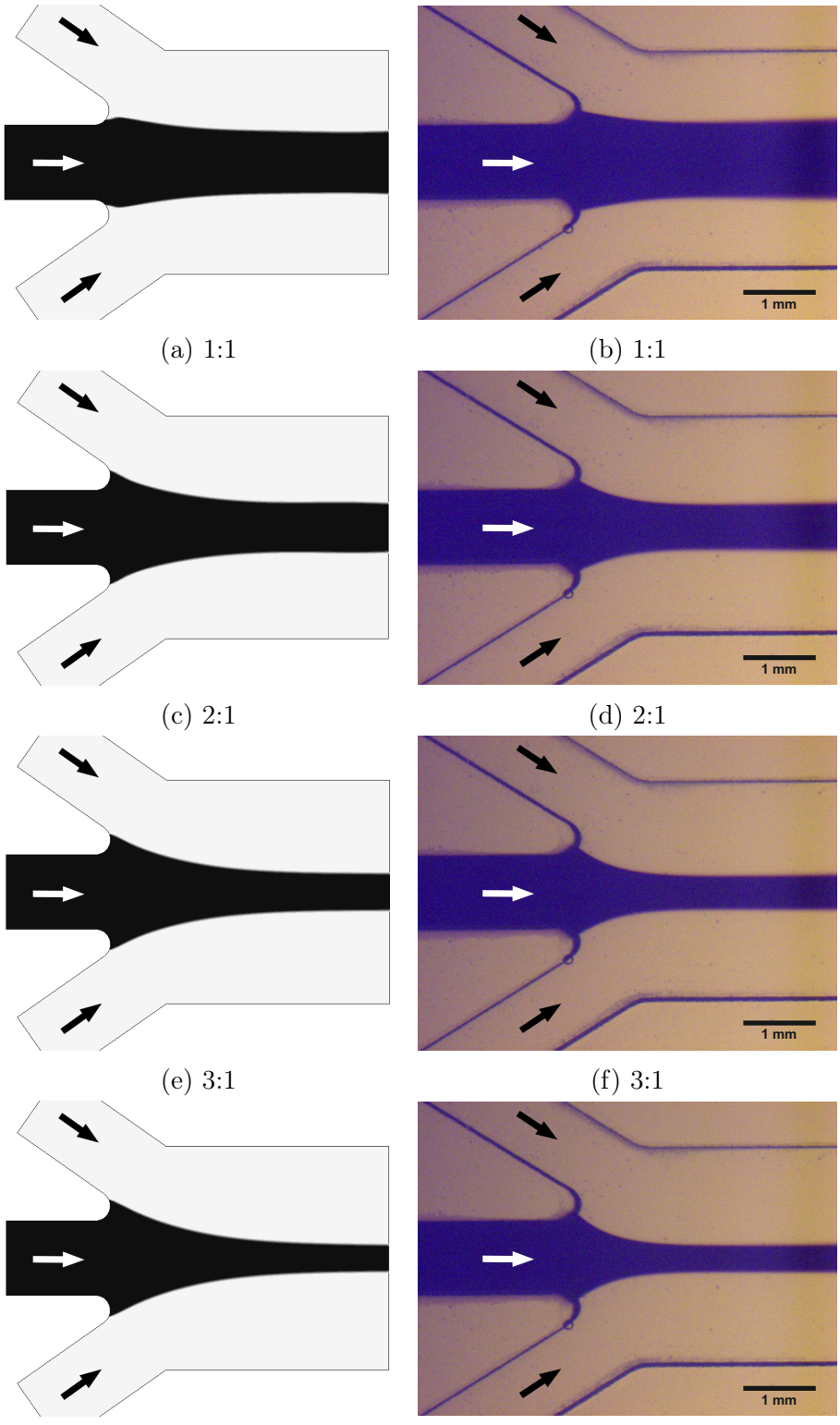
Changing the flow rate alters the pressure drop along the channel, back pressure and the magnitude of the fluid velocity but not the path of the streamlines. This means a laminar regime could be assumed for all flow rates simulated and experimentally tested, which was also suggested by the Reynolds number calculated.

Hydrodynamic focusing was verified with the use of microscopic visualization of water sheath flow and dye containing sample flow. The width of the focused stream was measured for different volumetric inflow ratios and magnitudes. Experimental data matched the proposed model and were also in-line with the numerical results.

The results presented here can be compared to a similar study presented by Lee *et al.* [287]. They successfully demonstrated the hyrodynamic focusing effect within a micro flow cytometer device and compared the normalized width of the hydrodynamically focused stream to the same model used in this thesis. They reduced

the focused stream width within a 500 μm wide fluid device to approximately 20 μm. The channel used in their work was six times smaller than the 3 mm wide channel used in this thesis, but the aspect ratio as well as the Reynolds number are comparable. Thus, the normalized width of the hydrodynamically focused stream presented in their work for the different volumetric inflow ratios compares well with the model and the normalized focused stream width presented here.

The symmetric hydrodynamic focusing works well in a wide channel with the sheath flows in the same horizontal plane. In a single plane, however, hydrodynamic focusing is intrinsically problematic due to the lack of vertical focusing. The non-uniform (parabolic) velocity distribution of vertically spread beads is known to cause complications in particle separation [353]; because beads near the top or the bottom channel wall will experience almost zero flow rate and thus will be effectively stuck in the system. This problem could be solved by using an axis-symmetric focusing device, which consists of two concentric capillaries [354–356]. However, in practice, such structures are a challenge to fabricate using photolithography based microfabrication techniques. As a result, the mass production of such devices might not be cost effective. Another approach is to use Dean vortices to focus the beads orthogonal to the sheath flow [357, 358]. This requires the centre inlet to be curved and also requires high velocities (Re $>>$ 1) to have a noticeable focusing effect. For these reasons an axis-symmetric hydrodynamic focusing was not explored further in this work. Not focussing the beads in both directions orthogonal to the central flow has a predicable impact on the efficiency of the microfluidic separation device.



(a) 1:1 (b) 1:1

(c) 2:1 (d) 2:1

(e) 3:1 (f) 3:1

(g) 4:1 (h) 4:1

Simulation Experiment

Figure 5.2: Comparison of the hydrodynamic focusing between the simulation and the experiment for different inlet flow rate ratios. The inlet flow rate ratio between the sheath and the sample flow ranges from 1 to 4, whereas the centre sample flow is kept at 100 μL/min. The sample flow is dyed with black ink for visibility. The directions of the flow streams are indicated by the arrows.

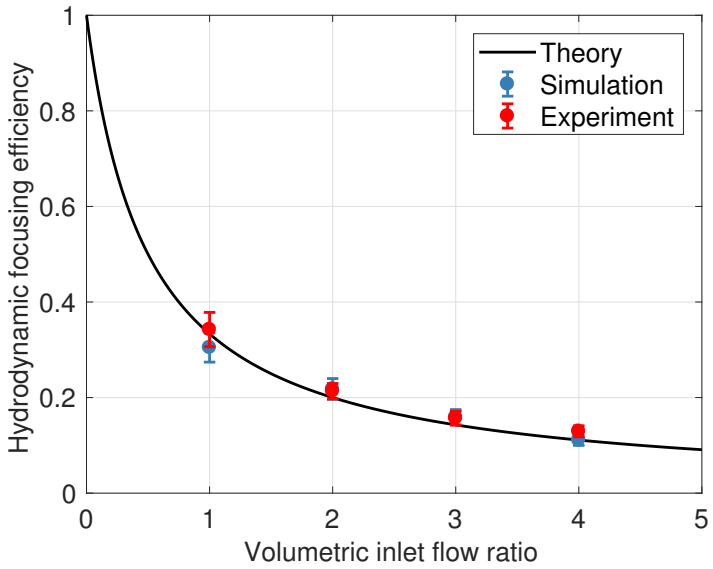


Figure 5.3: The normalized width ratio of the sample flow (w_c/w_0) plotted against multiple volumetric inlet flow rate ratios for different sample flow rates. The flow rates of the sample stream are 10 μL/min, 20 μL/min, 50 μL/min, 100 μL/min and 200 μL/min and the sheath flow rates are set according to the volumetric inlet flow rate ratio $\dot{Q}_c/\dot{Q}_s$. The channel's height to width ratio is $h_0/w_0 = 0.13$. The error bars show one standard deviation of the measured width of the sample stream for the different sample flow rates.

Chapter 6

Magnetic separation configuration

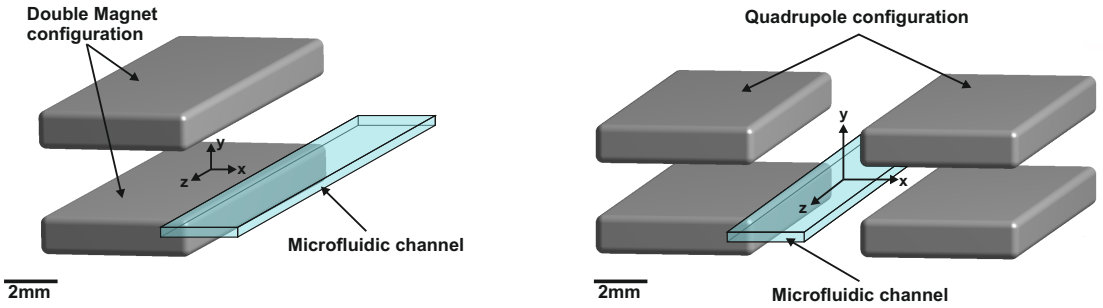
6.1 Introduction

A key objective was to design a novel magnet configuration that would enable continuous separation of magnetic particles of variable susceptibility while reducing particle interactions with the side walls of the microfluidic channel.

As seen in Chapter 1, magnetic separation configurations typically use a strong rare-earth magnet or an electromagnet in close proximity to the channel to attract and repel paramagnetic and diamagnetic particles, respectively. In either case, the force is always unidirectional; meaning all particles are either attracted or repelled from the magnet. The magnet configurations presented here had the ability to attract and repel superparamagnetic particles.

6.2 Magnet configurations

The two magnet configurations incorporated two or four bar magnets, which were placed at the side of the microfluidic channel, as depicted in Figure 6.1. The resulting forces on magnetic particles applied to their separation process was novel. Both configurations used N42 Neodymium magnets of dimension 20 mm $\times$ 6 mm $\times$ 1.5



(a) Double Magnet configuration (b) Quadrupole configuration

Figure 6.1: 3D schematic of the two magnet configurations used in this thesis. (a) shows the Double Magnet configuration and (b) the Quadrupole configuration and how the magnets are placed around the microfluidic channel. The dimensions of the magnets are 20 mm × 6 mm × 1.5 mm.

mm (First4Magnets®,UK), which could be machined conveniently to change their shape. The two geometries are referred to as Double Magnet and Quadrupole configuration throughout this thesis. All numerical results for the magnetic **B** field and the magnetophoretic driving force were obtained by using the previously described techniques for FEM and smoothing.

6.2.1 Double Magnet configuration

The Double Magnet configuration shown in Figure 6.1a was the most basic geometry used here. Two magnets were placed on top of each other in an attractive configuration, with both magnetizations pointing in the same direction. The microfluidic channel is located along the x axis to the right of the magnet configuration as depicted in Figure 6.2. The three geometric parameters of the system and their ratios, shown in Figure 6.2, were used to quantify the distribution of the magnetic field and force; height h and width w of the magnets and their vertical spacing a. The impact of varying two ratios was studied here: h/w (aspect ratio) and a/w (relative gap). As a conservative magnetic field ($\nabla \cdot \mathbf{B} = 0$), an intrinsic property of the magnetic flux density is the formation of complete closed flux loops around the magnet. The spatial distribution of the flux loops is a function of the number, position and magne-

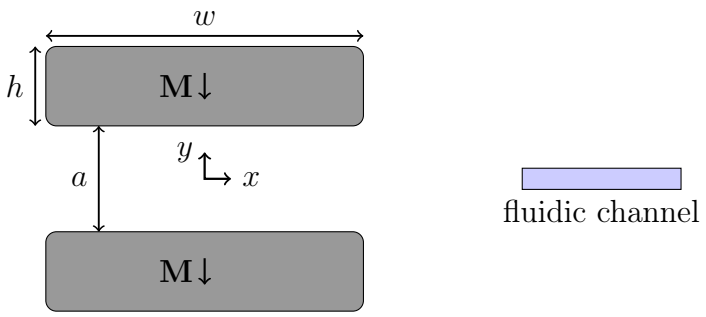


Figure 6.2: 2D slice diagram ($z = 0$) of the Double Magnet configuration used to generate the external magnetic field for separation. The rectangular permanent magnets (grey) are set up in attraction, with the magnetization in the negative y direction as indicated by the magnetization vector $\mathbf{M}$. The parameters w, h and a describe the width, the height (thickness) and the separation of the two magnets. The microfluidic channel is located (light blue) to the right of the magnet configuration. The schematic is not drawn to scale.

tization orientation of the magnets, and represents the vector field of the magnetic flux density $\mathbf{B}$. In Figure 6.3 the magnetic flux density and its field lines of the Double Magnet configuration is shown. The field lines formed loops around each individual magnet as well as around the whole magnet configuration. Due to the field lines looping around each individual magnet their superposition resulted in a region where magnetic flux density was zero ($|\mathbf{B}| = 0$ at point (2) in Figure 6.3) because of their opposing direction. Also, local flux density extrema (maximum or minimum) were generated where $\nabla|\mathbf{B}| = \mathbf{0}$ (point (1) and point (3) in Figure 6.3). Magnetic particles experience no force in a magnetic field if either the magnitude of the flux density is zero ($|\mathbf{B}| = 0$) or there is no field gradient ($\nabla|\mathbf{B}| = \mathbf{0}$), i.e. they are in a region of zero or a local minimum in magnetic energy density. In Figure 6.4 the magnetic flux density of the Double Magnet configuration is plotted along the x axis, starting at $x = y = z = 0$. Three points are indicted in Figure 6.4 where these conditions were met. Such points where no horizontal magnetic force is exerted are useful to trap or gather magnetic beads. One location, where particles experience no force was in the exact centre of the Double Magnet configuration for $x = 0$, labelled as (1) in Figure 6.3 and Figure 6.4. This point has already been

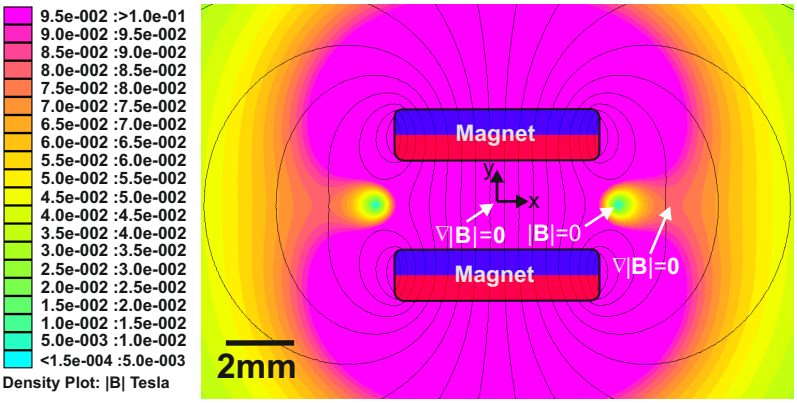
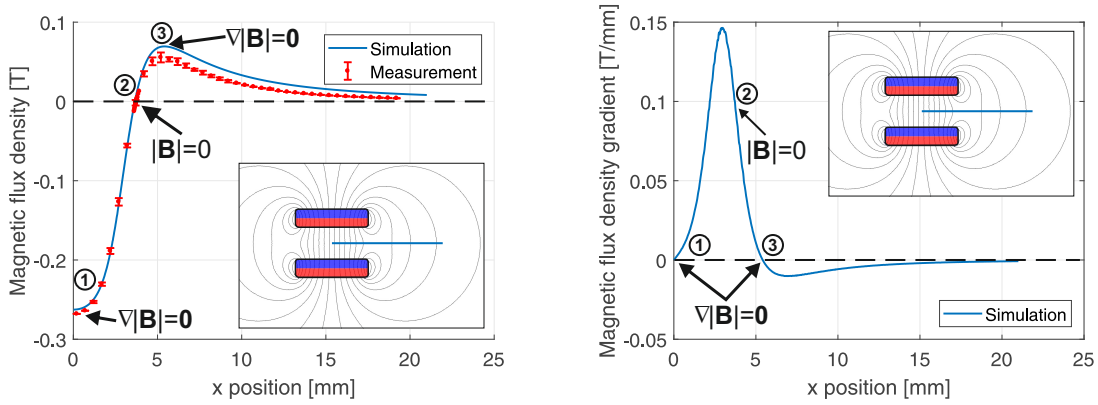


Figure 6.3: Modelling of the magnetic flux density $\mathbf{B}$ of the Double Magnet configuration in the plane $z = 0$ when the vertical separation $a = 3$ mm. The positions where the magnetic driving force is zero, and thus magnetic beads experience no horizontal magnetic force, are indicated by the points (1), (2) and (3).

exploited to trap magnetic beads [359]. At (2), where $|\mathbf{B}| = 0$, beads will not gather due to the gradient and thus should be avoided if the goal is to accumulate beads. The gathering point where $\nabla|\mathbf{B}| = \mathbf{0}$, point (3), on the other hand, appears to be a stable gathering point and will be further investigated in this study.

The stable gathering point at (3) was important for trapping and manipulating magnetic beads because any small disturbance to a bead's position will result in a restorative force to return it to the same point. This is best illustrated when plotting the magnetic force along the x axis, as shown in Figure 6.5a. The change in sign of the force resulted in regions where particles either experience an attractive or repulsive force. The direction in which superparamagnetic particles are moving, depending on their position, is also schematically illustrated in Figure 6.5b. In the following sections, different geometry parameters of the Double Magnet configuration (see Figure 6.2) and their influence on the gathering point outside of the magnet, point (3), will be investigated.



(a) (b)

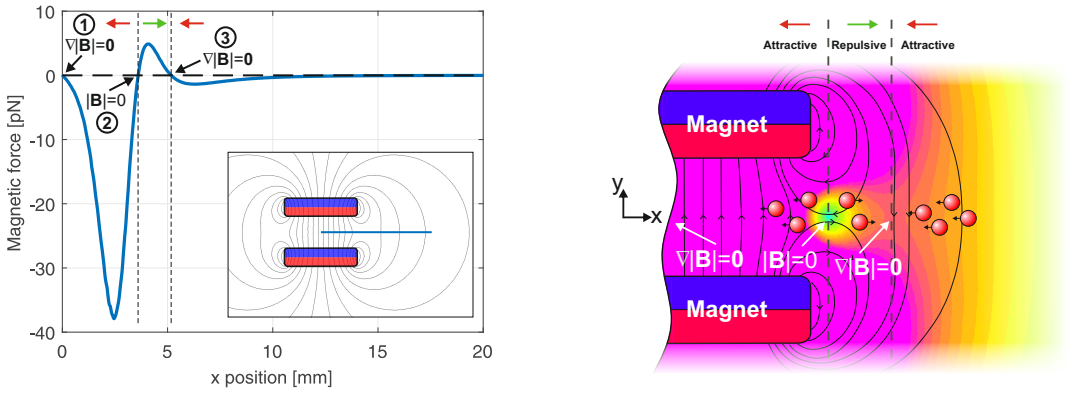
Figure 6.4: (a) Magnetic flux density and (b) flux density gradient of the Double Magnet configuration with a vertical separation $a = 3$ mm. The magnetic flux density is simulated and measured along the x axis, as indicated in the inset, starting at $x = y = z = 0$ mm. Due to symmetry, only the positive x axis is shown. Points (1), (2) and (3) indicate the positions where beads experience no horizontal magnetic force.

6.2.1.1 Effects of magnet aspect ratio

For the Double Magnet configuration, Figure 6.6 shows the simulated magnetophoretic driving force along the x axis, for different aspect ratios h/w ranging from 0.25 to 3. In this particular study, the magnet width w and vertical separation a were kept constant at 6 mm and 2 mm, respectively, while the thickness, h, of the two magnets was varied keeping h the same for both magnets.

From Figure 6.6 it can be seen that the gathering point (3) moved further away from the magnets with increasing aspect ratio. This also lowers the magnetophoretic driving force in the vicinity of the gathering point. At higher aspect ratios ($h/w \geq 3$), the gathering point disappeared because the magnet separation compared to their height became insignificant and the Double Magnet configuration can be regarded as approaching a single magnet.

The setup described in Section 3.9 was used to verify by experiment the behaviour of the gathering points for different aspect ratios (see Section 3.9.1). Figure 6.7 shows the experimental results revealing how the gathering position moved along



(a) (b)

Figure 6.5: (a) Magnetic force on a single Dynabead M270 bead along the x-axis when being exposed to the Double Magnet configuration. The arrows indicate the region where the particle experiences an attractive (red arrow) or a repulsive force (green arrow). The magnet configuration parameters are assumed to be 6 mm, 1.5 mm and 2.6 mm for the magnet width, magnet height and vertical spacing, respectively. (b) Schematic of the direction of movement of superparamagnetic beads when being exposed to the magnetic field of the Double Magnet configuration.

the x axis away from the magnets when the aspect ratio was increased for different magnetic bead types. The experimental observations affirmed the simulated results and it appeared that the gathering position and magnet aspect ratio had a linear relationship over the range investigated.

6.2.1.2 Effects of vertical separation between magnets

Figure 6.8 shows the evolution of the magnetophoretic driving force, as a function of the relative gap a/w. The aspect ratio h/w of the magnet was kept constant at 0.25 ($w = 6$ mm and $h = 1.5$ mm) and only the separation a was varied.

The position of the stable gathering point was again moved along the x axis away from the Double Magnet configuration when the vertical separation between the two magnets was increased. This can be better seen in the magnified section in Figure 6.8 by the moving intercept of the curves with the force = 0 line. Increasing the magnet separation resulted in both a lower magnetic flux magnitude and gradient

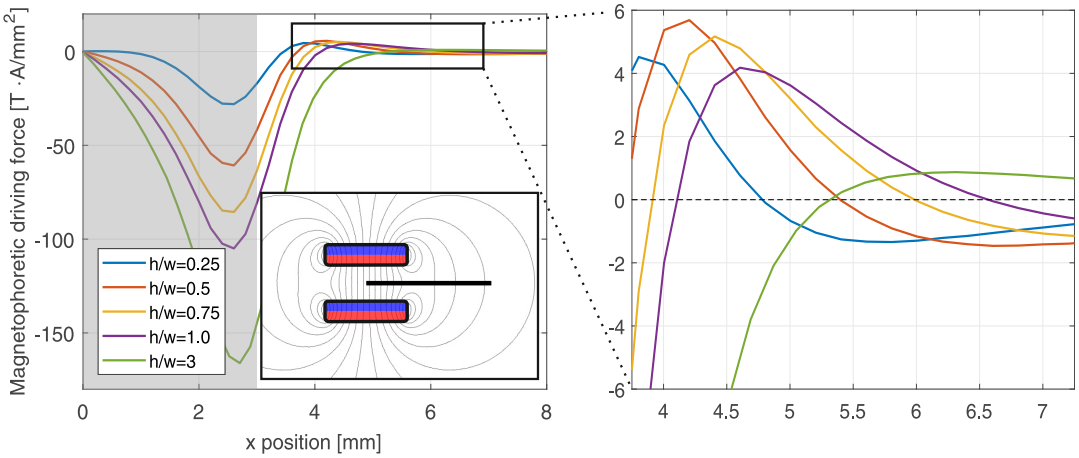


Figure 6.6: Magnetophoretic driving force of the Double Magnet configuration along the x axis for different aspect ratio h/w ranging from $0.25 - 3$. The shaded area indicates the overlap of the magnets along the x direction. The inset shows the line along which the magnetophoretic driving force is simulated. When the force is positive a magnetic bead will be pushed away from the magnets (to the right) and toward the magnets when negative. This change from right to left establishes the stable gathering points. Note that a larger aspect ratio moves the gathering point away from the magnet configuration.

outside of the magnets. This in turn led to a lower magnitude and gradient of the magnetophoretic driving force in and around the particle gathering region and thus the *separating power* was decreased.

Experimental observation of the gathering point for different magnetic bead types again revealed a linear relationship between the relative vertical gap, a/w, and the gathering point position, as shown in Figure 6.9. The gathering point of all bead types increased as the relative gap between the magnets increased, and the experimental values will be a good fit to the positions determined by the model.

Figure 6.10 shows the result of a similar experiment to that presented in Figure 6.9, however, only one bead type (Dynabeads M270) was used for significantly different concentrations. Based on Figure 6.10, changing the concentration appeared to have no effect on the position of the stable gathering position when varying the relative magnet separation ratio.

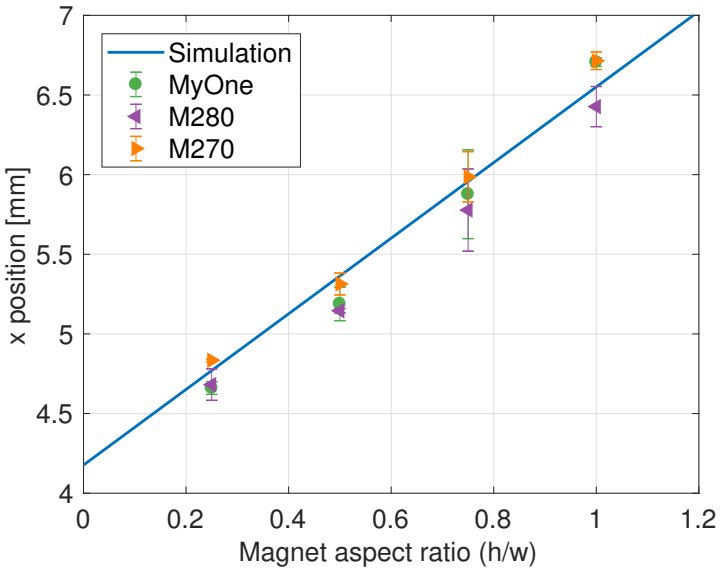


Figure 6.7: Observed behaviour of the position of the static gathering point outside of the Double Magnet configuration as a function of the magnet aspect ratio h/w while keeping $a = 2$ mm. The data is collected by experiment. The error bars are computed from different measurements of bead suspension of the same bead type but different bead concentrations.

6.2.1.3 Effects of tapered magnets

As seen previously in Section 6.2.1.1 and Section 6.2.1.2, changing the thickness or the vertical separation between the magnets, alters the strength of the magnetophoretic driving force as well as the position of the static gathering point. By tapering the magnets, these two effects can be combined. Tapering the magnets could also be used to gradually reduce the magnetophoretic driving force at the tail-end of the magnets in order to gently release particles into an exit flow that would otherwise be at risk of being trapped.

The two magnet shapes considered here that incorporate a taper are shown in Figure 6.11. The taper was either on the inner faces (Figure 6.11a) or the outer faces (Figure 6.11b), beginning halfway along the length of the magnets. In these diagrams, the channel flowed from left to right (z direction) whilst the magnetic force on the particles was predominantly in the x direction. Different tapering angles, θ,

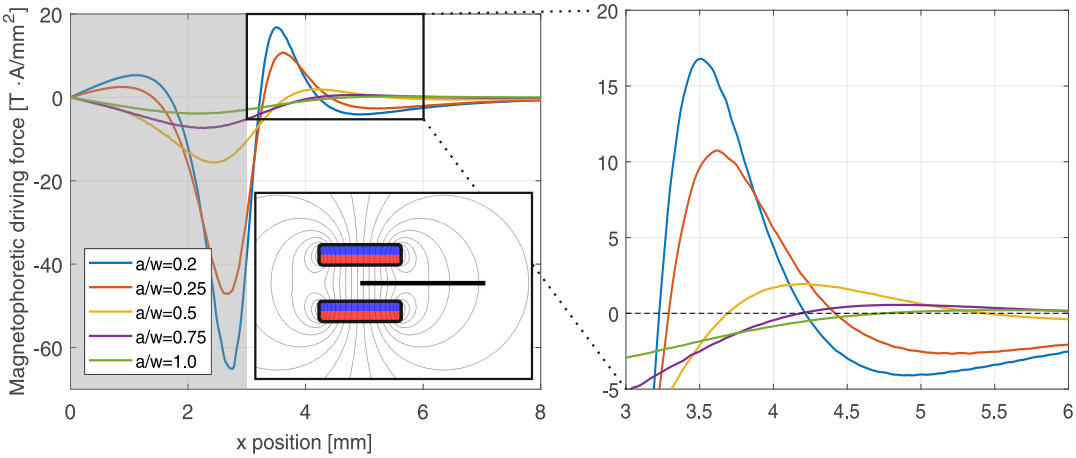


Figure 6.8: Magnetophoretic driving force of the Double Magnet configuration along the x axis at $y = 0$ for different separation ratios a/w ranging from 0.2 to 1. The shaded area indicates the region between the magnets along the x direction. Increasing the separation between the magnets moves the gathering point away from the magnets and reduces the magnetophoretic driving force.

were modelled assuming the starting magnet to be a N42 Neodymium magnet with dimensions 20 mm × 6 mm × 1.5 mm. The vertical separation was set to $a = 2.6$ mm. There are many tapered geometries that could be explored, but these simple structures were selected here for evaluation purposes.

In Figure 6.12 it can be seen that for both taper options, a larger tapering angle resulted in a lower magnetophoretic driving force around the static gathering position. This effect was more pronounced for the magnets which were tapered on the inner faces. This is due to the fact that the magnet separation increased with the taper.

The particle gathering positions were also affected by the taper, either pushing the gathering point out for magnets with inner tapers or pulling the gathering point in for magnets with outer tapers (see magnified section in Figure 6.12).

The inner taper configuration, shown in Figure 6.11a, was evaluated experimentally (see Figure 6.13). There was a clear difference in the static gathering position between the non-tapered and the tapered half of the magnet faces. An observable

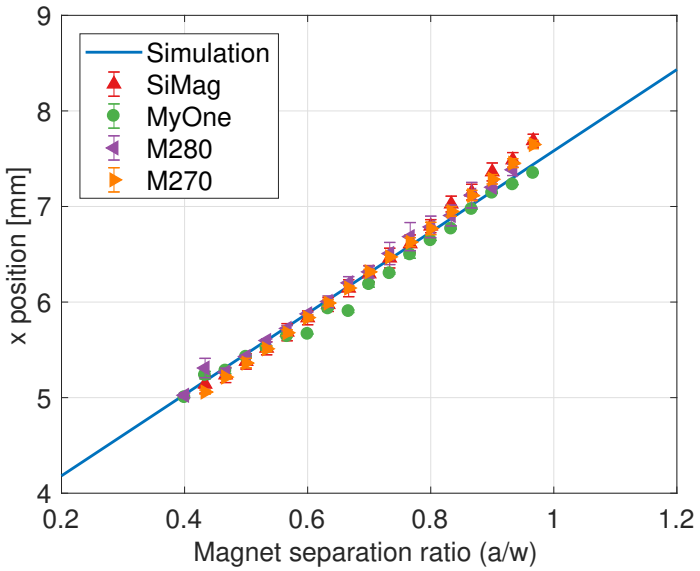


Figure 6.9: Experimental results of the observed gathering positions for different magnetic bead types and vertical separation ratios a/w. The error bars for each particle type are calculated from repeated measurements with different bead concentrations.

monotonic increase in the gathering position as the magnets became thinner, as well as a reduction in the particle concentration, could be observed.

6.2.2 Quadrupole configuration

A second Double Magnet was added to create a Quadrupole configuration, where the microfluidic channel was assumed to be always in the centre of the geometry. A 2D schematic of the Quadrupole configuration is shown in Figure 6.14.

The magnetic field generated by the Quadrupole configuration, is shown in Figure 6.15. Due to the arrangement of the magnets, the magnetic field was symmetric with respect to the origin of the coordinate system. Similarly to the Double Magnet configuration, the Quadrupole arrangement showed areas where the magnitude of the magnetic flux density was zero ($|\mathbf{B}| = 0$) because of oppositely directed field lines. There was also a region where the magnetic field gradient was equal to zero ($\nabla|\mathbf{B}| = \mathbf{0}$).

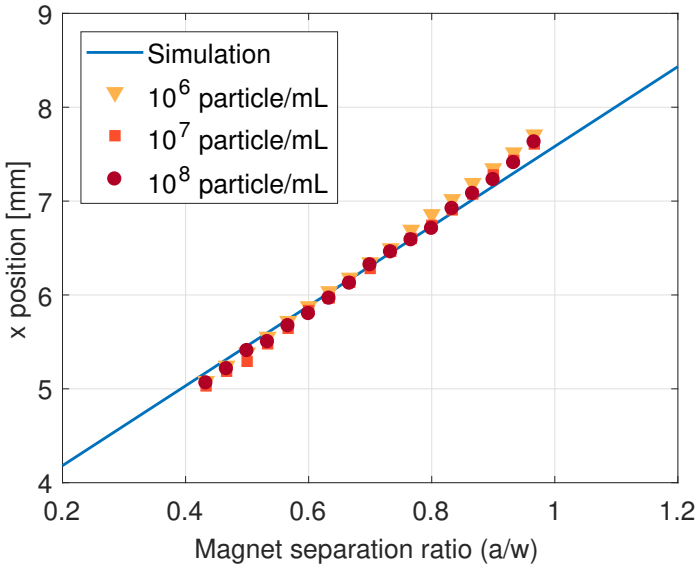
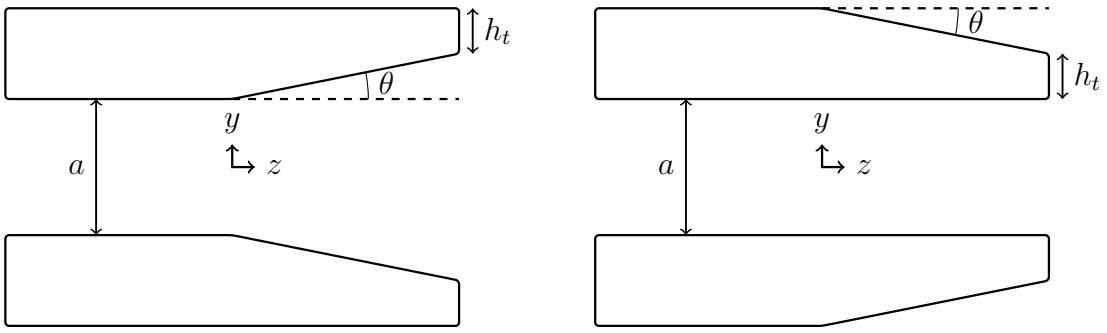


Figure 6.10: Experimental observations of the gathering positions at different vertical separation ratios a/w for Dynabeads M270 at three particle suspension concentrations.

The Quadrupole configuration, compared to the Double Magnet, had a higher magnetophoretic driving force and its gathering points, where no horizontal force acted on magnetic particles, ran along the z axis for a range of horizontal magnet separations b. This configuration leads to a potential increase in particle throughput due to two factors (i) the increased force and (ii) beads can be introduced through both sheath flow channels. However, as with the Double Magnet configuration, beads also feel a force in the vertical direction which is undesirable and larger in the Quadrupole configuration. These vertical forces cause the particles to drift to the top or bottom of the channel where they potentially get stuck. Thus, an optimal spacing between the two Double Magnets needed to be determined.

6.2.2.1 Effects of horizontal separation between magnet pairs

The magnetic Quadrupole configuration is subject to the same geometric constraints as the Double Magnet configuration. Figure 6.16 shows the magnetophoretic force along the x axis for the range of aspect ratios h/w and relative gap ratios a/w



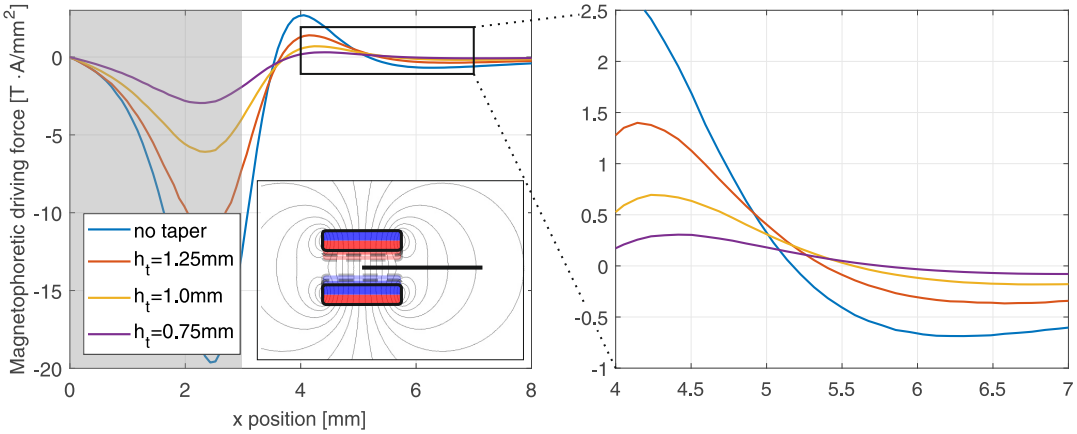
(a) Inner taper (b) Outer taper

Figure 6.11: Diagrams of the tapered magnet configurations: (a) inner taper (b) outer taper. The taper begins halfway along the length of the magnets and finishes at half the non-tapered thickness of the magnets. Schematic is not drawn to scale.

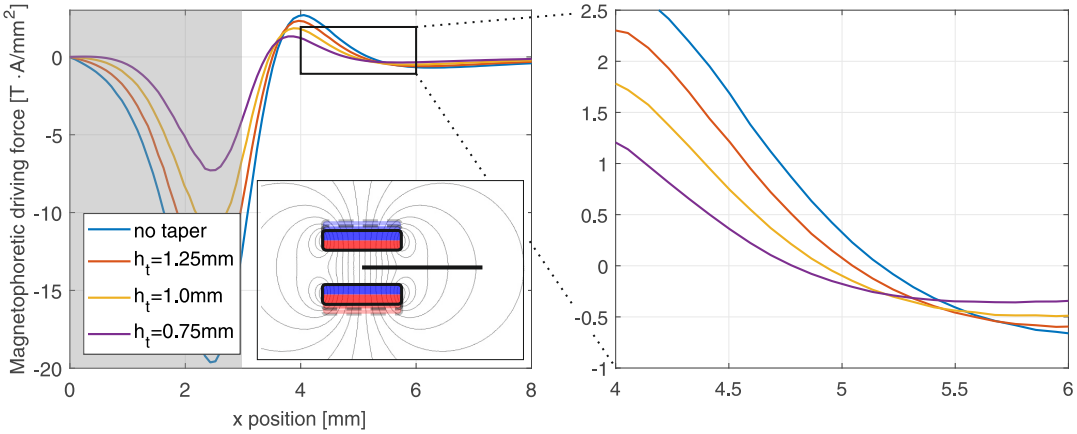
previously considered in the Double Magnet configuration analysis.

Figure 6.16a shows that for large aspect ratios ($h/w > 1$) the stable gathering position became unstable, where magnetic particles no longer drift to a specific area but move in opposite directions. This can be seen by the sign change of the magnetophoretic driving force. At the same time, small aspect ratios ($h/w = 0.1$) reduced the horizontal driving force because the magnetic $\mathbf{B}$ field and its gradient became smaller. Similarly, an increasing relative gap ratio, a/w, weakened the magnetic flux density and its gradient and thus, lowered the magnetophoretic driving force. Furthermore, the unstable gathering points, associated with $|\mathbf{B}| = 0$, are pushed toward the centre of the geometry as a/w increases and eventually ($a/w \geq 1$) are within the 3 mm wide fluidic channel (see Figure 6.16b).

However, besides the two ratios discussed above, the magnetic Quadrupole configuration introduces a nondimensional distance ratio b/a (see Figure 6.14), which is also considered here. For this reason, the magnetophoretic driving force was calculated in the area of the fluid channel ($x = \pm 1.5$ mm and $y = \pm 0.2$ mm) for different ratios b/a. Here, the vertical separation a was kept at 2 mm and only the horizontal distance b between the two double magnet configuration was changed. Due to the width of the iBidi channel ($w_f = 3$ mm), for distance $b < 3$ mm the magnet edges



(a) Inner taper



(b) Outer taper

Figure 6.12: Simulation of the magnetophoretic driving force for magnets with different angles of tapers. Taper angle is varied by changing the magnet thickness at the end of the taper between $h_t = 0.75$ mm and $h_t = 1.5$ mm. (a) Shows the magnetophoretic driving force when the magnets are tapered on the inside. (b) Shows the magnetophoretic driving force when the magnets are tapered on the outside. The magnets are simulated as N42 Neodymium magnets with original dimensions of 20 mm × 6 mm for length and width, respectively, and 1.5 mm for non-tapered height.

overlap with the channel and introduce an attractive force in their proximity. This would cause some beads at the edge of the channel to migrate toward the magnets. As this is an undesirable effect the analysis only considers values where $b \geq 3$. Figure 6.17 shows the vectors of the magnetophoretic driving force for the Quadrupole configurations at $z = 0$ for ratios b/a ranging from 1.5 to 3.

As the horizontal distance between the magnets increased, the absolute force de-

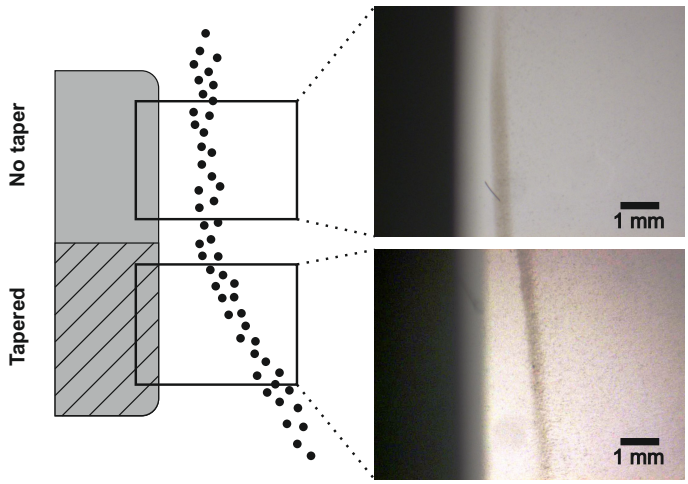


Figure 6.13: Static particle gathering band for the Double Magnet configuration using two tapered N42 NdFeB magnets. The magnets' original dimensions were 20 mm × 6 mm × 1.5 mm. The taper begins half way along the magnet and reduced the magnet thickness to half of its original thickness ($h_t \approx 0.75$ mm). There is an increase in the static equilibrium distance with decreasing magnet thickness.

creases, i.e. the driving force in x and y direction reduced. Thus, there is a trade-off between horizontal and the undesirable vertical driving forces. In this study, the best choice of distance b was determined by optimising the horizontal force so that beads move in the x direction toward their gathering position in the quickest possible manner. Given the physical limitation of the iBidi channel, which limits a to 2.6 mm, the optimal value of b was 3.5 mm.

6.3 Gathering line formation

In this section the formation of the gathering line is explored for different bead types using the magnetic field of the Double Magnet configuration. Bead suspensions with a high concentration ($10^6 - 10^8$ beads/mL) are required to make the gathering positions clearly visible. This is in contrast to the model developed in Chapter 2 for a diluted bead suspension, which determined trajectories of individual beads in the separation device. The aim here was different, and was to understand the dynamics and behaviour of the gathering process which requires the higher bead concentra-

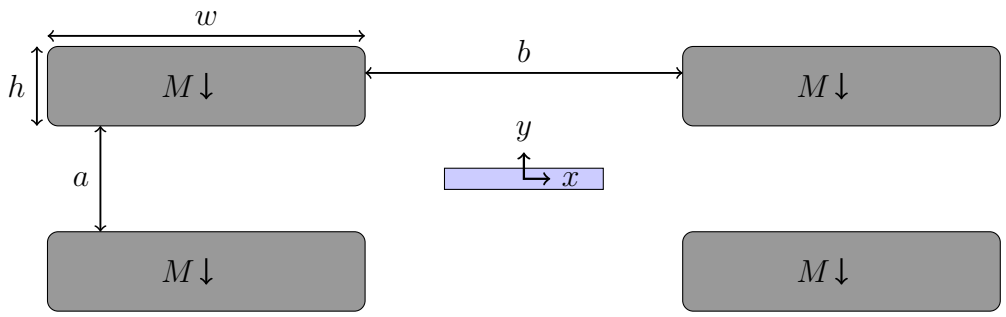


Figure 6.14: 2D slice diagram ($z = 0$) of the Quadrupole configuration used to generate the magnetic field for separation. The rectangular permanent magnets (grey) are set up in attraction, with their magnetization in the negative y direction. The microfluidic channel is located (light blue) in the centre of the two double magnet configurations. The parameters w, h and a describe the width, height and vertical separation for each pair of magnets (as previously defined). A new parameter b is the horizontal separation of the magnets as indicated in the picture. The schematic is not drawn to scale.

tions. Indeed, concentrated suspensions may occur in some separation applications, where higher throughput is required or applications that require particles to be trapped. Since no flow was required in this study, all experiments presented in this section were carried out in hydrostatic fluid chambers (see Section 3.3.4). As will be considered later, the gathering process is relevant to devices that use a pulse mode operation.

In the experiments here, all bead types formed an elongated elliptical band of high concentration around the stable gathering position that was visible by eye. The beads were densely packed in the centre of the ellipse with ends that tapered into narrow streams of reducing density. The particle band formed within a few seconds after the magnet configuration had been put in place. After less than 15 min, the particle band had mostly developed and no longer changed significantly over time, as shown in Figure 6.18. However, an absolute steady state, where no beads could be observed moving anywhere, could not be reached even after 12 hours.

The elliptical formation was attributed to the finite length of the magnets; the end effects of the magnets created a magnetic field gradient along the length of the

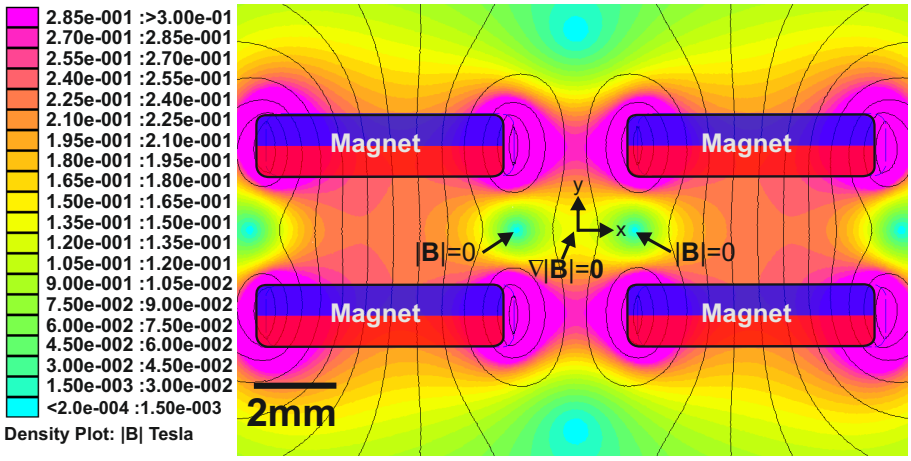
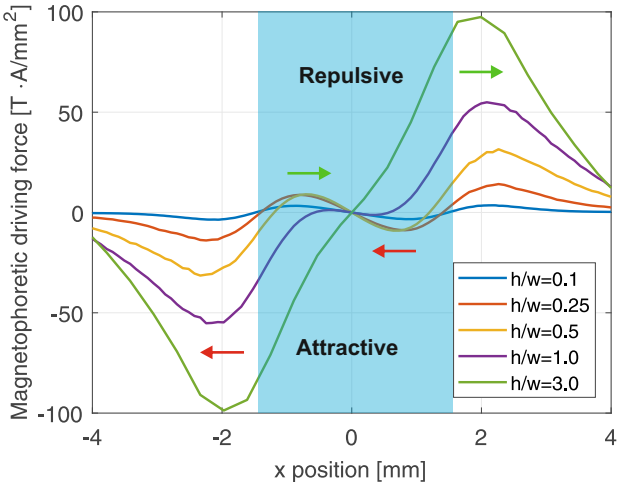


Figure 6.15: Modeling of the magnetic flux density **B** of the Quadrupole configuration at $z = 0$ when the vertical separation $a = 2.6$ mm. Three positions where the magnetic particles experience no horizontal magnetic driving force are indicated by point (1), (2) and (3).

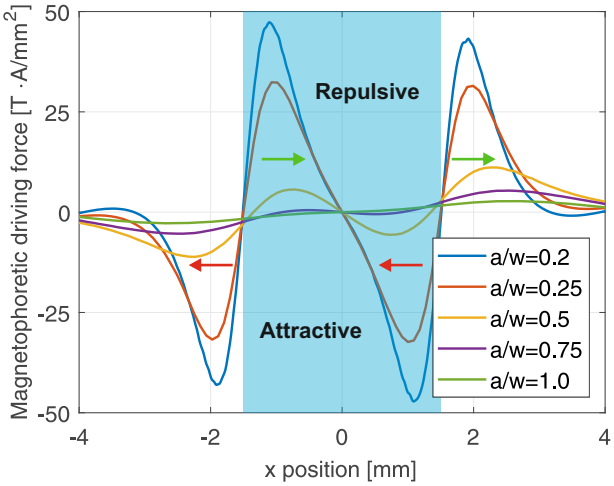
magnets (in the z direction) which cannot be neglected. There was a maximum **B** field at the middle of the magnets ($z = 0$) where particles migrated toward. This resulted in a higher density of beads in the vicinity of $z = 0$, and the elliptical shape.

The width of the elongated elliptical bands (w_b), measured as the minor axis of the ellipse, widened when the vertical separation between the two magnets was increased, while the major axis of the ellipse remained approximately constant in length; this behaviour is shown in Figure 6.19. Figure 6.19 also confirms that the gathering position moved when the vertical separation was increased (see Section 6.2.1.2 above). The increase in the width of the elliptical band was observed for each bead type considered. The band width at different separation distances was consistent for each bead type analysed, as shown in Figure 6.20. At larger relative separation distances ($a/w > 0.8$), the differences in width between the particle types deviated more significantly. This, however, was a result of the increased measurement uncertainty at larger separation distances.

When a paramagnetic bead experiences an external magnetic field, it will become magnetized and acquire a net magnetic dipole moment. Taking note of the direction



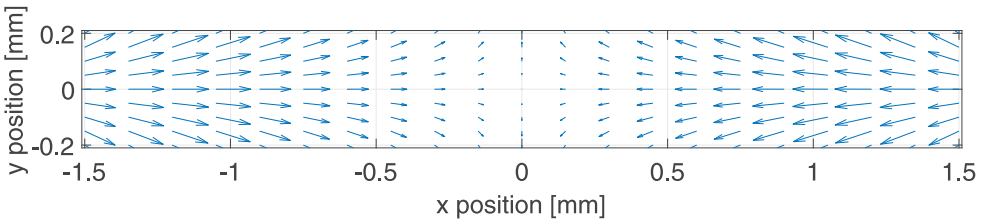
(a)



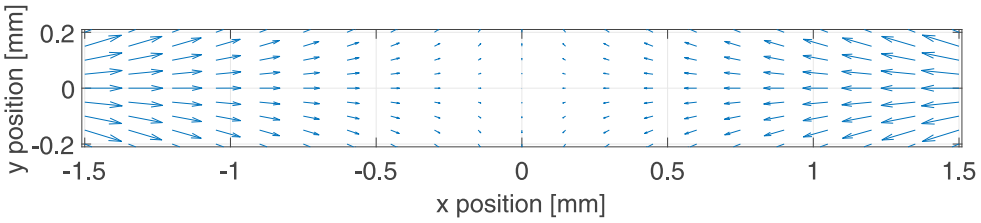
(b)

Figure 6.16: Simulation of the magnetic driving force along the x axis for different aspect and relative gap ratios. (a) Aspect ratio h/w ranging from $0.1 - 3$. (b) Relative gap ratio a/w ranging from $0.2 - 1.0$. The blue shading indicates the width of the 3 mm wide iBidi μ-slide III 3in3. Positive force (green arrows) implies beads moving from left to right, negative force (red arrows) implies beads moving to the left.

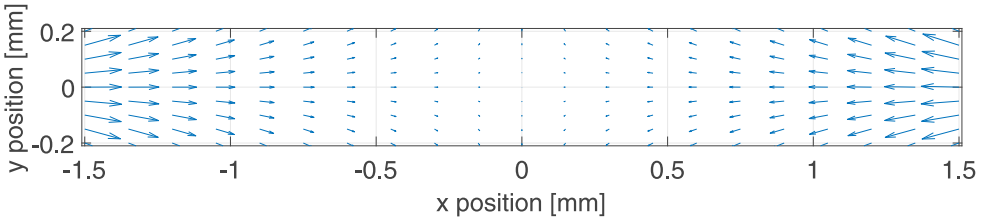
of the **B** field, the increase in width is attributed to the fact that adjacent beads repel each other when in the same plane because their induced dipoles point in a direction orthogonal to that plane. Thus, all beads compete for the space around them and become stationary when forces are balanced. Evidence of the formation of a regular lattice of single beads in a plane can be observed when using a lower



(a) $b = 4$ mm



(b) $b = 5$ mm



(c) $b = 6$ mm

Figure 6.17: 2D vector field of the magnetic driving of the Quadrupole configuration across the iBidi μ-slide cross-section at $z = 0$. The vertical gap a is kept constant at 2.6 mm and only the horizontal distance b is varied. From (a) to (c) the horizontal distance is increased from 4 mm to 6 mm. The vectored data shows how the magnetic driving force is reduced in x and y directions when b increases.

concentration of beads (see Appendix C). As the separation between the magnets is increased, the induced magnetic dipole in the beads decreases and it is assumed that this allows a wider spacing between the beads and hence a wider elliptical band.

Since individual beads repel each other, the widening effect of the elliptical band appears to be more prominent at higher concentration, as seen in Figure 6.21. At higher particle concentrations ($> 10^{10}$), particle agglomerates are more likely to occur. It could be seen that all bead suspensions naturally formed agglomerates in the vicinity of the gathering positions when particle interactions were significant.

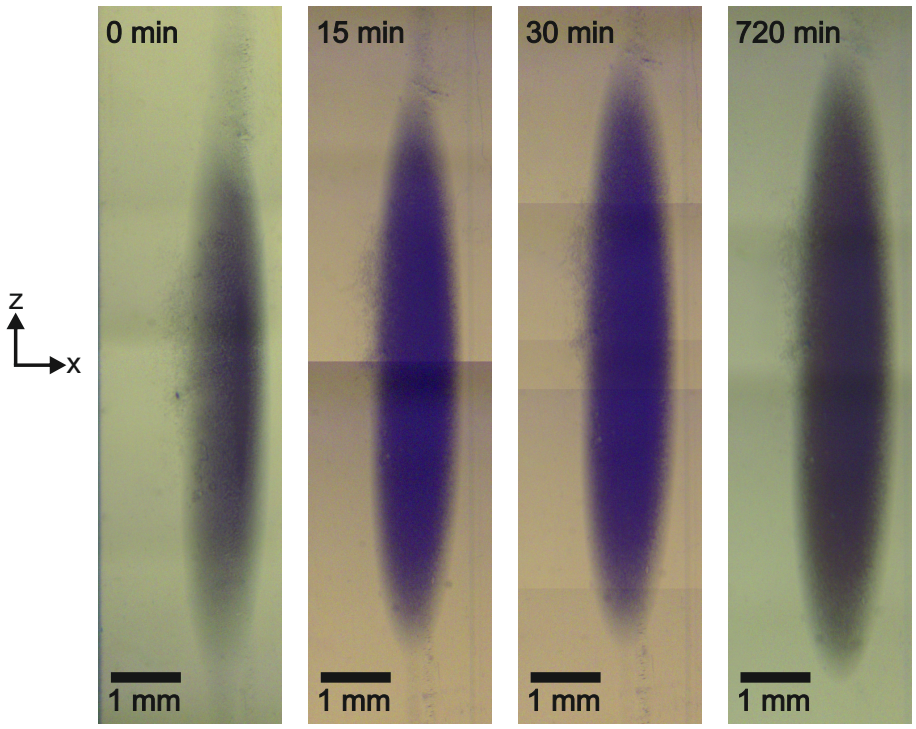


Figure 6.18: Elliptical band of beads after different time intervals. The elliptical bands are formed using the Double Magnet configuration, which is placed to the left. In order to make the band visible a bead suspension of Chemicell SiMAG beads with a concentration of 10^8 beads/mL was necessary.

The induced magnetic field causes neighbouring beads to aggregate when their dipole moments are aligned. This results in chains of beads aligned in the direction of the magnetic field lines toward the regions of higher magnetic field [360]. However, larger bead chains become unstable and collapse, forming larger and more complex aggregates [361], as seen in Figure 6.22. It is intuitive that these aggregates appear larger in size the closer they are to the centre of the equilibrium band. The higher density of beads is most likely to result in beads occupying a volume rather than competing for space in a plane. Examples of the aggregate patterns formed make it evident that forces due to bead interaction should be included when the density is high.

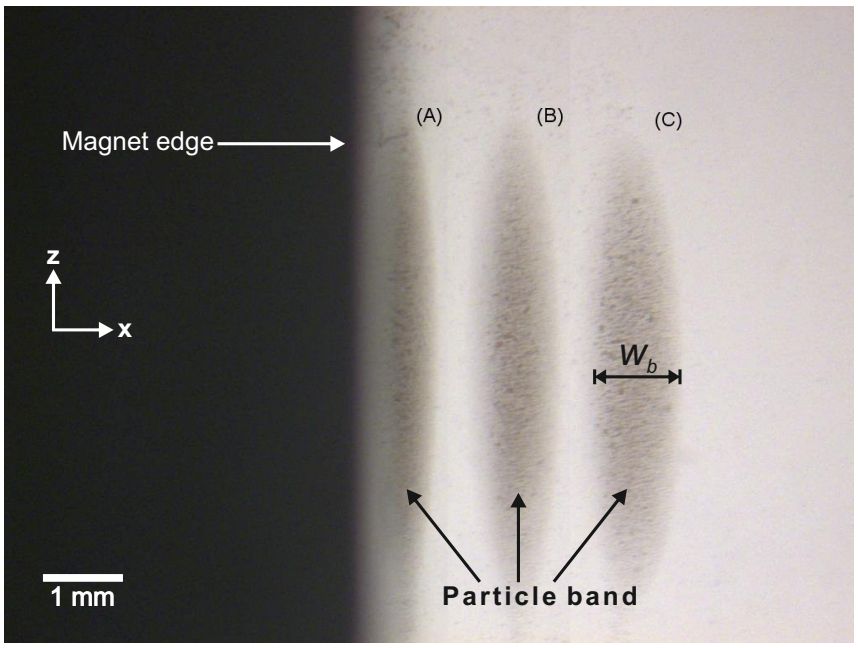


Figure 6.19: Overlay of three separate images visualising the formation of an elliptical band of magnetic beads (Chemicell SiMAG) around the gathering position at different vertical separations of the magnet: (A) $a = 3$ mm ($a/w = 0.5$), (B) $a = 4$ mm ($a/w = 0.66$) and (C) $a = 5$ mm ($a/w = 0.83$). Both the position of the static equilibrium and width of the band (w_b) increase with the magnet separation. To make the bead band visible, a bead concentration of approximately 10^8 beads/mL was necessary.

6.3.1 Gathering of particle agglomerates

In order to see whether aggregates have an effect on the elliptical band, suspensions of beads were pre-aggregated into large clusters by the temporary application of an external magnet. Figure 6.23 shows that pre-aggregated beads form narrower bands around the equilibrium position; the difference in the width of the band is more noticeable at larger vertical magnet separations (Figure 6.23c-6.23d).

The differences in the width of the band between the pre-aggregated and regular suspension is due to the relationship between the force on the beads and the random size of the aggregate. A larger cluster has a greater volume of magnetic material, resulting in a higher magnetic force. At the same time, a larger cluster induces a larger magnetic dipole, which can exert a larger repelling force. Thus, the width

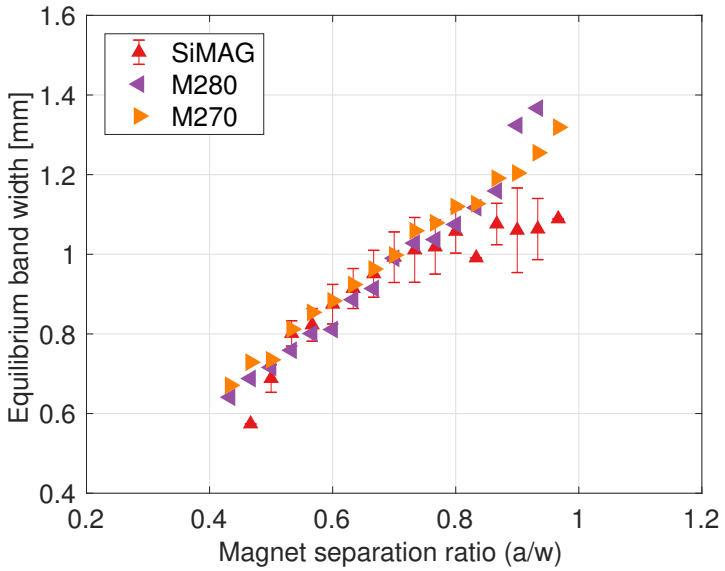


Figure 6.20: Width of the elliptical bead band around the equilibrium position of the Double Magnet configuration. The width of the elliptical band, measured as the minor axis of the ellipse, increases with increasing vertical magnet separation a. All particle suspensions use a concentration of $\approx 10^8$ particles/mL.

of the particle band is dependent on an equilibrium between the magnetic forces of the external field and the resultant induced magnetic field of the differently sized agglomerates. The relationship between the exerted magnetic force, the number of beads in the aggregate and mutual magnetisation, results in a complex network of connecting beads. This leads to a variation in the induced field that increases with the size of the aggregates [362]. Consequently, larger aggregates form a narrower band, with gaps between neighbouring aggregates. Larger spacing between the aggregates can be seen in Figure 6.23c compared to Figure 6.23a, indicating that the local field generated by the bead clusters was more influential when the magnet separation, a, was larger. What is certainly clear, is the fact that the beads did not compact into the tightest possible volume due to interaction with their neighbours.

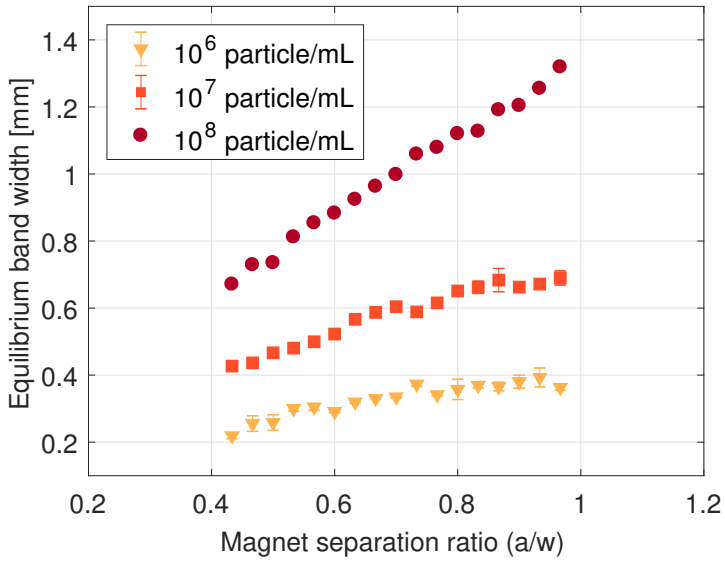


Figure 6.21: Width of the elliptical particle band around the equilibrium position for different particle suspension concentrations. The particle suspension is made of Dynabeads M270 particles with a particle concentration between 10^6 particles/mL and 10^8 particles/mL.

6.4 Discussion

The magnet configurations formed a stable gathering line outside of the magnet assemblies, where particles migrated toward. Initially, it might be thought that the magnetic beads should form a thin line due to the forces from the magnets. This is because any finite force on the bead, however small, would result in a drift velocity according to the equilibrium between the magnetic force and Stokes drag. The formation of a thick particle band demonstrates that particle interations should not be neglected at high particle concentations. The induced magnetic dipole fields of the beads caused other beads that were in close proximity to form a chain along lines of flux when their dipole moments align. At high bead concentrations, as seen in Chapter 4, more complicated 3D structures were formed and easily observed [206, 363, 364]. When beads are side-by-side, they no longer agglomerate but repel each other, which prevents them from approaching any closer. At lower concentrations when beads are able to arrange in a plane, the beads form a regular array with

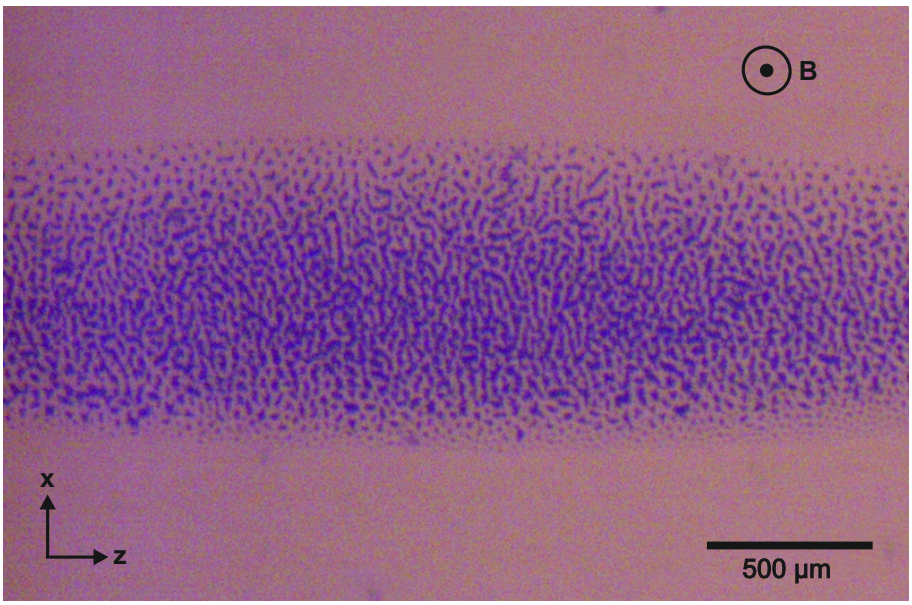


Figure 6.22: Close up view of the elliptical band of beads. The beads around the equilibrium position form agglomerates, larger in size in the centre of the elliptical band. The particles do not form a regular arrangement, but rather varying separation. The band was formed using Dynabeads' M270 with a concentration of $\approx 10^8$ particles/mL. The field lines of the applied magnetic field are pointing out of the plane.

an equilibrium distance between them. Clusters, in contrast, experience a larger repelling force between each other than single beads, which increases the equilibrium distance between them. The experimental results of the pre-aggregated suspensions support this interpretation because larger areas between aggregates devoid of beads could be seen.

Separation of biological entities for diagnostic purposes benefit when they are able to give a reliable result in a short time. The particle band, which separates the beads from the sample flow, typically formed within a few seconds. The band was visible by eye and did not appear to change significantly after 15 minutes in a hydrostatic environment. The time needed to gather the beads was within the time frame of other recently published batch separation processes, where separation times between $2-30$ minutes have been reported [199, 365]. The separation kinetics, however, are more complex when the beads are of different size or have a cell attachment, which

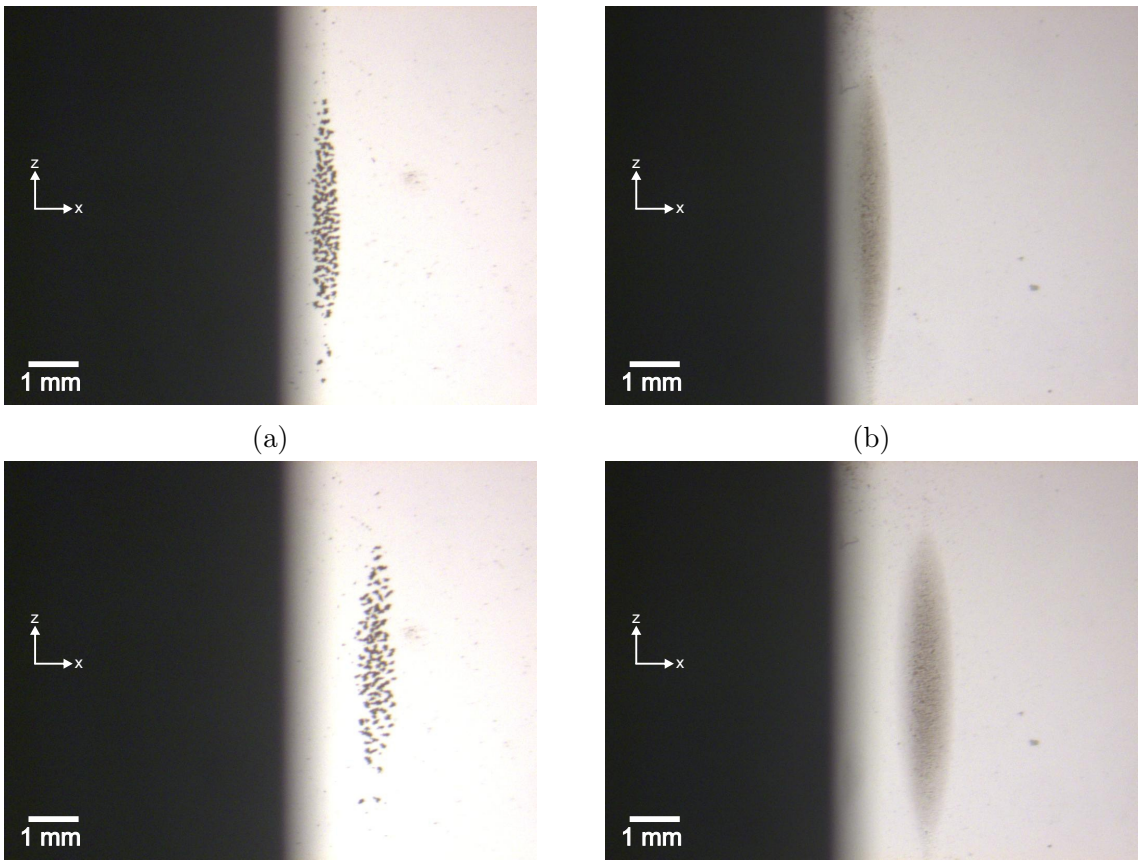


Figure 6.23: Experimental comparison of the gathering band formation between a fully suspended bead suspension (right hand side) and pre-aggregated bead suspension (left hand side). The vertical magnet separation a is increased from $a = 3.2$ mm to $a = 4$ mm in (a) to (c) and (b) to (d), respectively.

influences the gathering time [366–368].

The magnetic fields of the two proposed magnet configurations have the unique property, i.e. paramagnetic particles can experience a repelling force, which is normally only exploited for diamagnetic objects (see Section 1.4.2.1). The advantage of using diamagnetic objects is that many biological entities are diamagnetic (e.g. white blood cells), which enables a label-free separation. However, the diamagnetic effect is weak, with susceptibilies five order of magnitude smaller compared to the superparamagnetic beads used in this thesis [236, 239, 369, 370]. To demonstrate a similar separation efficiency with diamagnetic entities compared to what is achieved

with paramagnetic particles, larger particles ($5 - 20$ μm) suspended in a paramagnetic salt solution or ferrofluids have been used [371–374]. Another approach is to apply higher magnetic fields (up to 10 T) using superconducting magnets [236, 238]. However, most diamagnetic separation demonstrations reported in the literature could have achieved the same direction of magnetophoretic force by switching to paramagnetic particles and placing the magnet on the other side of the channel. If the magnet, however, can only be placed on one side of the channel due to geometry or fabrication restrictions and only a pushing force allows separation, the Double Magnet configuration provides an effective alternative to diamagnetic separation.

In the literature, diamagnetic repulsion has also been used for particle focusing using two magnets with their like poles facing [375–378]. The Quadrupole configuration can be used to achieve a similar focusing effect but for paramagnetic particles. It is expected that the Quadrupole configuration has the ability to achieve a stronger focusing effect over a wider distance than reported in [378], which allows for higher flow rates and thus quicker particle focusing.

Magnetic particle separation, however, has often been performed in a purely attractive manner, rather than repulsive. The Double Magnet configuration achieved a maximal attractive magnetic drive force of 1.5 TA/mm^2 given the constraints of the fluid channel. This is comparable to other magnetic separation devices where a permanent magnet is used; e.g. Xia *et al.* [222] achieved $0.8 - 3.6$ TA/mm^2, Pamme *et al.* [196, 379] reported $\approx 4 - 8$ TA/mm^2 and Afshar *et al.* [223] estimated the driving force of their design to be $7 - 20$ TA/mm^2, respectively. HGMS systems presented by Han *et al.* [219, 220] and Furlani [259] (see Chapter 1) report driving forces between $50 - 77$ TA/mm^2, which was achieved by integrating the magnetic structure into the fluid device and thus being in close proximity to the particle suspension. However, the integration of the magnetic components makes the channel fabrication more cumbersome.

6.5 Conclusion

Two new magnetic separation geometries were presented and analysed. Both configurations generated a magnetic field where the force vector on a paramagnetic bead changed its sign depending on position. This is novel compared to previous magnet configurations where particles experience a force in one direction only. The change in vector sign creates a line where magnetic beads experience no horizontal magnetic force and thus gather. Beads assembling along a gathering line as part of the separation process is a unique feature introduced in this thesis, which has potential for increasing separation efficiency.

The geometry parameters of the magnetic configurations determined the position of the gathering regions and also the magnitude of the magnetophoretic driving force. To establish a high driving force in the x direction and thus short separation time, the vertical gap a between the magnets should be as small as possible. Due to the thickness of the iBidi μ-slide, the vertical separation a of the magnets was limited to a minimum of $a_{min} = 2.6$ mm. For the Quadrupole configuration, the additional parameter b (horizontal gap between the two magnet pairs) maximised the horizontal driving force when being set to $b = 3.5$ mm.

The aspect ratio simulations concluded that magnets with low aspect ratios had a stronger separating power; i.e. thin rather than bulky bar magnets were more suitable, which also had the benefit of keeping the device compact. The relative vertical magnet separation simulations were important in providing a straightforward method for manipulating the position of the isolated beads. Varying the magnet separation could be used to adjust the particle trajectories during continuous flow. Likewise, the simulations of the tapered magnets showed the possibility of continuously altering the particle trajectories. Additionally, the reduction in the magnetophoretic driving force as the taper increased could be useful for releasing the separated beads back into the free-flow of the stream and thus avoiding trapping

beads.

The Quadrupole configuration exerted approximately three times higher magnetophoretic driving force compared to the Double Magnet configuration. In cases where the separation time needs to be short or a high throughput is required, the quadrupole configuration is more suitable.

A study using the Double Magnet configuration showed that beads did not gather into a thin line, but rather formed an elliptical band with a finite width which could be seen by eye. This implies certain constraints on the design of the fluid channels. Therefore, the outlet channel, through which the magnetic particles ultimately exit, needs to be of a sufficient width in order to receive all the beads in the gathered band. Since the maximum width of the elliptical band varies with the bead concentration, the dimensions of the exit channel will be a function of concentration.

Chapter 7

Magnetic particle separation simulation

7.1 Introduction

As discussed previously, magnetic particles can be manipulated using an external magnetic field, when in a surrounding liquid; this is known as magnetophoresis (see Chapter 4). The manipulation of magnetic beads allows for sorting or separation.

In this chapter, the effect of an external magnetic field on the trajectory of magnetic beads was simulated using the Lagrangian tracking scheme. Due to the assumed low particle concentration and small particle size, inter-particle forces could be neglected and one-way coupling could be assumed. A detailed description of the modelling approach can be found in Section 3.10.

7.2 Continuous separation of the two novel magnet configurations

The separation efficiency of the two presented magnet configurations (see Chapter 6) was simulated and experimentally verified. Two separation strategies were introduced and investigated: *continuous* mode and *pulse* mode.

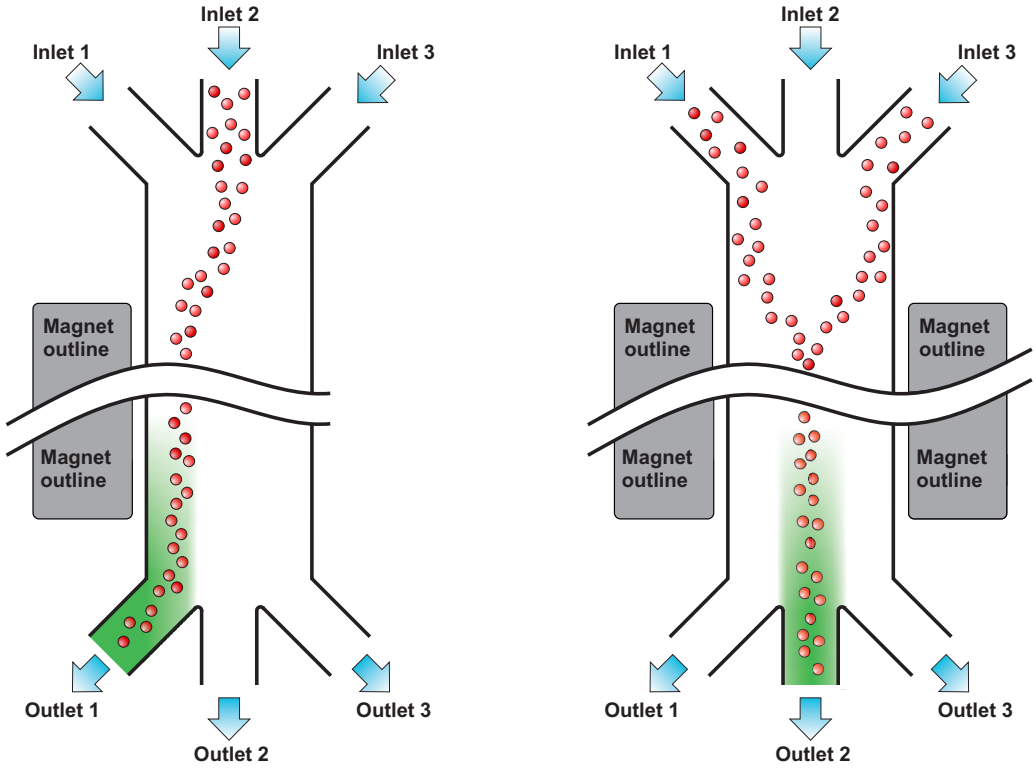
The separation efficiency of both magnet configurations are evaluated by using a Monte Carlo method where 400 individual bead trajectories were simulated, as described in Section 3.10 and Section 3.11. Depending on the magnet configuration, the beads were introduced through the centre inlet (inlet 2 in Figure 7.1a) and assumed to leave outlet 1, or through the sheath flow inlets (inlet 1 and inlet 3 in Figure 7.1b) and exit through outlet 2 for the Double Magnet or Quadrupole configuration, respectively.

The performance of the two magnet configurations used with the microfluidic separation device was determined by their collection efficiency ζ, which could be formulated in either absolute or relative terms. The absolute separation efficiency, ζ_a, is defined by the fraction of magnetic particles that enter the separation channel and leave the channel through the designated exit, whereas the relative separation efficiency, ζ_r, takes the ratio of the number of particles exiting the designated channel over the total number of particles from all exits. The two separation efficiencies can be mathematically expressed as follows:

$$\zeta_a = \frac{N_{out}^k}{N_{in}} \tag{7.1}$$

$$\zeta_r = \frac{N_{out}^k}{N_{out}} \tag{7.2}$$

where N_{in} and N_{out} are the total number of particles entering and leaving the system, respectively and N_{out}^k is the number of particles leaving the designated exit k. In this



(a) Double Magnet configuration (b) Quadrupole configuration

Figure 7.1: Schematic showing where magnetic beads are introduced into the iBidi separation device and where they expect to exit for the two different magnet configurations. (a) In the case of the Double Magnet configuration, magnetic beads are introduced through the centre inlet (inlet 2) and are considered separated if they exit through outlet 1. (b) For the Quadrupole configuration, magnetic beads are introduced through the two sheath flows (inlet 1 and inlet 3) and are expected to exit the device through outlet 2. The green shading indicates where beads are considered separated for each configuration.

study, the relative separation efficiency are simply referred to as *separation efficiency* if not stated otherwise.

7.2.1 Magnetic separation using the Double Magnet configuration

The separation efficiency of the novel Double Magnet configuration presented in Chapter 6 was simulated as described in Section 3.11.1. In the simulation, magnetic particles entered the iBidi μ-Slide III 3in3 separation device through inlet 2 and

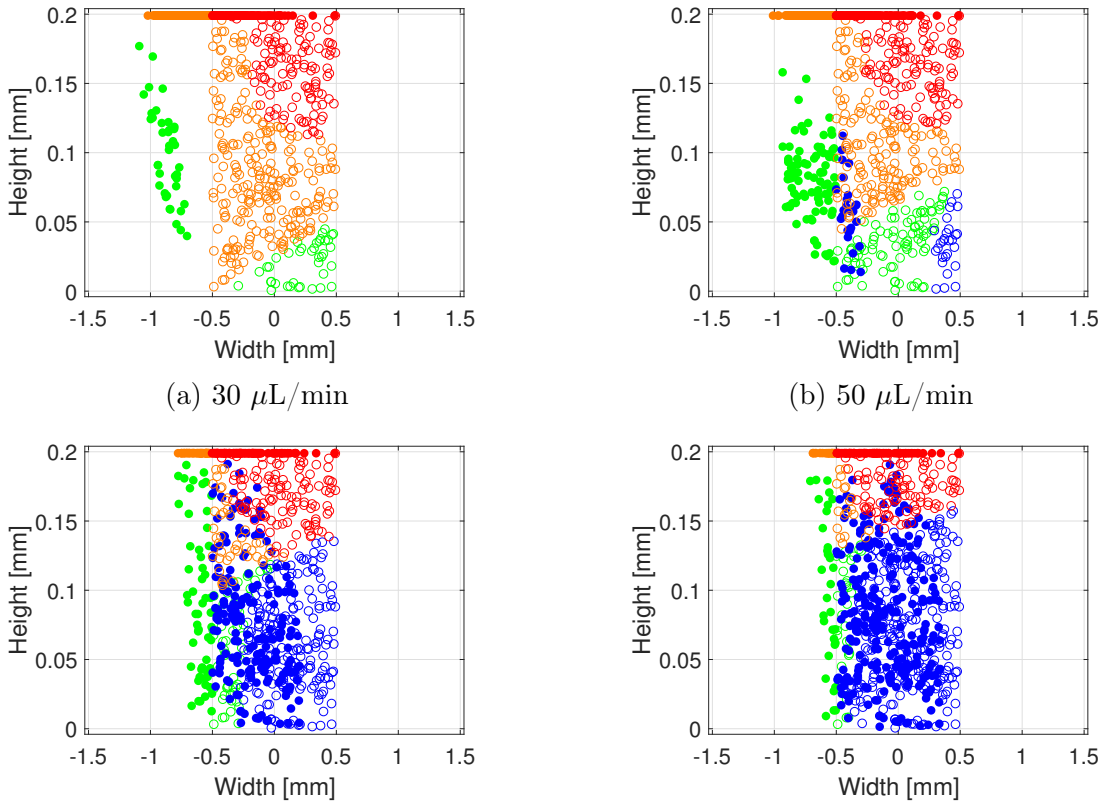
were considered to be separated as soon as they had moved into the highlighted area (green highlight) in Figure 7.1a and had reached the end of the fluid channel. Bead trajectories that touched the inner surface of the channel were terminated and those particles were considered to be trapped in approximately zero flow rate due to the no-slip boundary condition.

The individual trajectories of beads moving along the separation device were computed. Figure 7.2 shows the initial and final position of the magnetic beads across the channel cross-section, after their trajectory simulation had completed or terminated. Only the top half of the fluid channel ($|y| \leq 0.2]$ mm) was simulated. The different colours show beads (i) which reach the end of the channel and are successfully separated (green), (ii) reach the end of the channel but do not get separated (blue), (iii) get successfully separated but get trapped at the top of the channel surface (orange) or (iv) do not get separated and get trapped (red).

Considering Figure 7.2 it is evident that a limited number of beads were separated. Only beads entering at specific positions across the inlet (green circles) were drawn into the buffer flow without terminating at one of the internal surfaces of the channel; there was a unique area of success across the inlet cross section, which was also flow rate dependent. The reason why some beads were trapped was due to the vertical forces acting on the beads, causing them to drift upward toward the no-slip boundary condition at the channel wall. Thus, beads that touch the surface no longer move forward and are considered as trapped

Figure 7.3 presents the simulated separation efficiency and bead throughput of the Double Magnet configuration for the different magnetic bead types at different continuous flow rates. The susceptibilities were set to the values found in the bead magnetization study (see Section 4.4) and also adjusted according to the local magnetic field strength during the simulation.

It can be noted in Figure 7.3, that the separation efficiency and the particle through-

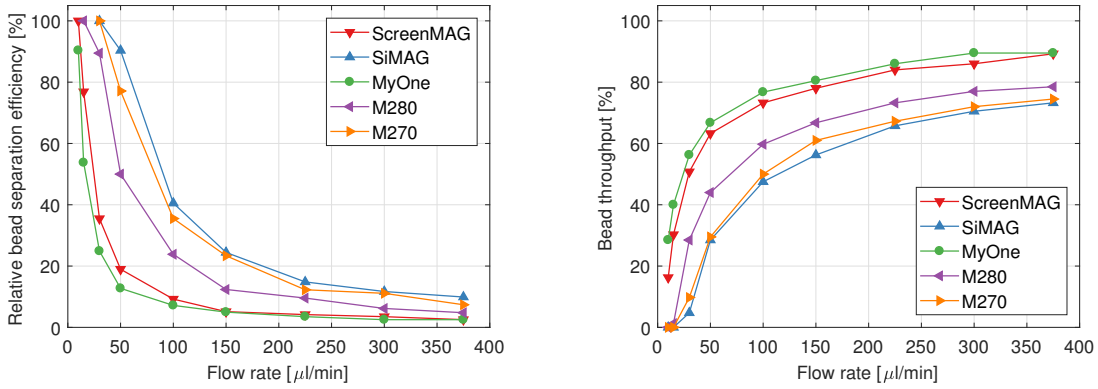


(a) 30 μL/min (b) 50 μL/min

(c) 150 μL/min (d) 300 μL/min

Figure 7.2: Scatter plot of the starting and end position of the bead trajectories for different flow rates ranging from 30 μL/min to 300 μL ($\bar{u}_p \approx 0.4 - 4.2$ mm/s) in (a)-(d). The open circles represent the starting position and the filled circles show their final position. The simulation is for the Double Magnet configuration while the particles have the properties of Chemicell SiMAG beads. The different colours correspond to the following: *green*-beads reach the end of the channel and get successfully separated, *blue*-beads reach the end of the channel but do not get separated, *orange*-beads get successfully separated but get trapped at the channel surface and *red*-beads do not get separated and get trapped. Higher separation efficiency is indicated by a large number of solid green beads compared to the total of solid green and blue beads.

put were inversely proportional. Also, using beads of higher magnetophoretic mobility improved the separation efficiency, with reduced throughput; i.e. there was a trade-off between the separation efficiency and throughput. For example, to have a separation efficiency of approximately 80%, which is comparable to separation efficiencies found in the literature, about 30% of the introduced beads can be collected at the designated outlet (see Figure 7.3).



(a) (b)

Figure 7.3: (a) Continuous separation efficiency and (b) throughput of the Double Magnet configuration for different bead types and flow rates. The flow rates range between 10 μL/min ($\bar{u}_p \approx 0.14$ mm/s) to 375 μL/min ($\bar{u}_p \approx 5.2$ mm/s). The bead properties are set to the physical properties found in Chapter 4.

The results obtained by simulation were verified experimentally for various flow rates, as described in Section 3.11.2. In these experiments SiMAG-Silanol beads (Chemicell) were used because they have a high magnetophoretic mobility (see Chapter 4) and sediment more slowly than Dynabeads M270. As described in Chapter 3, a bead concentration of 10^6 beads/mL ($v_p \approx 10^{-7}$) was used for the suspension, which is considered as a low concentration because $v_p < 10^{-6}$ (see Chapter 2.2.2).

Observations recorded with the CCD camera show a visible separation in the experiment and that the magnetic beads are continuously deflected by the magnet from the central sample flow into the buffer flow, as shown in Figure 7.4. This demonstrates that separation of magnetic beads was achieved.

The separation efficiency of the separation configuration using the Double Magnet was determined by analysing the collected outlet samples using flow cytometry. At flow rates $\leq$ 30 μL/min ($\bar{u}_p \approx 0.4$ mm/s), no beads were detected at any of the three outlets. Therefore, a higher flow rate ($>$ 30 μL/min) was needed for a viable throughput. Measuring the samples at the three outlet channels at total flow rates $>$ 150 μL/min indicated that more than 55% of magnetic beads had not

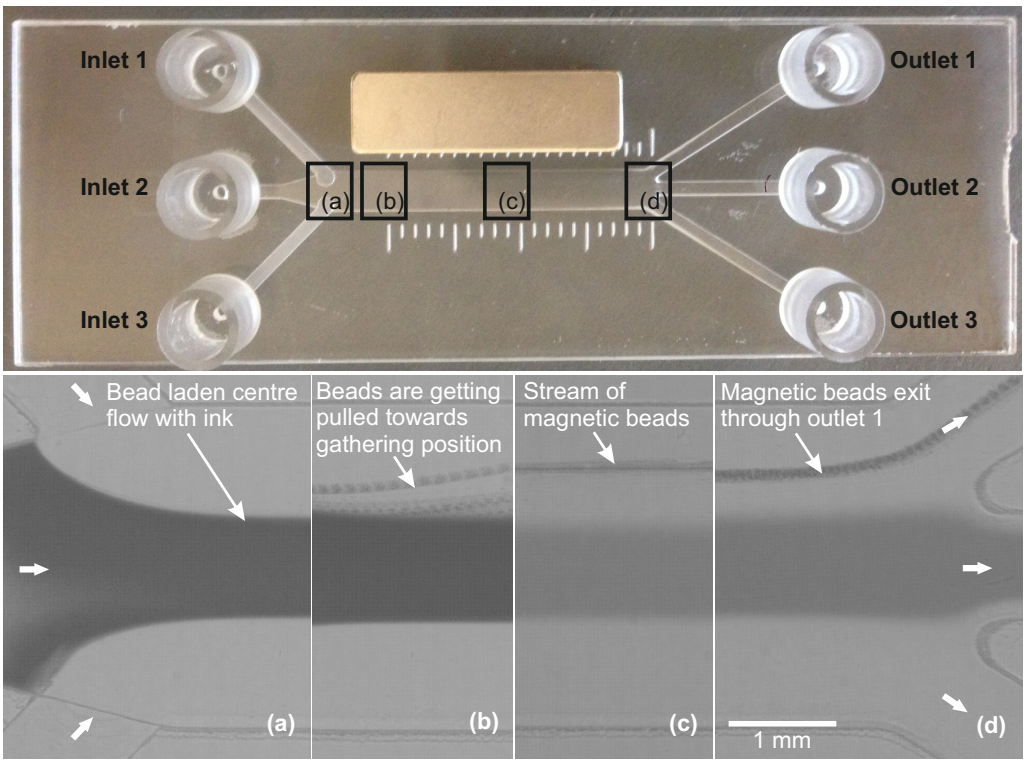


Figure 7.4: Gathering and streamlines of superimposed images of magnetic beads (Chemicell SiMAG) during the continuous magnetic separation experiment with the Double Magnet configuration. Magnetic beads are introduced through inlet 2 and expected to exit the device through outlet 1. Images (a)-(d) show the streamlines of the magnetic beads at different positions along the iBidi fluid channel when a flow rate of 150 μL/min is applied. The flow direction at the inlets and outlets is indicated by the bold arrows in (a) and (d).

been sufficiently deflected from the main sample flow and thus, not separated. These beads travelled through the device along their streamlines and exited through outlet 2, as depicted in Figure 7.5. This shows that an interaction time with the magnets of approximately $\approx$ 10 seconds was not sufficient to draw the particles from the sample into the buffer flow. A more detailed view of the continuous separation in Figure 7.5 can be found in Appendix B.

As expected from the numerical simulations, the separation efficiency of the Double Magnet configuration was found to be negatively correlated with the total flow rate (see Figure 7.5). The results of the experimental separation efficiency for the Double Magnet configuration, however, were $10\% - 15\%$ higher compared to the

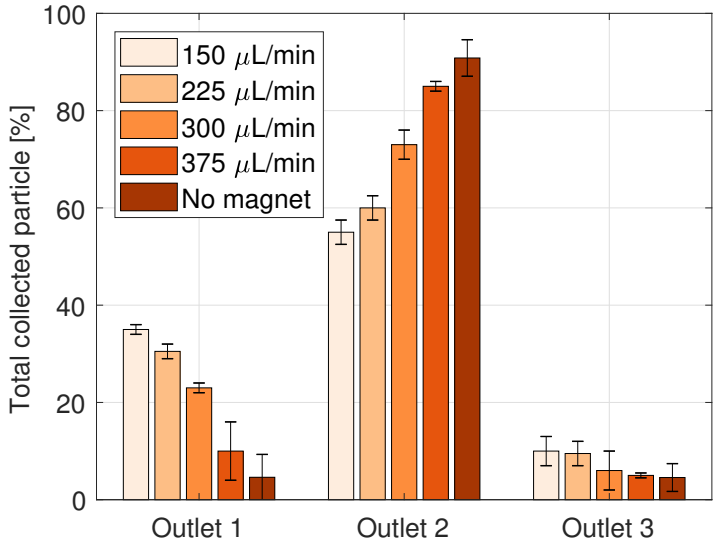


Figure 7.5: Experimental results of continuous separation efficiencies with the Double Magnet configuration for different flow rates. The flow rates stated here are the sum of all inlet flow rates while keeping their inlet flow rate ratios at $1:1:1$ across the different inlets. The experiment has been repeated 3 times for all shown flow rates.

simulation at corresponding flow rates. The better performance is most likely due to the fact that in the experiment, beads had a tendency to agglomerate and were then deflected more quickly than individual beads; this is an effect not currently modelled. The samples collected for the flow cytometer were ultrasonicated prior to the measurement to break up bead agglomerates, and therefore would have been counted as individual beads in the sample analysis. For flow rates > 375 μL/min ($\bar{u}_p \approx 5.2$ mm/s), the separation efficiency of the model and the experiments were comparable, because the fluid dynamics becomes the dominant factor whereas the effect of agglomerates were less significant.

The clearly visible separation, apparent in the photograph of Figure 7.4, suggests that an even higher separation efficiency should be obtained compared with that determined from the bead count, i.e. the beads appeared to be strongly gathered due to the dark band in the image, but the flow cytometer measurements did not support the anticipated separation efficiency. Further examination using higher

magnification revealed beads and agglomerations *stuck* at the top or the bottom of the channel due to the vertical magnetic forces, leading to a bold band of stationary beads. It is assumed that the distribution of the beads across the entire area of cross-section of the inlet channel and possible misalignment of the magnets contributed to the lower than expected performance.

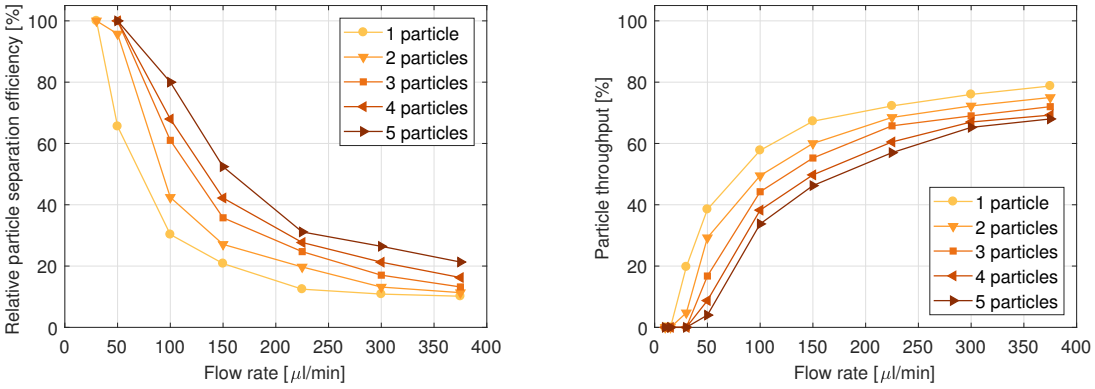
Based on the observations in the experiments the effect of bead agglomerates as well as magnet displacement errors was simulated as discussed in the following sections. Further, the influence of a cell cargo attached to a magnetic bead was investigated.

7.2.1.1 Effects of magnetic bead agglomerates

As soon as superparamagnetic beads are exposed to a magnetic field, they become magnetized and start attracting other magnetic particles in their vicinity. This causes beads to form agglomerates as can be observed in the magnetophoretic study for magnetic bead agglomerates (see Chapter 4). Even when starting from a fully suspended sample at low concentration ($\approx 10^6$ beads/mL), bead agglomerates can quickly form and bead-bead interactions can occur if beads happen to be close enough. Therefore, in order to understand the behaviour of more complex suspensions the trajectories of bead aggregates also needs to be studied.

The bead agglomerate model presented in Section 4.3 showed that the drag force on a chain of beads did not increase linearly with the number of beads, but its magnetic force did. This model was implemented in the simulation. Bead chains of up to 5 beads were studied here. Figure 7.6 shows the separation efficiency and throughput for different agglomerate sizes and flow rates.

Larger clusters experienced a higher magnetophoretic drift velocity (see Section 4.2.3), which explains the increasing relative separation efficiency in Figure 7.6a. It was noted, however, that the increased magnetically induced velocity also caused larger clusters to get stuck at the inner surface of the fluid channel which led to a lower



(a) (b)

Figure 7.6: (a) Magnetic separation efficiency and (b) throughput for different bead agglomerates using the Double Magnet configuration. The flow rates range between $30 - 375$ μL/min ($\bar{u}_p = 0.4 - 5.2$ mm/s) in the main channel. Bead agglomerates which have crossed the $x = -0.5$ mm line without colliding with an inner surface are considered to be separated. The bead properties for a single magnetic bead are set equal to the properties of a 1.0 μm sized SiMAG-Silanol (Chemicell) particle.

overall particle throughput (see Figure 7.6b).

7.2.1.2 Effects of magnet displacement error relative to the microfluidic separation device

The specific flux density patterns seen in Chapter 6 are only valid as long as the microfluidic separation device (see Section 3.3.2) is correctly positioned, i.e. placed along the central plane ($y = 0$) between the two magnets. If the microfluidic separation device is placed either side of this central position such that $y \geq 0.7$ mm, the gathering points vanish. Therefore, care needs to be taken when the device is assembled requiring sub-millimetre accuracy. Figure 7.7 shows a schematic of the critical vertical displacement used in this study of misalignment error. Misalignment of the two magnets in the horizontal $x - z$ plane, such that the two magnets are offset relative to each other, is less likely because the magnetic attraction force pulls the two magnets automatically into alignment with one exactly above the other. Thus, a horizontal magnet misalignment was not considered here.

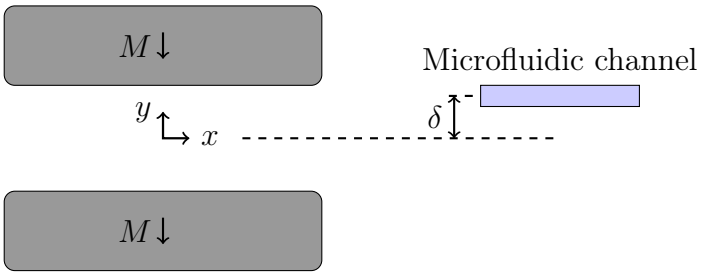
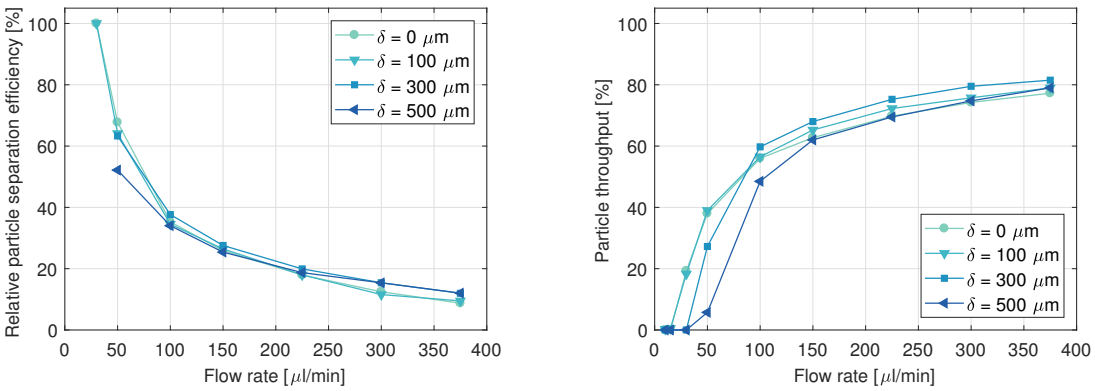


Figure 7.7: Schematic of vertical misalignment of the microfluidic separation device from its central plane ($y = 0$) position. The parameter δ is the distance the microfluidic channel is misplaced out of the centre.

Performance with displacement errors of the channel in the y direction at values of $\delta = 100$ μm, $\delta = 300$ μm and $\delta = 500$ μm was simulated; offset errors greater than 0.5 mm were regarded as unlikely. The $\mathbf{B}$ field inside the fluid channel was no longer symmetrical about the x axis due to the relative displacement of the channel compared to the magnets. Bead trajectories were simulated across the entire cross-section of the centre inlet channel (channel 2), with twice as many beads as in the previous simulations. Figure 7.8 shows the separation efficiency and the particle throughput for different flow rates and different channel offsets.



(a) (b)

Figure 7.8: (a) Magnetic separation efficiency and (b) bead throughput for flow rates ranging between $30 - 375$ μL/min ($\bar{u}_p = 0.4 - 5.2$ mm/s) in the main channel. The plot shows the results for a vertical displacement of the magnets of $\delta = 0$ μm, $\delta = 100$ μm, $\delta = 300$ μm and $\delta = 500$ μm.

The results in Figure 7.8 suggest that a small positive misalignment ($|\delta| > 0$) is ad-

vantageous for the magnetic separation process at low flow rates ($\dot{Q} \leq 100$ μL/min), while at higher flow rates ($\dot{Q} > 100$ μL/min) the effect of the misalignment becomes almost insignificant. This behaviour is caused by the fact that at higher flow rates beads have less time to interact with the magnets.

It is interesting to see that at small flow rates the relative separation efficiency is not a monotonic decreasing function with respect to the parameter δ. Due to the complex force pattern, different offset values of δ result in different relative separation efficiencies for different flow rates. The separation efficiency is dependent on what percentage of the cross-section of the fluid channel lies above or below the $y = 0$ symmetry plane. The more the fluid channel is displaced from its symmetry position (upwards or downwards), the larger the force on the beads in the vertical direction. There is a trade-off between the number of beads separated and the number of trapped beads. A larger offset does not necessarily impact the separation efficiency, but has a strong influence on throughput.

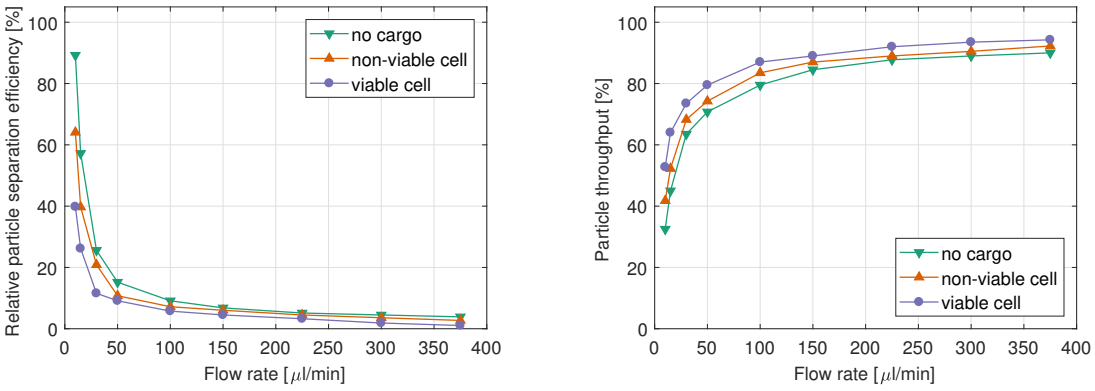
Since the uncertainty of the particle trajectories increases with a larger displacement error, the fluid channel should be carefully positioned at $y = 0$.

7.2.1.3 Effects of a cell cargo attached to a magnetic bead

For magnetic cell separations, a cell is attached to the magnetic beads as a cargo. Such biological cargo is normally nonmagnetic, or only weakly para- or diamagnetic, compared to the superparamagnetic bead [370, 380, 381].

For a cell bound to a magnetic bead, the model given in Equation 4.1 and Equation 4.2 predicts a smaller magnetophoretic drift velocity, and thus mobility, for the bead complex as a whole compared to a single magnetic bead. Wise *et al.* found that the magnetophoretic mobility of $1.05 - 2.8$ μm sized magnetic beads with a single 1.0 μm sized nonmagnetic spherical particle attached is reduced by $15 - 25\%$ [368]. The mobility of the bead complex is further reduced with increasing number of at-

tachments of nonmagnetic particles and their diameter. Additionally, Wise *et al.* compared the magnetophoretic mobility of Dynabeads MyOne microspheres, when attached to single living and dead *E. coli* bacteria. Such cell-bead complexes were observed to travel at a velocity approximately 49% (living) and 75% (dead) of that of a single bead with no cell cargo. In all cases observed, the nonmagnetic attachment aligned behind the magnetic bead in the direction of travel to reduce drag [368]. Figure 7.9 shows the relative separation efficiency and throughput for Dynabeads MyOne microspheres when they have a living or dead cell bound to them. For comparison, the data is also presented for an individual Dynabeads MyOne microsphere with no cell cargo attached.



(a) (b)

Figure 7.9: (a) Magnetic separation efficiency and (b) throughput for different total flow rates, ranging between $30 - 375$ μL/min ($\bar{u}_p = 0.4 - 5.2$ mm/s) in the main channel for beads with a viable or non-viable *E. coli* bacteria attached to a magnetic bead. The simulation is done for the Double Magnet configuration with the bead and mobility properties set to the experimentally found properties for Dynabeads MyOne in Chapter 4 and by Wise *et al.* [368].

7.2.2 Magnetic separation using the Quadrupole configuration

The Quadrupole configuration has potential for improved separation efficiencies due to its higher magnetophoretic force compared to the Double Magnet configuration

(see Section 6.2.2). However, there are higher vertical (y direction) forces, causing more beads to become trapped in the system. In order to investigate the vertical forces, three different magnet geometries for the Quadrupole configuration were modelled; simple bar magnet, tapered magnet and parabolic magnet. The three magnet geometries are shown in Figure 7.10(a). Figures 7.10(b)-7.10(c) show the simulated separation efficiencies and the corresponding particle throughput of the various magnet shapes derived from the models. The trajectories were simulated as outlined in Section 3.11.1 with the particles introduced in inlet 1, and separated from the sample flow into channel 2, as shown in Figure 7.1b.

Each magnet geometry in Figure 7.10(a) generates a different magnetic flux field and magnitude. The parabolic magnet generates a smaller horizontal magnetic driving force than the tapered or bar magnet and therefore has a lower separation efficiency across most flow rates, however, the parabolic shape reduces vertical forces on the magnetic particle, which improves particle throughput, as shown in Figure 7.10(b)-7.10(c). For example, at a flow rate of 100 μL/min ($\bar{u}_p \approx 1.4$ mm/s), a continuous separation efficiency of 100% and a 17% particle throughput was predicted in the simulation with the parabolic magnet geometry, whereas no beads could be recovered when simulating the tapered or bar magnet geometry under the same flow conditions. For comparison, the tapered and bar magnet geometry achieved a continuous relative separation efficiency of 100% at a flow rate of 225 μL/min ($\bar{u}_p \approx 3.1$ mm/s), but the particle throughput was reduced to 14.5% and 13.7%, respectively.

With increasing flow rate, the separation efficiency of all three magnet geometries reduced. The reduction in separation efficiency was most significant for the parabolic magnet geometry. This, on the other hand, increased the throughput of beads which could be collected and recycled through another separation cycle.

Compared to the simple Double Magnet configuration (see Figure 7.3), all three Quadrupole simulations could achieve a maximum separation efficiency of 100%

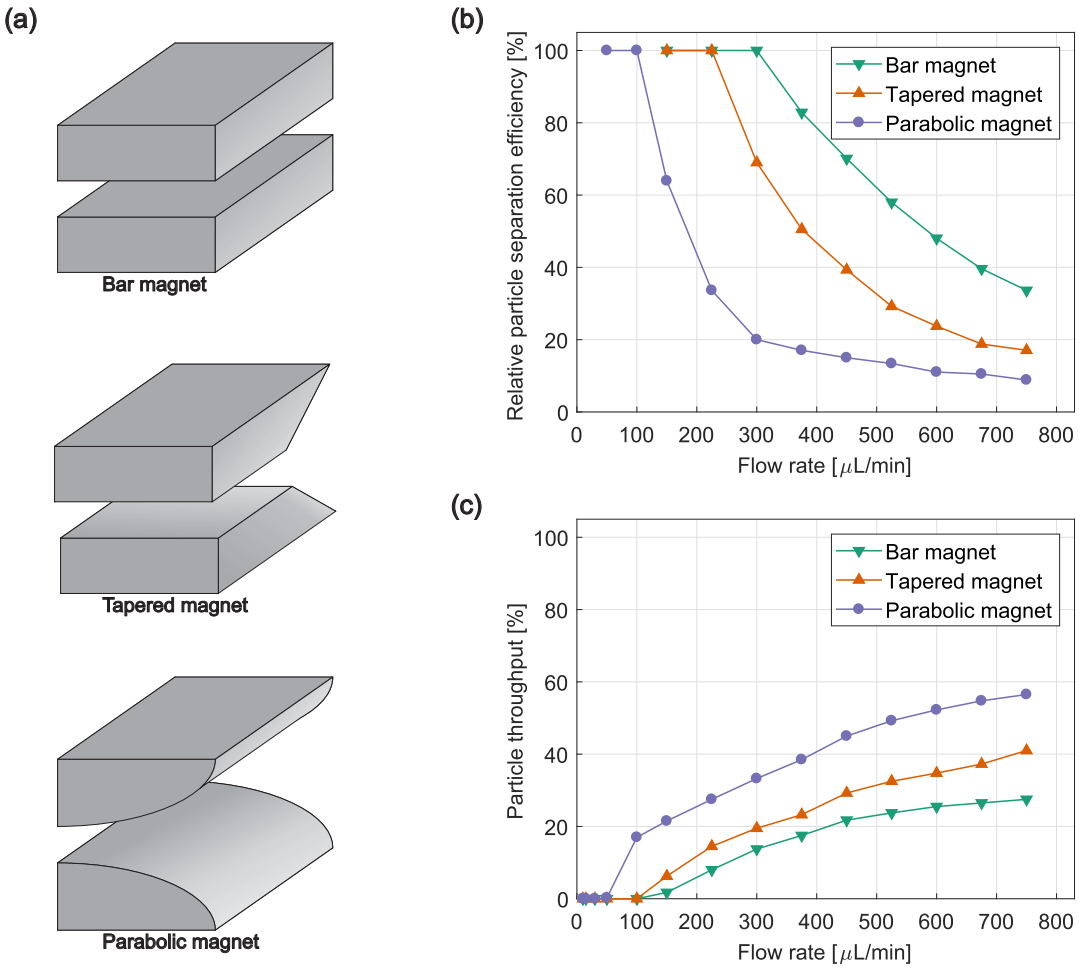


Figure 7.10: (a) Shows the different magnet geometries used to assemble the Quadrupole configuration. Only one side of the Quadrupole configuration is shown for simplicity. Simulation of (b) the relative magnetic separation efficiency and (c) throughput in continuous flow for Quadrupole configurations with three different magnet geometries. The flow rates range between 10 μL/min ($\bar{u}_p \approx 0.14$ mm/s) to 375 μL/min ($\bar{u}_p \approx 5.2$ mm/s). The bead properties are set to the physical properties of Chemicell SiMAG beads, found in Chapter 4.

with higher throughput at higher flow rates, which essentially reduces separation processing time. This evaluation was for separation of Chemicell SiMAG beads. The magnetic separation efficiency and throughput were, as with the Double Magnet configuration, negatively correlated. Therefore, the simulations predict again a trade-off between the continuous separation efficiency and bead recovery for each Quadrupole configuration.

The continuous separation of the Quadrupole configuration with bar magnets was also tested experimentally, as described in Section 3.11.2. Figure 7.11 shows the streamlines of the magnetic beads in continuous flow. A maximum separation efficiency of 55% was achieved when run continuously at a flow rate of 39 μL/min ($\bar{u}_p \approx 0.5$ mm/s).

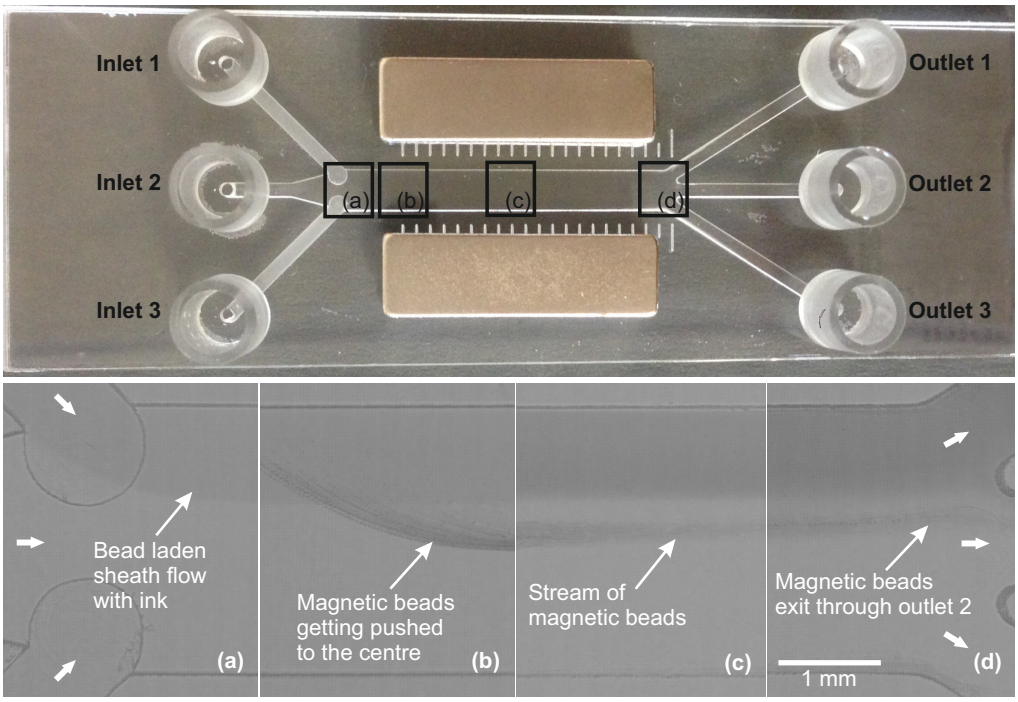


Figure 7.11: Gathering and streamlines of superimposed images of magnetic beads (Chemicell SiMAG) during the continuous magnetic separation experiment with the Quadrupole configuration. Images (a)-(d) show the streamlines of the magnetic beads at different positions along the iBidi fluid channel. The position of the various stages of the separation process is indicated by the black rectangles. Magnetic beads are introduced through inlet 1 only, for simplicity, and are expected to exit the device through outlet 2. The flow direction at the inlets and outlets is indicated by the bold arrows in (a) and (d).

As seen from the simulations and experiments, the Quadrupole configuration has the ability to continuously isolate magnetic beads and has proved more successful compared to both the experiments and simulations using the Double Magnet configuration. The experimentally found separation efficiency of the Quadrupole configuration for the tested flow rate was approximately half of what has been pre-

dicted by the simulations. The visually observed separation in the experiments led to the conclusion that beads were getting separated, but could not be collected. It was assumed that beads were getting trapped in the channel, because they moved towards areas of low fluid velocity at the surface of the channel. Therefore, the impact of beads approaching the inner surface of the fluid channel needed further attention, which is the topic in the next section.

7.3 Wall effects on the motion of a single particle

In the evaluations so far, the throughput was affected by beads becoming stuck at the fluid channel's inner surface, due to the undesirable vertical magnetophoretic forces. Thus, the motion of a rigid sphere in the vicinity of an internal wall might be relevant to this study. Therefore, the effect on the bead's motion when approaching a single plane wall was considered here.

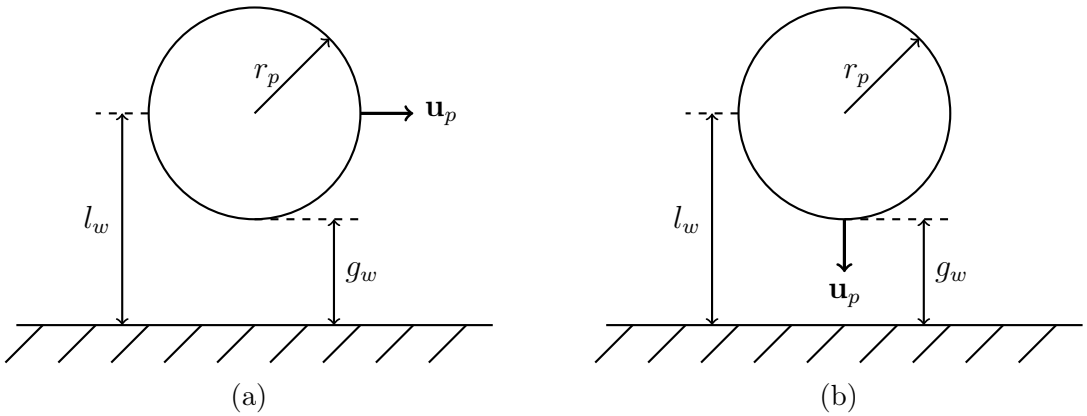


Figure 7.12: Spherical beads moving in proximity to a single plane wall experience different hydrodynamic forces when they move (a) along or (b) towards the wall.

Beads can move either along or towards the solid wall as shown in Figure 7.12. In either case, the hydrodynamic forces on the object change when the object moves in close proximity to the wall. In order to account for this effect, the magnetophoretic drift velocity should be adjusted. This is done by adding a correction factor, β, to

the Stokes drag [382, 383]:

$$\mathbf{F}_D = 6\pi\eta_f r_p \mathbf{u}\beta \tag{7.3}$$

Faxen worked out the influence of a single plane wall for spherical particles moving parallel to the wall and Brenner developed the model of a sphere moving towards a solid wall. The two Stokes' law correction factors for a spherical particle moving parallel ($\beta_\parallel$) or perpendicular ($\beta_\perp$) to a plane wall can be given by [382, 383]:

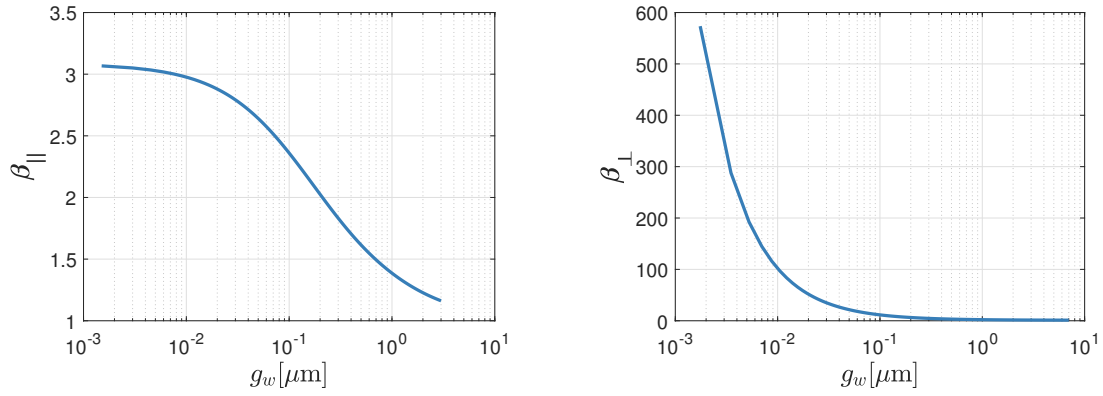
$$\beta_\parallel = \frac{1}{1 - \left(\frac{9}{16}\right)\left(\frac{r_p}{l_w}\right) + \left(\frac{1}{8}\right)\left(\frac{r_p}{l_w}\right)^3 - \left(\frac{45}{256}\right)\left(\frac{r_p}{l_w}\right)^4 - \left(\frac{1}{6}\right)\left(\frac{r_p}{l_w}\right)^5} \tag{7.4}$$

$$\beta_\perp = \frac{4}{3}\sinh(\varphi)\sum_{n=1}^{\infty}\frac{n(n+1)}{(2n-1)(2n+3)} \times \left[\frac{2\sinh(2n+1)\varphi + (2n+1\sinh(2\varphi))}{4\sinh^2(n+0.5)\varphi - (2n+1)^2\sinh^2(\varphi)} - 1\right] \tag{7.5}$$

where the particle radius is denoted by r_p and the distance of its midpoint from the plane by l_w, as depicted in Figure 7.12. The parameter φ is given by the following relationship:

$$\varphi = \cosh^{-1}(l_w/r_p) \tag{7.6}$$

Figure 7.13 shows the two correction factors, $\beta_\parallel$ and $\beta_\perp$, for a spherical particle moving at different distances away from a single wall. It can be seen that the correction factor approaches a constant value ($\beta_\parallel \approx 3$) when the particle is moving in close proximity to a wall (Figure 7.13a), whereas in the perpendicular case, the drag force correction factor increases infinitely (Figure 7.13b). This means that a rigid spherical particle in a viscous fluid can never make contact with a solid surface in a finite time. In practice, this is due to the lubrication force when the distance approaches zero [383–385].



(a) (b)

Figure 7.13: Wall correction factors for different distances from a plane surface for when a rigid sphere is moving (a) parallel or (b) perpendicular to the surface.

Particles that are travelling close to an internal surface of the microfluidic channel slow down in velocity because of the no-slip condition of the parabolic velocity profile of the fluid. Due to their finite size, as shown in Figure 7.14, the mean velocity of a particle which is at the channel's surface can be approximated by integrating Equation 2.10 along the diameter of the particle. The thin layer of liquid between the particle and wall that might be present in practice is assumed to be negligible compared to the particle diameter.

It was found that the bead's mean velocity, when moving along the wall, is more than 100 times smaller than the mean fluid velocity in the channel. Consequently, it takes at least 100 times longer for these beads to exit the separation device. This confirms the observation found through experiment, i.e. beads can be assumed as trapped on the time scale of continuous flow operation.

However, it could be shown experimentally that beads could be flushed out of the device if a flow rate of 10 mL/min or higher was used. Theoretically, flow rates as high as 112 mL/min remained in the laminar flow regime in the channel since the Reynolds number was below its critical value of Re $\approx$ 2300. Beads were therefore assumed to be flushed out of the system due to drag forces rather than eddies caused

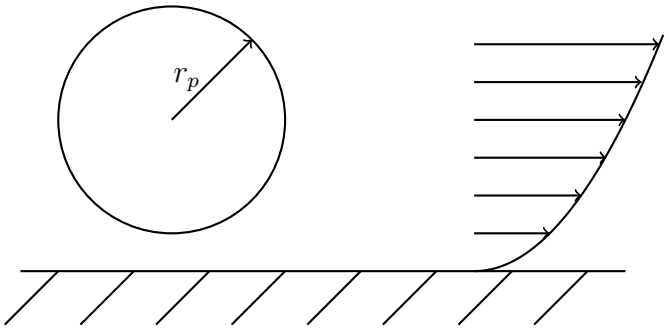


Figure 7.14: A spherical particle in a flow field in close proximity to a planar will experience a higher drag force due to its finite size.

by turbulence. At a flow rate of 10 mL/min, which is approximately $50 - 100$ times faster than the flow rates used in continuous separation (see Section 7.2), beads attached to the surface experience a mean velocity of 1.2 mm/s. The drawback of such high flow rates is, however, that the majority of beads would have an insufficient magnet interaction time (< 0.15 seconds) and would pass straight through the separation device with minimal response to the magnet. Consequently, such high flow rates would not be viable for continuous separation. A pulse mode of operating, where particles are gathered and flushed in alternating cycles is therefore proposed in the next section.

7.4 Magnetic separation in pulse mode

Due to the low separation efficiency compared to previously published separation devices [386], as well as the small particle throughput found in continuous separation for both magnet configurations (Double Magnet and Quadrupole), a *pulse mode* strategy was applied. In this strategy, the flow was paused before flushing the fluid channel with a high flow rate. While the flow rate was paused, magnetic beads had time to migrate to the gathering line. Beads attached to an inner surface of the fluid channel may no longer experience sufficient drag to move along the channel (z direction), but they are exposed to the magnetic field. This means, they are still

moving perpendicular to the channel long axis due to magnetophoresis, however, their drift along the channel wall is reduced by a factor of $\beta_{\parallel} \approx 3$, as explained above (see Figure 7.13a); these beads are gathering but not making progress along the channel.

The high flow rate during flushing, on the other hand, was able to move beads which were in contact with a surface and regarded as *stuck* in continuous separation. The flushing flow rate was still kept in the laminar regime, where it could be assumed that no turbulence occurs and that all beads follow their streamlines perfectly. This allowed recovery of most beads in the system and increased particle throughput.

The separation efficiencies of both magnet configurations, Double Magnet as well as Quadrupole configuration, were simulated for different pulse cycles between particle gathering ($|\dot{Q}| \approx 0$) and particle flushing ($|\dot{Q}| >> 0$), as described in Section 3.11. The fluid channel was assumed to be filled with particle laden fluid when the fluid flow was switched off ($\dot{Q} = 0$), and the particles were left for different time intervals. The consequences of beads being distributed over a volume of fluid when the channel was full was simulated by releasing a number of particles at different z positions along the length of the channel. The particles at each z slice were randomly scattered across the cross section of the channel, which was assumed to model the random distribution of particles when the channel was filled with particle suspension. Figure 7.15 shows the pulse separation efficiency at different positions along z for various pause intervals; 60, 100 and 200 seconds. The throughput is not shown here, because it was assumed that all particles are recovered when flushing. In this case, the relative separation efficiency is equivalent to the absolute efficiency. The wall effects, described in Section 7.3, were also incorporated in the simulation.

The simulations show that the longer the time intervals, the more beads reached their stable gathering points, which improved the separation efficiency. The time interval required to maintain a high separation efficiency, however, increased when

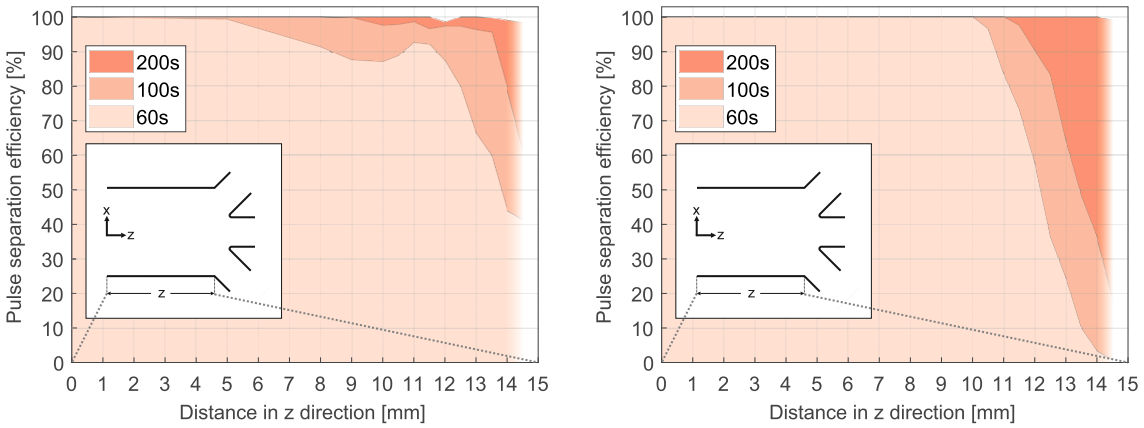


Figure 7.15: Separation efficiency of the (a) Double Magnet and (b) Quadrupole configuration in pulse mode operation when releasing particles across the channel's cross section at different z slices. Only half the length of the fluid channel ($z \geq 0$) is simulated due to symmetry as indicated by the insets. The properties of the beads are set to the properties of Dynabeads M270 found in Chapter 4.

releasing particles in the z direction further away from $z = 0$ because the magnetic field became weaker. Outside of the *impact zone* (-10 mm $< z <$ 10 mm) the magnetic field decayed quickly and its gathering points vanished. Magnetic beads outside of the impact zone ($z >$ 10 mm) during the pause cycle were not efficiently separated.

The increasing separation results for the Double Magnet configuration at $|z| \approx 11$ mm is worth noting. This is due to the increased magnetic flux density around the magnet edges, which makes the particles migrate more quickly to their stable gathering points.

7.4.1 Magnetic separation efficiency experiment in pulse mode

The pulse mode was experimentally tested for the Quadrupole configuration only, because this configuration was shown to be more efficient in separating magnetic beads, compared to the Double Magnet configuration. Figure 7.16 shows the experimentally found absolute separation efficiencies of the Quadrupole configuration

when run in pulse mode and continuous flow. The bar plot depicts the percentage of collected beads at each of the three channel outlets for three measurements, i.e. continuous flow, pulse operation and a control measurement run in continuous mode with no magnets. An absolute magnetic bead separation efficiency of up to 90% was achieved when run in pulse mode with a pulse interval of approximately 90 s. This results compared well with the pulse mode simulations where an absolute separation efficiency of 94% was predicted with a pause interval of 100 s.

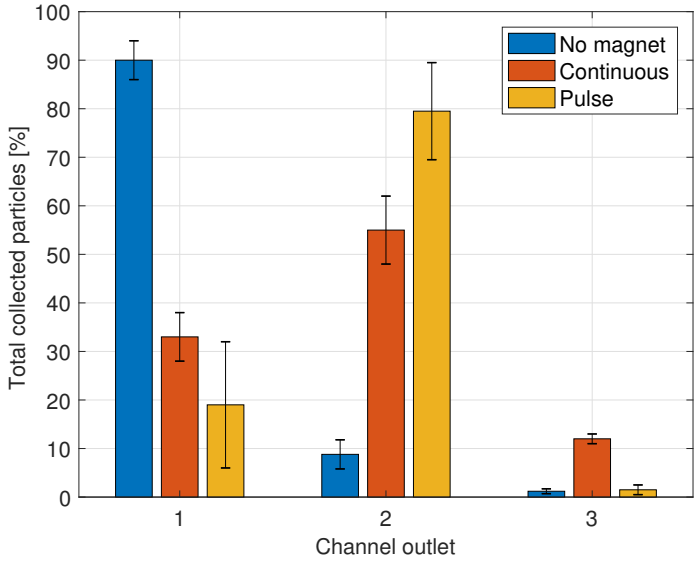


Figure 7.16: The separation efficiency of the Quadrupole configuration in continuous and pulsed mode compared to the control when no magnets is present. A flow rate of 39 μL/min ($\bar{u}_p \approx 0.5$ mm/s) is used in the continuous mode.

When the separation device was flushed at 1 mL/min, a back pressure of ≈ 34 Pa was estimated. The Harvard syringe pumps used in the experiments are capable of applying a linear force of 155 N, which is sufficient to overcome the increased back pressure and maintain the accuracy of the flow rate settings. Additionally, a very high back-pressure might have an adverse impact on the device structure or tubing joints. However, no evidence of such issues were observed during the experiments reported in this thesis.

7.5 Discussion and Conclusion

The separation efficiency for continuous flow of the Double Magnet configuration as well as for pulse flow in the Quadrupole configuration were investigated. The magnet configurations were designed to remove or concentrate magnetic particles from a sample suspension, the use of a gathering line is novel in this context.

In continuous mode, low magnification viewing had implied a good separation of the magnetic beads when using the Double Magnet and Quadrupole configuration setup. However, the maximum achieved continuous separation efficiencies were 35% and 55% for the Double Magnet and Quadrupole, respectively. These efficiencies are at the lower end of what has been previously reported in the literature, where separation efficiencies from 40% to over 90% have been achieved (see Table 1.2). Analysis by flow cytometry highlighted that, at the flow rates used, many beads passed through the device without being sufficiently deflected from the sample flow. For these beads the interaction time with the magnets was not sufficient even if comparable with reports in the literature [222, 230]. The deflection of the particles is coupled to the interaction time, which is a function of the applied flow rate. When the flow rate increases, the interaction time of the magnetic particles with the **B** field decreases, resulting in a smaller deflection. This negative correlation between flow rate and deflection (or relative separation efficiency) has been reported in the literature and verified in this chapter [387].

In the experiments a higher relative separation efficiency was obtained than predicted by the simulation. The discrepancy between the experiment and simulation was explained by simulating possible scenarios, such as different particle mobilities, particle agglomeration or misalignment of the microfluidic channel. It was seen in the experiments that beads, gathering at the surface of the fluid device, attract other beads and form clusters (see Section 6.3) which occasionally broke off when they became large. These bead interaction forces are not accurately represented in

the simulation, but contributed positively to the separation efficiency in the experiments. Most likely, a combination of these scenarios occur in the experiment, which explains the difference in relative separation efficiency of $10\% - 15\%$. However, the difference in performance between simulation and experiment became less relevant at flow rates > 375 μL/min.

The particle trajectory simulations showed that beads drift toward the top or bottom surface of the fluidic channel where they eventually move with almost zero velocity along the channel due to the parabolic velocity profile arising from the no-slip boundary conditions. However, the wall effect, i.e. increased drag, that was included in the mathematical model had a negligible effect on the results of the separation experiments when compared to the model without increased drag. These wall effects may only become relevant to particles that in effect stick to the surface of the channel. Particles in close proximity to a wall experience different electrostatic surface interactions; i.e. electric double layer forces and van der Waals forces. These surface forces need to be discussed because they may cause particle sticking.

Electrical double layer forces are associated with particles whose diameter is below 5 μm [388]. An electrical double layer exists when ions build up a layer of charge on an oppositely charged surface. Thus, particles experience an attractive force when their ion layers have opposing charge and conversely, are repelled when the ions have the same charge. However, for particle adhesion, the electrostatic double layer force can at best be of the same order of magnitude as the van der Waals force [389]. Thus, it is usually sufficient to only consider van der Waals forces in the case of adhesion. Van der Waals forces, however, are only the dominant adhesion forces if the particle is a few nm away from the other surface. In the research described, the particles needed to be $20 - 50$ nm away from the channel surface in order for the electrostatic forces to be stronger than the magnetic forces in vertical direction. In cases where the magnetic bead and internal surfaces are oppositely charged it will

be necessary to treat the channel with an appropriate surfactant.

Particles stuck to the inner surface of the channels in the absence of the magnetic field were not observed in the experiments. Furthermore, particles in suspension did not agglomerate when no magnetic field was present but were fully suspended in the liquid. This concludes that particles as well as the fluid channel surface had the same double layer charge arrangement and therefore, repel each other. The thickness of the double layer (Debye length) depends on the pH value but can be assumed to be between a few and several hundred nm. Even if a thickness of a couple hundred nm is assumed, particles that are 1 μm away from the surface have already slowed down by a factor ≈ 100 compared to the mean fluid velocity in the channel because of the parabolic velocity profile. For these reasons, electrostatic attraction of the beads to the channel surface was not seen to be the limiting factor for particle throughput but the low velocities at the channel walls was an issue. That is why both magnet configurations suffer from beads experiencing almost zero flow conditions when close to the inner surface of the channel.

In the simulation of continuous separation for single beads, a throughput of $\approx 30\%$ was achieved for all bead types while keeping the relative separation efficiency between 80% and 90%. Pamme *et al.* reported an experimentally determined bead throughput for M270 Dynabeads of approximately 16% when counting the beads leaving different outlets [390]. Their experiment can be compared to the simulations in this thesis, where a simulated throughput of 10% to 17% could be achieved with the Double Magnet and Quadrupole configuration using M270 Dynabeads.

The starting position of the beads introduced into the channel is a critical parameter in continuous separation and can only be fully simulated through the 3D model. In practice, beads injected into the inlet channel using a syringe pump are most likely evenly distributed across the inlet cross-section. Despite the use of hydrodynamic focusing, beads will be subject to different forces and velocities. These differences

are responsible for the trapping and *loss* of particles in the fluidic device. There is an optimal injection pattern for every continuous flow rate used, i.e. where particles need to be introduced into the system to be separated without getting trapped. If a more localised introduction of the beads were used in practice, the particle throughput and separation efficiency would be increased. In order to launch particles with such control, a 3D hydrodynamic focusing method should be considered, similar to that used in flow cytometry or described by Zborowski *et al.* [226, 391, 392].

Reducing the height of the channel could also have a beneficial effect for the particle throughput. If the height is reduced to only a couple of tens of micrometers, such that the diameter of the beads is only one order of magnitude smaller than the channel dimensions, beads would experience a larger fluid drag force when close to an internal surface and will more likely be recovered during continuous separation.

In order to recover all the injected magnetic particles a pulse mode of operation was introduced, where fast and slow flow rates were alternated. The study was restricted to Quadrupole configuration, due to its better performance. When operating in a pulsed mode, higher separation efficiency was predicted by simulation and confirmed in the experiments. In the experiments, a separation efficiency of 80% was achieved, which is an improvement compared to the continuous separation. The achieved separation efficiency of the pulse mode is also comparable to the literature (see Table 1.2)) where similar separation results were achieved within $10 - 15$ minutes [216, 217]. The throughput, however, exceeds most current separation devices, where values in the order of microlitre per minutes are commonly reported. Only the group of Zborowski *et al.* reported similar throughputs with values in the order of microlitre per minutes, but their fluid channel was approximately 1.5 times wider [226]. The simulations showed that an increase in pause time (slow flow rate) positively affected the absolute separation, since it allows a longer interaction time for the beads to be gathered. Since the magnetic field of the Quadrupole configu-

ration decays at a distance away from the magnet assembly, the pause time needs to be sufficiently long for those particles which are released outside of the magnetic interaction zone. Thus, a longer pause time has a positive effect on the separation efficiency, since it ensures enough time for the formation of the elliptical band around the gathering line. Once established, the width of the elliptical band was found to be less sensitive to time (see Section 6.3). The band width was dependent on the particle packing, which is governed by magnetic dipole interactions between individual particles and agglomerates, as shown in Appendix C. However, the band width did not exceed 1 mm even at a particle concentration of 10^8 beads/mL and, therefore, the particle packing would not have a detrimental impact on particle separation for the fluid channel geometry used in this study as the channel is sufficiently wide.

This chapter also showed that by tapering or physically shaping the magnets one can alter the magnetic flux to have the unique separating magnetic field along the entire length of the microfluidic device (no magnet edge effects), which will further improve the separation efficiency of the Quadrupole in pulse mode.

Chapter 8

Summary and Outlook

8.1 Summary of achievement

The aim of this project was to develop a model to accurately simulate the trajectories of single superparamagnetic microbeads in an external magnetic field to have a platform which can test and evaluate designs of magnetic separation devices. The model incorporated experimentally determined bead properties in order to best represent their behaviour in an applied magnetic field. The magnetic field was modelled in ANSYS and the magnetophoretic motion of the beads was simulated using a 3D Lagrangian tracking scheme. The trajectory simulations were used to analyse the separation efficiency of two novel magnet configurations under continuous flow and pulse flow mode. The simulations were also tested experimentally, which yielded benchmarks for validating the magnetophoretic particle transport model on a practical microfluidic platform.

In Chapter 1, an overview of the research area was given and the key concepts of microfluidic devices were defined. Further, various particle manipulation methods and their reported separation performance were summarized and critically compared. A similar summary and comparison was also given in the context of numerical mod-

elling approaches to simulate magnetic particle trajectories.

In Chapter 2, the physical concepts of fluid flow, magnetism, magnetic forces and magnetic deflection were outlined. In addition, statistical data analysis techniques that are used later in the thesis were explained.

Chapter 3 outlined the utilised materials and showed all chip designs used in the experiments. The chosen materials and devices were justified. Additionally, all procedures necessary to repeat the practical and numerical experiments were described in this chapter.

In Chapter 4, the magnetic responses of five commercially available beads were measured at different magnetic field magnitudes. Further, the chapter included SEM images of the beads to confirm their size distribution. The study concluded that even if Chemicell's SiMAG beads showed the highest magnetophoretic mobility, Dynabeads M270 are preferable for magnetic separation processes where an accurate control is needed, which is of particular importance in continuous separation to minimise particle loss.

Chapter 5 successfully demonstrated the hydrodynamic focusing effect within a microchannel. The hydrodynamic focusing effect was verified by simulations and experiments for different flow rates and flow rate ratios while remaining laminar flow. The sample stream could be accurately positioned and its width could be reduced to 4% of the channel width.

Chapter 6 presented two magnet configurations for magnetic separation, i.e. Double Magnet configuration and Quadrupole configuration. It was discovered that both configurations exhibit regions where magnetic particles experience no lateral magnetic force but formed a focussed band. The aim of the magnet configuration study was on controlling the region in which the beads are isolated and what effect different magnet configuration parameters have on the focussing band. The study has successfully demonstrated isolation of hydrodynamically pre-focused magnetic beads

into controlled regions with various particle types. The formation of the focussing band was also studied for different particle types, particle concentrations and time intervals.

In Chapter 7, the separation efficiency of both magnet configurations was simulated using a 3D Lagrangian tracking scheme and experimentally verified. The model simulations showed that the Double Magnet configuration, under continuous flow conditions, could achieve a relative separation efficiency of 100% at a flow rate of 10 μL/min or smaller. If the flow rate was increased, the relative separation efficiency was found to decrease. There also was a negative correlation between relative separation efficiency and particle throughput, i.e. improving throughput was detrimental to relative separation efficiency. Regarding throughput, simulations predicted that 85% of all the introduced particles can be recovered at a flow rate of $\dot{Q} = 375$ μL/min. The Double Magnetic configuration was also experimentally evaluated in this study. The experimentally determined separation efficiencies approximately matched the simulation results. Different scenarios were considered, which indicated that multiple effects and their combination play a role during magnetic separation.

The particle separation efficiency and throughput can be improved using a Quadrupole magnet configuration operating in pulse mode. An absolute separation efficiency of 80% could be achieved in the experiments and was confirmed by simulations. The pulse mode also had the advantage of minimising the number of beads lost in the system. This is especially important for biological separation where the targeted entities appear in small quantities such as required in the diagnosis of pre-eclampsia which is dependent on the small number of placental derived vesicles in the maternal blood plasma referred to in the thesis.

Existing clinical purification systems, e.g. the KingFisher Flex system by ThermoFisher Scientific or the MagNA Pure System by Roche, use tube based batch

processes. These systems offer a fully automated solution to purify a range of samples (e.g. whole blood or body fluids). Such systems perform multiple washing steps and particle isolation in a 96-well microtiter plate in $40-60$ min. The separation configurations presented in this thesis only perform the particle isolation step, but with the two proposed operation modes, continuous or pulsed, the sample throughput is at least one order of magnitude larger compared to the commercially available batch separation systems mentioned above. The tube based systems are limited by the 96-well microtiter plates which have a working volume of $200-300$ μL. This makes the presented approach particularly useful to processing large sample volumes containing low concentrations of biomarkers, e.g. urine samples. To date, pre-eclampsia is detected by traces of proteins found in urine. Therefore, the proposed magnetic separation device could already have an application for detecting pre-eclampsia when combined with the antibody binding molecule for placentile derived vesicles developed at the JR Hospital in Oxford [393].

The achieved separation efficiency, in particular in pulsed mode, is comparable with what has been previously reported in the literature (see Table 1.2). Research groups that have reported a separation efficiency of 90% or higher have mostly soft magnetic elements or use an electromagnet integrated into the fluid channel. This makes the fabrication process of the fluid channel more complex and thus potentially prone to errors and irregularities. With the separation geometry presented in this thesis, the magnet configuration can be kept separate from the fluid channel while keeping the ability to guide and focus magnetic beads along a predefined trajectory. The width of the focussing band where magnetic beads migrate to is independent of the beads used and thus, the magnetic separation process is less prone to variations in bead properties.

Having a robust and easy to use diagnostic assay that can process large sample volumes has been one of the key objectives of this thesis. The proposed magnetic

separation system is relevant to processing sample volumes up to $\approx$ 100 mL/h. Further, the two magnet configurations with their focussing band achieved a robust magnetic particle separation in a test environment. However, the loss of beads within the fluid channel remained a problem and needs to be addressed in the future to enable a more practical separation device.

In order to have an easy to use diagnostic assay that can potentially be used by clinicians also requires an easy setup and analysis process. The reduced fabrication costs ultimately allow for a disposable separation device, which will reduce the risk of sample contamination between separation processes and make the handling of the device easier. Thus, the device developed in this thesis would be best suited for the use by a laboratory technician since setting up the device still requires training. In order to also have the device used by clinicians, the device would greatly benefit from integrated downstream sample analysis and tests. So far, solutions for routine assays have automated the sample preparation, but no system exists to the author's knowledge that also performs sample analysis. Therefore, having the analysis integrated on the same device would be a further step towards a POC device that could eventually be used by patients.

It is further acknowledged by the author that the proposed device has only been tested with magnetic particle suspensions and buffer solutions and not on real clinical samples. Clinical samples are far more complex mixtures but the basic principles of operation will remain the same.

While the modelling method developed here was developed for magnetophoretic separations, on the wider scale the method could also be applied to similar on-chip continuous flow devices that involve the lateral deflection of particles flowing through liquid via the use of an external forces. A variation on microparticle device application could be the detection of specific proteins on the surface of cells by using antibody binding of magnetic nanoparticles (rather than micron-sized beads) to

these surface proteins. The exact number of magnetic nanoparticles bound to the cell would not be of relevance due to the gathering band.

The magnetic separation configuration could also be used to promote a chemical reaction on different reagents attached to the surface of mobile magnetic particles by moving the magnetic particles laterally across different solution streams. The lateral movement of the particles can be controlled by controlling the gathering band, which can be adjusted by machining the magnets.

Additionally, the method reported in this thesis for determination of magnetic susceptibility could be used by manufacturers of magnetic particles for quality control of their magnetic beads.

8.2 Future Work

The devices proposed here could be a valuable alternative for magnetic separation by guiding particles along a customized path, with high potential for further development in a cascade of downstream analysis of the sorted particles. In order to move toward a commercial application, using the proposed magnet configurations, certain components of the existing design need further investigation.

8.2.1 Simulation of suspension with higher order agglomerates

It has been shown in this work that different effects, e.g. particle agglomerations, can reduce the separation efficiency. In future analysis, the model should be extended to enable particle suspension simulations which include a distribution of higher order agglomerates. This would allow determination of the impact on separation efficiency of agglomerates in a particle suspensions.

8.2.2 Magnetic microparticle synthesis

Magnetic microparticles, which are the central element of the magnetic separation, should be investigated more thoroughly. Only when their physical structure is fully understood, can one make accurate predictions about their magnetic behaviour. Especially, the iron content and its variation among different particles leads to variability in the performance of magnetic particle separation. Scanning electron microscope or transmission electron microscope can give further insight into the particle structure. However, in order to optimise the properties of magnetic particles for continuous flow separation it is better to synthesise the particles *in house* or obtain them through a collaboration with an external group, as reported in reference [331]. There is a significant interest in the synthesis of superparamagnetic microparticles for a range of applications [394–396].

8.2.3 Optimisation of magnet geometry and configuration

This work has shown that it is possible to guide magnetic particles along a well-defined trajectory by using a Double Magnet or Quadrupole configuration. However, vertical forces negatively affected the particle separation efficiency. It has been shown that by physically shaping the magnets, (e.g. by tapering), vertical forces can be reduced and the gathering points can be adjusted for specific microfluidic channel geometries. This work has demonstrated the effect of tapered magnets and parabolically shaped magnet edges, but further optimisation is possible. Future work should analyse different tapering angles and parabolic magnet shapes, as well as their combination, to generate a magnetic field which bests suits the purpose of continuously separating magnetic beads, while maximising bead throughput.

With the Double Magnet or Quadrupole configuration in place, magnetic beads align in specific areas, and can be guided along defined trajectories. This opens the potential to manipulate by magnetophoresis the beads along complex trajectories

to per perform specific tasks, e.g. transferring across a multilaminar flow to initiate a chemical reaction or binding biomarkers to the magnetic beads.

8.2.4 Localised particle injection

The particles' trajectory is influenced by their initial release positions. The variation in position results in different magnetic drift forces and interaction time with the magnet and is mainly responsible for particles getting trapped in the system. A more accurate localized particle injection, using 3D flow focussing prior to particles entering the channel, could improve reproducibility and increase their separation efficiency, especially in continuous particle separation where the interaction time with the magnet is key. Beads could be accurately injected into the inlet channel through a nozzle. Figure 8.1 shows a *sweet spot* where beads should be continuously injected in order to avoid particle-wall interaction. However, in order to achieve a high separation efficiency, position, velocity and magnetophoretic mobility of the particles need to be optimised. For a commercial application, the ease of use is important. The prototype presented in this thesis took half an hour or more to setup and the bead collection process required significant practice. With further development, it would be entirely possible to fabricate a disposable separation device requiring minimal setup, and in which the buffer and bead suspensions can be injected under automation, being drawn and delivered to solution reservoirs. This would remove some of the labour intensive steps in diagnostic protocols such as the ELISA analysis, and promote the integration of other microfluidic based systems. This could lead to more complex diagnostic biochemistry being performed on very low concentration of target biomarkers, and offer cheap, fast and highly specific sensors.

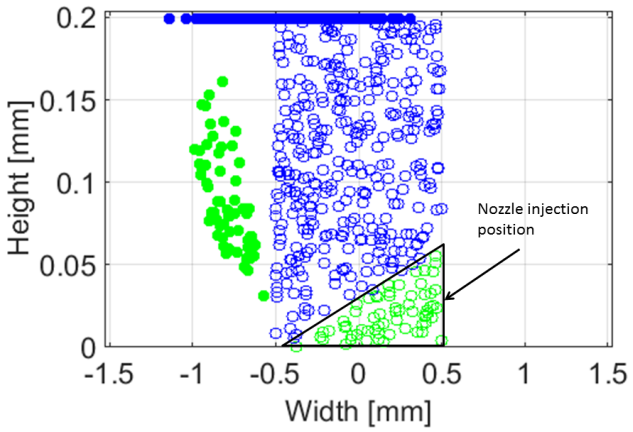


Figure 8.1: Preferred initial release position of magnetic beads to achieve a high continuous separation efficiency in a double magnet configuration. The different colours correspond to the following: *green*−beads get successfully separated and *blue*−beads are trapped in the system. The open and filled circles represent starting and end position of the beads, respectively. This figure shows the continuous separation at $\dot{Q} = 10$ μL/min.

Bibliography

[1] George M. Whitesides. The origins and the future of microfluidics. *Nature*, 442(7101):368–373, 2006.

[2] Reka Geczy, Monica Agnoletti, Mikkel F. Hansen, Jörg P. Kutter, Katayoun Saatchi, and Urs O. Häfeli. Microfluidic approaches for the production of monodisperse, superparamagnetic microspheres in the low micrometer size range. *Journal of Magnetism and Magnetic Materials*, 471:286–293, February 2019.

[3] K.E. Petersen. Silicon as a mechanical material. *Proceedings of the IEEE*, 70(5):420–457, May 1982.

[4] A. Manz, N. Graber, and H.M. Widmer. Miniaturized total chemical analysis systems: A novel concept for chemical sensing. *Sensors and Actuators B: Chemical*, 1(1–6):244–248, 1990.

[5] Andrew J. Demello. Control and detection of chemical reactions in microfluidic systems. *Nature*, 442(7101):394–402, 2006.

[6] Paul Yager, Thayne Edwards, Elain Fu, Kristen Helton, Kjell Nelson, Milton R. Tam, and Bernhard H. Weigl. Microfluidic diagnostic technologies for global public health. *Nature*, 442:412, July 2006.

[7] Andrea W. Chow. Lab-on-a-chip: Opportunities for chemical engineering. *American Institute of Chemical Engineers Journal*, 48(8):1590–1595, 2002.

[8] Derek L. Englert, Michael D. Manson, and Arul Jayaraman. Flow-based microfluidic device for quantifying bacterial chemotaxis in stable, competing gradients. *Applied and environmental microbiology*, 75(13):4557–4564, 2009.

[9] Peter B. Lillehoj, Hideaki Tsutsui, Bahram Valamehr, Hong Wu, and Chih-Ming Ho. Continuous sorting of heterogeneous-sized embryoid bodies. *Lab on a Chip*, 10(13):1678–1682, 2010.

[10] Challa S.S.R. Kumar. *Microfluidic devices in nanotechnology: applications*. John Wiley & Sons, 2010.

[11] Kazuo Hosokawa. The future of microfluidics for biomarker detection. *Bioanalysis*, 5(17):2073–2075, 2013.

[12] Stephen J. Haswell, Robert J. Middleton, Brian O'Sullivan, Victoria Skelton, Paul Watts, and Peter Styring. The application of micro reactors to synthetic chemistry. *Chemical Communications*, 5(5):391–398, 2001.

[13] Paul Watts and Stephen J. Haswell. The application of micro reactors for organic synthesis. *Chemical Society Reviews*, 34(3):235–246, 2005.

[14] Elisabeth Verpoorte. Microfluidic chips for clinical and forensic analysis. *Electrophoresis*, 23(5):677–712, 2002.

[15] Katie M. Horsman, Joan M. Bienvenue, Kiev R. Blasier, and James P. Landers. Forensic DNA analysis on microfluidic devices: a review. *Journal of Forensic Sciences*, 52(4):784–799, 2007.

[16] Jennifer A. Oakley, Kirsty J. Shaw, Peter T. Docker, Charlotte E. Dyer, John Greenman, Gillian M. Greenway, and Stephen J. Haswell. Development of

a bi-functional silica monolith for electro-osmotic pumping and DNA clean-up/extraction using gel-supported reagents in a microfluidic device. *Lab on a Chip*, 9(11):1596–1600, 2009.

[17] Kirsty J. Shaw, Lauren Thain, Peter T. Docker, Charlotte E. Dyer, John Greenman, Gillian M. Greenway, and Stephen J. Haswell. The use of carrier RNA to enhance DNA extraction from microfluidic-based silica monoliths. *Analytica Chimica Acta*, 652(1):231–233, 2009.

[18] Jonas O. Tegenfeldt, Christelle Prinz, Han Cao, Richard L. Huang, Robert H. Austin, Stephen Y. Chou, Edward C. Cox, and James C. Sturm. Micro- and nanofluidics for DNA analysis. *Analytical and Bioanalytical Chemistry*, 378(7):1678–1692, 2004.

[19] Uvaraj Ng, Alphonsus H.C.and Uddayasankar and Aaron R. Wheeler. Immunoassays in microfluidic systems. *Analytical and Bioanalytical Chemistry*, 397(3):991–1007, 2010.

[20] J.G.E. Gardeniers and A. van den Berg. Lab-on-a-chip systems for biomedical and environmental monitoring. *Analytical and Bioanalytical Chemistry*, 378(7):1700–1703, 2004.

[21] Leanne Marle and Gillian M. Greenway. Microfluidic devices for environmental monitoring. *TrAC Trends in Analytical Chemistry*, 24(9):795–802, 2005.

[22] Paul A. Greenwood and Gillian M. Greenway. Sample manipulation in micro total analytical systems. *TRAC Trends in Analytical Chemistry*, 21(11):726–740, 2002.

[23] Angel Ríos, Alberto Escarpa, María Cristina González, and Agustín Crevillén. Challenges of analytical microsystems. *TrAC Trends in Analytical Chemistry*, 25(5):467–479, 2006.

[24] Kyle Strimbu and Jorge A. Tavel. What are biomarkers? *Current Opinion in HIV and AIDS*, 5(6):463–466, November 2010.

[25] Sascha Sauer, Bodo M.H. Lange, Johan Gobom, Lajos Nyarsik, Harald Seitz, and Hans Lehrach. Miniaturization in functional genomics and proteomics. *Nature Reviews*, 6(6):465, 2005.

[26] Sandor Spisak, Zsolt Tulassay, Bela Molnar, and Andras Guttman. Protein microchips in biomedicine and biomarker discovery. *Electrophoresis*, 28(23):4261–4273, 2007.

[27] Emmanuel Delamarche, David Juncker, and Heinz Schmid. Microfluidics for processing surfaces and miniaturizing biological assays. *Advanced Materials*, 17(24):2911–2933, 2005.

[28] Rosalyn S. Yalow and Solomon A. Berson. Immunoassay of endogenous plasma insulin in man. *Obesity*, 4(6):583–600, 1996.

[29] Caifu Chen, Dana A. Ridzon, Adam J. Broomer, Zhaohui Zhou, Danny H. Lee, Julie T. Nguyen, Maura Barbisin, Nan Lan Xu, Vikram R. Mahuvakar, and Mark R. Andersen. Real-time quantification of micrornas by stem-loop rt-pcr. *Nucleic Acids Research*, 33(20):e179–e179, 2005.

[30] G. Sitta Sittampalam, Nathan P. Coussens, Henrike Nelson, Michelle Arkin, Douglas Auld, Chris Austin, Bruce Bejcek, Marcie Glicksman, James Inglese, Philip W. Iversen, Zhuyin Li, James McGee, Owen McManus, Lisa Minor, Andrew Napper, John M. Peltier, Terry O. Riss, Joseph Trask Jr., and Jeff Weidner. *Assay Guidance Manual*. National Center for Advancing Translational Sciences, 2004.

[31] Lisa Plitnick and Danuta Herzyk. *Nonclinical development of novel biologics, biosimilars, vaccines and specialty biologics*. Academic Press, 2013.

[32] Joël S. Rossier and Hubert H. Girault. Enzyme linked immunosorbent assay on a microchip with electrochemical detection. *Lab on a Chip*, 1(2):153–157, 2001.

[33] Daniel R. Gossett, Westbrook M. Weaver, Albert J. Mach, Soojung Claire Hur, Henry Tat Kwong Tse, Wonhee Lee, Hamed Amini, and Dino Di Carlo. Label-free cell separation and sorting in microfluidic systems. *Analytical and Bioanalytical Chemistry*, 397(8):3249–3267, 2010.

[34] Kathryn H. Ching. Lateral flow immunoassay. In *ELISA: Methods and Protocols*, pages 127–137. Springer, 2015.

[35] Samuel K. Sia and Larry J. Kricka. Microfluidics and point-of-care testing. *Lab on a Chip*, 8(12):1982–1983, 2008.

[36] Peter B. Luppa, Carolin Müller, Alice Schlichtiger, and Harald Schlebusch. Point-of-care testing (poct): Current techniques and future perspectives. *TrAC Trends in Analytical Chemistry*, 30(6):887–898, 2011.

[37] Levent Yobas, Kum-Cheong Tang, Shien-Eit Yong, and Eleana Kye-Zheng Ong. A disposable planar peristaltic pump for lab-on-a-chip. *Lab on a Chip*, 8(5):660–662, 2008.

[38] A. Nisar, Nitin Afzulpurkar, Banchong Mahaisavariya, and Adisorn Tuantranont. Mems-based micropumps in drug delivery and biomedical applications. *Sensors and Actuators B: Chemical*, 130(2):917–942, March 2008.

[39] S.S. Wang, X.Y. Huang, and C. Yang. Valveless micropump with acoustically featured pumping chamber. *Microfluidics and Nanofluidics*, 8(4):549–555, April 2010.

[40] Partha Kumar Das and A. B. M. Toufique Hasan. Mechanical micropumps and their applications: A review. *AIP Conference Proceedings*, 1851(1):020110, June 2017.

[41] Kwang W. Oh and Chong H. Ahn. A review of microvalves. *Journal of Micromechanics and Microengineering*, 16(5):R13, 2006.

[42] Jisong Zhang, Kai Wang, Andrew R. Teixeira, Klavs F. Jensen, and Guangsheng Luo. Design and scaling up of microchemical systems: A review. *Annual Review of Chemical and Biomolecular Engineering*, 8:285–305, 2017.

[43] Nam-Trung Nguyen and Zhigang Wu. Micromixers–a review. *Journal of Micromechanics and Microengineering*, 15(2):R1, 2004.

[44] Oliver Geschke, Henning Klank, and Pieter Telleman. *Microsystem Engineering of Lab-on-a-chip Devices*. John Wiley & Sons, 2004.

[45] Chun-Che Lin, Jung-Hao Wang, Hui-Wen Wu, and Gwo-Bin Lee. Microfluidic immunoassays. *Journal of the Association for Laboratory Automation*, 15(3):253–274, June 2010.

[46] Pierre-Alain Auroux, Dimitri Iossifidis, Darwin R. Reyes, and Andreas Manz. Micro total analysis systems. 2. analytical standard operations and applications. *Analytical Chemistry*, 74(12):2637–2652, 2002.

[47] Howard A. Stone and S. Kim. Microfluidics: basic issues, applications, and challenges. *American Institute of Chemical Engineers Journal*, 47(6):1250–1254, 2001.

[48] Kuo-Kang Liu, Ren-Guei Wu, Yun-Ju Chuang, Hwa Seng Khoo, Shih-Hao Huang, and Fan-Gang Tseng. Microfluidic systems for biosensing. *Sensors*, 10(7):6623–6661, 2010.

[49] Jigang Wu, Guoan Zheng, and Lap Man Lee. Optical imaging techniques in microfluidics and their applications. *Lab on a Chip*, 12(19):3566–3575, 2012.

[50] Kuo-Hoong Lee, Yuan-Deng Su, Shean-Jen Chen, Fan-Gang Tseng, and Gwo-Bin Lee. Microfluidic systems integrated with two-dimensional surface plasmon resonance phase imaging systems for microarray immunoassay. *Biosensors and Bioelectronics*, 23(4):466–472, 2007.

[51] Jing Kong, Lei Jiang, Xiaoou Su, Jianhua Qin, Yuguang Du, and Bingcheng Lin. Integrated microfluidic immunoassay for the rapid determination of clenbuterol. *Lab on a Chip*, 9(11):1541–1547, 2009.

[52] Ping Yao, Zhu Liu, Steve Tung, Zaili Dong, and Lianqing Liu. Fully automated quantification of insulin concentration using a microfluidic-based chemiluminescence immunoassay. *Journal of Laboratory Automation*, 21(3):387–393, 2016.

[53] Ivo Šafařík and Mirka Šafaříková. Magnetic nanoparticles and biosciences. *Nanostructured Materials*, pages 1–23, 2002.

[54] M. Schuster, E. Wasserbauer, C. Ortner, K. Graumann, A. Jungbauer, F. Hammerschmid, and G. Werner. Short cut of protein purification by integration of cell-disrupture and affinity extraction. *Bioseparation*, 9(2):59–67, 2000.

[55] Jaana Vuosku, Laura Jaakola, Soile Jokipii, Katja Karppinen, Terttu Kämäräinen, Veli-Pekka Pelkonen, Anne Jokela, Tytti Sarjala, Anja Hohtola, and Hely Häggman. Does extraction of DNA and RNA by magnetic fishing work for diverse plant species? *Molecular Biotechnology*, 27(3):209–215, 2004.

[56] Siu Wai Yeung and I-Ming Hsing. Manipulation and extraction of genomic

DNA from cell lysate by functionalized magnetic particles for lab on a chip applications. *Biosensors and Bioelectronics*, 21(7):989–997, 2006.

[57] Jean-Luc Guesdon and Stratis Avrameas. Magnetic solid phase enzyme-immunoassay. *Immunochemistry*, 14(6):443–447, 1977.

[58] Kara E. McCloskey, Jeffrey J. Chalmers, and Maciej Zborowski. Magnetic cell separation: characterization of magnetophoretic mobility. *Analytical Chemistry*, 75(24):6868–6874, 2003.

[59] Maciej Zborowski and Jeffrey J. Chalmers. *Magnetic cell separation*, volume 32. Elsevier, 2011.

[60] Zenjiro Osawa, Koichi Kawauchi, Masao Iwata, and Hideki Harada. Effect of polymer matrices on magnetic properties of plastic magnets. *Journal of Materials Science*, 23(7):2637–2644, 1988.

[61] Diandra L. Leslie-Pelecky and Reuben D. Rieke. Magnetic properties of nanostructured materials. *Chemistry of Materials*, 8(8):1770–1783, 1996.

[62] Urs O. Häfeli and Gayle J. Pauer. In vitro and in vivo toxicity of magnetic microspheres. *Journal of Magnetism and Magnetic Materials*, 194(1–3):76–82, 1999.

[63] R. Müller, H. Steinmetz, R. Hiergeist, and W. Gawalek. Magnetic particles for medical applications by glass crystallisation. *Journal of Magnetism and Magnetic Materials*, 272-276, Part 2(0):1539–1541, 2004.

[64] Michael L. Vadala, Michael A. Zalich, David B. Fulks, Tim G. St. Pierre, James P. Dailey, and Judy S. Riffle. Cobalt-silica magnetic nanoparticles with functional surfaces. *Journal of Magnetism and Magnetic Materials*, 293(1):162–170, 2005.

[65] Jongnam Park, Eunwoong Lee, Nong-Moon Hwang, Misun Kang, Sung Chul Kim, Yosun Hwang, Je-Geun Park, Han-Jin Noh, Jae-Young Kim, Jae-Hoon Park, and Taeghwan Hyeon. One-nanometer-scale size-controlled synthesis of monodisperse magnetic iron oxide nanoparticles. *Angewandte Chemie*, 117(19):2932–2937, 2005.

[66] Daniel Horák, Michal Babič, Hana Macková, and Milan J. Beneš. Preparation and properties of magnetic nano- and microsized particles for biological and environmental separations. *Journal of Separation Science*, 30(11):1751–1772, 2007.

[67] A. Bourlinos, A. Simopoulos, D. Petridis, H. Okumura, and G. Hadjipanayis. Silica-maghemite nanocomposites. *Advanced Materials*, 13(4):289–291, 2001.

[68] Nicole Jaffrezic-Renault, Claude Martelet, Yann Chevolot, and Jean-Pierre Cloarec. Biosensors and bio-bar code assays based on biofunctionalized magnetic microbeads. *Sensors*, 7(4):589–614, 2007.

[69] Pedro Tartaj, Maria del Puerto Morales, Sabino Veintemillas-Verdaguer, Teresita Gonzalez-Carreno, and Carlos J. Serna. The preparation of magnetic nanoparticles for applications in biomedicine. *Journal of Physics D: Applied Physics*, 36(13):R182–R197, 2003.

[70] Ranjan Ganguly and Ishwar K Puri. Microfluidic transport in magnetic mems and biomems. *Wiley Interdisciplinary Reviews: Nanomedicine and Nanobiotechnology*, 2(4):382–399, 2010.

[71] Martin A.M. Gijs. Magnetic bead handling on-chip: new opportunities for analytical applications. *Microfluidics and Nanofluidics*, 1(1):22–40, 2004.

[72] Quentin A. Pankhurst, J. Connolly, S.K. Jones, and J.J. Dobson. Applica-

tions of magnetic nanoparticles in biomedicine. *Journal of Physics D: Applied Physics*, 36(13):R167–R181, 2003.

[73] Neil A. Campbell, Brad Williamson, and Robin J. Heyden. *Biology: exploring life*. Boston, Massachusetts: Pearson Prentice Hall, 2006.

[74] L. Collier, J. Oxford, and P. Kellam. *Human Virology*. Oxford Univeristy Press, 2011.

[75] Tetsuya Osaka, Tadashi Matsunaga, Takuya Nakanishi, Atsushi Arakaki, Daisuke Niwa, and Hironori Iida. Synthesis of magnetic nanoparticles and their application to bioassays. *Analytical and Bioanalytical Chemistry*, 384(3):593–600, 2006.

[76] An-Hui Lu, Elena L. Salabas, and Ferdi Schüth. Magnetic nanoparticles: synthesis, protection, functionalization, and application. *Angewandte Chemie*, 46(8):1222–1244, 2007.

[77] Ke-Tai Guo, Richard Schäfer, Angela Paul, Annika Gerber, Gerhard Ziemer, and Hans P. Wendel. A new technique for the isolation and surface immobilization of mesenchymal stem cells from whole bone marrow using high-specific dna aptamers. *Stem cells*, 24(10):2220–2231, 2006.

[78] Matthew J. Tomlinson, Sophie Tomlinson, Xuebin B. Yang, and Jennifer Kirkham. Cell separation: Terminology and practical considerations. *Journal of Tissue Engineering*, 4:2041731412472690, 2013.

[79] Shigeo Takaishi, Tomoyuki Okumura, Shuiping Tu, Sophie S.W. Wang, Wataru Shibata, Ramanathan Vigneshwaran, Shanisha A.K. Gordon, Yutaka Shimada, and Timothy C. Wang. Identification of gastric cancer stem cells using the cell surface marker cd44. *Stem cells*, 27(5):1006–1020, 2009.

[80] Valeri H. Terry, Ian C. D. Johnston, and Celsa A. Spina. Cd44 microbeads accelerate hiv-1 infection in t cells. *Virology*, 388(2):294–304, 2009.

[81] Hideaki Tsutsui and Chih-Ming Ho. Cell separation by non-inertial force fields in microfluidic systems. *Mechanics Research Communications*, 36(1):92–103, 2009.

[82] Andreas Lenshof and Thomas Laurell. Continuous separation of cells and particles in microfluidic systems. *Chemical Society Reviews*, 39(3):1203–1217, 2010.

[83] Richard G. Miller and R.A. Phillips. Separation of cells by velocity sedimentation. *Journal of Cellular Physiology*, 73(3):191–201, 1969.

[84] Howard C. Berg. *Random walks in biology.* Princeton University Press, 1993.

[85] Dean Buckner, Robert G. Graw, Robert J. Eisel, Edwards Henderson, and Seymour Perry. Leukapheresis* by continuous flow centrifugation (cfc) in patients with chronic myelocytic leukemia (cml). *Blood*, 33(2):353–369, 1969.

[86] Christian de Duve. Exploring cells with a centrifuge. *Science*, 189(4198):186–194, 1975.

[87] Wei Liu, Yufang Hou, Huahai Chen, Handong Wei, Weiran Lin, Jichang Li, Ming Zhang, Fuchu He, and Ying Jiang. Sample preparation method for isolation of single-cell types from mouse liver for proteomic studies. *Proteomics*, 11(17):3556–3564, 2011.

[88] Udara Dharmasiri, Małgorzata A. Witek, Andre A. Adams, and Steven A. Soper. Microsystems for the capture of low-abundance cells. *Annual Review of Analytical Chemistry*, 3:409–431, 2010.

[89] Andrew J. Armstrong, Matthew S. Marengo, Sebastian Oltean, Gabor Kemeny, Rhonda Bitting, James Turnbull, Christina I. Herold, Paul K. Marcom, Daniel George, and Mariano Garcia-Blanco. Circulating tumor cells from patients with advanced prostate and breast cancer display both epithelial and mesenchymal markers. *Molecular Cancer Research*, 9(8):997–1007, 2011.

[90] Yuchao Chen, Peng Li, Po-Hsun Huang, Yuliang Xie, John D. Mai, Lin Wang, Nam-Trung Nguyen, and Tony Jun Huang. Rare cell isolation and analysis in microfluidics. *Lab on a Chip*, 14(4):626–645, 2014.

[91] W.A. Bonner, H.R. Hulett, R.G. Sweet, and L.A. Herzenberg. Fluorescence activated cell sorting. *Review of Scientific Instruments*, 43(3):404–409, 1972.

[92] Menake E. Piyasena and Steven W. Graves. The intersection of flow cytometry with microfluidics and microfabrication. *Lab on a Chip*, 14(6):1044–1059, 2014.

[93] Kevin L. Holmes, Benjamin Fontes, Philip Hogarth, Richard Konz, Simon Monard, Charles H. Pletcher, Robert B. Wadley, Ingrid Schmid, and Stephen P. Perfetto. International society for the advancement of cytometry cell sorter biosafety standards. *Cytometry. Part A*, 85(5):434–453, March 2014.

[94] Jamil El-Ali, Peter K. Sorger, and Klavs F. Jensen. Cells on chips. *Nature*, 442(7101):403, 2006.

[95] Eric K. Sackmann, Anna L. Fulton, and David J. Beebe. The present and future role of microfluidics in biomedical research. *Nature*, 507(7491):181, 2014.

[96] Arthur Ashkin, J.M. Dziedzic, and T. Yamane. Optical trapping and manipulation of single cells using infrared laser beams. *Nature*, 330(6150):769–771, 1987.

[97] David G. Grier. A revolution in optical manipulation. *Nature*, 424(6950):810–816, 2003.

[98] Ying Huang, Karla L. Ewalt, Marcus Tirado, Robert Haigis, Anita Forster, Donald Ackley, Michael J. Heller, James P. O'Connel, and Michael Krihak. Electric manipulation of bioparticles and macromolecules on microfabricated electrodes. *Analytical Chemistry*, 73(7):1549–1559, 2001.

[99] Adrian Neild, Stefano Oberti, Gerald Radziwill, and Jürg Dual. Simultaneous positioning of cells into two-dimensional arrays using ultrasound. *Biotechnology and Bioengineering*, 97(5):1335–1339, 2007.

[100] L.E. Helseth, T.M. Fischer, and T.H. Johansen. Domain wall tip for manipulation of magnetic particles. *Physical Review Letters*, 91(20):208302, 2003.

[101] Benjamin B. Yellen, Randall M. Erb, Hui S. Son, Rodward Hewlin Jr, Hao Shang, and Gil U. Lee. Traveling wave magnetophoresis for high resolution chip based separations. *Lab on a Chip*, 7(12):1681–1688, 2007.

[102] Randall M. Erb, David S. Sebba, Anne A. Lazarides, and Benjamin B. Yellen. Magnetic field induced concentration gradients in magnetic nanoparticle suspensions: theory and experiment. *Journal of Applied Physics*, 103(6):063916, 2008.

[103] P. Sajeesh and Ashis Kumar Sen. Particle separation and sorting in microfluidic devices: a review. *Microfluidics and Nanofluidics*, 17(1):1–52, 2014.

[104] Elodie Sollier, Hervé Rostaing, Patrick Pouteau, Yves Fouillet, and Jean-Luc Achard. Passive microfluidic devices for plasma extraction from whole human blood. *Sensors and Actuators B: Chemical*, 141(2):617–624, 2009.

[105] Timothy A. Crowley and Vincent Pizziconi. Isolation of plasma from whole blood using planar microfilters for lab-on-a-chip applications. *Lab on a Chip*, 5(9):922–929, 2005.

[106] Hong Miao Ji, Victor Samper, Yu Chen, Chew Kiat Heng, Tit Meng Lim, and Levent Yobas. Silicon-based microfilters for whole blood cell separation. *Biomedical Microdevices*, 10(2):251–257, 2008.

[107] Xing Chen, Chang Chun Liu, and Hui Li. Microfluidic chip for blood cell separation and collection based on crossflow filtration. *Sensors and Actuators B: Chemical*, 130(1):216–221, 2008.

[108] Siyang Zheng, Henry K. Lin, Bo Lu, Anthony Williams, Ram Datar, Richard J. Cote, and Yu-Chong Tai. 3d microfilter device for viable circulating tumor cell (ctc) enrichment from blood. *Biomedical Microdevices*, 13(1):203–213, 2011.

[109] Li Shi Lim, Min Hu, Mo Chao Huang, Wai Chye Cheong, Alfred Tau Liang Gan, Xing Lun Looi, Sai Mun Leong, Evelyn Siew-Chuan Koay, and Mo-Huang Li. Microsieve lab-chip device for rapid enumeration and fluorescence in situ hybridization of circulating tumor cells. *Lab on a Chip*, 12(21):4388–4396, 2012.

[110] Peitao Lv, Zhewen Tang, Xingjie Liang, Mingzhou Guo, and Ray P.S. Han. Spatially gradated segregation and recovery of circulating tumor cells from peripheral blood of cancer patients. *Biomicrofluidics*, 7(3):034109, 2013.

[111] Xiaoyun Fan, Chunping Jia, Jun Yang, Gang Li, Hongju Mao, Qinghui Jin, and Jianlong Zhao. A microfluidic chip integrated with a high-density pdms-based microfiltration membrane for rapid isolation and detection of circulating tumor cells. *Biosensors and Bioelectronics*, 71:380–386, 2015.

[112] Kiichi Sato, Manabu Tokeshi, Tamao Odake, Hiroko Kimura, Takeshi Ooi, Masayuki Nakao, and Takehiko Kitamori. Integration of an immunosorbent assay system: analysis of secretory human immunoglobulin a on polystyrene beads in a microchip. *Analytical Chemistry*, 72(6):1144–1147, 2000.

[113] Richard D. Oleschuk, Loranelle L. Shultz-Lockyear, Yuebin Ning, and D. Jed Harrison. Trapping of bead-based reagents within microfluidic systems: on-chip solid-phase extraction and electrochromatography. *Analytical Chemistry*, 72(3):585–590, 2000.

[114] Shashi K. Murthy, Palaniappan Sethu, Gordana Vunjak-Novakovic, Mehmet Toner, and Milica Radisic. Size-based microfluidic enrichment of neonatal rat cardiac cell populations. *Biomedical Microdevices*, 8(3):231–237, 2006.

[115] Palaniappan Sethu, Aaron Sin, and Mehmet Toner. Microfluidic diffusive filter for apheresis (leukapheresis). *Lab on a Chip*, 6(1):83–89, 2006.

[116] Virginia VanDelinder and Alex Groisman. Perfusion in microfluidic cross-flow: separation of white blood cells from whole blood and exchange of medium in a continuous flow. *Analytical Chemistry*, 79(5):2023–2030, 2007.

[117] Hisham Mohamed, James N. Turner, and Michele Caggana. Biochip for separating fetal cells from maternal circulation. *Journal of Chromatography A*, 1162(2):187–192, 2007.

[118] Sarah M. McFaul, Bill K. Lin, and Hongshen Ma. Cell separation based on size and deformability using microfluidic funnel ratchets. *Lab on a Chip*, 12(13):2369–2376, 2012.

[119] Pascal Preira, Véronique Grandne, J.-M. Forel, Sylvain Gabriele, M. Camara, and Olivier Theodoly. Passive circulating cell sorting by deformability using a microfluidic gradual filter. *Lab on a Chip*, 13(1):161–170, 2013.

[120] Yousang Yoon, Seonil Kim, Jusin Lee, Jaewoong Choi, Rae-Kwon Kim, Su-Jae Lee, Onejae Sul, and Seung-Beck Lee. Clogging-free microfluidics for continuous size-based separation of microparticles. *Scientific Reports*, 6:26531, 2016.

[121] Marko T. Blom, Emil Chmela, Johannes G.E. Gardeniers, Rob Tijssen, M. Elwenspoek, and Albert van den Berg. Design and fabrication of a hydrodynamic chromatography chip. *Sensors and Actuators B: Chemical*, 82(1):111–116, 2002.

[122] Marko T. Blom, Emil Chmela, R. Edwin Oosterbroek, Rob Tijssen, and Albert van den Berg. On-chip hydrodynamic chromatography separation and detection of nanoparticles and biomolecules. *Analytical Chemistry*, 75(24):6761–6768, 2003.

[123] Masumi Yamada, Megumi Nakashima, and Minoru Seki. Pinched flow fractionation: continuous size separation of particles utilizing a laminar flow profile in a pinched microchannel. *Analytical Chemistry*, 76(18):5465–5471, 2004.

[124] Junya Takagi, Masumi Yamada, Masahiro Yasuda, and Minoru Seki. Continuous particle separation in a microchannel having asymmetrically arranged multiple branches. *Lab on a Chip*, 5(7):778–784, 2005.

[125] Yuushi Sai, Masumi Yamada, Masahiro Yasuda, and Minoru Seki. Continuous separation of particles using a microfluidic device equipped with flow rate control valves. *Journal of Chromatography A*, 1127(1):214–220, 2006.

[126] Takahiro Kawamata, Masumi Yamada, Masahiro Yasuda, and Minoru Seki. Continuous and precise particle separation by electroosmotic flow control in microfluidic devices. *Electrophoresis*, 29(7):1423–1430, 2008.

[127] Jason P. Beech, Stefan H. Holm, Karl Adolfsson, and Jonas O. Tegenfeldt. Sorting cells by size, shape and deformability. *Lab on a Chip*, 12(6):1048–1051, 2012.

[128] Lotien Richard Huang, Edward C. Cox, Robert H. Austin, and James C. Sturm. Continuous particle separation through deterministic lateral displacement. *Science*, 304(5673):987–990, 2004.

[129] David W. Inglis, John A. Davis, Robert H. Austin, and James C. Sturm. Critical particle size for fractionation by deterministic lateral displacement. *Lab on a Chip*, 6(5):655–658, 2006.

[130] John A. Davis, David W. Inglis, Keith J. Morton, David A. Lawrence, Lotien R. Huang, Stephen Y. Chou, James C. Sturm, and Robert H. Austin. Deterministic hydrodynamics: taking blood apart. *Proceedings of the National Academy of Sciences*, 103(40):14779–14784, 2006.

[131] R. Huang, T.A. Barber, M.A. Schmidt, R.G. Tompkins, M. Toner, D.W. Bianchi, R. Kapur, and W.L. Flejter. A microfluidics approach for the isolation of nucleated red blood cells (nrbcs) from the peripheral blood of pregnant women. *Prenatal Diagnosis*, 28(10):892–899, 2008.

[132] Zongbin Liu, Fei Huang, Jinghui Du, Weiliang Shu, Hongtao Feng, Xiaoping Xu, and Yan Chen. Rapid isolation of cancer cells using microfluidic deterministic lateral displacement structure. *Biomicrofluidics*, 7(1):011801, 2013.

[133] Siyi Lai, Shengnian Wang, Jun Luo, L. James Lee, Shang-Tian Yang, and Marc J. Madou. Design of a compact disk-like microfluidic platform for enzyme-linked immunosorbent assay. *Analytical Chemistry*, 76(7):1832–1837, 2004.

[134] Jiwoon Park, Vijaya Sunkara, Tae-Hyeong Kim, Hyundoo Hwang, and Yoon-Kyoung Cho. Lab-on-a-disc for fully integrated multiplex immunoassays. *Analytical Chemistry*, 84(5):2133–2140, 2012.

[135] Tae-Hyeong Kim, Juhee Park, Chi-Ju Kim, and Yoon-Kyoung Cho. Fully integrated lab-on-a-disc for nucleic acid analysis of food-borne pathogens. *Analytical Chemistry*, 86(8):3841–3848, April 2014.

[136] W.R. Dean and J.M. Hurst. Note on the motion of fluid in a curved pipe. *Mathematika*, 6(1):77–85, 1959.

[137] Robert Gorkin, Jiwoon Park, Jonathan Siegrist, Mary Amasia, Beom Seok Lee, Jong-Myeon Park, Jintae Kim, Hanshin Kim, Marc Madou, and Yoon-Kyoung Cho. Centrifugal microfluidics for biomedical applications. *Lab on a Chip*, 10(14):1758–1773, 2010.

[138] Robert Burger, Daniel Kirby, Macdara Glynn, Charles Nwankire, Mary O'Sullivan, Jonathan Siegrist, David Kinahan, Gerson Aguirre, Gregor Kijanka, and Robert A. Gorkin. Centrifugal microfluidics for cell analysis. *Current Opinion in Chemical Biology*, 16(3):409–414, 2012.

[139] Robert Burger and Jens Ducrée. Handling and analysis of cells and bioparticles on centrifugal microfluidic platforms. *Expert Review of Molecular Diagnostics*, 12(4):407–421, 2012.

[140] Mary Amasia and Marc Madou. Large-volume centrifugal microfluidic device for blood plasma separation. *Bioanalysis*, 2(10):1701–1710, 2010.

[141] David J. Kinahan, Sinéad M. Kearney, Macdara T. Glynn, and Jens Ducrée. Spira mirabilis enhanced whole blood processing in a lab-on-a-disk. *Sensors and Actuators A: Physical*, 215:71–76, 2014.

[142] Charles E. Nwankire, Anita Venkatanarayanan, Thomas Glennon, Tia E. Keyes, Robert J. Forster, and Jens Ducrée. Label-free impedance detection of cancer cells from whole blood on an integrated centrifugal microfluidic platform. *Biosensors and Bioelectronics*, 68:382–389, 2015.

[143] Dino Di Carlo. Inertial microfluidics. *Lab on a Chip*, 9(21):3038–3046, 2009.

[144] Dino Di Carlo, Daniel Irimia, Ronald G. Tompkins, and Mehmet Toner. Continuous inertial focusing, ordering, and separation of particles in microchannels. *Proceedings of the National Academy of Sciences*, 104(48):18892–18897, 2007.

[145] Dino Di Carlo, Jon F. Edd, Daniel Irimia, Ronald G. Tompkins, and Mehmet Toner. Equilibrium separation and filtration of particles using differential inertial focusing. *Analytical Chemistry*, 80(6):2204–2211, 2008.

[146] Sathyakumar S. Kuntaegowdanahalli, Ali Asgar S. Bhagat, Girish Kumar, and Ian Papautsky. Inertial microfluidics for continuous particle separation in spiral microchannels. *Lab on a Chip*, 9(20):2973–2980, 2009.

[147] Aman Russom, Amit K. Gupta, Sunitha Nagrath, Dino Di Carlo, Jon F. Edd, and Mehmet Toner. Differential inertial focusing of particles in curved low-aspect-ratio microchannels. *New Journal of Physics*, 11(7):075025, 2009.

[148] Han Wei Hou, Majid Ebrahimi Warkiani, Bee Luan Khoo, Zi Rui Li, Ross A. Soo, Daniel Shao-Weng Tan, Wan-Teck Lim, Jongyoon Han, Ali Asgar S. Bhagat, and Chwee Teck Lim. Isolation and retrieval of circulating tumor cells using centrifugal forces. *Scientific Reports*, 3, 2013.

[149] Nivedita Nivedita and Ian Papautsky. Continuous separation of blood cells in spiral microfluidic devices. *Biomicrofluidics*, 7(5):054101, 2013.

[150] Guofeng Guan, Lidan Wu, Ali Asgar Bhagat, Zirui Li, Peter C.Y. Chen, Shuzhe Chao, Chong Jin Ong, and Jongyoon Han. Spiral microchannel with rectangular and trapezoidal cross-sections for size based particle separation. *Scientific Reports*, 3, 2013.

[151] Majid Ebrahimi Warkiani, Guofeng Guan, Khoo Bee Luan, Wong Cheng Lee, Ali Asgar S. Bhagat, Parthiv Kant Chaudhuri, Daniel Shao-Weng Tan, Wan Teck Lim, Soo Chin Lee, and Peter C. Y. Chen. Slanted spiral microfluidics for the ultra-fast, label-free isolation of circulating tumor cells. *Lab on a Chip*, 14(1):128–137, 2014.

[152] Vahidreza Parichehreh, Krishnakiran Medepallai, Karan Babbarwal, and Palaniappan Sethu. Microfluidic inertia enhanced phase partitioning for enriching nucleated cell populations in blood. *Lab on a Chip*, 13(5):892–900, 2013.

[153] Randall Morgan Erb. *Magnetic Manipulation and Assembly of Multicomponent Particle Suspensions*. PhD dissertation, Duke University, 2009.

[154] Karel Svoboda and Steven M. Block. Optical trapping of metallic rayleigh particles. *Optics Letters*, 19(13):930–932, 1994.

[155] Jonathan Leach, Kurt Wulff, Gavin Sinclair, Pamela Jordan, Johannes Courtial, Laura Thomson, Graham Gibson, Kayode Karunwi, Jon Cooper, and Zsolt John Laczik. Interactive approach to optical tweezers control. *Applied Optics*, 45(5):897–903, 2006.

[156] Karl Otto Greulich. Manipulation of cells with laser microbeam scissors and optical tweezers: a review. *Reports on Progress in Physics*, 80(2):026601, 2016.

[157] Keir C. Neuman and Attila Nagy. Single-molecule force spectroscopy: optical tweezers, magnetic tweezers and atomic force microscopy. *Nature Methods*, 5(6):491–505, 2008.

[158] Alexandr Jonáš and Pavel Zemanek. Light at work: The use of optical forces for particle manipulation, sorting, and analysis. *Electrophoresis*, 29(24):4813–4851, 2008.

[159] Arthur Ashkin. Acceleration and trapping of particles by radiation pressure. *Physical Review Letters*, 24(4):156, 1970.

[160] Tudor N. Buican, Miriam J. Smyth, Harry A. Crissman, Gary C. Salzman, Carleton C. Stewart, and John C. Martin. Automated single-cell manipulation and sorting by light trapping. *Applied Optics*, 26(24):5311–5316, 1987.

[161] Mark M. Wang, Eugene Tu, Daniel E. Raymond, Joon Mo Yang, Haichuan Zhang, Norbert Hagen, Bob Dees, Elinore M. Mercer, Anita H. Forster, and Ilona Kariv. Microfluidic sorting of mammalian cells by optical force switching. *Nature Biotechnology*, 23(1):83, 2005.

[162] Thomas D. Perroud, Julia N. Kaiser, Jay C. Sy, Todd W. Lane, Catherine S. Branda, Anup K. Singh, and Kamlesh D. Patel. Microfluidic-based cell sorting of francisella tularensis infected macrophages using optical forces. *Analytical Chemistry*, 80(16):6365–6372, 2008.

[163] Xiaolin Wang, Shuxun Chen, Marco Kong, Zuankai Wang, Kevin D. Costa, Ronald A. Li, and Dong Sun. Enhanced cell sorting and manipulation with combined optical tweezer and microfluidic chip technologies. *Lab on a Chip*, 11(21):3656–3662, 2011.

[164] Applegate Jr., W. Robert, Dawn N. Schafer, Wafa Amir, Jeff Squier, Tor Vestad, John Oakey, and David W.M. Marr. Optically integrated microfluidic systems for cellular characterization and manipulation. *Journal of Optics A*, 9(8):S122, 2007.

[165] Ting-Hsiang Wu, Yue Chen, Sung-Yong Park, Jason Hong, Tara Teslaa, Jiang F. Zhong, Dino Di Carlo, Michael A. Teitell, and Pei-Yu Chiou. Pulsed laser triggered high speed microfluidic fluorescence activated cell sorter. *Lab on a Chip*, 12(7):1378–1383, 2012.

[166] Robert M. Simmons, Jeffrey T. Finer, Steven Chu, and James A. Spudich. Quantitative measurements of force and displacement using an optical trap. *Biophysical Journal*, 70(4):1813–1822, 1996.

[167] Erwin J.G. Peterman, Frederick Gittes, and Christoph F. Schmidt. Laser-induced heating in optical traps. *Biophysical Journal*, 84(2):1308–1316, 2003.

[168] Joel Voldman. Electrical forces for microscale cell manipulation. *Annual Review of Biomedical Engineering*, 8:425–454, 2006.

[169] Kazunori Takahashi, Akihiro Hattori, Ikurou Suzuki, Takanori Ichiki, and Kenji Yasuda. Non-destructive on-chip cell sorting system with real-time microscopic image processing. *Journal of Nanobiotechnology*, 2(1):5, 2004.

[170] Bo Yao, Guo-an Luo, Xue Feng, Wei Wang, Ling-xin Chen, and Yi-ming Wang. A microfluidic device based on gravity and electric force driving for flow cytometry and fluorescence activated cell sorting. *Lab on a Chip*, 4(6):603–607, 2004.

[171] Feng Guo, Xing-Hu Ji, Kan Liu, Rong-Xiang He, Li-Bo Zhao, Zhi-Xiao Guo, Wei Liu, Shi-Shang Guo, and Xing-Zhong Zhao. Droplet electric separator microfluidic device for cell sorting. *Applied Physics Letters*, 96(19):193701, 2010.

[172] John M. Lackie. *The dictionary of cell & molecular biology*. Academic Press, 2007.

[173] Ying Huang, Sunghae Joo, Melanie Duhon, Michael Heller, Bruce Wallace, and Xiao Xu. Dielectrophoretic cell separation and gene expression profiling on microelectronic chip arrays. *Analytical Chemistry*, 74(14):3362–3371, 2002.

[174] Eric B. Cummings and Anup K. Singh. Dielectrophoresis in microchips containing arrays of insulating posts: theoretical and experimental results. *Analytical Chemistry*, 75(18):4724–4731, 2003.

[175] Louise M. Barrett, Andrew J. Skulan, Anup K. Singh, Eric B. Cummings, and Gregory J. Fiechtner. Dielectrophoretic manipulation of particles and cells using insulating ridges in faceted prism microchannels. *Analytical Chemistry*, 77(21):6798–6804, 2005.

[176] Michael D. Vahey and Joel Voldman. An equilibrium method for continuous-flow cell sorting using dielectrophoresis. *Analytical Chemistry*, 80(9):3135–3143, 2008.

[177] Lisen Wang, Lisa A. Flanagan, Noo Li Jeon, Edwin Monuki, and Abraham P. Lee. Dielectrophoresis switching with vertical sidewall electrodes for microfluidic flow cytometry. *Lab on a Chip*, 7(9):1114–1120, 2007.

[178] Il Doh and Young-Ho Cho. A continuous cell separation chip using hydrodynamic dielectrophoresis (dep) process. *Sensors and Actuators A: Physical*, 121(1):59–65, 2005.

[179] Barbara Roda, Andrea Zattoni, Pierluigi Reschiglian, Myeong Hee Moon, Mara Mirasoli, Elisa Michelini, and Aldo Roda. Field-flow fractionation in bioanalysis: a review of recent trends. *Analytica Chimica Acta*, 635(2):132–143, 2009.

[180] Jody Vykoukal, Daynene M. Vykoukal, Susanne Freyberg, Eckhard U. Alt, and Peter R.C. Gascoyne. Enrichment of putative stem cells from adipose tissue

using dielectrophoretic field-flow fractionation. *Lab on a Chip*, 8(8):1386–1393, 2008.

[181] Martin Gröschl. Ultrasonic separation of suspended particles-part i: Fundamentals. *Acta Acustica united with Acustica*, 84(3):432–447, 1998.

[182] Martin Gröschl. Ultrasonic separation of suspended particles-part ii: Design and operation of separation devices. *Acta Acustica united with Acustica*, 84(4):632–642, 1998.

[183] Linda Johansson, Fredrik Nikolajeff, Stefan Johansson, and Sara Thorslund. On-chip fluorescence-activated cell sorting by an integrated miniaturized ultrasonic transducer. *Analytical Chemistry*, 81(13):5188–5196, July 2009.

[184] Michael Ward, Patrick Turner, Marc DeJohn, and Gregory Kaduchak. Fundamentals of acoustic cytometry. *Current Protocols in Cytometry*, pages 1–22, 2009.

[185] Ivo Leibacher, Philipp Hahn, and Jürg Dual. Acoustophoretic cell and particle trapping on microfluidic sharp edges. *Microfluidics and Nanofluidics*, 19(4):923–933, 2015.

[186] Steven M. Woodside, James M. Piret, Martin Gröschl, Ewald Benes, and Bruce D. Bowen. Acoustic force distribution in resonators for ultrasonic particle separation. *American Institute of Chemical Engineers Journal*, 44(9):1976–1984, 1998.

[187] Filip Petersson, Lena Åberg, Ann-Margret Swärd-Nilsson, and Thomas Laurell. Free flow acoustophoresis: microfluidic-based mode of particle and cell separation. *Analytical Chemistry*, 79(14):5117–5123, 2007.

[188] Robert K. Adair. Constraints on biological effects of weak extremely-low-frequency electromagnetic fields. *Physical Review A*, 43(2):1039–1040, 1991.

[189] T. Grahl and H. Märkl. Killing of microorganisms by pulsed electric fields. *Applied Microbiology and Biotechnology*, 45(1-2):148–157, 1996.

[190] S. Solé, A. Merkoci, and S. Alegret. New materials for electrochemical sensing iii. beads. *TrAC Trends in Analytical Chemistry*, 20(2):102–110, 2001.

[191] Chong Wing Yung, Jason Fiering, Andrew J. Mueller, and Donald E. Ingber. Micromagnetic-microfluidic blood cleansing device. *Lab on a Chip*, 9(9):1171–1177, 2009.

[192] Kazunori Hoshino, Yu-Yen Huang, Nancy Lane, Michael Huebschman, Jonathan W. Uhr, Eugene P. Frenkel, and Xiaojing Zhang. Microchip-based immunomagnetic detection of circulating tumor cells. *Lab on a Chip*, 11(20):3449–3457, 2011.

[193] Christopher M. Earhart, Casey E. Hughes, Richard S. Gaster, Chin Chun Ooi, Robert J. Wilson, Lisa Y. Zhou, Eric W. Humke, Lingyun Xu, Dawson J. Wong, and Stephen B. Willingham. Isolation and mutational analysis of circulating tumor cells from lung cancer patients with magnetic sifters and biochips. *Lab on a Chip*, 14(1):78–88, 2014.

[194] Maciej Zborowski and Jeffrey J. Chalmers. Magnetophoresis: fundamentals and applications. *Wiley Encyclopedia of Electrical and Electronics Engineering*, 2015.

[195] G. Friedman and B. Yellen. Magnetic separation, manipulation and assembly of solid phase in fluids. *Current Opinion in Colloid & Interface Science*, 10(3):158–166, 2005.

[196] Nicole Pamme. Magnetism and microfluidics. *Lab on a Chip*, 6(1):24–38, 2006.

[197] Zeta Tak For Yu, Koh Meng Aw Yong, and Jianping Fu. Microfluidic blood cell sorting: Now and beyond. *Small*, 10(9):1687–1703, 2014.

[198] Stefan Miltenyi, Werner Muller, Walter Weichel, and Andreas Radbruch. High gradient magnetic cell separation with macs. *Cytometry*, 11(2):231–238, 1990.

[199] Miltenyi Biotec. Miltenyi biotec webpage. `http://www.miltenyibiotec.com`, Last accessed on 2017-08-12.

[200] Andreas Thiel, Alexander Scheffold, and Andreas Radbruch. Immunomagnetic cell sorting-pushing the limits. *Immunotechnology*, 4(2):89–96, 1998.

[201] Nguyen T.K. Thanh. *Magnetic nanoparticles: from fabrication to clinical applications*. CRC press, 2012.

[202] Jin-Woo Choi, Chong H. Ahn, Shekhar Bhansali, and H.Thurman Henderson. A new magnetic bead-based, filterless bio-separator with planar electromagnet surfaces for integrated bio-detection systems. *Sensors and Actuators B: Chemical*, 68(1–3):34–39, 2000.

[203] Jin-Woo Choi, Trifon M. Liakopoulos, and Chong H. Ahn. An on-chip magnetic bead separator using spiral electromagnets with semi-encapsulated permalloy. *Biosensors and Bioelectronics*, 16(6):409–416, 2001.

[204] Tao Deng, Mara Prentiss, and George M. Whitesides. Fabrication of magnetic microfiltration systems using soft lithography. *Applied Physics Letters*, 80(3):461–463, 2002.

[205] M.B. Karpova, J. Schoumans, I. Ernberg, J. I. Henter, M. Nordenskjöld, and B. Fadeel. Raji revisited: cytogenetics of the original burkitt's lymphoma cell line. *Leukemia*, 19(1):159, 2005.

[206] Antoine-Emmanuel Saliba, Laure Saias, Eleni Psychari, Nicolas Minc, Damien Simon, François-Clément Bidard, Claire Mathiot, Jean-Yves Pierga, Vincent Fraisier, and Jean Salamero. Microfluidic sorting and multimodal typing of cancer cells in self-assembled magnetic arrays. *Proceedings of the National Academy of Sciences*, 107(33):14524–14529, 2010.

[207] Daniel Horak, Zuzana Svobodova, Julien Autebert, Benoit Coudert, Zdeněk Plichta, Karel Kralovec, Zuzana Bilkova, and Jean-Louis Viovy. Albumin-coated monodisperse magnetic poly (glycidyl methacrylate) microspheres with immobilized antibodies: Application to the capture of epithelial cancer cells. *Journal of Biomedical Materials Research Part A*, 101(1):23–32, 2013.

[208] Zuzana Svobodova, Jana Kucerova, Julien Autebert, Daniel Horak, Lenka Bruckova, Jean-Louis Viovy, and Zuzana Bilkova. Application of an improved magnetic immunosorbent in an ephesia chip designed for circulating tumor cell capture. *Electrophoresis*, 35(2-3):323–329, 2014.

[209] Nikola Pekas, Michael Granger, Mark Tondra, Anthony Popple, and Marc D. Porter. Magnetic particle diverter in an integrated microfluidic format. *Journal of Magnetism and Magnetic Materials*, 293(1):584–588, 2005.

[210] Caroline Derec, Claire Wilhelm, Jacques Servais, and Jean-Claude Bacri. Local control of magnetic objects in microfluidic channels. *Microfluidics and Nanofluidics*, 8(1):123–130, 2010.

[211] Adam C. Siegel, Sergey S. Shevkoplyas, Douglas B. Weibel, Derek A. Bruzewicz, Andres W. Martinez, and George M. Whitesides. Cofabrication of electromagnets and microfluidic systems in poly (dimethylsiloxane). *Angewandte Chemie*, 118(41):7031–7036, 2006.

[212] Sergey S. Shevkoplyas, Adam C. Siegel, Robert M. Westervelt, Mara G. Pren-

tiss, and George M. Whitesides. The force acting on a superparamagnetic bead due to an applied magnetic field. *Lab on a Chip*, 7(10):1294–1302, 2007.

[213] Tian Fook Kong, Hendrik Santoso Sugiarto, Hwi Fen Liew, Xinghua Wang, Wen Siang Lew, Nam-Trung Nguyen, and Yong Chen. An efficient microfluidic sorter: implementation of double meandering micro striplines for magnetic particles switching. *Microfluidics and Nanofluidics*, 10(5):1069–1078, 2011.

[214] David W. Inglis, Robert Riehn, R.H. Austin, and J.C. Sturm. Continuous microfluidic immunomagnetic cell separation. *Applied Physics Letters*, 85(21):5093–5095, 2004.

[215] David W. Inglis, Robert Riehn, James C. Sturm, and Robert H. Austin. Microfluidic high gradient magnetic cell separation. *Journal of Applied Physics*, 99(8):08K101, 2006.

[216] Seonyoung Kim, Song-I. Han, Min-Jae Park, Chang-Wan Jeon, Young-Don Joo, In-Hak Choi, and Ki-Ho Han. Circulating tumor cell microseparator based on lateral magnetophoresis and immunomagnetic nanobeads. *Analytical Chemistry*, 85(5):2779–2786, 2013.

[217] Jeong Won Park, Nae-Rym Lee, Sung Mok Cho, Moon Youn Jung, Chunhwa Ihm, and Dae-Sik Lee. Microdevice for separation of circulating tumor cells using embedded magnetophoresis with v-shaped ni-co nanowires and immuno-nanomagnetic beads. *Electronics and Telecommunications Research Institute Journal*, 37(2):233–240, 2015.

[218] Jinhee Jung and Ki-Ho Han. Lateral-driven continuous magnetophoretic separation of blood cells. *Applied Physics Letters*, 93(22):223902, 2008.

[219] Ki-Ho Han and A. Bruno Frazier. Paramagnetic capture mode magne-

tophoretic microseparator for high efficiency blood cell separations. *Lab on a Chip*, 6(2):265–273, 2006.

[220] Ki-Ho Han, Arum Han, and A. Bruno Frazier. Microsystems for isolation and electrophysiological analysis of breast cancer cells from blood. *Biosensors and Bioelectronics*, 21(10):1907–1914, 2006.

[221] Bai-Yan Qu, Zhi-Yong Wu, Fang Fang, Zhi-Ming Bai, Dong-Zhi Yang, and Shu-Kun Xu. A glass microfluidic chip for continuous blood cell sorting by a magnetic gradient without labeling. *Analytical and Bioanalytical Chemistry*, 392(7-8):1317, 2008.

[222] Nan Xia, Tom P. Hunt, Brian T. Mayers, Eben Alsberg, George M. Whitesides, Robert M. Westervelt, and Donald E. Ingber. Combined microfluidic-micromagnetic separation of living cells in continuous flow. *Biomedical Microdevices*, 8(4):299–308, 2006.

[223] Rana Afshar, Yves Moser, Thomas Lehnert, and Martin A.M. Gijs. Magnetic particle dosing and size separation in a microfluidic channel. *Sensors and Actuators B: Chemical*, 154(1):73–80, 2011.

[224] Liping Sun, Maciej Zborowski, Lee R. Moore, and Jeffrey J. Chalmers. Continuous, flow-through immunomagnetic cell sorting in a quadrupole field. *Cytometry Part A*, 33(4):469–475, 1998.

[225] Maciej Zborowski, Liping Sun, Lee R. Moore, P. Stephen Williams, and Jeffrey J. Chalmers. Continuous cell separation using novel magnetic quadrupole flow sorter. *Journal of Magnetism and Magnetic Materials*, 194(1–3):224–230, 1999.

[226] Maciej Zborowski and Jeffrey J. Chalmers. Rare cell separation and analysis by magnetic sorting. *Analytical Chemistry*, 83(21):8050–8056, 2011.

[227] Francesca Carpino, Maciej Zborowski, and P. Stephen Williams. Quadrupole magnetic field-flow fractionation: a novel technique for the characterization of magnetic nanoparticles. *Journal of Magnetism and Magnetic Materials*, 311(1):383–387, 2007.

[228] P. Stephen Williams, Francesca Carpino, and Maciej Zborowski. Theory for nanoparticle retention time in the helical channel of quadrupole magnetic field-flow fractionation. *Journal of Magnetism and Magnetic Materials*, 321(10):1446–1451, 2009.

[229] David J. Kennedy, Paul Todd, Sam Logan, Matthew Becker, Klearchos K. Papas, and Lee R. Moore. Engineering quadrupole magnetic flow sorting for the isolation of pancreatic islets. *Journal of Magnetism and Magnetic Materials*, 311(1):388–395, 2007.

[230] Nicole Pamme and Andreas Manz. On-chip free-flow magnetophoresis: Continuous flow separation of magnetic particles and agglomerates. *Analytical Chemistry*, 76(24):7250–7256, 2004.

[231] Nicole Pamme and Claire Wilhelm. Continuous sorting of magnetic cells via on-chip free-flow magnetophoresis. *Lab on a Chip*, 6(8):974–980, 2006.

[232] Hitoshi Watarai, Masayori Suwa, and Yoshinori Iiguni. Magnetophoresis and electromagnetophoresis of microparticles in liquids. *Analytical and Bioanalytical Chemistry*, 378(7):1693–1699, 2004.

[233] Tsunehisa Kimura, Masafumi Yamato, and Akihiro Nara. Particle trapping and undulation of a liquid surface using a microscopically modulated magnetic field. *Langmuir*, 20(3):572–574, 2004.

[234] Tsunehisa Kimura, Yukiko Sato, Fumiko Kimura, Masakazu Iwasaka, and

Shoogo Ueno. Micropatterning of cells using modulated magnetic fields. *Langmuir*, 21(3):830–832, 2005.

[235] Adam Winkleman, Raquel Perez-Castillejos, Katherine L. Gudiksen, Scott T. Phillips, Mara Prentiss, and George M. Whitesides. Density-based diamagnetic separation: devices for detecting binding events and for collecting unlabeled diamagnetic particles in paramagnetic solutions. *Analytical Chemistry*, 79(17):6542–6550, 2007.

[236] Mark D. Tarn, Noriyuki Hirota, Alexander Iles, and Nicole Pamme. On-chip diamagnetic repulsion in continuous flow. *Science and Technology of Advanced Materials*, 10(1):014611, 2009.

[237] Sally A. Peyman, Er Yee Kwan, Oliver Margarson, Alexander Iles, and Nicole Pamme. Diamagnetic repulsion–a versatile tool for label-free particle handling in microfluidic devices. *Journal of Chromatography A*, 1216(52):9055–9062, 2009.

[238] Martin Vojtíšek, Mark D. Tarn, Noriyuki Hirota, and Nicole Pamme. Microfluidic devices in superconducting magnets: on-chip free-flow diamagnetophoresis of polymer particles and bubbles. *Microfluidics and Nanofluidics*, 13(4):625–635, 2012.

[239] Mark D. Tarn, Sally A. Peyman, and Nicole Pamme. Simultaneous trapping of magnetic and diamagnetic particle plugs for separations and bioassays. *RSC Advances*, 3(20):7209–7214, 2013.

[240] Christopher E. Brennen. *Fundamentals of multiphase flow*. Cambridge University Press, 2005.

[241] Hugo A. Jakobsen. *Chemical reactor modeling: multiphase reactive flows*. Springer Science & Business Media, 2014.

[242] Lixing Zhou. Two-phase turbulence models in eulerian-eulerian simulation of gas-particle flows and coal combustion. *Procedia Engineering*, 102:1677–1696, 2015.

[243] Mostafa A. Rizk. Mathematical modeling of densely loaded, particle-laden turbulent flows. *Atomization and Sprays*, 3(1), 1993.

[244] Dimitri Gidaspow. *Multiphase flow and fluidization: continuum and kinetic theory descriptions*. Academic press, 1994.

[245] Ansys Fluent. 12.0 user's guide. *Ansys Inc.*, 5:1–2620, 2009.

[246] ANSYS Fluent. 12.0 theory guide. *Ansys Inc.*, 5:1–780, 2009.

[247] Gérard Gouesbet and Alain Berlemont. Eulerian and lagrangian approaches for predicting the behaviour of discrete particles in turbulent flows. *Progress in Energy and Combustion Science*, 25(2):133–159, 1999.

[248] Santiago Laín, Martin Sommerfeld, and Johannes Kussin. Experimental studies and modelling of four-way coupling in particle-laden horizontal channel flow. *International Journal of Heat and Fluid Flow*, 23(5):647–656, 2002.

[249] D.C. Cohen Stuart, C.R. Kleijn, and S. Kenjereš. An efficient and robust method for lagrangian magnetic particle tracking in fluid flow simulations on unstructured grids. *Computers & Fluids*, 40(1):188–194, 2011.

[250] G.T. Csanady. Turbulent diffusion of heavy particles in the atmosphere. *Journal of the Atmospheric Sciences*, 20(3):201–208, 1963.

[251] M.R. Wells and D.E. Stock. The effects of crossing trajectories on the dispersion of particles in a turbulent flow. *Journal of Fluid Mechanics*, 136:31–62, 1983.

[252] J.Y. Tu and C.A.J. Fletcher. Numerical computation of turbulent gas-solid particle flow in a 90° bend. *American Institute of Chemical Engineers Journal*, 41(10):2187–2197, 1995.

[253] Sally A. Peyman, Alexander Iles, and Nicole Pamme. Rapid on-chip multi-step (bio) chemical procedures in continuous flow-manoeuvring particles through co-laminar reagent streams. *Chemical Communications*, pages 1220–1222, 2008.

[254] Ulrike Lehmann, Smail Hadjidj, Virendra K. Parashar, Caroline Vandevyver, Amar Rida, and Martin A. M. Gijs. Two-dimensional magnetic manipulation of microdroplets on a chip as a platform for bioanalytical applications. *Sensors and Actuators B: Chemical*, 117(2):457–463, 2006.

[255] Aymeric Vié, Frédérique Laurent, and Marc Massot. Size-velocity correlations in hybrid high order moment/multi-fluid methods for polydisperse evaporating sprays: Modeling and numerical issues. *Journal of Computational Physics*, 237:177–210, 2013.

[256] Frederique Laurent, Aymeric Vie, Christophe Chalons, Rodney O. Fox, and Marc Massot. A hierarchy of eulerian models for trajectory crossing in particle-laden turbulent flows over a wide range of stokes numbers. *Center for Turbulence Research Annual Research Briefs*, 2012:193, 2013.

[257] Enrica Masi, Olivier Simonin, Eleonore Riber, P. Sierra, and Laurent Y.M. Gicquel. Development of an algebraic-closure-based moment method for unsteady eulerian simulations of particle-laden turbulent flows in very dilute regime. *International Journal of Multiphase Flow*, 58:257–278, 2014.

[258] Edward P. Furlani and Y. Sahoo. Analytical model for the magnetic field

and force in a magnetophoretic microsystem. *Journal of Physics D: Applied Physics*, 39(9):1724, 2006.

[259] Edward P. Furlani. Magnetophoretic separation of blood cells at the microscale. *Journal of Physics D: Applied Physics*, 40(5):1313, 2007.

[260] Edward P. Furlani. Magnetic biotransport: analysis and applications. *Materials*, 3(4):2412–2446, 2010.

[261] Ashok Sinha, Ranjan Ganguly, Anindya K. De, and Ishwar K. Puri. Single magnetic particle dynamics in a microchannel. *Physics of Fluids*, 19(11):117102, 2007.

[262] Ashok Sinha, Ranjan Ganguly, and Ishwar K. Puri. Magnetic separation from superparamagnetic particle suspensions. *Journal of Magnetism and Magnetic Materials*, 321(14):2251–2256, 2009.

[263] Krishanu Nandy, Sayani Chaudhuri, Ranjan Ganguly, and Ishwar K. Puri. Analytical model for the magnetophoretic capture of magnetic microspheres in microfluidic devices. *Journal of Magnetism and Magnetic Materials*, 320(7):1398–1405, 2008.

[264] Nipu Modak, Amitava Datta, and Ranjan Ganguly. Cell separation in a microfluidic channel using magnetic microspheres. *Microfluidics and Nanofluidics*, 6(5):647, 2009.

[265] Saud A. Khashan and Edward P. Furlani. Effects of particle-fluid coupling on particle transport and capture in a magnetophoretic microsystem. *Microfluidics and Nanofluidics*, 12(1-4):565–580, 2012.

[266] Saud A Khashan and Edward P Furlani. Coupled particle-fluid transport and

magnetic separation in microfluidic systems with passive magnetic functionality. *Journal of Physics D: Applied Physics*, 46(12):125002, 2013.

[267] Nipu Modak, Amitava Datta, and Ranjan Ganguly. Numerical analysis of transport and binding of a target analyte and functionalized magnetic microspheres in a microfluidic immunoassay. *Journal of Physics D: Applied Physics*, 43(48):485002, 2010.

[268] Edward P. Furlani and Xiaozheng Xue. A model for predicting field-directed particle transport in the magnetofection process. *Pharmaceutical Research*, 29(5):1366–1379, 2012.

[269] E.L. Tóth, A. Füredi, K. Iván, and Péter Fürjes. Simulation and experimental validation of particle trapping in microfluidic magnetic separation (mms) system. *Procedia Engineering*, 168:1458–1461, 2016.

[270] Katarina Radulović, Filip Radovanović, Danijela Randjelović, Vesna Jović, Jelena Lamovec, Dana Vasiljević-Radović, and Zoran Jakčić. Modelling the size separation of ndfeb magnetic microparticles by magnetophoresis and gravity settling. In *2nd International Conference on Electrical, Electronic and Computing Engineering IcETRAN 2015*, Belgrade, 2015. ETRAN Society.

[271] J.W. Haverkort, S. Kenjereš, and C. R. Kleijn. Computational simulations of magnetic particle capture in arterial flows. *Annals of Biomedical Engineering*, 37(12):2436, 2009.

[272] Christopher W. Redman and Ian L. Sargent. Latest advances in understanding preeclampsia. *Science*, 308(5728):1592–1594, 2005.

[273] Angela Calvert. Isis insights: Cognitive developments, 2012.

[274] Paul Harrison, Chris Gardiner, and Ian L. Sargent. *Extracellular Vesicles in Health and Disease*. CRC Press, 2014.

[275] Frank M. White. *Viscous fluid flow*, volume 3. McGraw-Hill New York, 2006.

[276] John Happel and Howard Brenner. *Low Reynolds number hydrodynamics: with special applications to particulate media*, volume 1. Springer Science & Business Media, 2012.

[277] Susanne C. Brenner and Ridgway Scott. *The mathematical theory of finite element methods*, volume 15. Springer, 2008.

[278] Siu-Wing Cheng, Tamal K. Dey, and Jonathan Shewchuk. *Delaunay mesh generation*. CRC Press, 2012.

[279] L. Gary Leal. *Laminar Flow and Convective Transport Processes: Scaling Principles and Asymptotic Analysis*. Butterworth-Heinmann, 1993.

[280] Edward M. Purcell. Life at low reynolds number. *American Journal of Physics*, 45(1):3–11, 1977.

[281] William Morrow Kays, Michael E Crawford, and Bernhard Weigand. *Convective heat and mass transfer*. Tata McGraw-Hill Education, 2012.

[282] Henrik Bruus. *Theoretical microfluidics*. Oxford University Press, 2007.

[283] S. Elghobashi. On predicting particle-laden turbulent flows. *Applied Scientific Research*, 52(4):309–329, 1994.

[284] D. Hryb, M. Cardozo, S. Ferro, and M. Goldschmit. Particle transport in turbulent flow using both lagrangian and eulerian formulations. *International Communications in Heat and Mass Transfer*, 36(5):451–457, 2009.

[285] Joel P. Golden, Gusphyl A. Justin, Mansoor Nasir, and Frances S. Ligler. Hydrodynamic focusing - a versatile tool. *Analytical and Bioanalytical Chemistry*, 402(1):325–335, 2012.

[286] Marek Dziubiński. Hydrodynamic focusing for micro-rheological single-particle study. *Korea-Australia Rheology Journal*, 27(1):11–15, 2015.

[287] Gwo-Bin Lee, Chih-Chang Chang, Sung-Bin Huang, and Ruey-Jen Yang. The hydrodynamic focusing effect inside rectangular microchannels. *Journal of Micromechanics and Microengineering*, 16(5):1024, 2006.

[288] T. Stiles, R. Fallon, T. Vestad, J. Oakey, D.W.M. Marr, J. Squier, and R. Jimenez. Hydrodynamic focusing for vacuum-pumped microfluidics. *Microfluidics and Nanofluidics*, 1(3):280–283, 2005.

[289] John M.D. Coey. *Magnetism and magnetic materials*. Cambridge University Press, 2010.

[290] Bernard Dennis Cullity and Chad D. Graham. *Introduction to magnetic materials*. John Wiley & Sons, 2011.

[291] Hans Chrisitan Oersted. Experiments on the effect of a current of electricity on the magnetic needles. *Annals of Philosophy*, 16:273–277, 1820.

[292] Ralph Skomski. *Simple models of magnetism*. Oxford University Press, 2008.

[293] S. Chikazumi and S. Charap. *Physics of Magnetism*. J. Wiley & Sons, 1964.

[294] Kannan M. Krishnan. *Fundamentals and applications of magnetic materials*. Oxford University Press, 2016.

[295] Robert C O'handley. *Modern magnetic materials: principles and applications*, volume 830622677. Wiley New York, 2000.

[296] William Fuller Brown Jr. Thermal fluctuations of a single-domain particle. *Journal of Applied Physics*, 34(4):1319–1320, 1963.

[297] T.K. McNab, R.A. Fox, and A.J.F. Boyle. Some magnetic properties of magnetite (fe3o4) microcrystals. *Journal of Applied Physics*, 39(12):5703–5711, 1968.

[298] Ronald E Rosensweig. *Ferrohydrodynamics*. Courier Corporation, 2013.

[299] L. Néel. Théorie du traînage magnétique des ferromagnétiques en grains fins avec application aux terres cuites. *Annales de Géophysique*, 5:99–136, 1949.

[300] Geir Fonnum, Christer Johansson, Astrid Molteberg, Steen Morup, and Elin Aksnes. Characterisation of Dynabeads® by magnetization measurements and Mössbauer spectroscopy. *Journal of Magnetism and Magnetic Materials*, 293(1):41–47, 2005.

[301] Urs O. Häfeli, Martin A. Lobedann, Julia Steingroewer, Lee R. Moore, and Judy Riffle. Optical method for measurement of magnetophoretic mobility of individual magnetic microspheres in defined magnetic field. *Journal of Magnetism and Magnetic Materials*, 293(1):224–239, 2005.

[302] Naomi Wise, Tim Grob, Karl Morten, Ian Thompson, and Steve Sheard. Magnetophoretic velocities of superparamagnetic particles, agglomerates and complexes. *Journal of Magnetism and Magnetic Materials*, 384:328–334, 2015.

[303] Kara E. McCloskey, Jeffrey J. Chalmers, and Maciej Zborowski. Magnetophoretic mobilities correlate to antibody binding capacities. *Cytometry*, 40(4):307–315, 2000.

[304] Roel Wirix-Speetjens, Wim Fyen, Kaidong Xu, Jo De Boeck, and Gustaaf

Borghs. A force study of on-chip magnetic particle transport based on tapered conductors. *Magnetics, IEEE Transactions on*, 41(10):4128–4133, 2005.

[305] P.G.T. Saffman. The lift on a small sphere in a slow shear flow. *Journal of Fluid Mechanics*, 22(2):385–400, 1965.

[306] E. Kreyszig. *Advanced Engineering Mathematics 9th Edition with Wiley Plus WebCT Powerpack Set*. John Wiley & Sons Canada, Limited, 2006.

[307] Martin A. Plonus. *Applied electromagnetics*. McGraw-Hill College, 1978.

[308] T. Abbasov, S. Herdem, and M. Köksal. Particle capture in axial magnetic filters with power law flow model. *Journal of Physics D: Applied Physics*, 32(10):1097, 1999.

[309] Richard Courant, Kurt Friedrichs, and Hans Lewy. On the partial difference equations of mathematical physics. *IBM Journal of Research and Development*, 11(2):215–234, 1967.

[310] James Clerk Maxwell. *A treatise on Electricity and Magnetism*. Oxford Univeristy Press, 1873.

[311] ANSYS Inc. *ANSYS Maxwell 3D user's guide - Maxwell 3D*, 2010.

[312] Solomon Grigor'evich Mikhlin. *Variational methods in mathematical physics*, volume 1. Pergamon Press, Oxford, 1964.

[313] Mark Ainsworth and J. Tinsley Oden. *A posteriori error estimation in finite element analysis*, volume 37. John Wiley & Sons, 2011.

[314] Rüdiger Verfürth. *A Posteriori Error Estimation Techniques for Finite Element Methods*. Oxoford University Press, 2013.

[315] Ivo Babuška and Werner C. Rheinboldt. A posteriori error analysis of finite element solutions for one-dimensional problems. *SIAM Journal on Numerical Analysis*, 18(3):565–589, 1981.

[316] Olgierd C. Zienkiewicz and Jian Z. Zhu. A simple error estimator and adaptive procedure for practical engineerng analysis. *International Journal for Numerical Methods in Engineering*, 24(2):337–357, 1987.

[317] Olgierd C. Zienkiewicz and Craig A.W. Adaptive mesh refinement and a posteriori error estimation for the p-version of the finite element method. *Adaptive Computational Methods for Partial Differential Equations*, 16:33, 1983.

[318] Roxy Peck, Chris Olsen, and Jay L. Devore. *Introduction to statistics and data analysis*. Cengage Learning, 2015.

[319] George E.P. Box, William Gordon Hunter, and J. Stuart Hunter. *Statistics for experimenters: an introduction to design, data analysis, and model building*, volume 1. JSTOR, 1978.

[320] Paul R. Rosenbaum and Donald B. Rubin. Constructing a control group using multivariate matched sampling methods that incorporate the propensity score. *The American Statistician*, 39(1):33–38, 1985.

[321] Bernard W. Silverman. *Density estimation for statistics and data analysis*, volume 26. CRC press, 1986.

[322] Robert V. Hogg and Allen T. Craig. *Introduction to mathematical statistics.(5th edition)*. Upper Saddle River, New Jersey: Prentice Hall, 1995.

[323] Lawrence B. Mohr. *Understanding significance testing*, volume 73. Sage, 1990.

[324] Glenn D. Israel. *Determining sample size.* University of Florida Cooperative Extension Service, Institute of Food and Agriculture Sciences, EDIS Gainesville, 1992.

[325] Chemicell GmbH. http://www.chemicell.com/home/index.html, 2017.

[326] ThermoFisher Scientific. https://www.thermofisher.com/uk/en/home.html, October 2017.

[327] Philipp Rinklin, Hans-Joachim Krause, and Bernhard Wolfrum. On-chip control of magnetic particles. *Physica Status Solidi A: Applications and Materials Science*, 209(5):871–874, 2012.

[328] Matthias Samwer, Heinz-Jürgen Dehne, Felix Spira, Martin Kollmar, Daniel W. Gerlich, Henning Urlaub, and Dirk Görlich. The nuclear f-actin interactome of xenopus oocytes reveals an actin-bundling kinesin that is essential for meiotic cytokinesis. *The EMBO journal*, 32(13):1886–1902, 2013.

[329] Olayinka Oduwole, David Tim Grob, and Steve Sheard. Comparison between simulation and experimentally observed interactions between two magnetic beads in a fluidic system. *Journal of Magnetism and Magnetic Materials*, 407:8–12, 2016.

[330] R.L. Burden and J.D. Faires. *Numerical Analysis.* Mathematics Series. Brooks/Cole, 2001.

[331] Maciej Zborowski, Lee R. Moore, P. Stephen Williams, and Jeffrey J. Chalmers. Separations based on magnetophoretic mobility. *Separation Science and Technology*, 37(16):3611–3633, 2002.

[332] Roy Josephus Stephanus Derks. *Particle dynamics in magneto-fluidic microsystems.* PhD dissertation, Technische Universiteit Eindhoven, 2010.

[333] D.A. Clark and D.W. Emerson. Notes on rock magnetization characteristics in applied geophysical studies. *Exploration Geophysics*, 22(3):547–555, 1991.

[334] Christopher P. Hunt, Bruce M. Moskowitz, and Subir K. Banerjee. Magnetic properties of rocks and minerals. *Rock Physics & Phase Relations: A Handbook of Physical Constants*, pages 189–204, 1995.

[335] Ajay Kumar Gupta and Mona Gupta. Synthesis and surface engineering of iron oxide nanoparticles for biomedical applications. *Biomaterials*, 26(18):3995–4021, 2005.

[336] Private communication with chemicell, October 2014.

[337] Urs O. Häfeli, Wolfgang Schütt, Joachim Teller, and Maciej Zborowski. *Scientific and clinical applications of magnetic carriers*. Springer Science & Business Media, 2013.

[338] Zorione Herrasti, Erica de la Serna, Gisela Ruiz-Vega, and Eva Baldrich. Developing enhanced magnetoimmunosensors based on low-cost screen-printed electrode devices. *Reviews in Analytical Chemistry*, 35(2):53–85, 2016.

[339] G. Kasper, T. Niida, and M. Yang. Measurements of viscous drag on cylinders and chains of spheres with aspect ratios between 2 and 50. *Journal of Aerosol Science*, 16(6):535–556, 1985.

[340] E.R. Flynn and H.C. Bryant. A biomagnetic system for in vivo cancer imaging. *Physics in Medicine and Biology*, 50(6):1273, 2005.

[341] Natalie L. Adolphi, Dale L. Huber, Jason E. Jaetao, Howard C. Bryant, Debbie M. Lovato, Danielle L. Fegan, Eugene L. Venturini, Todd C. Monson, Trace E. Tessier, and Helen J. Hathaway. Characterization of magnetite

nanoparticles for SQUID-relaxometry and magnetic needle biopsy. *Journal of Magnetism and Magnetic Materials*, 321(10):1459–1464, 2009.

[342] L.T. Hien, L.K. Quynh, V.T. Huyen, B.D. Tu, N.T. Hien, D.M. Phuong, P.H. Nhung, D.T.H. Giang, and N.H. Duc. Dna-magnetic bead detection using disposable cards and the anisotropic magnetoresistive sensor. *Advances in Natural Sciences: Nanoscience and Nanotechnology*, 7(4):045006, 2016.

[343] David M. Diez, Christopher D. Barr, and Mine Cetinkaya-Rundel. *OpenIntro statistics*. CreateSpace, 2012.

[344] Jie Xu, Kalpesh Mahajan, Wei Xue, Jessica O. Winter, Maciej Zborowski, and Jeffrey J. Chalmers. Simultaneous, single particle, magnetization and size measurements of micron sized, magnetic particles. *Journal of Magnetism and Magnetic Materials*, 324(24):4189–4199, 2012.

[345] Kim van Ommering, Jeroen H. Nieuwenhuis, Leo J. van IJzendoorn, Bert Koopmans, and Menno W. J. Prins. Confined brownian motion of individual magnetic nanoparticles on a chip: Characterization of magnetic susceptibility. *Applied Physics Letters*, 89(14):142511, 2006.

[346] Mark D. Tarn, Sally A. Peyman, Damien Robert, Alexander Iles, Claire Wilhelm, and Nicole Pamme. The importance of particle type selection and temperature control for on-chip free-flow magnetophoresis. *Journal of Magnetism and Magnetic Materials*, 321(24):4115–4122, 2009.

[347] Brajalal Sinha, S. Anandakumar, Sunjong Oh, and CheolGi Kim. Micromagnetometry for susceptibility measurement of superparamagnetic single bead. *Sensors and Actuators A: Physical*, 182:34–40, 2012.

[348] Hakho Lee, Donhee Ham, and Robert M. Westervelt. *CMOS Biotechnology*. Springer, 2007.

[349] Peng Li, Devrim Kilinc, Ying-Fen Ran, and Gil U. Lee. Flow enhanced nonlinear magnetophoretic separation of beads based on magnetic susceptibility. *Lab on a Chip*, 13(22):4400–4408, 2013.

[350] Natalie L. Adolphi, Dale L. Huber, Howard C. Bryant, Todd C. Monson, Danielle L. Fegan, JitKang Lim, Jason E. Trujillo, Trace E. Tessier, Debbie M. Lovato, and Kimberly S. Butler. Characterization of single-core magnetite nanoparticles for magnetic imaging by squid relaxometry. *Physics in Medicine and Biology*, 55(19):5985, 2010.

[351] Scott S.H. Tsai, Ian M. Griffiths, and Howard A. Stone. Microfluidic immunomagnetic multi-target sorting-a model for controlling deflection of paramagnetic beads. *Lab on a Chip*, 11(15):2577–2582, 2011.

[352] Ruey-Jen Yang, Chih-Chang Chang, Sung-Bin Huang, and Gwo-Bin Lee. A new focusing model and switching approach for electrokinetic flow inside microchannels. *Journal of Micromechanics and Microengineering*, 15(11):2141, 2005.

[353] Anders Wolff, Ivan Ryberg Perch-Nielsen, U.D. Larsen, P. Friis, Goran Goranovic, Claus Riber Poulsen, Jörg Peter Kutter, and Pieter Telleman. Integrating advanced functionality in a microfabricated high-throughput fluorescent-activated cell sorter. *Lab on a Chip*, 3(1):22–27, 2003.

[354] Shoji Takeuchi, Piotr Garstecki, Douglas B. Weibel, and George M. Whitesides. An axisymmetric flow-focusing microfluidic device. *Advanced Materials*, 17(8):1067–1072, 2005.

[355] Petra Paiè, Francesca Bragheri, Rebeca Martinez Vazquez, and Roberto Osellame. Straightforward 3d hydrodynamic focusing in femtosecond laser fabricated microfluidic channels. *Lab on a Chip*, 14(11):1826–1833, 2014.

[356] Harold van Schevensteen. Microfluidic separation of magnetic beads. MEng thesis, University of Oxford, 2014.

[357] Xiaole Mao, John Robert Waldeisen, and Tony Jun Huang. Microfluidic drifting–implementing three-dimensional hydrodynamic focusing with a single-layer planar microfluidic device. *Lab on a Chip*, 7(10):1260–1262, 2007.

[358] Michael A. Daniele, Darryl A. Boyd, David R. Mott, and Frances S. Ligler. 3d hydrodynamic focusing microfluidics for emerging sensing technologies. *Biosensors and Bioelectronics*, 67:25–34, 2015.

[359] Mélanie Gassner, Anne-Laure Abonnenc, Hong-Xu Chen, Jacques Morandini, Jacques Josserand, Joel S Rossier, Jean-Marc Busnel, and Hubert H Girault. Magnetic forces produced by rectangular permanent magnets in static microsystems. *Lab on a Chip*, 9(16):2356–2363, 2009.

[360] Benjamin B. Yellen, Ondrej Hovorka, and Gary Friedman. Arranging matter by magnetic nanoparticle assemblers. *Proceedings of the National Academy of Sciences of the United States of America*, 102(25):8860–8864, 2005.

[361] Jordi Faraudo, Jordi S. Andreu, Carles Calero, and Juan Camacho. Predicting the self-assembly of superparamagnetic colloids under magnetic fields. *Advanced Functional Materials*, 26(22):3837–3858, 2016.

[362] W. Möller, Iku Nemoto, and Joachim Heyder. Effect of magnetic bead agglomeration on cytomagnetometric measurements. *IEEE Transactions on Nanobioscience*, 2(4):247–254, 2003.

[363] Frank Wittbracht, B. Eickenberg, Alexander Weddemann, and Andreas Hütten. Towards a programmable microfluidic valve: Formation dynamics of two-dimensional magnetic bead arrays in transient magnetic fields. *Journal of Applied Physics*, 109(11):114503, 2011.

[364] Frank Wittbracht, Alexander Weddemann, Bernhard Eickenberg, M. Zahn, and Andreas Hütten. Enhanced fluid mixing and separation of magnetic bead agglomerates based on dipolar interaction in rotating magnetic fields. *Applied Physics Letters*, 100(12):123507, 2012.

[365] Jianhan Lin, Min Li, Yanbin Li, and Qi Chen. A high gradient and strength bioseparator with nano-sized immunomagnetic particles for specific separation and efficient concentration of e. coli o157:h7. *Journal of Magnetism and Magnetic Materials*, 378(Supplement C):206–213, March 2015.

[366] Hengyi Xu, Zoraida P. Aguilar, Lily Yang, Min Kuang, Hongwei Duan, Yonghua Xiong, Hua Wei, and Andrew Wang. Antibody conjugated magnetic iron oxide nanoparticles for cancer cell separation in fresh whole blood. *Biomaterials*, 32(36):9758–9765, 2011.

[367] Uğur Tamer, İsmail H Boyacı, Erhan Temur, Adem Zengin, Ilker Dincer, and Yalçın Elerman. Fabrication of magnetic gold nanorod particles for immunomagnetic separation and sers application. *Journal of Nanoparticle Research*, 13(8):3167–3176, 2011.

[368] Naomi Wise. *The Development of a Biosensor for the Detection of Pathogenic Bacteria in Water*. PhD dissertation, University of Oxford, 2015.

[369] Fengshan Shen, Hyundoo Hwang, Young Ki Hahn, and Je-Kyun Park. Label-free cell separation using a tunable magnetophoretic repulsion force. *Analytical Chemistry*, 84(7):3075–3081, 2012.

[370] M. Takayasu, D.R. Kelland, and J.V. Minervini. Continuous magnetic separation of blood components from whole blood. *IEEE Transactions on Applied Superconductivity*, 10(1):927–930, March 2000.

[371] Jian Zeng, Yanxiang Deng, Pallavi Vedantam, Tzuen-Rong Tzeng, and Xiangchun Xuan. Magnetic separation of particles and cells in ferrofluid flow through a straight microchannel using two offset magnets. *Journal of Magnetism and Magnetic Materials*, 346:118–123, 2013.

[372] Yilong Zhou and Xiangchun Xuan. Diamagnetic particle separation by shape in ferrofluids. *Applied Physics Letters*, 109(10):102405, 2016.

[373] Yilong Zhou, Le Song, Liandong Yu, and Xiangchun Xuan. Continuous-flow sheathless diamagnetic particle separation in ferrofluids. *Journal of Magnetism and Magnetic Materials*, 412:114–122, 2016.

[374] Yilong Zhou, Le Song, Liandong Yu, and Xiangchun Xuan. Inertially focused diamagnetic particle separation in ferrofluids. *Microfluidics and Nanofluidics*, 21(1):14, 2017.

[375] Taotao Zhu, Francisco Marrero, and Leidong Mao. Continuous separation of non-magnetic particles inside ferrofluids. *Microfluidics and Nanofluidics*, 9(4-5):1003–1009, 2010.

[376] Taotao Zhu, Darcy J. Lichlyter, Mark A. Haidekker, and Leidong Mao. Analytical model of microfluidic transport of non-magnetic particles in ferrofluids under the influence of a permanent magnet. *Microfluidics and Nanofluidics*, 10(6):1233–1245, 2011.

[377] Litao Liang, Junjie Zhu, and Xiangchun Xuan. Three-dimensional diamagnetic particle deflection in ferrofluid microchannel flows. *Biomicrofluidics*, 5(3):034110, 2011.

[378] Angeles Ivón Rodríguez-Villarreal, Mark D. Tarn, Leigh A. Madden, Julia B. Lutz, John Greenman, Josep Samitier, and Nicole Pamme. Flow focussing of

particles and cells based on their intrinsic properties using a simple diamagnetic repulsion setup. *Lab on a Chip*, 11(7):1240–1248, 2011.

[379] Sally A. Peyman, Alexander Iles, and Nicole Pamme. Mobile magnetic particles as solid-supports for rapid surface-based bioanalysis in continuous flow. *Lab on a Chip*, 9(21):3110–3117, 2009.

[380] Jun Yang, Ying Huang, Xujing Wang, Xiao-Bo Wang, Frederick F. Becker, and Peter R.C. Gascoyne. Dielectric properties of human leukocyte subpopulations determined by electrorotation as a cell separation criterion. *Biophysical Journal*, 76(6):3307–3314, 1999.

[381] Maciej Zborowski, Graciela R. Ostera, Lee R. Moore, Sarah Milliron, Jeffrey J. Chalmers, and Alan N. Schechter. Red blood cell magnetophoresis. *Biophysical Journal*, 84(4):2638–2645, 2003.

[382] Hilding Faxén. Der widerstand gegen die bewegung einer starren kugel in einer zähen flüssigkeit, die zwischen zwei parallelen ebenen wänden eingeschlossen ist. *Annalen der Physik*, 373(10):89–119, 1922.

[383] Howard Brenner. The slow motion of a sphere through a viscous fluid towards a plane surface. *Chemical Engineering Science*, 16(3):242–251, 1961.

[384] Raymond G. Cox and Howard Brenner. The slow motion of a sphere through a viscous fluid towards a plane surface-ii small gap widths, including inertial effects. *Chemical Engineering Science*, 22(12):1753–1777, 1967.

[385] Robert H. Davis, Jean-Marc Serayssol, and E.J. Hinch. The elastohydrodynamic collision of two spheres. *Journal of Fluid Mechanics*, 163:479–497, 1986.

[386] Erica D. Pratt, Chao Huang, Benjamin G. Hawkins, Jason P. Gleghorn, and

Brian J. Kirby. Rare cell capture in microfluidic devices. *Chemical Engineering Science*, 66(7):1508–1522, April 2011.

[387] Rui Cheng, Taotao Zhu, and Leidong Mao. Three-dimensional and analytical modeling of microfluidic particle transport in magnetic fluids. *Microfluidics and Nanofluidics*, 16(6):1143–1154, 2014.

[388] R. Allen Bowling. A theoretical review of particle adhesion. In *Particles on Surfaces 1*, pages 129–142. Springer, 1988.

[389] H. Krupp. Particle adhesion theory and experiment. *Advances in Colloid and Interface Science*, 1(2):111 – 239, 1967.

[390] Nicole Pamme, Jan C.T. Eijkel, and Andreas Manz. On-chip free-flow magnetophoresis: Separation and detection of mixtures of magnetic particles in continuous flow. *Journal of Magnetism and Magnetic Materials*, 307(2):237–244, 2006.

[391] Guisheng Zhuang, Thomas G. Jensen, and Jörg P. Kutter. Detection of unlabeled particles in the low micrometer size range using light scattering and hydrodynamic 3d focusing in a microfluidic system. *Electrophoresis*, 33(12):1715–1722, 2012.

[392] A.S. Utada, El Lorenceau, D.R. Link, P.D. Kaplan, H.A. Stone, and D.A. Weitz. Monodisperse double emulsions generated from a microcapillary device. *Science*, 308(5721):537–541, 2005.

[393] Rebecca A. Dragovic, Jennifer H. Southcombe, Dionne S. Tannetta, Christopher W. G. Redman, and Ian L. Sargent. Multicolor flow cytometry and nanoparticle tracking analysis of extracellular vesicles in the plasma of normal pregnant and pre-eclamptic women. *Biology of Reproduction*, 89(6), 2013.

[394] Ming Ma, Yu Zhang, Wei Yu, Hao-ying Shen, Hai-qian Zhang, and Ning Gu. Preparation and characterization of magnetite nanoparticles coated by amino silane. *Colloids and Surfaces A: Physicochemical and Engineering Aspects*, 212(2–3):219–226, 2003.

[395] Xianqiao Liu, Huizhou Liu, Jianmin Xing, Yueping Guan, Zhiya Ma, Guobin Shan, and Chengli Yang. Preparation and characterization of superparamagnetic functional polymeric microparticles. *China Particuology*, 1(2):76–79, 2003.

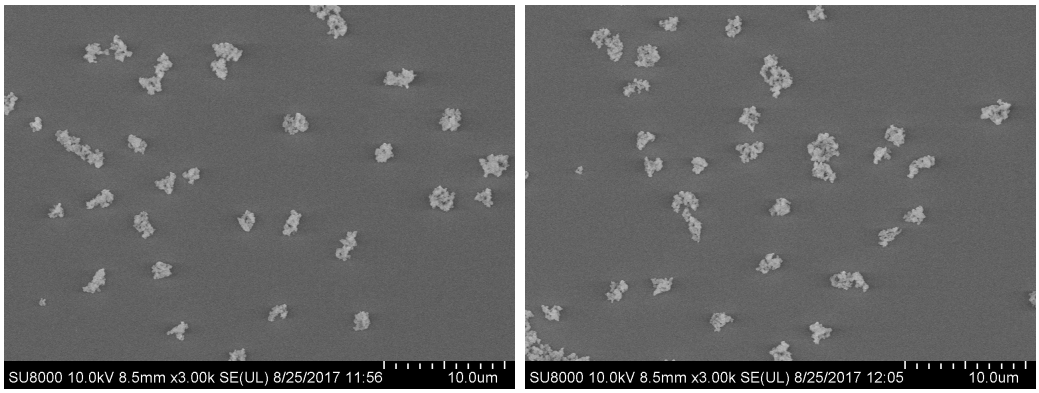
[396] Xianqiao Liu, Zhiya Ma, Jianmin Xing, and Huizhou Liu. Preparation and characterization of amino-silane modified superparamagnetic silica nanospheres. *Journal of Magnetism and Magnetic Materials*, 270(1–2):1–6, 2004.

Appendix A

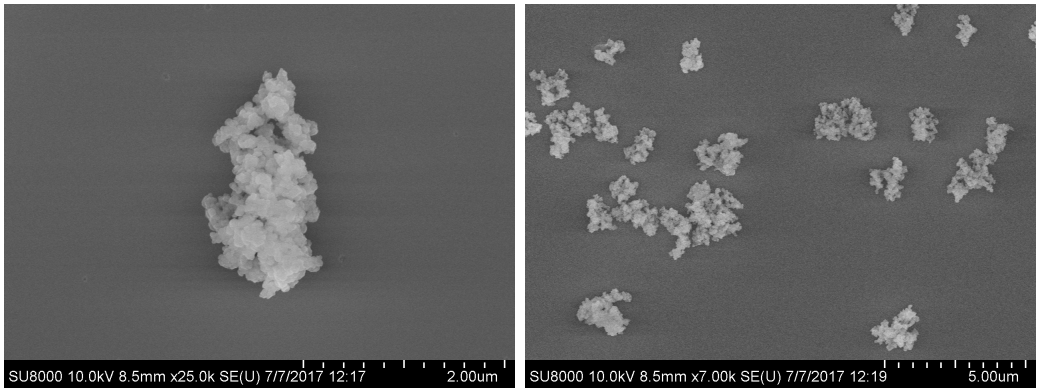
Magnetic bead imaging

A.1 SEM images of magnetic beads

All magnetic bead types were imaged using scanning electron microscopy (SEM). The SEM images were used to visualize the particles' shape and to estimate their size distribution. The following pictures show the SEM images of the various particle types. Similar images can be found in the literature [338].



(a)



(b)

Figure A.1: SEM images of magnetic Chemicell beads. (a) Chemicell ScreenMAG beads. (b) Chemicell SiMAG beads.

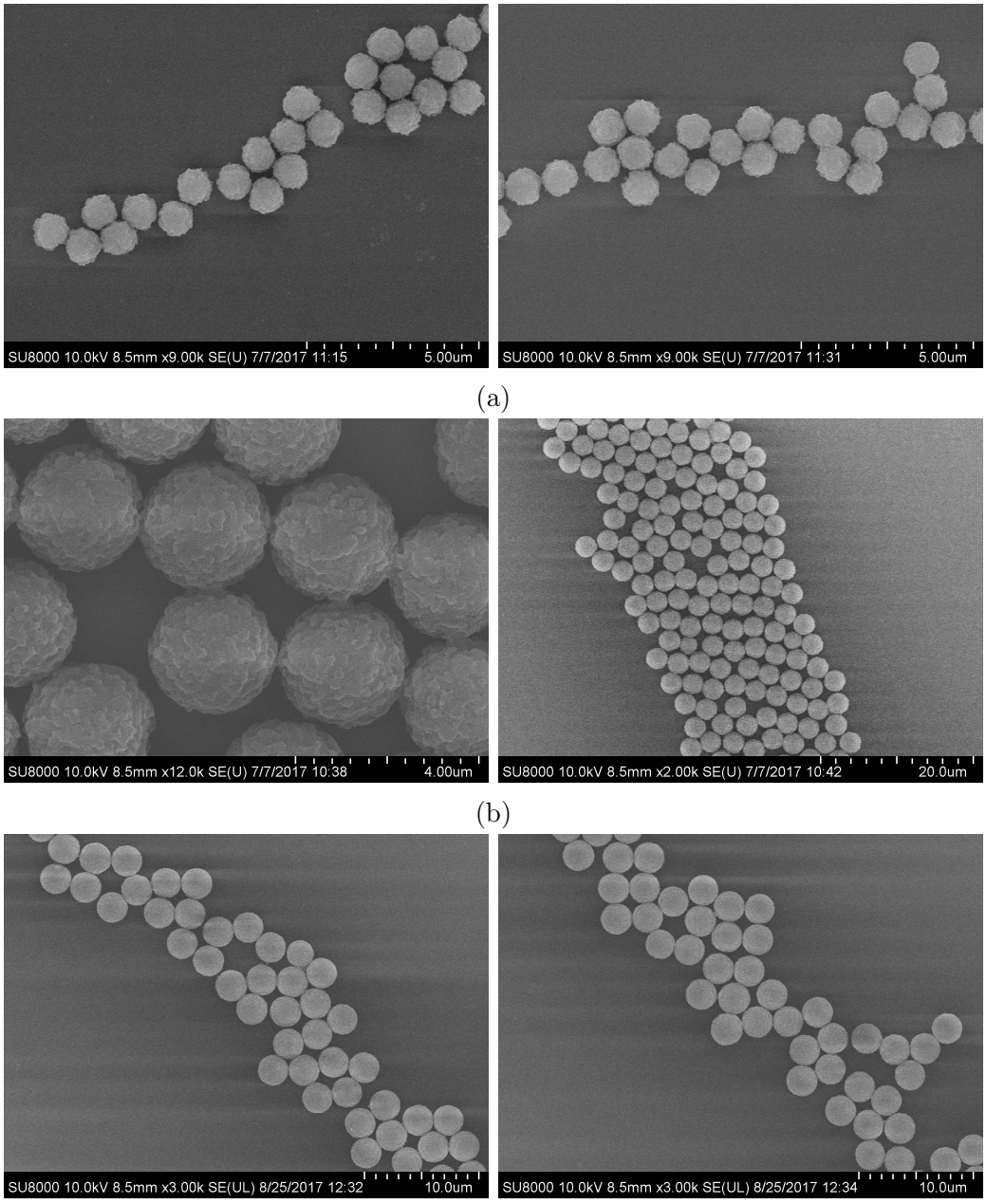


Figure A.2: SEM images of magnetic Dynabead microspheres. (a) Dynabeads My-One. (b) Dynabeads M280. (c) Dynabeads M270.

Appendix B

Magnetic bead separation

B.1 Magnetic bead separation in continuous flow

Experimental results of the continuous separation using the Double Magnet configuration. The flow rate ratio was kept as close as possible to 1 : 1 : 1 for all flow rates.

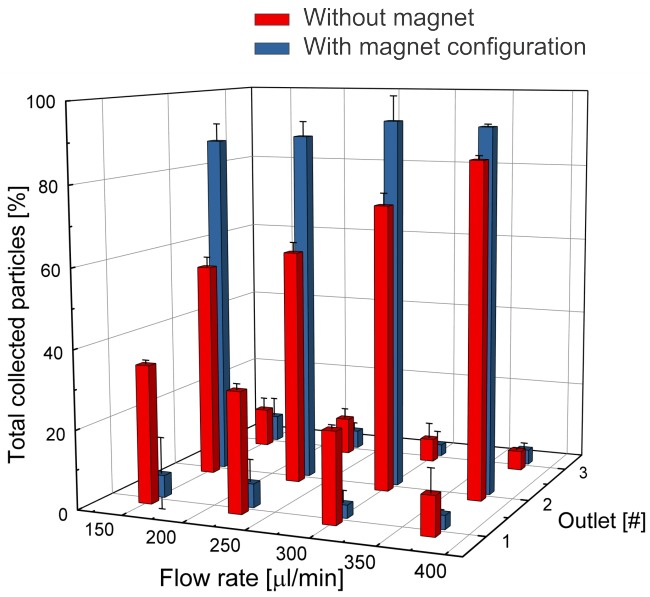


Figure B.1: Comparison of the magnetic bead separation efficiency in continuous flow. The bar plot shows the relative separation of the iBidi μ-Slide III 3in3 with and without the double magnet configuration in place. The flow rate is the sum of all inlet flow rates.

Appendix C

Superparamagnetic microspheres in an external magnetic field

C.1 Interaction between single superparamagnetic microspheres

Magnetic particles induce a magnetic dipole when exposed to an external magnetic field. The induced magnetic dipoles of the particles all point in the same direction. Thus, the magnetic particles experience a repellent force (F_{p*}) between each other. This phenomena can be seen in Figure C.1 where the single magnetic particles have all approximately the same distance to each other. The inset in Figure C.1 schematically shows the repelling force between two particles.

C.2 Interaction between superparamagnetic agglomerations

The magnetic particles formed mostly chains but also more complicated 3D structures when being exposed to an external magnetic field, as seen in Figure C.2. The

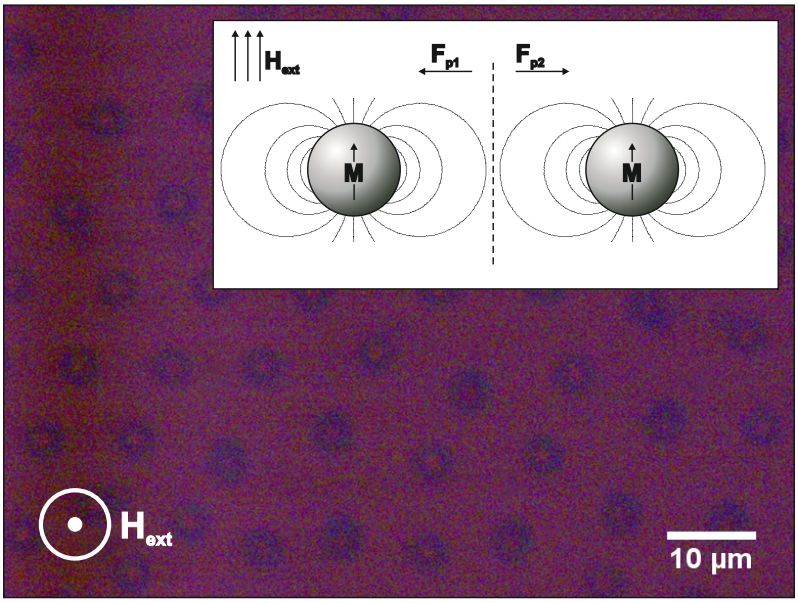
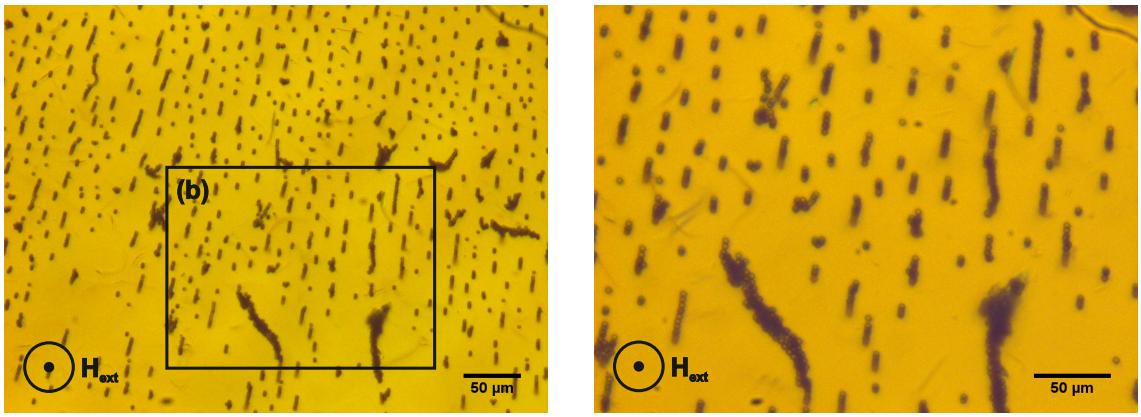


Figure C.1: Magnetic particles (Dynabeads M270) induce a magnetic dipole once they are exposed to an external magnetic field (H_{ext}). The induced dipoles of the particles point all in the same direction (out of plane). This causes a repelling magnetic force between all magnetic particles, which prevents them from touching each other. The inset schematically shows the induced magnetic dipole (M) and the direction of the repelling force, F_{p*}, the two particles experience when getting closer.

fact that the chains and larger agglomerates go out of focus shows that the particles align along the field lines of the external magnetic field H_{ext}.



(a) 10× magnification (b) 20× magnification

Figure C.2: (a) Magnetic particles interact with each other and form chains or more complicated 3D structures. (b) Magnified view of the framed section in Figure C.2a. The particle agglomerates are mostly out of focus since they align along the field lines of the external magnetic field, H_{ext}, which points out of plane.